Imperial College London

Developing Organic Semiconductors with Mixed Ionic and Electronic Transport for Organic Bioelectronics

Iuliana Petruța Maria

Submitted in partial fulfilment of the requirements for the degree of

Doctor of Philosophy in Chemistry

Imperial College London

Department of Chemistry

August 2020

I Declaration

The work described in this thesis was carried out in the Department of Chemistry at Imperial College London between October 2016 and March 2020 under the supervision of Professor Iain McCulloch. I certify that all the work herein is my own unless stated otherwise.

Iuliana Petruța Maria, August 2020

II Copyright Declaration

The copyright of this thesis rests with the author. Unless otherwise indicated, its contents are licensed under a Creative Commons Attribution-Non Commercial-No Derivatives 4.0 International Licence (CC BY-NC-ND). Under this licence, you may copy and redistribute the material in any medium or format on the condition that you credit the author, do not use it for commercial purposes and do not distribute modified versions of the work. When reusing or sharing this work, ensure you make the licence terms clear to others by naming the licence and linking to the licence text. Please seek permission from the copyright holder for uses of this work that are not included in this licence or permitted under UK Copyright Law.

III Acknowledgements

First, I would like to thank Prof Iain McCulloch for his supervision, guidance and continuous encouragement during my time at Imperial College London. I am very grateful for your support and trust in my abilities, as well as the opportunities I was given to learn and grow throughout my PhD.

I am also thankful to the members of the group for creating such a friendly and supportive atmosphere at work: Ada, Adam, Alex, Andy, Ben, Cameron, Craig, Du, Flo, Helen, Hu, James, Karl, Mark, Matt, Max, Maxime, Nicola, Rawad, Raj, Sam, Sarah, Weimin, Xingxing and Zeinab. I am particularly thankful to Dr Alexander Giovannitti for training me when I joined the lab, introducing me to the field and all the helpful discussions over the past few years. I am also grateful to the students I had the chance to co-supervise in the lab, for their hard work and dedication during their projects: Xizi, Sophie and Shao-Ling. I also want to thank members of the Heeney group for making both Harwood and MSRH labs such a great place to work, in particular Tom, Notina, Charlotte, Qiao, Pete, Florian, Filip, Fei, Shengyu and Martina. I will definitely remember the good times (and often failures) of working in the synthesis labs and it has been great a pleasure working with you all.

I would also like to thank Prof Jonathan Rivnay and his group for hosting me at Northwestern University and their invaluable contributions to my projects. I am particularly grateful to Dr Bryan Paulsen for teaching me how to fabricate transistors and helping me understand better the physics behind devices. I also had the great opportunity to collaborate with Prof Sahika Inal and her group members, David, Achilleas, Jokubas at KAUST- thank you for your contributions, great discussions and useful insight.

I would also like to thank my friends in other departments, in halls and back at home for always being supportive and making my PhD years much more enjoyable. Finally, I would like to thank my family and my boyfriend for their endless support, understanding and encouragement for everything I do.

IV Abstract

Organic semiconductors have demonstrated great ability to act as electroactive components at the interface with biological media, featuring in numerous bioelectronic applications over the past two decades. Electron-transporting (n-type) materials, in particular, are essential for probing biological events that involve generation of electrons such as metabolite sensing or for developing electrochemical complementary inverters. However, current n-type materials have a narrow scope and low performance compared to their p-type counterparts, providing ample opportunities for improvement through chemical design. This work explores the relationship between the structure of n-type polymers, their electrochemical activity and their performance in organic electrochemical transistors (OECTs) operating in aqueous electrolytes.

The polymer series designed in this work consist of electron deficient units functionalised with polar ethylene glycol side chains, which ensure penetration and transport of hydrated ions into the bulk of the polymer. Using the widely investigated naphthalene diimide (NDI)-bithiophene motif, it was found that introduction of alkyl spacers in between the conjugated backbone and the ethylene glycol units improves the electronic mobility and operational stability of the polymer in OECTs. Next, the NDI core was laterally extended to enhance the polymer backbone coplanarity, with the aim of improving its charge transport properties. The naphthodithiophene diimide unit led to the development of polymers with improved stability during extended cycling relative to their NDI-based analogues, as well as stable n-type OECT operation in aqueous electrolytes. The third study employed a backbone engineering strategy to increase the electron affinity of isoindigo-based copolymers and allow n-type operation within the electrochemical window of water. The polarity of OECT operation was controlled through subtle backbone modifications, achieving a transition from unipolar p-type to unipolar n-type operation with a thickness-normalised g_m of up to 60.10 and 0.148 S/cm, respectively.

Contents

I Declaration **3**

II Copyright Declaration **4**

III Acknowledgements **5**

IV Abstract **7**

V Abbreviations **12**

VI Publications **15**

Chapter 1. Introduction **17**

1.1 Organic Electronics 18
1.1.1 Introduction to organic semiconductors 18
1.1.2 Charge transport in organic semiconductors 20
1.1.3 Principles of organic field-effect transistors 22
1.2 Mixed ionic-electronic transport in polymers 27
1.2.1 Introduction to mixed ionic-electronic transport 27
1.2.2 Conjugated polymers in organic bioelectronics 29
1.2.3 Organic electrochemical transistors 31
1.2.4 Extracting material parameters from OECT performance 34
1.3 OECT channel materials 37
1.3.1 P-type channel materials 37
1.3.2 N-type channel materials 42
1.3.3 Applications of n-type OECT materials 46
1.3.4 Design considerations for n-type OECT materials 48
1.4 Thesis aims and overview 50

Chapter 2. The effect of alkyl spacers on the mixed ionic-electronic conduction properties of naphthalene diimide-copolymers **52**

2.1 General information and attributions 53
2.2 Introduction 53
2.3 Synthesis of the polymers 56
2.4 Properties of the polymers 59

2.5 Electrochemical activity in aqueous electrolytes 61
2.6 GIWAXS analysis of the polymers 65
2.6.1 Structural properties of the neat polymer films 65
2.6.2 Influence of aqueous electrolytes on the structural properties 68
2.7 Electrical characterisation 71
2.7.1 OFET performance 71
2.7.2 OECT performance 72
2.7.3 Stability measurements 77
2.8 Conclusions 79
Chapter 3. Increasing the backbone coplanarity of naphthalene diimide-copolymers with mixed ionic and electronic conduction 81
3.1 General information and attributions 82
3.2 Introduction 82
3.3 Density Functional Theory calculations 84
3.4 Synthesis 86
3.4.1 Synthesis of the side chains 86
3.4.2 Synthesis of the NDI monomers 88
3.4.3 Synthesis of the NDTI monomers 89
3.4.4 Synthesis of the polymers 92
3.5 Physical and optoelectronic properties 94
3.6 GIWAXS analysis of the polymer films 96
3.7 Electrochemical activity in aqueous electrolytes 99
3.7.1 Cyclic voltammetry of the polymer films 99
3.7.2 Spectroelectrochemical measurements of the polymer films 101
3.7.3 EQCM-D analysis 103
3.8 OECT performance 105
3.8.1 OECT performance of P3gNDI 105
3.8.2 OECT performance of P4gNDTI 108
3.9 Conclusions 111
Chapter 4. Tuning the electron affinity of isoindigo-based copolymers for n-type operation in OECTs 113
4.1 General information and attributions 114
4.2 Introduction 114
4.3 Synthesis of the polymers 117

4.4 Properties of the polymers 119
4.5 GIWAXS analysis of the polymer thin films 122
4.6 Characterisation of the T2 and T2FBT copolymers 126
4.6.1 Electrochemical activity in aqueous electrolytes 126
4.6.2 QCM-D analysis 127
4.6.3 OECT performance 128
4.7 Characterisation of the TzBT copolymers 134
4.7.1 Interaction with aqueous electrolytes 134
4.7.2 OECT performance 137
4.8 Conclusions 140
4.9 Synthetic progress towards other AII copolymers 142
Chapter 5. Experimental procedures 145
5.1 Synthetic procedures for Chapter 2 149
5.2 Synthetic procedures for Chapter 3 155
5.2.1 Synthesis of the linear side chains 155
5.2.2 Synthesis of the branched side chains 158
5.2.3 Synthesis of the NDI monomers 164
5.2.4 Synthesis of the NDTI monomers 166
5.2.5 Synthesis of the polymers 174
5.3 Synthetic procedures for Chapter 4 178
5.3.1 Synthesis of the monomers 178
5.3.2 Synthesis of the polymers 182
5.3.3 Synthesis of acceptor-acceptor polymers 186
Conclusions and Outlook 188
Bibliography 192
Appendices 208
Appendix A. Supplementary figures for Chapter 2 209
Appendix B. Supplementary figures for Chapter 3 212
Appendix C. Supplementary figures for Chapter 4 215
Appendix D. K^+ ion sensors for plant monitoring 218
D1. Introduction 218
D2. Synthesis of the small molecule 220
D3. Optical response upon ion complexation 223

D4. Conclusions and outlook..... 225
D5. Experimental procedures 226
D6. References..... 235
Appendix E. NMR Spectra..... 237

V Abbreviations

δ	chemical shift
λ	wavelength
°	degrees
μ	mobility
Å	angstrom
AII	azaisoindigo
BT	benzo[c][1,2,5]thiadiazole
br.	broad
C	celsius
C^*	volumetric capacitance
calc.	calculated
CB	chlorobenzene
CV	cyclic voltammetry
d	channel thickness
$Đ$	dispersity
DCB	dichlorobenzene
DCM	dichloromethane
DFT	density functional theory
DMF	*N*,*N*'-dimethylformamide
DPP	diketopyrrolopyrrole
EA	electron affinity
EG	ethylene glycol
E_g	band gap
EG-OFET	electrolyte-gated organic field-effect transistor
EI	electron ionisation
EIS	electrochemical impedance spectroscopy
equiv	equivalents
EQCM-D	electrochemical quartz crystal microbalance with dissipation monitoring
eV	electron volt

GIWAXS	grazing incidence wide-angle X-ray scattering
g_m	transconductance
GPC	gel permeation chromatography
HOMO	highest occupied molecular orbital
HQSC	heteronuclear single quantum coherence
HRMS	high-resolution mass spectrometry
ICT	intramolecular charge transfer
I_D	drain current
II	isoindigo
IP	ionisation potential
IR	infrared
ITO	indium tin oxide
J	coupling constant
L	channel length
LUMO	lowest unoccupied molecular orbital
m/z	mass to charge
MALDI	matrix-assisted laser desorption/ionisation
MeCN	acetonitrile
MeOH	methanol
M_n	number average molecular weight
MOSFET	metal-oxide-semiconductor field-effect transistor
MS	mass spectrometry
M_w	weight average molecular weight
n-BuLi	*N*-bromosuccinimide
NDI	naphthalene diimide
NDTI	naphthodithiophene diimide
NIR	near-infrared
NMR	nuclear magnetic resonance
NTI	naphtho[2,3-b]thiophene diimide
OECT	organic electrochemical transistor
OFET	organic field-effect transistor
OLED	organic light-emitting diode
OMIEC	organic mixed ionic-electronic conductor

OPV	organic photovoltaics
ORR	oxygen reduction reaction
OSC	organic semiconductor
P(*o*-tol)$_3$	tri(*o*-tolyl)phosphine
Pd$_2$(dba)$_3$	tris(dibenzylideneacetone)dipalladium(0)
PESA	photoelectron spectroscopy in air
PPh$_3$	triphenylphosphine
ppm	parts per million
QCM-D	quartz crystal microbalance with dissipation monitoring
rpm	revolutions per minute
S_N2	second-order nucleophilic substitution
S_NH	nucleophilic hydrogen substitution
soln.	solution
T2	bithiophene
T2FBT	5,6-difluoro-4,7-di(thiophen-2-yl)-benzothiadiazole
TBAPF$_6$	tetrabutylammonium hexafluorophosphate
T_d	decomposition temperature
TGA	thermogravimetric analysis
THF	tetrahydrofuran
TLC	thin layer chromatography
ToF	time-of-flight
Ts	tosyl
TzBT	4,7-dithiazolyl-benzothiadiazole
UV-Vis	ultraviolet-visible
v/v	volume by volume
V_D	drain voltage
V_G	gate voltage
V_T	threshold voltage
W	channel width

VI Publications

(1) **I. P. Maria**, A. Giovannitti, B. D. Paulsen, A. Savva, R. Wu, A. Basu, R. Hallani, W. Du, T. D. Anthopoulos, S. Inal, J. Rivnay, I. McCulloch. The effect of alkyl spacers on the mixed ionic-electronic conduction properties of n-type polymers. **2020**, submitted.

(2) **I. P. Maria**, B. D. Paulsen, W. Du, J. Surgailis, G. T. Harrison, C. Combe, S. De Wolf, S. Inal, J. Rivnay, I. McCulloch. Tuning the electron affinity of isoindigo-based copolymers for n-type operation in organic electrochemical transistors. **2020**, in preparation.

Other work carried out during my PhD has contributed to the following publications, but the results will not be discussed in this thesis:

(3) A. Giovannitti, **I. P. Maria**, D. Hanifi, M. J. Donahue, D. Bryant, K. J. Barth, B. E. Makdah, A. Savva, D. Moia, M. Zetek, P. R. F. Barnes, O. G. Reid, S. Inal, G. Rumbles, G. G. Malliaras, J. Nelson, J. Rivnay, I. McCulloch. The Role of the Side Chain on the Performance of N-Type Conjugated Polymers in Aqueous Electrolytes. *Chem. Mater.* **2018**, *30*, 2945–2953.

(4) I. McCulloch, A. Giovannitti, **I. P. Maria**, N-type conjugated polymers, International Patent Application No. PCT/GB2018/051347, Filed 18 May 2018.

(5) A. M. Pappa, D. Ohayon, A. Giovannitti, **I. P. Maria**, A. Savva, I. Uguz, J. Rivnay, I. McCulloch, R. M. Owens, S. Inal. Direct Metabolite Detection with an N-Type Accumulation Mode Organic Electrochemical Transistor. *Science Advances* **2018**, *4*, eaat0911.

(6) V. Venkatraman, J. T. Friedlein, A. Giovannitti, **I. P. Maria**, I. McCulloch, R. R. McLeod, J. Rivnay. Subthreshold Operation of Organic Electrochemical Transistors for Biosignal Amplification. *Advanced Science* **2018**, *5*, 1800453.

(7) W. Du, D. Ohayon, C. Combe, L. Mottier, **I. P. Maria**, R. S. Ashraf, H. Fiumelli, S. Inal, I. McCulloch. Improving the Compatibility of Diketopyrrolopyrrole Semiconducting Polymers for Biological Interfacing by Lysine Attachment. *Chem. Mater.* **2018**, *30*, 6164–6172.

(8) Y. Zhang, A. Savva, S. Wustoni, A. Hama, **I. P. Maria**, A. Giovannitti, I. McCulloch, S. Inal.Visualizing the Solid–Liquid Interface of Conjugated Copolymer Films Using Fluorescent Liposomes. *ACS Appl. Bio Mater.* **2018**, *1*, 1348–1354.

(9) D. Moia, A. Giovannitti, A. A. Szumska, **I. P. Maria**, E. Rezasoltani, M. Sachs, M. Schnurr, P. R. F. Barnes, I. McCulloch, J. Nelson. Design and Evaluation of Conjugated Polymers with Polar Side Chains as Electrode Materials for Electrochemical Energy Storage in Aqueous Electrolytes. *Energy Environ. Sci.* **2019**, *12*, 1349–1357.

(10) M. Moser, K. J. Thorley, F. Moruzzi, J. F. Ponder, **I. P. Maria**, A. Giovannitti, S. Inal, I. McCulloch. Highly Selective Chromoionophores for Ratiometric Na^+ Sensing Based on an Oligoethyleneglycol Bridged Bithiophene Detection Unit. *Journal of Materials Chemistry C* **2019**, *7*, 5359–5365.

(11) A. Savva, D. Ohayon, J. Surgailis, A. F. Paterson, T. C. Hidalgo, X. Chen, **I. P. Maria**, B. D. Paulsen, A. J. Petty, J. Rivnay, I McCulloch, S. Inal. Solvent Engineering for High-Performance n-Type Organic Electrochemical Transistors. *Advanced Electronic Materials* **2019**, *5*, 1900249.

(12) D. Ohayon, G. Nikiforidis, A. Savva, A. Giugni, S. Wustoni, T. Palanisamy, X. Chen, **I. P. Maria**, E. Di Fabrizio, P. M. F. J. Costa, I. McCulloch, S. Inal. Biofuel Powered Glucose Detection in Bodily Fluids with an N-Type Conjugated Polymer. *Nature Materials* **2020**, *19*, 456–463.

(13) X. Wu, A. Surendran, M. Moser, S. Chen, B. T. Muhammad, **I. P. Maria**, I. McCulloch, W. L. Leong. Universal Spray-Deposition Process for Scalable, High-Performance, and Stable Organic Electrochemical Transistors. *ACS Appl. Mater. Interfaces* **2020**, *12*, 20757–20764.

(14) A. Melianas, T. J. Quill, G. LeCroy, Y. Tuchman, H. v. Loo, S. T. Keene, A. Giovannitti, H. R. Lee, **I. P. Maria**, I. McCulloch, A. Salleo. Temperature-Resilient Solid-State Organic Artificial Synapses for Neuromorphic Computing. *Science Advances* **2020**, *6*, eabb2958.

(15) A. F. Paterson, A. Savva, S. Wustoni, L. Tsetseris, B. D. Paulsen, H. Faber, A. H. Emwas, X. Chen, G. Nikiforidis, T. C. Hidalgo, M. Moser, **I. P. Maria**, J. Rivnay, I. McCulloch, T. D. Anthopoulos, S. Inal. Water Stable Molecular N-Doping Produces Organic Electrochemical Transistors with High Transconductance and Record Stability. *Nature Communications* **2020**, *11*, 3004.

CHAPTER 1

Introduction

1.1 Organic Electronics

The rapidly growing demand for electronic devices with flexible, cost-efficient components has led to remarkable progress in organic electronics, with technologies such as organic light-emitting diode (OLED) displays and organic photovoltaic (OPV) modules already available in global markets. The interest in organic semiconductors (OSC) for electronic applications stems from their compatibility with flexible substrates, synthetic tunability and low energy processing methods, in contrast with their inorganic counterparts. Due to these reasons, organic semiconductors are actively investigated for the development of thin-film transistors,[1–3] organic solar cells,[4,5] energy storage[6,7] and neuromorphic computing.[8,9] More recently, new challenges have arisen from the emerging field of organic bioelectronics, which aims to couple organic electronics with biological systems for therapy, diagnostics and healthcare monitoring.[10–15]

1.1.1 Introduction to organic semiconductors

Organic semiconductors comprise a broad range of conjugated small molecules and polymers with sp^2-hybridised centres along a path of alternating single and double bonds. The overlap between unhybridised p_z orbitals perpendicular to the σ-framework gives rise to delocalised π-orbitals. Extended conjugation increases the range over which atomic orbitals can interact and leads to a broadening of the highest occupied and lowest unoccupied molecular orbitals (HOMO and LUMO) into electronic bands (**Figure 1.1**). Using inorganic semiconductor terminology, this gives rise to an occupied valence band and an unoccupied conduction band separated by a band gap (E_g).[16,17] A similar effect occurs due to interactions between the π-electronic density on adjacent molecules. This combination of intra- and inter-molecular delocalisation has a central role in determining the optical and charge transport properties exploited in a wide range of organic electronics applications.

The band gap can be also interpreted as the difference between the energy required to remove an electron from the top of the valence band (ionisation potential, IP) and the energy gained by adding an electron to the bottom of the conduction band (electron affinity, EA).[16,17] For polymers, the band gap generally decreases as the number of repeat units increases, until a certain effective conjugation length has been reached. At this point, the band gap stabilises and becomes independent of the degree of polymerisation or molecular weight.[18] The energy of the band gap determines the wavelength of light required to promote electrons from the valence band to the conduction band (absorption), as well as the wavelength of light emitted upon radiative relaxation (emission). Organic semiconductors typically absorb in the visible range of light, with band gaps between 1 eV and 4 eV.[19]

Organic semiconductors have a low density of mobile charge carriers and a low electrical conductivity in their pristine state. Charge carriers can be generated by introducing electrons into the conduction band or holes into the valence band through doping or electrical injection. Delocalisation of π-orbitals provides ideal pathways for the transport of electrons or holes, giving rise to electrical conductivity.

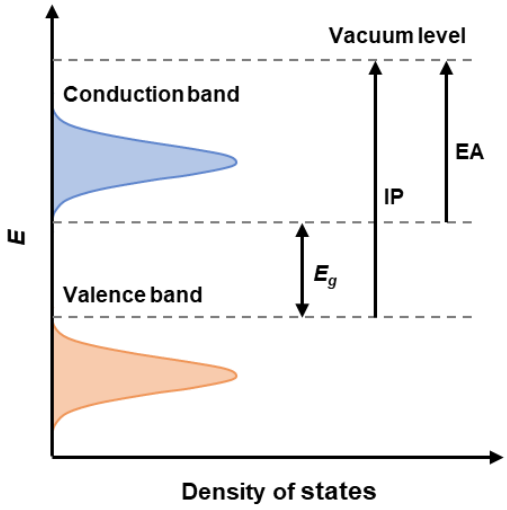


Figure 1.1. Schematic representation of the energy bands and band gap of an organic semiconductor, showing the density of states approximated with Gaussian distributions. (adapted from literature).[17]

1.1.2 Charge transport in organic semiconductors

The transport of electronic charges in the bulk of semiconducting polymers requires a combination of intrachain transport, facilitated by delocalisation of π-orbitals across the polymer chain and interchain transport, facilitated by π-π stacking of adjacent chains. The charge carrier mobility (μ) is a measure of the speed at which charge carriers can be transported under an applied electric field and is the main performance criterion for organic semiconductors. Extensive research in understanding structure-property relationships and the mechanisms of charge transport has led to the development of materials with hole and electron mobilities of up to ~ 20 $cm^2\ V^{-1}\ s^{-1}$ and 9 $cm^2\ V^{-1}\ s^{-1}$, respectively.[20] Interestingly, the charge carrier mobility along isolated polymer chains has been reported to be several orders of magnitude higher, reaching 600 $cm^2\ V^{-1}\ s^{-1}$ in ladder-type polymers.[21] This suggests that the limiting step of charge transport in organic semiconductors is generally the interchain transport.

For polymers with high charge carrier mobilities, the mechanism of charge transport has been described using the Boltzmann band model, where the transport occurs through diffusion facilitated by delocalisation of charge carrier wavefunctions over several molecules (**Figure 1.2a**).[20,22,23] Recent studies have estimated that band-like charge transport is only applicable to systems exhibiting $\mu \gtrsim 50\ cm^2\ V\ s^{-1}$, whereas most organic semiconductors show much lower charge carrier mobilities.[23,24] Due to the presence of weak van der Waals intermolecular interactions, organic semiconductors are characterised by intermolecular vibrations and structural disorder, which limits the degree of delocalisation of charge carriers. When charge carriers are localised on individual molecular sites, the charge transport proceeds as a series of hopping events between these sites ($\mu \lesssim 0.5\ cm^2\ V^{-1}\ s^{-1}$, **Figure 1.2c**).[23,25] An intermediate regime of charge transport has also been identified, in which there is a transient localisation of charge carriers on timescales shorter than the timescale of intermolecular vibrations. (**Figure 1.2b**).[25,26]

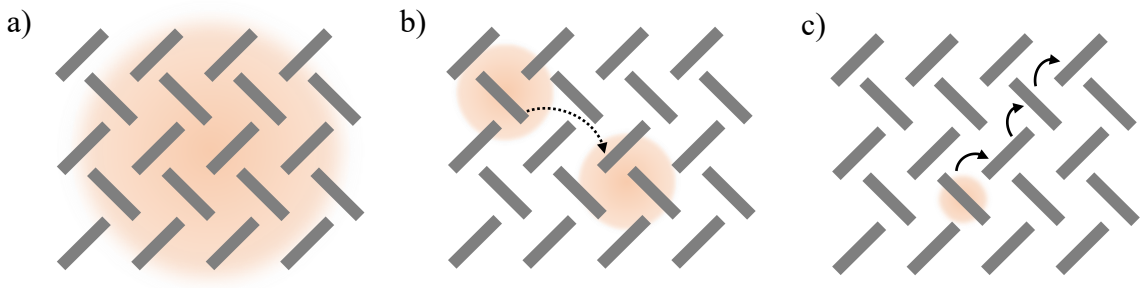


Figure 1.2. Schematic representation of the charge transport mechanism in (a) the Boltzmann band, (b) transient localisation and (c) hopping regimes. Organic semiconductor molecules are indicated in grey and the charge delocalisation is shown as orange areas (adapted from literature).[20,23]

To facilitate intrachain charge transport, many research efforts have been directed at increasing the coplanarity of adjacent monomer units and minimising the degree of energetic disorder along the polymer backbone. Fused monomers with rigid aromatic cores and extended π-conjugation have proved to be highly useful in this context.[1,27–29] For instance, replacing thiophene units in **P3HT** with a fused thienothiophene unit in **PBTTT** led to an increase in hole mobility by an order of magnitude (**Figure 1.3a**).[27] Other strategies include the use of non-covalent through-space interactions such as S···O interactions[30] or H-bonding,[31] which can act as a barrier for rotation and planarise the backbone (**Figure 1.3b**).

Backbone coplanarity and rigidity play an important role in facilitating interchain transport as well, allowing for more efficient π-π stacking. In addition to the molecular structure of the OSC, interchain charge transport is closely linked to the arrangement of the organic semiconductor in solid state, which determines the extent of orbital overlap. The vast majority of conjugated polymers are semicrystalline and show a heterogeneous microstructure with a mixture of crystalline and amorphous regions. As the charge transport occurs largely between the crystalline regions,[32] formation of tie-chains bridging adjacent crystalline domains is

critical for establishing a pathway for charge transport.[23,33,34] The probability of forming tie chains has been correlated with the molecular weight of the conjugated polymer, where a longer chain shows more intercrystallite connectivity .[33,35]

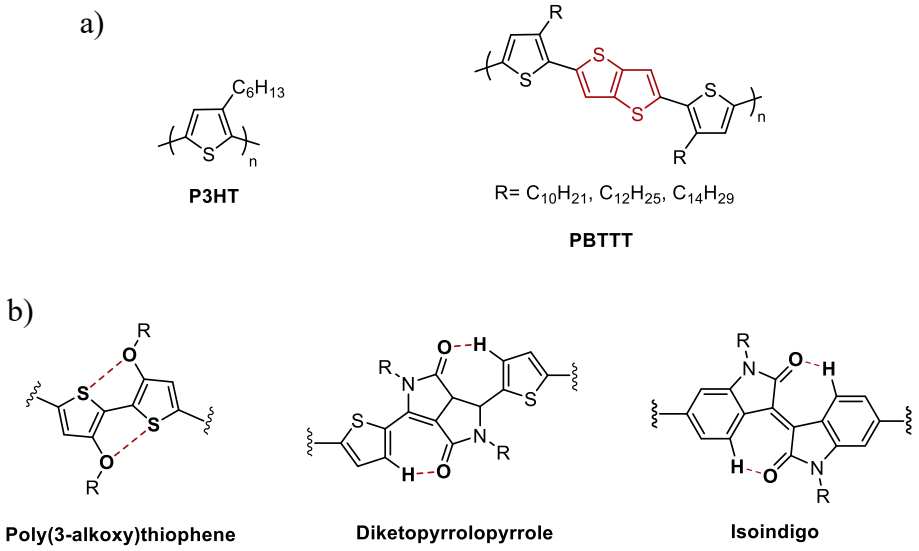


Figure 1.3. (a) Structures of **P3HT** and **PBTTT** polymers. (b) Planarising S···O and H-bonding interactions in poly(3-alkoxy)thiophene, diketopyrrolopyrrole and isoindigo backbones.

1.1.3 Principles of organic field-effect transistors

A solid-state device which has leveraged the charge transport properties of organic semiconductors is the organic field-effect transistor (OFET). Research efforts to incorporate organic semiconductors in FET configurations date back to the work of Tsumura et al. in 1986, who demonstrated a charge carrier mobility of ~ 10^{-5} cm^2 V^{-1} s^{-1}.[36] Despite the poor transistor characteristics, this example opened up promising directions for the development of electronic circuits on low-cost flexible substrates at near ambient temperature and pressure. With significant advances in understanding their device physics, OFETs are also used to characterise organic semiconductors and extract charge carrier mobilities for benchmarking different materials.[1,17,37,38]

The components of an OFET with a top gate bottom contact (TG-BC) architecture are illustrated in **Figure 1.4**. In an OFET, the electrical current is measured between a source and a drain electrode, which define the active channel where the organic semiconductor is deposited as a thin film. A gate electrode, which is separated from the organic semiconductor by a dielectric, allows switching of the device between its ON and OFF states. Several other device architectures can be fabricated depending on application requirements, all sharing the same working principle.[39]

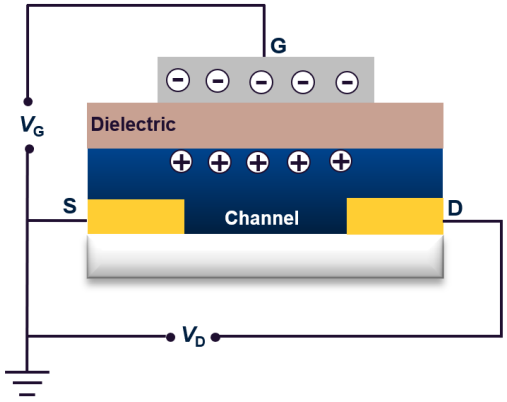


Figure 1.4. Schematic representation of an OFET showing the source (S), drain (D) and gate (G) and charge accumulation under an applied gate and drain bias.

Due to the low electrical conductivity of semiconducting materials in their pristine state, OFETs typically show a near-zero current and are therefore in their OFF state without an applied gate bias (V_G). Upon applying a gate bias, the dielectric becomes polarised and a layer of charge carriers accumulates at the dielectric-semiconductor interface, forming a conducting channel between the source and drain electrodes (**Figure 1.4**). Application of a drain voltage (V_D) drives the flow of charge carriers between the source and drain electrodes and generates an electronic current (I_D). The applied gate voltage has to be higher than a certain threshold voltage (V_T) before a drain current can be recorded. The threshold voltage is a result of inherent trap states in every organic semiconductor and device, which need to be filled first by the applied V_G. When $|V_D| \ll |V_G - V_T|$, the transistor operates in the linear regime and the drain

current increases linearly with the drain voltage following Ohm's law. As the drain voltage to increases to $|V_D| = |V_G - V_T|$, the charge carriers near the drain electrode are depleted and the channel becomes "pinched-off". A further increase to $|V_D| > |V_G - V_T|$ moves the pinch-off point towards the source and extends the depletion region. Under these conditions, the drain current no longer increases with applied drain potential and the transistor operates in saturation regime. The dependence of I_D on biasing conditions in the linear and saturation regime can be described according to Schockley equations (1) and (2), involving the channel width (W), the channel length (L), the charge carrier mobility (μ) and the capacitance of the dielectric (C).

$$I_{D-lin} = \frac{W}{L} \mu C (V_G - V_T) V_D \qquad (1)$$

$$I_{D-sat} = \frac{W}{2L} \mu C (V_G - V_T)^2 \qquad (2)$$

The current-voltage characteristics of OFETs are represented using transfer and output plots (**Figure 1.5**). For the output characteristics, I_D is measured as a function of V_D for different V_G, showing both linear and saturation operation regimes. The transfer plots show I_D as a function of V_G for a particular V_D, which can correspond to either the linear or saturation regime.

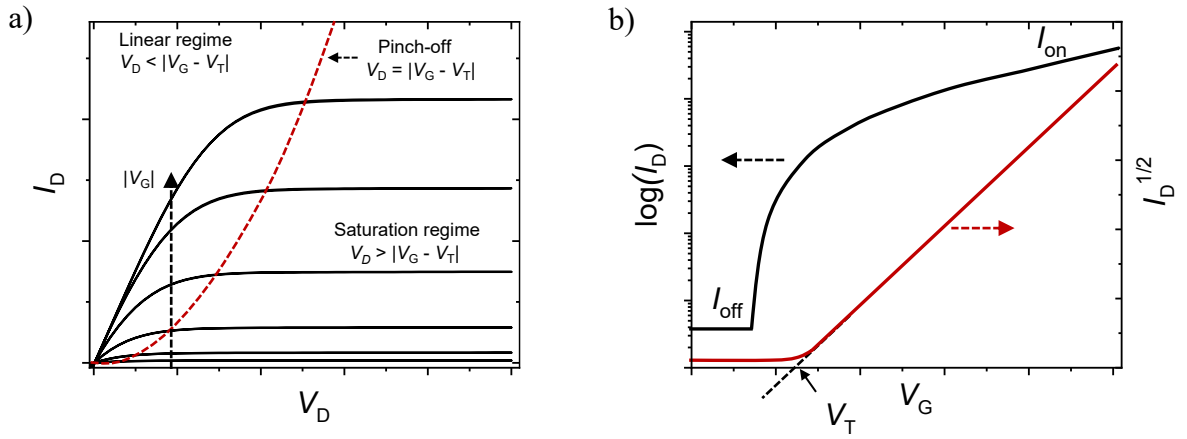


Figure 1.5. Current-voltage characteristics of an OFET: (a) output curve showing the drain current as a function of the drain voltage for different gate voltages and (b) transfer curve in the saturated regime showing the drain current as a function of gate voltage on a semi-log scale (black) and as a square root (red).

The transfer and output characteristics allow derivation of a series of key parameters for evaluating the performance of the device and channel material. The threshold voltage of the device can be obtained by extrapolating a plot of $\sqrt{I_D}$ versus V_G as illustrated in **Figure 1.5b**. Another parameter is the ratio between the drain current in the ON state at a particular V_D and the drain current in the OFF state (ON/OFF ratio), which describes the switching performance of the device. A high OFF current and consequently a low ON/OFF ratio are often indicative of unintentional doping of the organic semiconductor or current leakage.[20]

Additionally, starting from the Schockley equations (1) and (2), the transfer characteristics allow extraction of the charge carrier mobility (μ), in the linear and saturation regime according to equations (3) and (4):

$$\mu_{lin} = \frac{L}{WCV_D}\frac{\partial I_D}{\partial V_G} \qquad (3)$$

$$\mu_{sat} = \frac{2L}{WC}\left(\frac{\partial \sqrt{I_D}}{\partial V_G}\right)^2 \qquad (4)$$

The Schockley equations and equations (3) and (4) used to extract charge carrier mobility are derived using the gradual channel approximation, which assumes that the transverse gate electric field is much larger than the longitudinal electric field between the source and drain and that the mobility is independent of the charge carrier density.[20,40] This implies that the linearity of the relationship of I_D on V_G (linear regime) or $\sqrt{I_D}$ on V_G (saturation regime) is very important for accurate determinations of μ. However, 'kinks' in the transfer characteristics due to contact resistance often lead to deviations from this ideal case and overestimation of μ values. The challenge of extracting μ in devices with non-ideal characteristics, as well as methods for more accurate analysis have been discussed in detail in several recent reports.[20,40–42]

Replacing the conventional gate dielectric used in OFETs with an ionically conducting and electronically insulating electrolyte (e.g. aqueous salt solutions, ionic liquids, ionic gels or

polyelectrolytes) led to the development of a particular class of field-effect transistors, the electrolyte-gated field-effect transistor (EG-OFET) presented in **Figure 1.6**.[3,43] EG-OFETs follow similar working principles to conventional OFETs, relying on the application of a gate voltage to control the number of charge carriers accumulated at the channel interface. In this case, upon applying a gate bias, the charge carriers in the semiconductor channel are compensated by electrolyte ions which migrate and accumulate at the semiconductor-electrolyte interface, as well as the gate-electrolyte interface. EG-OFETS benefit from a high electric double layer (EDL) capacitance at the semiconductor-electrolyte interface, allowing operation at low voltages (< 1 V).[3] A remarkable operation regime occurs when the semiconductor is permeable to ions and allows accumulation of charge carriers throughout its bulk, forming the basis of numerous technologies that rely on the coupling between ions and electronic species, as discussed in the following sections.

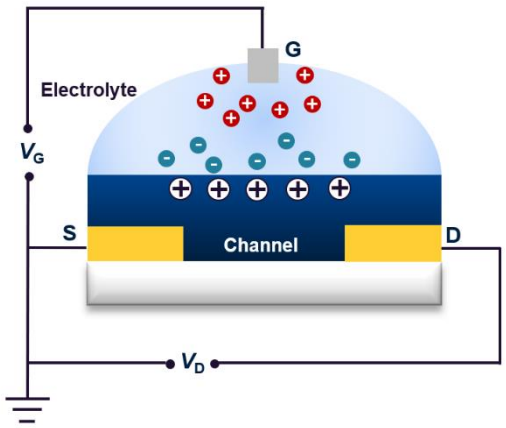


Figure 1.6. Schematic representation of an EG-OFET, showing the source (S), drain (D), gate (G) and charge accumulation under an applied gate and drain bias.

1.2 Mixed ionic-electronic transport in polymers

1.2.1 Introduction to mixed ionic-electronic transport

The electronic transport abilities of conjugated polymers have been extensively exploited to advance organic electronics applications such as organic thin-film transistors (Section 1.1), organic photovoltaics and organic light-emitting diodes. More recently, conjugated polymers have experienced a surge of novel electrochemical applications which require ionic transport, in addition to electronic transport. Such conjugated polymers that efficiently conduct both ionic and electronic currents are commonly termed organic mixed ionic-electronic conductors (OMIECs).

Ion transport has been extensively studied in the context of non-conjugated polymers such as poly(ethyleneoxide) (PEO) derivatives.[44] In this case, ion motion occurs through random hopping assisted by segmental motion of the PEO polymer chains. Ionic transport in conjugated polymers, however, has been explored on a much more limited basis. The simultaneous presence of electronic carriers obstructs the use of common techniques such as conductivity and diffusion measurements to measure ionic transport.[45] A moving front experiment developed by Malliaras et al. established a straightforward platform for estimating ion-drift mobility in poly(ethylenedioxythiophene)-poly(styrenesulfonate) (**PEDOT:PSS**) when in contact with aqueous electrolytes. Small cations such as K^+ or Na^+ were found to have higher mobilities in **PEDOT:PSS** than their electrophoretic mobility in bulk water, enabled by extensive hydration of the **PEDOT:PSS** film.[46] A more recent computational model investigating the diffusion of Na^+ and Cl^- through a similar OMIEC found that the ion diffusion coefficients decrease exponentially with decreasing hydration level.[47] At high hydration, large clusters of water molecules create percolation pathways for ion transport through the polymer matrix. In contrast, a decrease in hydration level leads to smaller and more disconnected water

clusters, hence a smaller number of diffusion paths. Using in situ electrochemical microscopy, Giridharagopal et al. showed that ion uptake in conjugated polymers is suppressed in stiffer, more ordered domains of the film.[48] These studies provide evidence that contrary to electronic transport, ion transport in OMIECs is promoted by loose structures that can accommodate considerable free volume and undergo swelling in contact with an electrolyte.

One of the first investigated effects of ion inclusion in conjugated polymers is the increase in electrical conductivity in contact with a metal electrode and an electrolyte.[49] Upon introducing ionic charges, charge carriers are generated along the polymer backbone in order to maintain charge neutrality. This electrostatic stabilisation of excess ionic charge by charge carriers provided by the metal electrode is commonly referred to as electrochemical doping. If the ionisation potential of the polymer is sufficiently low, generation of holes stabilised by anions is energetically favourable (p-type doping). Conversely, if the electron affinity of the polymer is high, generation of electrons stabilised by cations is favoured (n-type doping). The increase in conductivity during doping has been attributed to the formation of polaronic/bipolaronic species associated with new energetic states within the band gap of the polymer. At high doping levels, the overlap between adjacent polaron/ bipolaron bands leads to shrinking of the band gap and causes a transition to a metallic-like state.[50]

The degree of electrochemical doping can be modulated by applying a bias through an electrolyte. The strength of the coupling between ionic and electronic charge is captured by capacitance C, which represents the amount of charge induced in a given potential window. This coupling provides the foundation of transduction between ionic and electronic environments or charge storage in most OMIEC-based applications. Examples of technologies which leverage mixed conduction in conjugated polymers include electrochromics[51–53], energy storage,[54–56] neuromorphic computing,[57] artificial muscles[58] and organic bioelectronics.[59–64]

The following sections of this thesis will be focused on mixed ionic-electronic transport in conjugated polymers for bioelectronics applications.

1.2.2 Conjugated polymers in organic bioelectronics

Electronic components that can either trigger biological events or monitor signals and physiological states have promising applications in new healthcare technologies. Constructing such devices requires materials that are not only soft and biocompatible, but also can convert biological signals into electrical ones and vice versa (**Figure 1.7**).

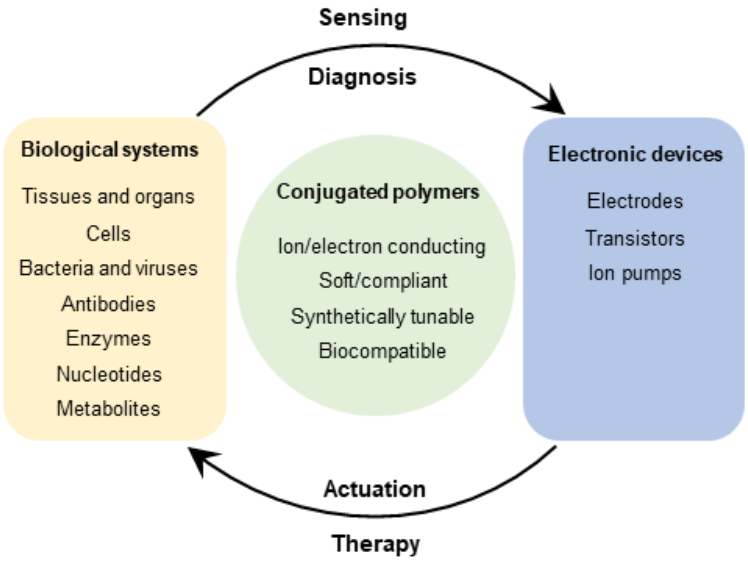


Figure 1.7. Conjugated polymers in organic bioelectronics for sensing or actuation (adapted from literature).[11]

Signal transmission and regulation of key cellular processes in biological systems rely on ionic currents.[10] Due to their ability to support both ionic and electronic currents, conjugated polymers have emerged as ideal mediators between biological systems and electronics, giving rise to the field of organic bioelectronics.[10] An early implementation of conjugated polymers for interfacing with biological systems are conjugated polymer-coated electrodes. Malliaras and co-workers demonstrated the use of a conducting polymer (**PEDOT:PSS**) to coat electrode arrays for in vivo electrocorticography, which were able to record typical epileptic activity in

rats.[65] The same group extended the initial use of **PEDOT:PSS** as a coating for electrodes to transistor configurations, which allowed local signal amplification and recordings of lower amplitude neural signals.[66] Since then, transistor configurations where the conjugated polymer acts as the channel material have been successfully used to amplify electrophysiological signals associated with the human brain, muscle and cardiac activity,[61,67,68] but also as selective biosensors for the detection of electrolytes[69] and key metabolites such as lactate or glucose.[62,64] The transduction of signals can occur in the opposite direction as well, where an electronic signal is used to stimulate a biological event. For instance, an organic electronic ion pump based on **PEDOT:PSS** implanted on the spinal cord of a rat was used for localised delivery of an inhibitory neurotransmitter to treat neuropathic pain.[60]

In addition to their ion-to-electron conversion abilities, conjugated polymers are mechanically flexible and can preserve their conductivity under repeated strain, which has made them highly attractive for devices that mimic human skin[70] and wearable biosensors.[71,72] For example, incorporation of **PEDOT:PSS** in hydrogel networks allowed tuning of the elastic modulus to match biological tissues, whilst maintaining a high electrical conductivity (> 10 S m^{-1}).[73]

Conjugated polymers also offer numerous possibilities for chemical modification to tailor their biological functionality for specific applications. For instance, Bao and co-workers demonstrated functionalisation of a semiconducting polymer thin film with Au nanoparticles, which could couple to a thiolated DNA aptamer to selectively detect thrombin proteins.[74] In another example, hydroxyl groups generated on the surface of conjugated polymers were used to immobilise antibodies for the detection of *E. coli* bacteria, via reactions with epoxide-containing silanes and subsequent ring-opening by the bacteria antibodies.[75]

Further examples of bioelectronics applications employing conjugated polymers have been discussed in several comprehensive reviews.[11,15,76–78]

1.2.3 Organic electrochemical transistors

A particular device architecture which has shown efficient signal transduction between ion- and electron-mediated systems in organic bioelectronics is the organic electrochemical transistor (OECT). Originally reported by Wrighton et al. in 1984,[79] OECTs belong to the class of electrolyte-gated transistors and feature a three-terminal architecture with a source, a drain and a gate electrode (**Figure 1.8a**). In a typical OECT, the source and drain electrodes are bridged by an active channel (an OMIEC) in which charge carriers (holes or electrons) are transported. The gate electrode is immersed into an electrolyte rich in mobile ions, which is in direct contact with the OMIEC deposited as a film.[80] The technique traditionally used to deposit the channel material involves mechanical peel-off of a sacrificial layer of parylene C, avoiding exposure to harsh plasma or solvent treatments.[81–83]

During the operation of an OECT, a voltage bias is applied between the source and drain electrodes (V_D), driving an electronic current (I_D) through the channel. The magnitude of this current is modulated by an input voltage at the gate electrode (V_G), which controls the extraction/injection of ions from the electrolyte into the channel and therefore the doping state of the channel material.

Depending on the level of doping of the channel material at zero gate bias, two OECT operation modes can be identified: depletion or accumulation mode. When conducting polymers such as **PEDOT:PSS** with an excess of mobile electronic charge carriers are used, the OECT operates in depletion mode. In the absence of a gate bias, the sulfonate groups of the PSS polyelectrolyte compensate the mobile holes along the PEDOT conjugated backbone and at negative drain potentials, a hole current flows across the channel (ON state, **Figure 1.8b**). When a positive gate voltage is applied, cations from the electrolyte are injected into the channel, charge-balancing the PSS anions and decreasing the number of holes across the channel. As the

channel material is de-doped, the drain current decreases and the device reaches the OFF state (OFF state, **Figure 1.8b**).

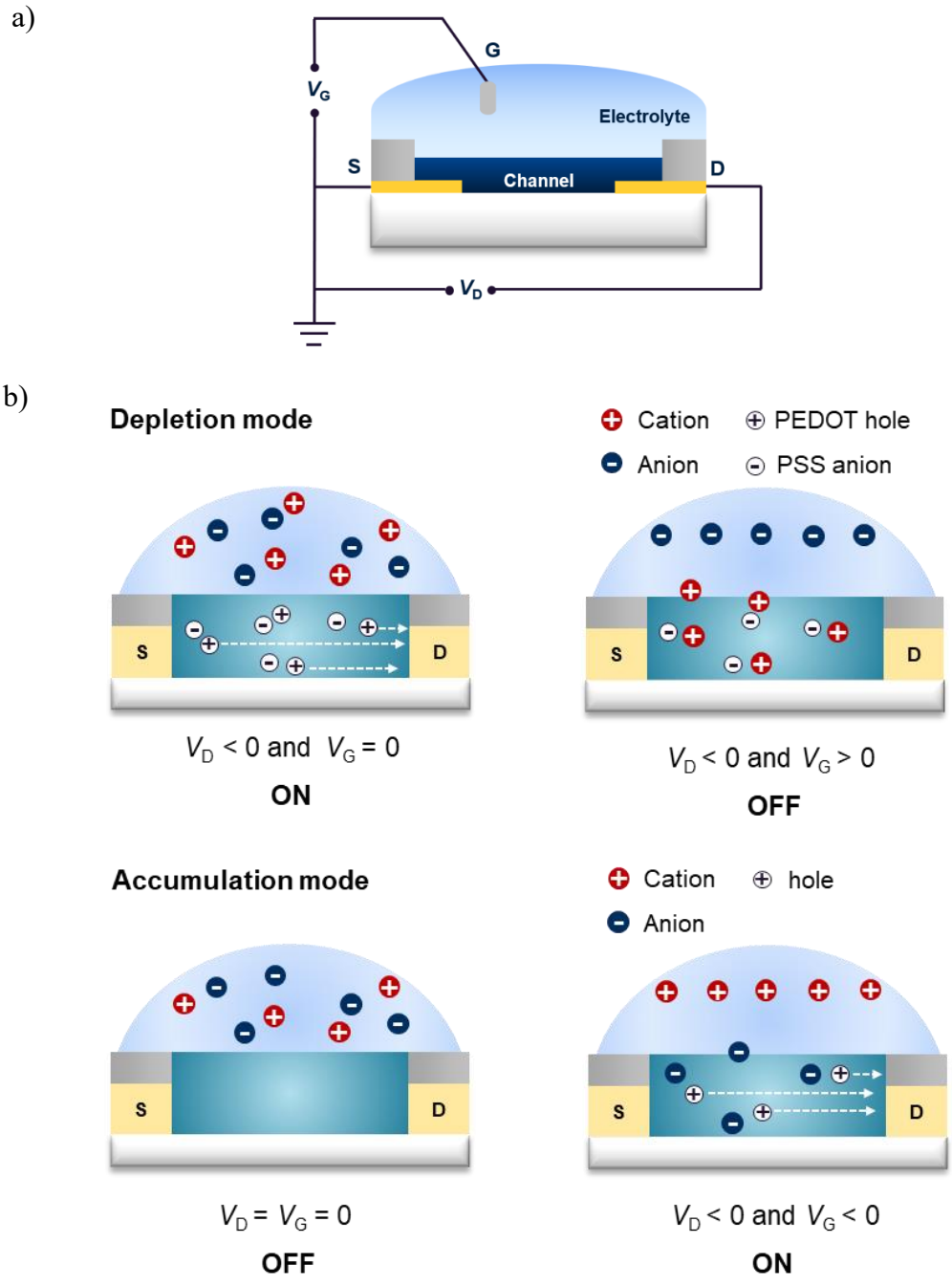


Figure 1.8. (a) Schematic representation of an organic electrochemical transistor (OECT), showing the source (S), drain (D) and gate (G) (b) Working principle of OECTs operating in depletion and accumulation mode for a p-type channel material.

Conversely, accumulation mode OECTs employ organic semiconductors which are de-doped in their pristine state and the device is OFF at zero gate bias. Upon applying a negative gate voltage, anions driven into the channel dope the film leading to an accumulation of holes across the channel and bringing the device to the ON state (**Figure 1.8b**). N-type accumulation OECTs follow a similar working principle. However, since the channel current is carried by electrons and the charge balance is provided by injected cations, the required drain and gate biases are opposite in sign with respect to p-type OECTs.

Such devices which turn on in the presence of an analyte and therefore operate in accumulation mode are often preferred for sensing applications as they consume low power and show superior ON/OFF ratios.[84] Operation of OECTs in an accumulation/depletion hybrid mode has also been demonstrated by Inganas and co-workers using a conjugated polyelectrolyte which is semi-doped in the absence of a gate voltage.[85] The material achieved a high amplification close to zero gate bias, which is an attractive feature for applications involving sensitive biological systems such as lipid membranes, cells and tissue.[83]

Regardless of the operation mode, the electrolyte ions can penetrate the active material and modulate the electronic conductivity throughout its entire volume in an OECT.[68] This 3D interaction of the active material with the electrolyte is the identifying feature of OECTs and a remarkable advantage over EG-OFETs. For many applications, OECTs operate as amplifying transducers, converting small changes in the gate voltage into electric signals (i.e. changes in the drain current I_D). The bulk nature of the OECT response gives a volumetric capacitance, which can be many orders of magnitude larger than the electrical double layer capacitance residing at the electrolyte-channel interface specific for EG-OFETs. This leads to higher amplification of the current compared to other transistor technologies at equivalent biasing conditions and geometries.[68] In addition, it allows operation at low voltages, rendering OECTs

suitable for biological applications where the narrow electrochemical window of the aqueous media limits the applied potentials to ~ 1.2 V.[86,87]

The device parameter which quantifies the ability of OECTs to amplify an input signal is the transconductance g_m and is given by the first derivative of the transfer characteristics ($\partial I_D/\partial V_G$). A commonly used model reported by Bernards et al. divides the OECT into an electronic circuit, which accounts for the flow of electronic charge in the channel and an ionic circuit, which accounts for the flow of ions in the electrolyte.[88] Relying on analogies with charge transport in metal oxide semiconductor field-effect transistors (MOSFET), the Bernards model allows derivation of an equation for the OECT transconductance g_m.. In the saturation regime, the transconductance is given by:[68,88]

$$g_m = \frac{W \times d}{L} \mu C^* (V_T - V_G) \qquad (5)$$

Accordingly, the transconductance shows a direct dependence on the thickness of the active layer d, the volumetric capacitance (C^*) and the OECT charge carrier mobility (μ), where L and W are the channel length and width, respectively, and V_T is the threshold voltage. Given the scaling of g_m with channel thickness d, a higher transconductance can be obtained for devices with a thicker semiconductor channel. This is however at the expense of the response time. As the redistribution of ionic charges and doping/de-doping processes are slower, the OECT response to a change in gate voltage is also slower for a thicker active layer.[89] Beyond altering the device footprint, tuning the ionic and electronic properties of the active material in order to maximise C^* and μ and thereby g_m offers many more possibilities to explore.

1.2.4 Extracting material parameters from OECT performance

Organic electrochemical transistors rely on channel materials that are able to: (1) transport electronic charge, represented by the charge carrier mobility, μ and (2) store ionic charge, represented by the volumetric capacitance, C^*. With both ionic and electronic elements

captured, OECTs have become useful test platforms for evaluating the performance of organic mixed conductors.

While the transconductance (g_m) assesses the performance of the device as an amplifier, it does not allow a fair comparison between different channel materials due to its scaling with geometry parameters and applied biases. Many recent studies focused on material development have reported thickness-normalised transconductance values (i.e. g_m/d) to account for variations in the channel thickness.[90–92]

Recently, Inal and co-workers proposed that the key figure of merit from a material design perspective is the product μC^*.[93] The authors note that this product can be deduced from the g_m of a single device with known geometry parameters and applied bases according to equation (5). For a more rigorous analysis, the transconductance of multiple devices of different geometries can be measured to allow plotting the g_m versus $W\,d\,L^{-1}\,(V_T - V_G)$, where the slope gives the μC^* product.[93]

The μC^* product can be also found by determining each property separately using other techniques. The volumetric capacitance C^* can be measured by performing electrochemical impedance spectroscopy (EIS) measurements of polymer-coated electrodes. The EIS results can be typically fit to an equivalent circuit to extract a capacitance value which can be normalised by the product of the electrode area and film thickness to give the volumetric capacitance C^*.[93]

As both ionic and electronic charges are present in the OECT channel, the charge carrier mobility cannot be extracted directly from the device transfer characteristics as described for organic field-effect transistors (Section 1.1). Instead, charge carrier mobilities can be estimated using simultaneous measurements of drain and gate current at varying frequencies as detailed by Rivnay et al.[94] Matching the measured impedance (from the gate current I_G) with the

impedance derived from the drain current I_D yields the hole/electron transit time, τ_e. Using the hole/electron transit time in the channel (τ_e), the channel length (L) and the applied drain voltage (V_D), the OECT mobility can be estimated according to the following equation:[93]

$$\mu_{OECT} = \frac{L^2}{\tau_e \, V_D} \qquad (6)$$

When comparing the μC^* product extracted from the device transconductance and the value obtained by measuring μ and C* independently, Inal et al. found a good agreement for all studied channel materials.[93] Therefore, by using EIS and impedance matching measurements in addition to OECT transfer characteristics, the terms of the μC^* product can be decoupled. Deconvoluting the electronic mobility from the volumetric charge storage capacity is particularly relevant for materials evaluation and development as the limiting factors are more easily identified.

While the μC^* product is typically used to quantify the properties of the material, it can be influenced by other factors as well. For example, Savva et al. demonstrated that optimising the processing conditions by changing the solvent used for casting the film is a good strategy to increase both the electron mobility and volumetric capacitance of n-type copolymers.[91] The nature of the electrolyte is also expected to strongly influence the ion-polymer interaction and consequently the μC^* product. Recently, Flagg et al. showed that higher doping levels and drain currents can be achieved when gating a hydrophobic conjugated polymer with aqueous electrolytes containing large molecular anions such as hexafluorophosphate compared to smaller atomic anions.[95] A similar trend was observed for a conjugated polymer with polar side chains, where anions with a larger crystallographic radius led to an increase in the μC^* product and the transconductance of the device.[96]

It should be also noted that the μC^* product relates to the steady-state performance of the device (i.e. g_m) and it does not provide information on the device speed. Fast response times

are particularly important for applications requiring high-frequency recordings such as monitoring single-neuron action potentials.[97] The transient responses are normally measured by recording I_D as a function of time, upon applying square-wave gate voltages at a fixed V_D. These measurements assess the switching ability of the device and the ON (τ_{ON}) and OFF (τ_{OFF}) switching times, defined as the time required to reach 90% and 10% of the I_D for the ON and OFF state, respectively.[98,99]

1.3 OECT channel materials

The design of OECT channel materials has experienced rapid growth in recent years as researchers target new applications, improved performance and stability, as reported in several comprehensive reviews.[100–103] This section focuses on channel materials that advanced the understanding of OECT operation or elucidated key structure-property relationships.

1.3.1 P-type channel materials

The prototypical channel material for a variety of applications that leverage mixed conduction has been **PEDOT:PSS** (**Figure 1.9**), since its first use as an OECT active layer in 2002 by Berggren and co-workers.[104] **PEDOT:PSS** has been particularly attractive due to its stability, high hole conductivity above 2000 S cm^{-1} and commercial availability in the form of aqueous dispersions.[105] These dispersions are typically described as colloidal gel particles with a hydrophobic PEDOT-rich core that is stabilised in aqueous media by a hydrophilic PSS-rich shell.[106–108] Following deposition and drying, the **PEDOT:PSS** thin films are believed to show a pancake-like morphology[108] with evidence of π-stacking.[109] Several reports demonstrate that **PEDOT:PSS** consistently achieves a g_m in the range of mS and a response time in the range of tens of ms in spin-coated devices, which are suitable for most OECT-based applications.[68,82,110] The performance can be further enhanced by the addition of co-solvent additives such as ethylene glycol (EG) in the casting dispersion. Rivnay et al. demonstrated

that **PEDOT:PSS** films cast from formulations with higher EG content showed an increase in the size of the PEDOT-rich domain and tighter π-stacking, leading to opposite trends in electronic and ionic conductivity.[106] While electronic conductivity increased due to enhanced aggregation, the ionic mobility in the resulting closely packed structures was lower. A balance between these two factors was found at 5 vol% EG, where the OECTs exhibited a peak g_m of ~ 8 mS (W = 50 μm, L = 50 μm, d = 174 nm).[106]

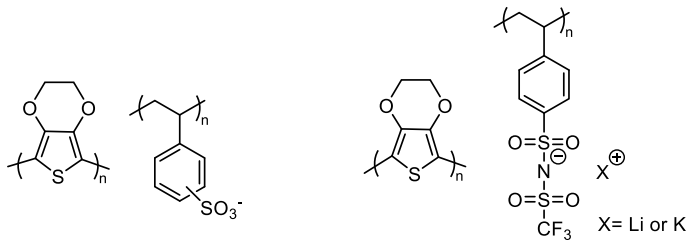


Figure 1.9. Examples of conjugated polymer composites used as OECT channel materials.

Despite the attractive properties of **PEDOT:PSS**, one disadvantage is the acidity of the PSS polyanion, limiting its suitability for certain in vivo applications such as bioelectronic implants. This motivated the design of a new series of PEDOT derivatives where the sulfonate functional groups on the polyanion were replaced with less acidic (trifluoromethylsulfonyl)sulfonylimide (TFSI) groups. **PSTFSI** polymers (**Figure 1.9**) containing polystyrene backbones of different molecular weights were able to match the g_m and switching speed of **PEDOT:PSS** devices reasonably well, with the top performer showing a peak g_m of 3.41 mS (W = 100 μm, L = 10 μm, d = 200 nm).[111] Due to intrinsic doping, a key drawback of these conjugated polymer composites has been the depletion-mode operation of the devices (Section 1.2).[112] Recently, van de Burgt et al. have overcome this problem for **PEDOT:PSS**-based devices by adding aliphatic amines to the polymer dispersion as de-dopant molecules, which allowed accumulation mode operation and tuning of the operation voltage.[113]

Despite these recent developments and the good performance in OECTs, several drawbacks remain unaddressed for PEDOT-based composites. Their complex microstructure and morphology limit their use as model systems for establishing structure-property relationships. In addition, the presence of bulky, electrically insulating polyanion dopants lowers the volume fraction of PEDOT in the film and limits their volumetric capacitance C^* (< 100 F cm^{-3}).[93,114]

In order to address these limitations, attention has been recently focused on single-component systems, where the ion conducting component is covalently attached to the conjugated backbone, typically as a side chain. Inal and co-workers opened a new direction by introducing the conjugated polyelectrolyte **PTHS** (**Figure 1.10**) for OECT applications.[84] The authors exploited the high hole mobility specific for polythiophenes and the hydrophilic nature of the side chains bearing a sulfonate group to achieve a peak g_m of 3.0 mS (W = 250 µm, L = 5 µm, d = 60 nm) in optimised devices. As the pendant sulfonate group is compensated by a tetrabutylammonium ion, **PTHS** has semiconducting character in its pristine form and operates in accumulation mode in OECTs.

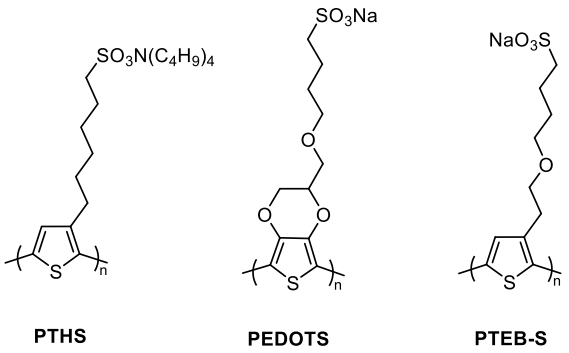


Figure 1.10. Examples of conjugated polyelectrolytes used as OECT channel materials.

Conjugated polyelectrolytes where the ionic groups on the side chains are compensated by charge on the conjugated backbone and thereby operate in depletion mode have also been reported. One example of a self-doped conjugated polyelectrolyte is **PEDOTS** (**Figure 1.10**), which features a PEDOT backbone functionalised with alkylsulfonate side chains. The electron

donating ethylenedioxy moiety directly attached to the conjugated system decreases the ionisation potential and leads to hole stabilisation, rendering **PEDOTS** conducting in its pristine form. When used as an OECT channel material, **PEDOTS** achieved a high peak g_m of 16.2 mS (W = 1125 µm, L = 20 µm, d = 75 nm).[98] By blending **PEDOTS** with a semiconducting conjugated polyelectrolyte, **PTEB-S** (**Figure 1.10**), it was possible to operate the OECT in a hybrid accumulation/depletion mode, albeit with slightly lower peak g_m compared to the neat polymer (< 12.0 mS for W = 1125 µm, L = 20 µm, d = 55 to 75 nm). Devices fabricated with these blends also showed faster switching speeds, which the authors attributed to enhanced ion transport in the rougher fibrillar morphology.[98] Due to the high solubility of **PEDOTS** in aqueous media, an ionic liquid ($BMIMBF_4$) had to be used as the electrolyte, limiting its use for biological applications. The hydrophilic character of **PEDOTS** was later decreased by the same group through counterion exchange with ammonium salts with long hydrophobic alkyl chains. The resulting ammonium complexes allowed fabrication of active layers with good stability in aqueous OECTs and showed a peak g_m of 11.0 mS, however for significantly thicker and wider channels (W = 39000 µm, L = 20 µm, d = 720 nm).[85]

A recent addition to accumulation mode OECT channel materials are conjugated semiconducting polymers functionalised with ethylene glycol side chains. The strategy of attaching ethylene glycol side chains onto established backbone motifs leverages the knowledge accumulated on charge transport in traditional organic semiconductors, such as those used for organic photovoltaics and field-effect transistors. Several studies have demonstrated that hydrophilic ethylene glycol side chains endow conjugated polymer backbones with the ability to swell in aqueous electrolytes and therefore facilitate the transport of hydrated ions. These polymers are typically processed from common organic solvents and show remarkable stability as thin films in aqueous media, with no requirements for formulation additives or cross-linkers.[86,90,115–119]

The first report by Nielsen et al. exemplified this design strategy on a series of p-type polymer backbones containing benzodithiophene (BDT) or bithiophene (T2) units with triethylene glycol side chains.[118] The study investigated the effect of backbone conformation and side chain density on the p-type OECT operation. It was found that polymers containing electron rich glycolated bithiophene units show significantly lower oxidation potential in aqueous electrolytes and superior electrochemical stability compared to the BDT-based polymers. A high density of glycol chains led to an increase in the π-π stacking distance and predominantly face-on orientation in the solid state, which the authors correlated with lower mobility and g_m in OECTs. Remarkably, the top performing material **p(g2T-T)** (**Figure 1.11**) displayed higher g_m than **PEDOT:PSS** at all tested device dimensions, achieving a peak g_m of 21 mS and switching speeds in the millisecond range (W = 100 μm, L = 10 μm, d = 160 nm). Following the proven success of TEG-functionalised bithiophene units, Giovannitti et al. substituted the thiophene comonomer with a more rigid thieno[3,2]thiophene (TT) unit to further reduce the π-π stacking distances. The resulting polymer, **p(gT2-TT)** (**Figure 1.11**), showed higher OECT hole mobility than **p(gT2-T)**, with values of 0.95 and 0.28 $cm^2\ V^{-1}\ s^{-1}$ respectively. Devices also displayed a record g_m of 27 mS (W = 100 μm, L = 10 μm, d = 40 nm), excellent stability and fast switching times.[86] By fabricating additional OECT devices with different footprints and analysing the μC^* product, Inal and co-workers confirmed that **p(gT2-TT)** outperformed all other state-of-the-art p-type channel materials to date, with a μC^* of $261 \pm 29\ F\ cm^{-1}\ V^{-1}\ s^{-1}$.[93]

However, a recent follow-up study revealed that de-doped **p(gT2-TT)** films undergo a spontaneous oxygen reduction reaction when immersed in aqueous electrolytes affording H_2O_2, with potentially detrimental effects for energy storage or sensing applications.[120] The authors postulated that channel materials with IPs higher than 4.9 eV are required in order to shift the operational voltages of the OECT to a range where this competing process is

minimised. Backbone engineering led to the development of **p(gPyDPP)** (**Figure 1.11**) with a larger IP (4.92 eV *cf.* 4.5 eV for **p(gT2-TT)**), which showed no formation of H_2O_2 during device operation in the presence of oxygen.[120] An approach focused on enhancing the operational stability of p-type accumulation mode materials was recently reported by Yue et al.[116] In this case, hybrid alkyl/glycol side chains were used to tune the hydrophilicity of a series of donor-acceptor copolymers comprising isoindigo and EDOT units. It was found that polymer **PIBET-AO** (**Figure 1.11**) bearing a hybrid alkyl/glycol side chains shows enhanced operational stability and substrate adhesion in contact with aqueous electrolytes compared to the analogues containing EG side chains only.[116]

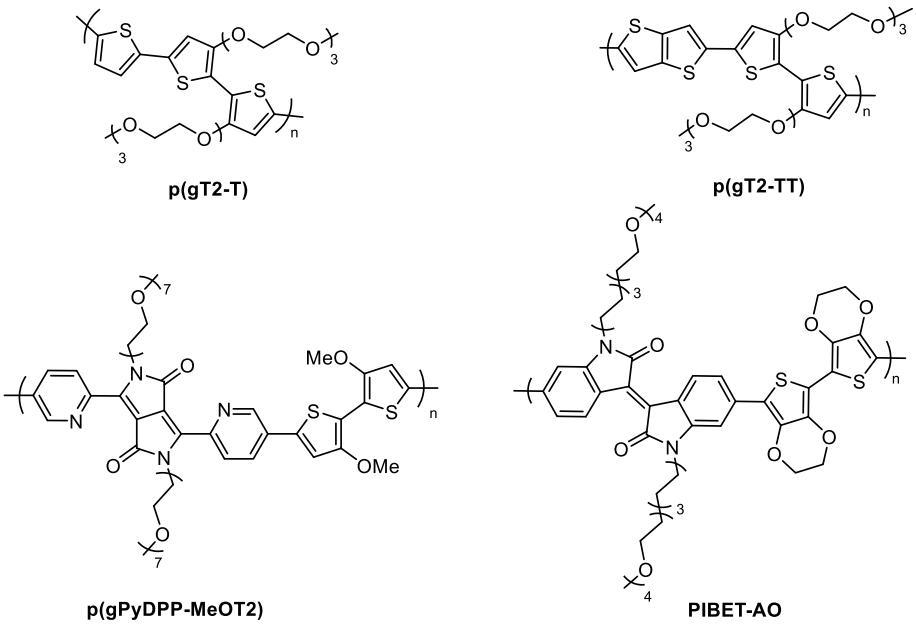


Figure 1.11. Examples of p-type semiconducting polymers used as OECT channel materials.

1.3.2 N-type channel materials

Similar strategies of tethering ion-transporting EG side chains to tailor traditional organic semiconductors for OECTs has also been recently applied for the development of n-type channel materials. The first example of stable operation of an n-type OECT in aqueous electrolytes was reported by Giovannitti et al.[115] Electron deficient naphthalene diimide units

functionalised with EG side chains were copolymerised with bithiophene units to obtain the same backbone motif as one of the most studied n-type polymers in organic electronics, N2200.[121,122] The resulting polymer, **p(gNDI-gT2)** (**Figure 1.12**), showed remarkable long-term stability during pulsed experiments, but it suffered from low amplification. The peak g_m and μC^* product (**Table 1.1**) for the reported devices were several orders of magnitude lower than those typically observed for p-type channel materials (Section 1.3.1). A more in-depth analysis showed that although **p(gNDI-gT2)** exhibits a record C^* of 397 F cm^{-3}, the overall performance in OECTs is limited by its poor charge transport properties, with an electron mobility of only 3.1×10^{-4} cm^2 V^{-1} s^{-1}.[93,115]

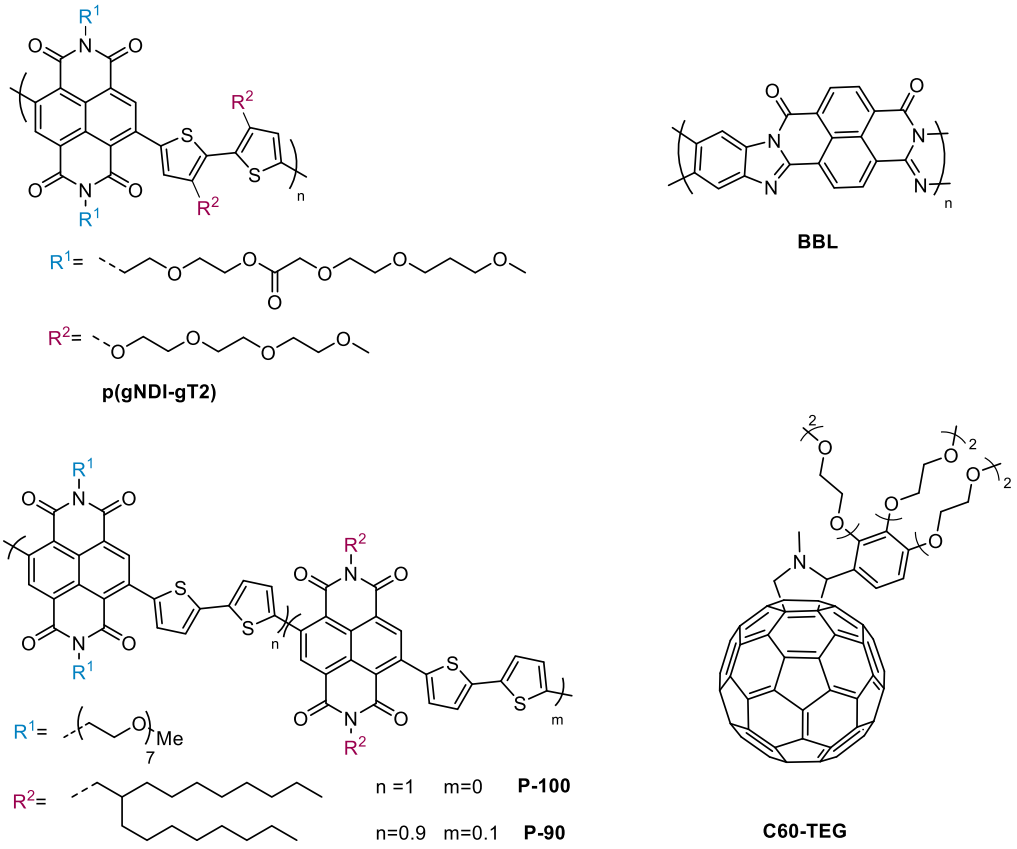


Figure 1.12. Examples of n-type semiconducting polymers and small molecules used as OECT channel materials.

The effect of glycol chain density on the properties of n-type polymers for OECTs was explored further for a series of polymers comprising the same naphthodithiophene diimide-bithiophene backbone. In this study, the hydrophobic 2-octyldocecyl side chains of N2200 were gradually exchanged for more hydrophilic heptakis(ethylene glycol) side chains to afford seven random copolymers with glycol chain densities ranging from 0% (**P-0**) to 100% (**P-100**), with examples shown in **Figure 1.12**.[90] High densities of EG side chain led to an increase in the degree of swelling in aqueous electrolytes, with > 100% swelling for **P-100**. Polymers with high degree of swelling (**P-75** to **P-100**) showed lower reduction potentials in water, due to more facile ion penetration into the bulk of the material during electrochemical doping. Electrochemical impedance measurements identified two charging regimes: **P-0** to **P-50** show electrostatic accumulation of charges at the semiconductor-electrolyte interface, whereas **P-75** to **P-100** can be charged volumetrically. Similar differences in the operation regimes were also observed in transistor configurations. Glycol percentages > 50% were required for OECT operation in aqueous electrolytes, while polymers with lower glycol percentages could only perform moderately well in OFETs. It is noteworthy that increasing the glycol side chain density impaired the electron mobility of the conjugated polymer, although a higher capacitance could be accessed. A good balance between these two factors was achieved for **P-90**, which showed the highest μC^* and normalised g_m within the series (**Table 1.1**). When comparing with the previously reported **p(gNDI-gT2)**,[115] copolymers within this series showed inferior normalised g_m. This was attributed to a 2-fold decrease in volumetric capacitance, while maintaining a similar charge carrier mobility (**Table 1.1**), however the structural features that led to these effects have not been elucidated yet.

As an alternative approach, Sun et al. demonstrated that ladder-type conjugated polymers such as **BBL** (**Figure 1.12**) can also be used for n-type OECT operation.[123] Taking advantage of the high electron conductivity and electron affinity of **BBL**, the OECTs exhibited good operational

stability and high transconductance. Due to the lack of electrically insulating side chains, **BBL** showed a remarkable volumetric capacitance of 930 F cm^{-3}. However, a drawback of **BBL**-based devices was the slow response time, attributed to poor ion diffusion throughout the channel. One strategy to overcome this limitation could be functionalisation of the polymer backbone with polar side chains that promote ion migration.[123] However, this is expected to have a detrimental effect on both C^* and μ, due to lowering of the active volume and disrupting of the structural order, respectively.[90]

It should be also noted that **BBL**-based devices were evaluated using interdigitated electrode arrays,[123] rather than a typical OECT planar architecture.[83] A recent study by Mayer and co-workers revealed that g_m does not have a straightforward linear dependence on the channel aspect ratio (W/L) for OECTs with interdigitated electrodes and intricate 2D geometries.[124] Therefore, it remains debatable whether a comparison between **BBL** and previously reported n-type materials based on normalised g_m and derived μC^* provides reliable structure-property relationships.

Beyond conjugated polymers, Bischak and co-workers recently demonstrated that small molecule acceptors can be also tailored for OECT operation.[125] A fullerene derivative bearing ethylene glycol side chains (**C60-TEG**, **Figure 1.12**) showed n-type OECT operation with a record high μC^* of ~ 7.0 F cm^{-1} V^{-1} s^{-1}. Surprisingly, this effect did not translate into high amplification in OECT devices, as the peak g_m was approximately one order of magnitude lower than **p(gNDI-gT2)** after considering the differences in device footprints (**Table 1.1**). Furthermore, **C60-TEG**-based devices showed a decrease in current of 15% upon repeated cycling for 5 min, rendering them impractical for long-term device operation. However, this study opened up new directions for material design as improved stability upon reduction could potentially be achieved using fullerene derivatives with higher electron affinities.[125]

Table 1.1. Overview of OECT performance of current n-type channel materials

Material	*W/L*	g_m (S/cm)[a]	C^* (F/cm^3)[b]	μ_e (cm^2 V^{-1}s^{-1})[c]	$\mu_e C^*$ (F cm^{-1} V^{-1}s^{-1})[d]	$[\mu_e C^*]$ (F cm^{-1} V^{-1}s^{-1})[e]
p(gNDI-gT2)[93,115]	10	1.09	397	3.1×10^{-4}	0.12	0.18 ± 0.01[e]
P-75[90]	10	0.14	188.0	1.46×10^{-4}	0.027	–
P-90[90]	10	0.21	198.2	2.38×10^{-4}	0.047	–
P-100[90]	10	0.20	192.4	1.96×10^{-4}	0.038	–
BBL[123]	1950	539	930 ± 40	–	–	0.65*
C60-TEG[f] [125]	20	0.29	220 ± 50	–	–	7.0 ± 2.0[e]

[a] OECT peak transconductance normalized by channel thickness. [b] Determined from electrochemical impedance spectroscopy measurements. [c] Determined from carrier transit time through impedance matching methods. [d] Calculated from independently measured μ_{el} and C^*. [e] Calculated from OECT transfer characteristics by fitting a plot of g_m versus $W d L^{-1} (V_G - V_T)$ for multiple devices with varying dimensions. *$[\mu_e C^*]$ was estimated from the transfer characteristics of one reported OECT device with known channel dimensions and biasing conditions. [f] Devices were fabricated using degassed 0.1 M KCl electrolyte solutions instead of 0.1 M NaCl solutions in ambient conditions.

1.3.3 Applications of n-type OECT materials

N-type materials with mixed ionic-electronic conduction are particularly promising for developing the complexity and functions of OECT-based technologies. A research area which benefits from n-type channel materials is enzymatic sensing of metabolites. Recently, **P-90** was used to fabricate an OECT-based enzymatic sensor for the detection of lactate with a highly specific and sensitive response.[62] High selectivity for lactate was achieved by drop-casting a solution of lactate oxidase (LOx) on the **P-90** channel, without the need for any additional chemical treatments to immobilise the enzyme or integration of electron transfer mediators. Upon successive additions of lactate to the electrolyte solution, the shift in effective gate voltage modulated the conductivity of **P-90**, leading to a drain current response. With a rational choice of the gate and drain voltages, **P-90**-based OECTs were able to respond to micromolar

concentrations and detect a wide range of concentrations of lactate between 10 μM to 100 mM.[62] Sensing of glucose using **P-90**-based devices was also achieved, this time using glucose oxidase (GOx) to catalyse the enzymatic reaction.[64] Going one step further, the GOx functionalised **P-90** film was used as an anode and paired with a p-type copolymer as the cathode to fabricate an enzymatic biofuel cell. Notably, the **P-90** based biofuel cell was able to harvest glucose and oxygen and operate as a self-powered glucose sensor in aqueous electrolytes.[64] The authors postulated that a key element in the sensing mechanism is spontaneous electron transfer from the enzyme to **P-90**, enabled by its high electron affinity.[64] However, a recent study showed that the electrons generated in the enzymatic reaction are more likely to undergo reduction of O_2 to form H_2O_2, instead of direct electron transfer to **P-90**.[126] In order to promote spontaneous electron transfer from GOx, the highly electron deficient complex TTF-TCNQ was employed due to its higher electron affinity (4.55 eV) compared to the reduced $FADH_2$ co-factor of the enzyme (4.38 eV).[127] This emphasises the need for designing solution-processable n-type channel materials with high electron affinities.

N-type channel materials are also key components in electrochemical complementary inverters, which allow greater circuit speeds and reduced power consumption.[103] The first example of a complementary inverter based entirely on electrochemical operation was recently reported by Sun and co-workers by combining a n-type **BBL**-based OECT with a p-type OECT based on poly(3-carboxy-pentyl-thiophene). Although the inverter showed a relatively high gain at low supply voltages (> 11 at 0.6 V),[123] its speed is currently much lower than technologically relevant figures.[103]

The opportunities to drive forward these emerging applications are very limited as the development of n-type channel materials is still at an early stage. Progress in this area requires new design strategies, which in turn require a better understanding of the closely linked relationships between mixed conduction and chemical structure.

1.3.4 Design considerations for n-type OECT materials

Several strategies have been used successfully to improve the OECT performance of p-type semiconducting polymers with mixed conduction, yet a comparable performance among n-type materials remains difficult to achieve. While many p-type OECT materials show μC^* > 100 F cm^{-1} V^{-1} s^{-1} and thickness-normalized g_m approaching 1000 S/cm, most n-type materials show μC^* between 0.1–1 F cm^{-1} V^{-1} s^{-1} and thickness-normalised g_m less than 1 S/cm.[93]

Similar gaps in performance between p-type and n-type organic semiconductors have been traditionally reported in other transistor-based technologies, such as OFETs.[128–130] This has been attributed to the instability of n-type polymers in ambient conditions,[87,131] rather than intrinsic differences between the transport mechanisms of electrons and holes.[132] In most cases, the instability in air is due to redox reactions between the corresponding radical anion and atmospheric water/oxygen, which leads to a reduction in the number of mobile electrons available.[87] This has been linked to shifts in the threshold voltage, decrease in field-effect mobility or increase in the OFF current in OFETs under ambient conditions.[131,133,134] Experimental and theoretical studies have identified that in order to prevent the electron polaron from reducing ambient species, an electron affinity between 4.1 and 4.3 eV is needed.[37,129,135–137] It should be noted that degradation pathways caused by specific interactions between the electronic orbitals of acceptor units and molecular oxygen or water, rather than the particular energy of the LUMO level have also been reported.[131] Nonetheless, high electron affinities are expected to be crucial for stable operation of OECTs in ambient conditions, where the n-type channel material is in direct contact with an aqueous media and is specifically designed to support hydrated ions.

In addition to stability, a key design challenge for n-type OECT materials is achieving volumetric penetration of hydrated dopant ions without disrupting the pathways for electron

transport. High electron mobility is closely linked to strong intermolecular orbital overlap between neighbouring chains, which is typically found in polymers with well-connected crystalline domains.[1,130] However, charge transport in OECT channels is complex, due to the presence of dopants and solvent molecules from the electrolyte. Several studies have shown that electrochemical doping leads to swelling and morphological changes as the film reorganises to accommodate the additional volume of ions.[48,91,95,96,138,139] When OECTs are operating in aqueous electrolytes, the films do not only uptake ions, but also several molecules of water due to the hydration shell carried by the dopants.[95,140] For instance, a recent study by Flagg et al. estimated that during electrochemical oxidation of **P3HT**, the influx of small anions such as Cl^- is accompanied by ~ 10–13 molecules of water. Polymers specifically engineered to uptake hydrated ions, such as those bearing hydrophilic side chains, show swelling and crystal lattice expansion even in the absence of an electrochemical bias.[139,140] Recent investigations show that the majority of water molecules reside in the amorphous regions of the polymers,[139] while ions infiltrate into the crystallites along the side chain directions during OECT operation.[18,67] This higher level of hydration in the amorphous regions leads to heterogenous swelling across the polymer film upon doping. Such morphological features due to excessive swelling hinder electron transport, as high degrees of volumetric expansion of the amorphous domains can disrupt the connections between the crystalline regions of the polymer.[139–141] Therefore, although some degree of hydration is beneficial for ion transport, the swelling ability of the channel material needs to be controlled for efficient charge transport and overall performance in OECTs.

Accumulation of cations in the lamellar spacing of the crystallites during doping could also lead to strong electrostatic interactions between the injected ions and the electronic charges on the polymer backbone. Backbone or side chain engineering strategies focused on preventing

the infiltration of dopant ions close to the backbone could be beneficial for minimising this coulombic charge-pinning effect and enhancing the OECT electron mobility.

These design considerations highlight the complex interplay between efficient ionic transport, electronic transport and ionic-electronic coupling required for n-type OECT materials. While their design can draw on strategies developed in the field of organic electronics, most design principles need to be adapted. As OECT-based applications that require n-type materials continue to mature, there is a growing need for design principles that take into consideration the interactions of n-type polymers with water and dopant ions.

1.4 Thesis aims and overview

The overall aim of this work is to develop n-type organic semiconductors with mixed ionic-electronic transport for bioelectronics applications based on organic electrochemical transistors (OECTs). Due to its extensive use, current material design strategies for OECT-based applications are mostly built upon studies of the p-type conducting polymer, **PEDOT:PSS**. By investigating three series of copolymers, this work aims to establish structure-property relationships specific for n-type semiconductors operating in aqueous electrolytes. Particular focus is given to the role of polymer structure in determining their swelling ability, electrochemical activity, stability and performance in OECTs.

Chapter 2 presents a series of naphthalene diimide-bithiophene (NDI-T2) copolymers functionalised with hybrid alkyl-glycol side chains, where the conjugated backbone is segregated from the ethylene glycol units within the side chain by an alkyl spacer. This chapter explores the ability of alkyl spacers to prevent excessing swelling of the polymers and minimise structural deformation when exposed to aqueous electrolytes. The optimum side chain composition for high stability and balanced mixed conduction is identified using a combination of electrochemical and OECT measurements.

Chapter 3 focuses on increasing the polymer backbone coplanarity by lateral extension of the NDI core to a naphthodithiophene diimide (NDTI) unit, with the aim of increasing the strength of intermolecular interactions and improving the charge transport properties. The solubility and molecular weight of the NDTI-based copolymers are optimised by carefully adjusting the structure and length of the ethylene glycol side chains. The discussion focuses on the effect of enhanced backbone coplanarity on the structural order, electrochemical activity and swelling ability in aqueous media.

Chapter 4 investigates a backbone engineering strategy to tune the electron affinity of isoindigo-based polymers for stable n-type OECT operation within the electrochemical window of water. By systematically altering the energy levels, distinct p-type, ambipolar and n-type OECT operation are achieved within the same polymer series. The chapter investigates the relationships between polymer energetics, interaction with aqueous electrolytes and operation in OECTs.

CHAPTER 2

The effect of alkyl spacers on the mixed ionic-electronic conduction properties of naphthalene diimide-copolymers

2.1 General information and attributions

Polymer **p(gNDI-gT2)** used for this study was provided by Dr Alexander Giovannitti (McCulloch Group, Imperial College London) and synthesised as previously reported.[142] Polymer **p(C3-gNDI-gT2)** was previously synthesised by Dr Alexander Giovannitti (McCulloch Group, Imperial College London); scale-up and characterisation of the polymer were performed by the author. GPC measurements in chloroform were performed by Dr Rawad Hallani (McCulloch Group, KAUST) and PESA and NIR UV-Vis measurements were performed by Weiyuan Du (McCulloch Group, KAUST). QCM, EQCM, EIS and OECT measurements were performed by Dr Achilleas Savva (Inal Group, KAUST). OFET devices were fabricated and analysed by Dr Aniruddha Basu (Anthopoulos Group, KAUST). GIWAXS measurements were performed and analysed by Dr Bryan Paulsen and Ruiheng Wu (Rivnay Group, Northwestern University).

2.2 Introduction

The nature of the side chains is known to have a strong influence on the properties of semiconducting polymers, such as solubility, stability, electrochemical activity, molecular packing and charge transport.[143] Past examples have shown that exchanging the hydrophobic alkyl chains of solution-processable conjugated polymers with hydrophilic ethylene glycol (EG) side chains is a versatile strategy to promote mixed ionic-electronic transport.[86,90,115,116,118,144] Through careful side chain engineering, n-type polymers can now operate in accumulation-mode OECTs with a high volumetric capacitance (C^*) ranging from 200 to 400 F cm^{-3} in aqueous environments.[90,115] Despite recent progress, n-type polymers still suffer from low electron mobilities and show μC^* products ≈ three orders of magnitude lower than their p-type counterparts, as discussed in Section 1.3. While many strategies for improving

the electron mobility of OFET materials have been reported,[1,17] the relationship between polymer structure and charge transport in OECTs remains less clear.

Functionalisation of n-type backbone motifs with polar EG side chains increases the hydrophilicity of the polymer and promotes the uptake of hydrated ions upon exposure to an aqueous electrolyte, with a swelling percentage that can be as high as 102%.[90] Excessive swelling of the polymer film can lead to drastic morphological changes, with detrimental effects on the charge transport properties.[139,141] Several strategies have therefore been employed to control the hydration state of the channel material, including varying the concentration of the electrolyte[140] or the nature of the anions.[95,96] In an alternative approach, Flagg et al. used thermal annealing to improve the crystallinity of a polymer film, which limited the extent of swelling.[139] A more systematic approach to modulate the swelling ability of the channel material is by varying the density of EG side chains. This was previously achieved by synthesising random copolymers containing monomers bearing either alkyl or EG side chains in different ratios.[90,141] Recently, Yue et al. reported the use of hybrid alkyl-glycol side chains to improve the operational stability of a p-type isoindigo-based copolymer.[116] In this chapter, it is hypothesised that hybrid alkyl-glycol side chains with different ratios between the alkyl/glycol fractions could be used to tune the swelling ability of the polymer film and balance its ionic and electronic transport properties.

A previous report showed that the relative position of the alkyl unit within a hybrid alkyl-glycol side chain with respect to the conjugated backbone has significant impact on the electronic transport properties.[145] The polymer in which the alkyl unit was adjacent to the conjugated backbone showed a shorter π-stacking distance and a longer correlation length, which resulted in a superior electron mobility in OFET devices. In the context of OECTs, it is unclear whether improving the long-range ordering in the dry state would translate into a superior OECT mobility when operating in aqueous media. However, it was reasoned that inserting a

hydrophobic alkyl unit adjacent to the polymer backbone could prevent penetration of the hydrated dopant ions close to the backbone and minimise coulombic charge-pinning of the polaron (**Figure 2.1a**), hence improving the OECT mobility.

This chapter investigates the electrochemical behaviour and OECT performance in aqueous electrolytes of a series of NDI-T2 copolymers functionalised with hybrid alkyl-glycol chains, where the conjugated backbone is segregated from the EG units by an alkyl spacer. Starting from the previously reported polymer **p(gNDI-gT2)** (Section 1.3.2),[115] two derivatives featuring either a C_3- or a C_6-alkyl spacer were designed (**Figure 2.1b**). Increasing the length of the alkyl spacer was investigated as a potential design strategy to modulate the swelling, optimise the mixed ionic-electronic transport properties and improve the operational stability of n-type materials.

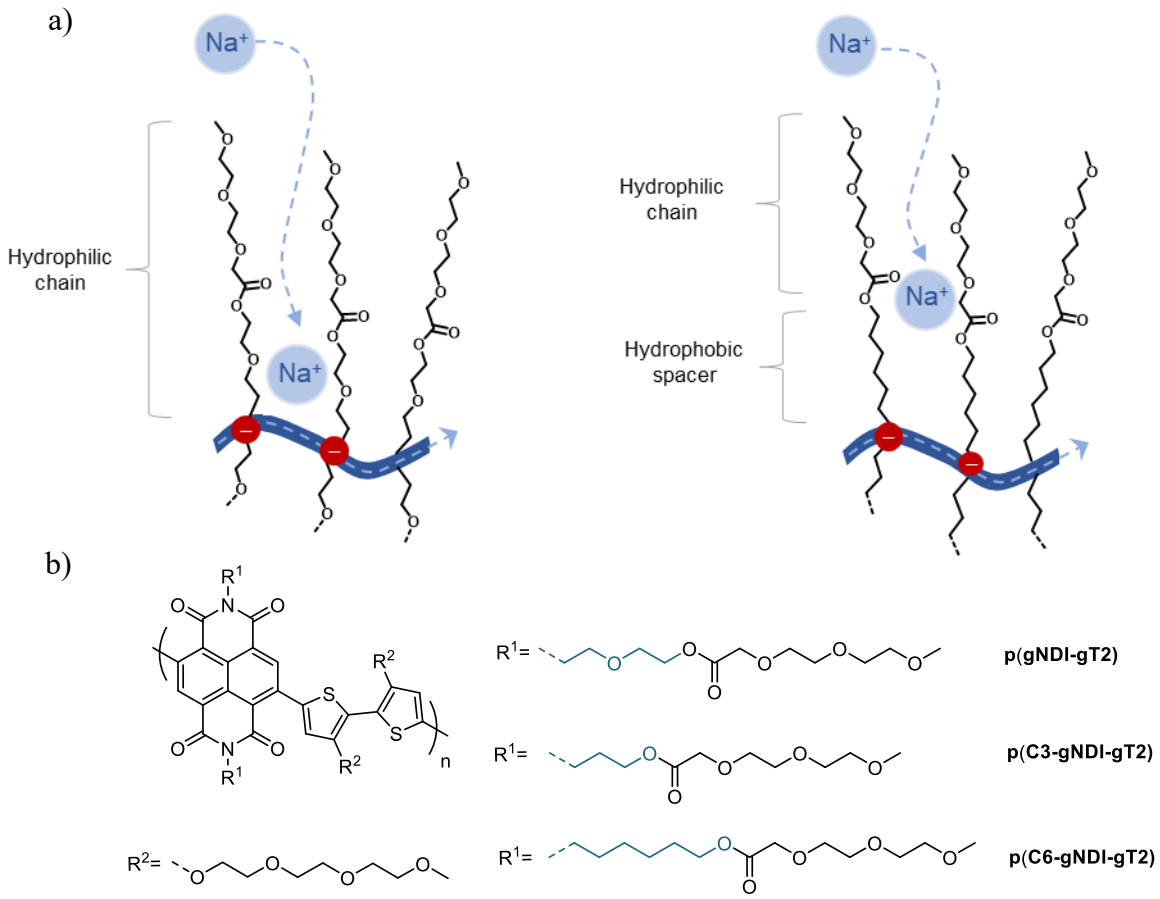
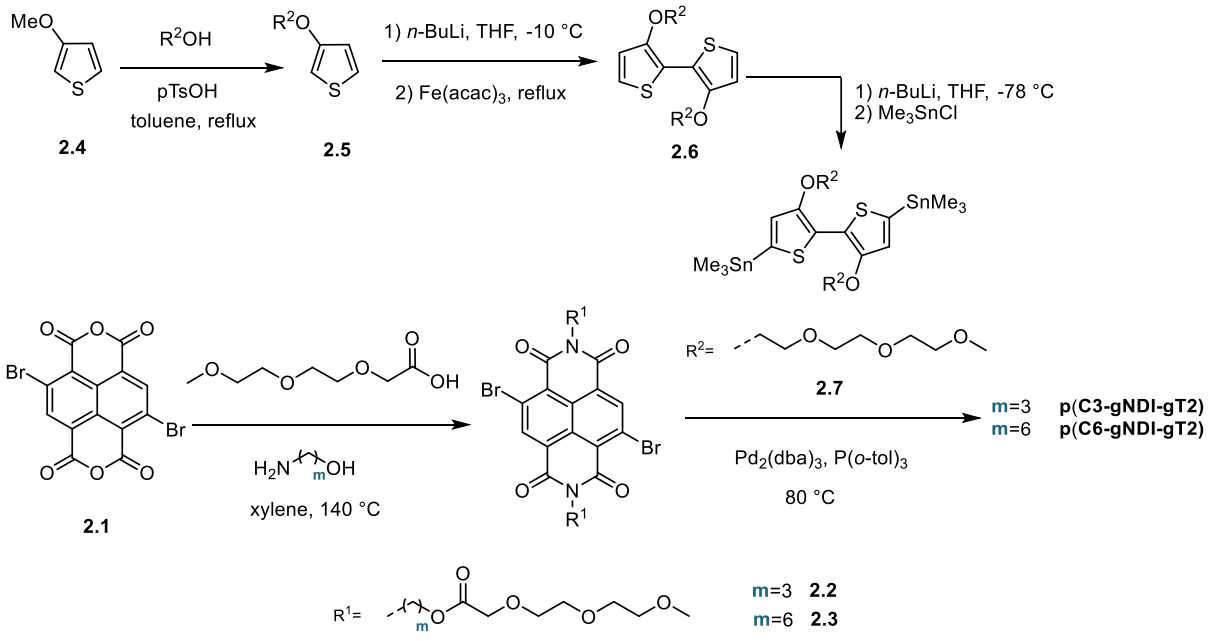


Figure 2.1. (a) Schematic representation of the side chain engineering strategy and (b) the structures of copolymers studied in this chapter.

2.3 Synthesis of the polymers

Symmetric NDI monomers with alkyl side chains at the imide-position can be prepared from commercially available 2,6-dibromonaphthaleneanhydride via a condensation reaction with the appropriate primary amine. However, in the case of hybrid alkyl-EG side chains, the synthesis of the amine precursor involves a series of substitution reactions and is often tedious.[116,145] A one pot synthesis of NDI derivatives with complex EG side chains such as **p(gNDI-gT2)** (**Figure 2.1**) was reported by Giovannitti et al.[115] 2,6-Dibromonaphthaleneanhydride was treated with a commercially available amino-alcohol and a carboxylic acid, achieving both functionalisation at the imide-position and extension of the side chain via an ester linkage in one step. As various amino-alcohols can be chosen for this condensation reaction, the ester-linked side chains allow a versatile approach to screen alkyl spacers of various lengths starting from 2,6-dibromonaphthaleneanhydride.



Scheme 2.1. Synthesis of the polymers **p(C3-gNDI-gT2)** and **p(C6-gNDI-gT2)**.

Accordingly, monomers **2.2** and **2.3** were prepared from 2,6-dibromonaphthaleneanhydride (**2.1**) using excess 2-[2-(2-methoxyethoxy)ethoxy]acetic acid with 3-amino-1-propanol and 6-amino-1-propanol, respectively (**Scheme 2.1**). The formation of the monomers was confirmed by NMR analysis. The HSQC spectra in the side chain region for both monomers are shown in **Figure 2.2**. Monomer **2.3** shows additional methylene proton signals resonating from δ 1.79 to 1.45 ppm, correlated with four carbon signals from δ 25.9 to 28.8 ppm, which is consistent with the presence of an extended C_6-alkyl spacer.

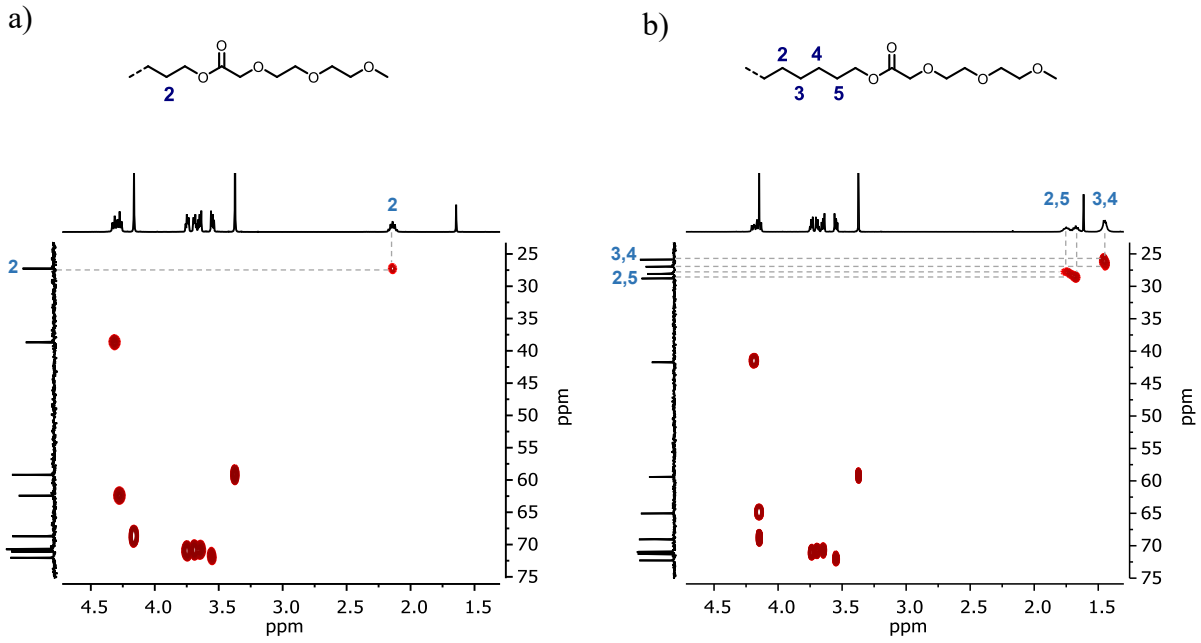


Figure 2.2. HQSC spectra of monomers (a) **2.2** and (b) **2.3** showing ^{1}H-^{13}C correlations for the side chain region.

Monomers **2.2** and **2.3** were obtained in a yield of 36% and 44%, respectively, following purification by preparative gel permeation chromatography in chloroform. Although modest, the yields are comparable to previously reported values for the synthesis of NDI derivatives.[90,121] The low yields of the condensation reaction of **2.1** with primary amines are typically due to the formation of core-substituted amine side products via nucleophilic aromatic substitution of the bromine atoms.[146] It should be noted that attempts to purify the monomers by column chromatography led to even lower isolated yields (< 15%). Due to their high

polarity, elution of the monomers required the addition of methanol to the solvent mixture, which could have led to a transesterification reaction and degradation on the column.

The comonomer **2.7** (**Scheme 2.1**) was functionalised with additional triethylene glycol chains at the 3,3'-positions to ensure solubility of the polymers in common organic solvents such as chloroform.[115] 3-Methoxythiophene (**2.4**) was subjected to an acid catalysed transetherification reaction with triethylene glycol monomethyl ether to give **2.5**. Following a protocol by Nielsen et al.,[118] selective head to head coupling of **2.5** to give **2.6** was achieved by lithiation with *n*-BuLi at –10 °C, followed by the addition of stoichiometric amounts of $Fe(acac)_3$. **2.6** was lithiated at the 2-position with *n*-BuLi and quenched with trimethyltin chloride to give the distannylated bithiophene monomer **2.7**.

Polymers **p(C3-gNDI-gT2)** and **p(C6-gNDI-gT2)** were prepared by Stille cross-coupling of the NDI monomers with the bithiophene comonomer **2.7** (**Scheme 2.1**). The polymerisation reaction was carried out at a relatively low temperature of 80 °C in DMF. These conditions were chosen in order to limit the molecular weight of the polymer and ensure a high yield of the chloroform soluble fractions.[142] Polymers **p(C3-gNDI-gT2)** and **p(C6-gNDI-gT2)** were obtained in good yields of 83% and 70%, respectively and they both showed good solubility in chloroform at room temperature.

2.4 Properties of the polymers

The number average molecular weights (M_n) measured by gel permeation chromatography using polystyrene as the standard and chloroform as the eluent at 40 °C are summarised in **Table 2.1**. It should be noted that bimodal molecular weight distributions were observed for all polymers, most likely due to aggregation of the polymers in chloroform solutions. Similar weight distributions have been previously reported for NDI-T2 polymers with high densities of EG side chains and are expected to lead to an overestimation of molecular weight.[90] Indeed, when the molecular weight distribution was analysed by matrix-assisted laser desorption/ionization time-of-flight spectrometry (MALDI-ToF), polymer chains only up to 7–9 repeating units were detected (**Table 2.1**, **Figure A1** in Appendix A).

Table 2.1. Properties of the copolymers

Polymer	M_n [$Đ$] (kDa)[a]	Repeat units[b]	T_d (°C)[c]	E_g (eV)[d]	EA (eV)[e]	IP (eV)[f]
p(gNDI-gT2)	16.8 [3.04]	7	334	0.8	4.04	5.05
p(C3-gNDI-gT2)	32.4 [2.27]	9	311	0.9	4.06	5.17
p(C6-gNDI-gT2)	20.2 [2.68]	8	323	0.9	3.98	5.11

[a] Number-average molecular weight (M_n) and dispersity ($Đ$) (GPC versus polystyrene standards in chloroform). [b] MALDI-ToF. [c] Temperature for 5% weight-loss from thermogravimetric analysis. [d] Optical band gap estimated from thin film absorption onset. [e] Cyclic voltammetry of the polymer thin films on ITO coated glass substrates in acetonitrile with 0.1 M tetrabutylammonium hexafluorophosphate as the supporting electrolyte. [f] Measured by photoelectron spectroscopy in air.

The thermogravimetric analysis (TGA) data indicates that all polymers have good thermal stability, with decomposition temperatures above 300 °C (**Table 2.1**, **Figure A2** in Appendix A). The decomposition temperatures are however lower compared to NDI-T2 analogues with linear EG side chains (*cf.* ~ 390 °C for **P-100**),[90] which can be attributed to the presence of less thermally stable ester groups.[147]

The optoelectronic properties of the polymers series are summarised in **Table 2.1**. Photoelectron spectroscopy in air (PESA) measurements were carried out to calculate the ionisation potentials (IP). The IP of both **p(C3-gNDI-gT2)** (5.17 eV) and **p(C6-gNDI-gT2)** (5.11 eV) bearing alkyl spacers were found to be higher than that of **p(gNDI-gT2)** (5.05 eV). This result is in line with previous observations, where decreasing the density of EG chains leads to an increase in the IP.[86,90,148,149]

The electron affinities (EA) of the polymer series were measured by cyclic voltammetry of the thin films in 0.1 M tetrabutylammonium hexafluorophosphate ($TBAPF_6$) in acetonitrile (**Table 2.1**, **Figure A3** in Appendix A). The EA values are comparable across the series, ranging from 3.98 to 4.06 eV. Due to electron decoupling of the imide substituents from the NDI core, the lack of major differences in EA values upon varying the side chains is common for NDI derivatives.[150] The similarity between these polymers implies that any differences in n-type doping processes should be due to differences in the side chain structure, rather than energy levels.

The UV-Vis absorption spectra in solution (chloroform) and thin film of the polymer series are shown in **Figure 2.3**. As for other NDI-T2 copolymers,[151] the spectra show a high energy absorption band at ~ 400 nm, ascribed to the π-π * transition and a broad low energy band at ~ 1000 nm, due to internal charge transfer (ICT). In chloroform solutions, additional peaks can be observed for all polymers between 980–1100 nm, indicative of aggregation between the polymer chains. The optical band gaps were estimated from the absorption onset of the thin-film spectra, resulting in similar values of about 0.9 eV for all polymers (**Table 2.1**). Notably, the thin film absorption spectrum of **p(C3-gNDI-gT2)** shows aggregation features with a low energy shoulder peak at 1172 nm, suggesting enhanced order of the polymer chains.[152]

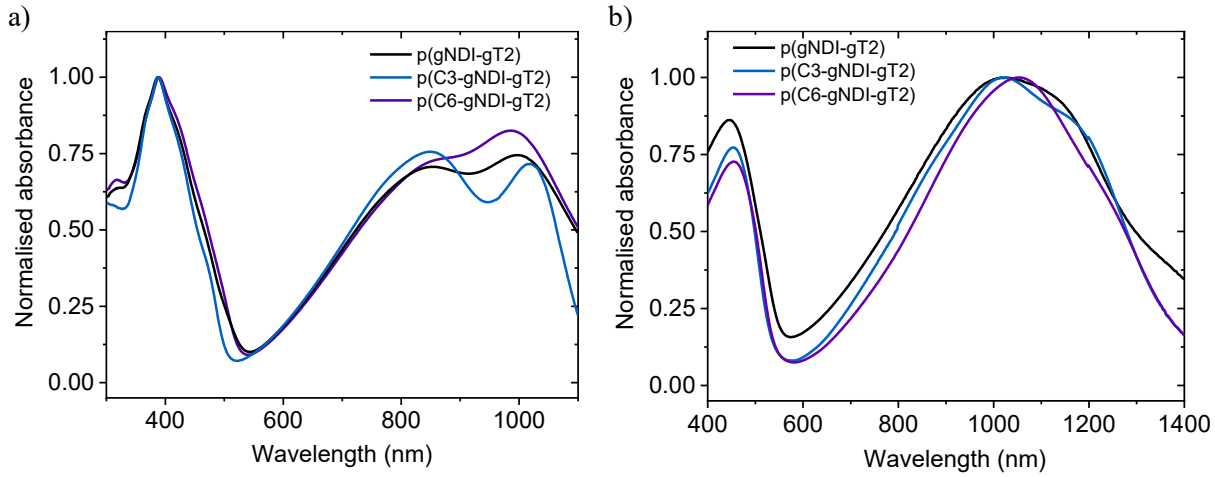


Figure 2.3. UV-Vis Spectra of the polymers (a) in chloroform solution and (b) as thin films on glass substrates using a UV-Vis NIR detector.

2.5 Electrochemical activity in aqueous electrolytes

An understanding of the electrochemical processes in aqueous electrolytes is of great importance for rationalising OECT characteristics. Low reduction potentials are desired for operation in aqueous environments to avoid electrolysis of water and reduction of oxygen.[87] Cyclic voltammetry (CV) measurements of the thin films were carried out in aqueous solutions of NaCl (0.1 M) to study the influence of alkyl spacers on the reduction potential, as well as the stability of the redox reactions.

As shown in **Figure 2.4**, all polymers can be charged and discharged in the aqueous electrolyte. Polymers **p(gNDI-gT2)** and **p(C3-gNDI-gT2)** show comparable reduction onsets of approximately –0.11 V versus the Ag/AgCl reference electrode. Upon extending the alky spacer to a C_6-alkyl unit, the reduction onset shifts by $\Delta V = 0.09$ V to a more negative value. As the copolymers have identical backbones and EA, the shift in the reduction potential is most likely due to the lower density of hydrophilic units within the side chains and a larger activation barrier for ion penetration.[90,141] It should be noted that due to the relatively small IP of the polymers, oxidative processes can also be observed within the applied potential range.

However, the current response was low compared with the reduction processes, indicative of predominantly n-type nature.

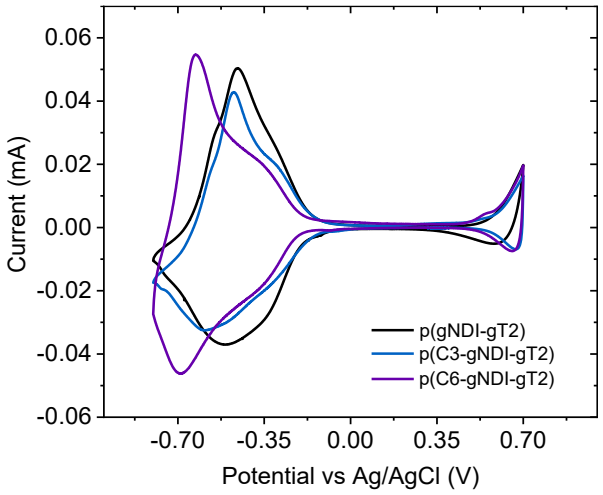


Figure 2.4. Cyclic voltammetry of the polymer films on ITO coated glass substrates in degassed 0.1 M NaCl aqueous solution with a scan rate of 100 mV s^{-1} and a Ag/AgCl reference electrode (2^{nd} cycle).

The n-type doping processes in aqueous electrolytes were further evaluated using spectroelectrochemical measurements. The evolution of the UV-Vis spectra was monitored as the polymers underwent electrochemical reduction under an applied potential from 0 to –0.8 V and the results are presented in **Figure 2.5**. All polymers show a gradual reduction in intensity of the low energy ICT band and a simultaneous increase in intensity of new absorption features between 810–830 nm and 500–650 nm. These spectral changes are consistent with formation of a polaronic species during electrochemical reduction, as previously demonstrated using time-dependent density functional theory (TD-DFT) calculations.[54]

In line with the CV data, polymer **p(C6-gNDI-gT2)** shows a slightly larger onset of polaron formation (i.e. the bias at which the relative absorption of the ICT band decreases and the absorption of the polaronic species increases) and smaller changes in absorption intensity with respect to the other copolymers (**Figure 2.5d** and **Figure 2.5e**). Despite the slight differences

in reduction onsets, all polymers show reversible polaron formation up to –0.8 V and recover the features of the initial spectrum when the potential is reversed to 0 V.

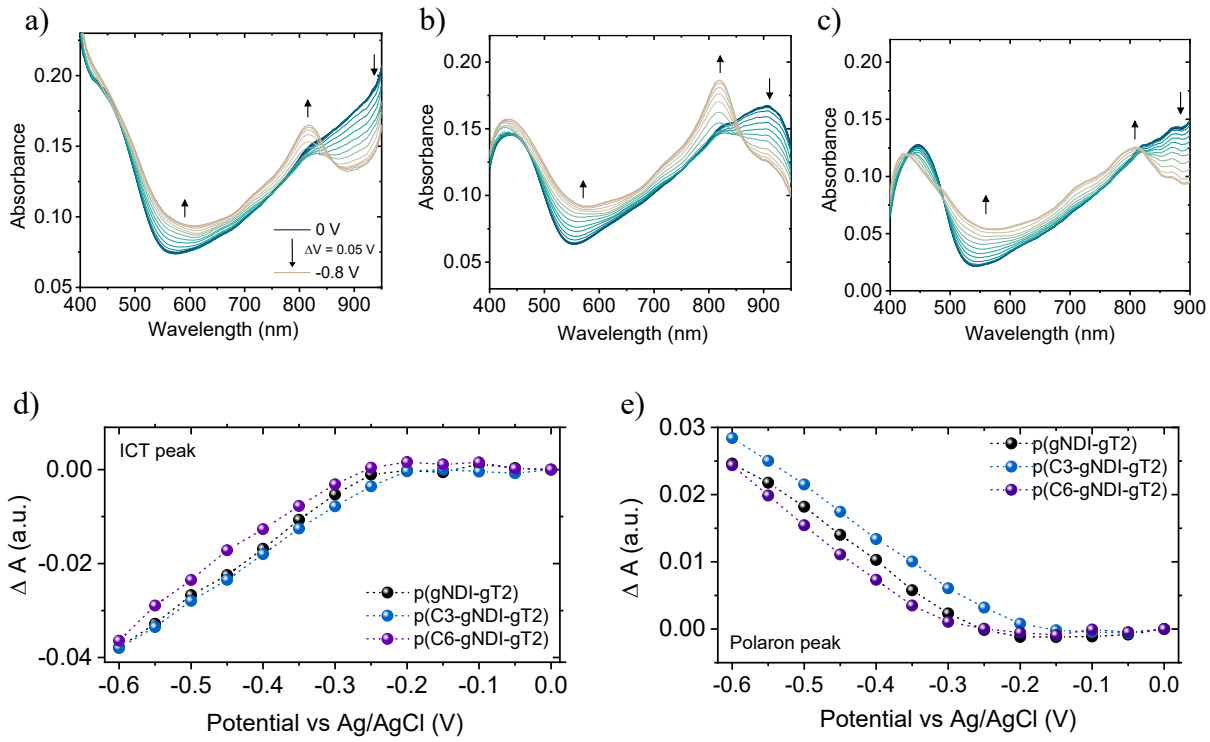


Figure 2.5. Evolution of the UV-Vis absorption spectrum during charging between 0 and –0.8 V in 0.1 M NaCl aqueous solution using a scan rate of 50 mVs^{-1} for (a) **p(gNDI-gT2)**, (b) **p(C3-gNDI-gT2)** and (c) **p(C6-gNDI-gT2)**. Relative difference between the absorbance recorded with bias (0 V to –0.6 V in steps of 50 mV) and the initial spectrum without bias of the (d) ICT peak (926 nm) and (e) polaron peak (540 nm).

The abilities of the polymer films to uptake water and ions upon electrochemical doping were investigated using electrochemical quartz crystal microbalance with dissipation monitoring (EQCM-D). A QCM-D sensor allows recordings of the changes in mass of a polymer film deposited on a piezoelectric crystal, which manifest as a change in oscillation frequency (*f*) and dissipation of energy (*D*).[153] A decrease in the oscillation frequency indicates an increase in the mass of the film.[154] First, QCM-D measurements were used to determine the swelling of

the polymers in contact with a 0.1 M NaCl aqueous solution prior to reduction/oxidation, due to passive diffusion of ions and water from the electrolyte into the films (**Figure 2.6a**, raw data in **Figure A4** in Appendix A). Polymer **p(gNDI-gT2)** showed the largest passive swelling of 44%. Introducing alkyl spacers led to a decrease in the swelling ability to 28% for **p(C3-gNDI-gT2)** and 13% for **p(C6-gNDI-gT2)**.

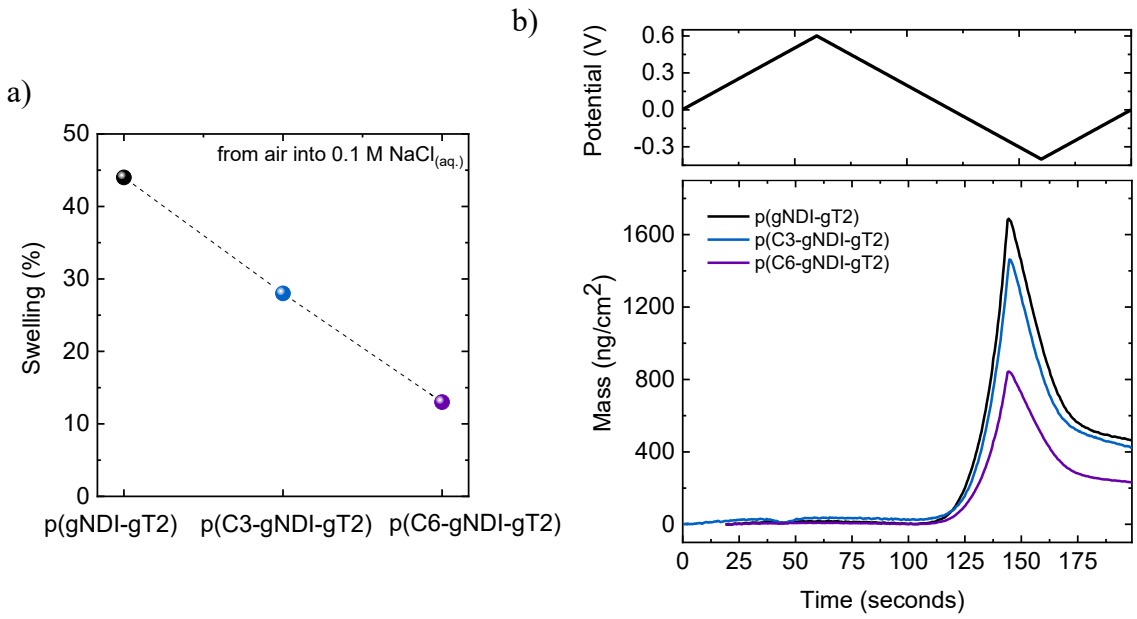


Figure 2.6. (a) Swelling percentage of polymer films when immersed in 0.1 M NaCl aqueous solution from QCM-D measurements (raw data in **Figure A4** in Appendix A) (b) EQCM-D for polymer films for one doping cycle (up to –0.40 V versus Ag/AgCl) in 0.1 M NaCl aqueous solution.

A similar trend was observed when measuring the changes in mass triggered by a doping potential. **Figure 2.6b** shows the applied voltage versus Ag/AgCl and the change in mass as a function of time for a single voltage sweep (0 V to 0.6 V to –0.40 V to 0 V). During electrochemical reduction of an n-type material, hydrated cations migrate into the polymer film to compensate for the electronic charges generated on the NDI units. In line with this doping process, the mass uptake increases with the applied potential for all polymers (**Figure 2.6b**). A lower gain in mass for the same doping potential is observed as alkyl spacers are introduced.

For instance, at a bias of –0.3 V, the mass accumulated within the **p(C6-gNDI-gT2)** film is half the mass accumulated within the **p(gNDI-gT2)** film, with values of 0.84 μg/cm^2 and 1.68 μg/cm^2, respectively. In addition, when the potential is reverted to 0 V, a fraction of the injected mass remains in the polymer films, which is lower for the polymers bearing hybrid alkyl-glycol side chains.

The swelling behaviour of the polymers both with and without an applied bias indicates that functionalisation with alkyl spacers allows modulation of the hydration state of the polymer film. In agreement with previous studies,[90,141] decreasing the density of EG units, in this case correlated with extending the length of the alkyl spacer, leads to a lower swelling ability in aqueous electrolytes. Previous reports have shown that a low swelling ability hinders ion penetration into the bulk of the material and leads to high reduction potentials, which could preclude stable operation within the electrochemical window of water.[90] Notably, the hybrid side chains of **p(C3-gNDI-gT2)** and **p(C6-gNDI-gT2)** provide an appropriate balance of hydrophilic and hydrophobic units for controlling the swelling of the polymer, while still allowing reversible electrochemical reduction with onsets lower than –0.20 V (*cf.* passive swelling of ~ 40% and reduction onset of –0.25 V versus Ag/AgCl for **P-90**).[90]

2.6 GIWAXS analysis of the polymers

2.6.1 Structural properties of the neat polymer films

Grazing incidence wide angle X-ray scattering (GIWAXS) measurements of the thin films on p+ doped Si wafer substrates were carried out to investigate the morphology of the polymers. **Figure 2.7** shows the 2D GIWAXS patterns, as well as in-plane and out-of-plane line cuts of the as-spun thin films and **Table 2.2** at the end of Section 2.6 summarises the relevant peak parameters. The general microstructure is similar to other NDI-T2 analogues,[90,91,155] showing

a mixture of edge-on and face-on crystallites with varying degrees of isotropic character. The enhanced out-of-plane π-stack scattering and in-plane backbone scattering indicates that the majority of domains are oriented face-on.

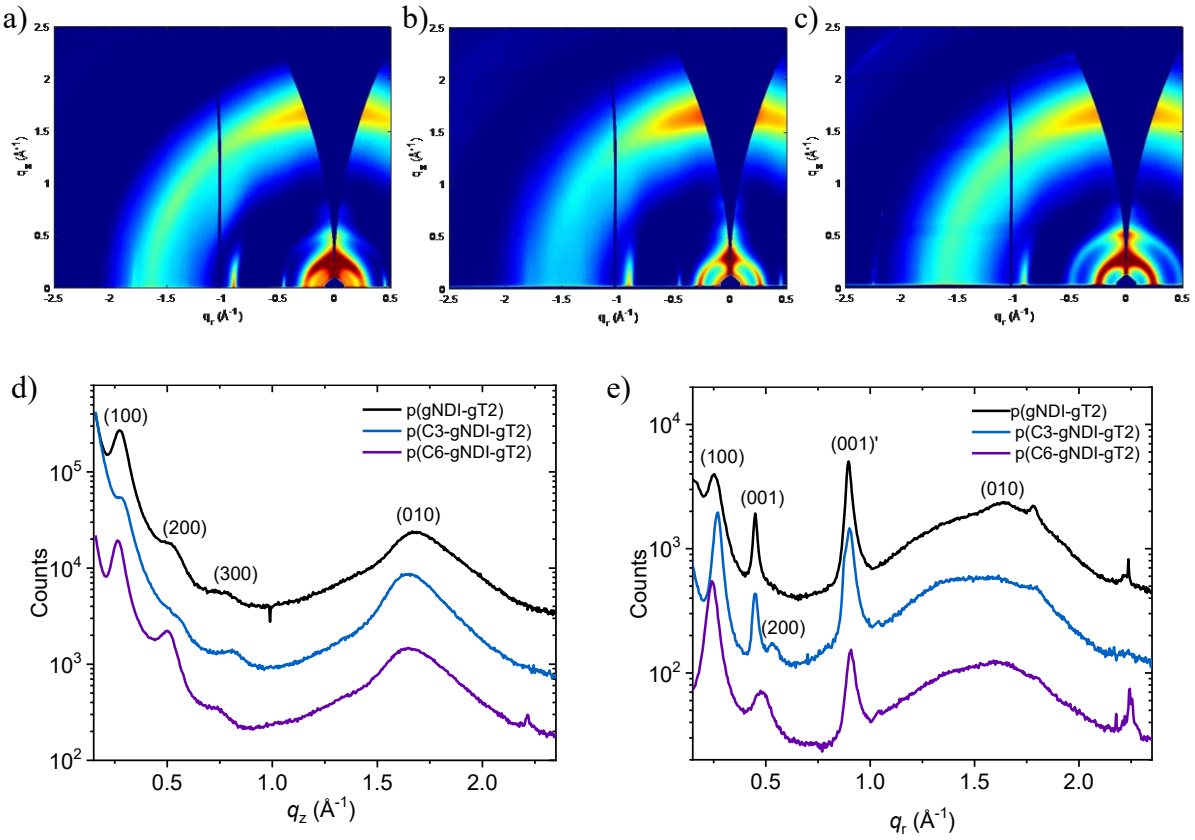


Figure 2.7. GIWAXS of neat as-cast films: q_r-q_z maps of scattered X-ray intensity from thin films of (a) **p(gNDI-gT2)** (b) **p(C3-gNDI-gT2)** and (c) **p(C6-gNDI-gT2)** polymers and (d) out-of-plane (q_z) and (e) in-plane (q_r) line cuts of each polymer.

Both polymers functionalised with alkyl spacers show a slight (~ 0.05 Å) out-of-plane π-stack expansion relative to **p(gNDI-gT2)**. The polymer having a C_3-alkyl spacer, **p(C3-gNDI-gT2),** shows stronger out-of-plane π-stack scattering compared to **p(gNDI-gT2)** and **p(C6-gNDI-gT2)**. All films show evidence of three orders of out-of-plane lamellar scattering. Increasing the fraction of alkyl chains leads to an increase in in-plane lamellar scattering and the emergence of a second order lamellar peak for **p(C3-gNDI-gT2)** and **p(C6-gNDI-gT2)**. As

expected, polymer **p(C3-gNDI-gT2)** with the shortest overall length of the side chain shows a contracted lamellar *d*-spacing both in- and out-of-plane compared with the rest of the series. Previous studies have shown that NDI-T2 based polymers display two polymorphs which differ in terms of stacking of the T2 and NDI units: Form I where the polymer chains orient with alternating NDI-to-NDI and T2-to-T2 units producing a longer backbone periodicity and Form II where the polymer chains orient with mixed NDI-to-T2 units producing a shorter backbone periodicity.[156] The ratio between the in-plane backbone scattering peak associated with Form I (noted as (001)) and Form II (noted as (001)') provides an indication of the relative content of each polymorph. Polymers **p(gNDI-gT2)** and **p(C3-gNDI-gT2)** show evidence of both polymorphs in a similar ratio, with a preference for Form II crystallites. Upon introducing alkyl spacers, the magnitude of both of (001) and (001)' peaks decreases, leading to indistinguishable Form I peaks for **p(C6-gNDI-gT2)**. Interestingly, the presence of only Form II stacking did not result in a transition to predominately edge-on orientation, as it was previously reported for analogues with alkyl side chains.[157]

To quantitatively assess the long-range packing order, the GIWAXS data was fit to extract the disorder associated coherence length (ξ), both in the backbone direction (as assessed from the in-plane (001)' peak) and in the lamellar direction (as assessed for the in-plane (100) peak).[158] Notably, **(C3-gNDI-gT2)** shows the largest coherence lengths (213 and 345 Å) within the polymer series, as assessed by the in-plane (100) and (001)' peaks, respectively.

2.6.2 Influence of aqueous electrolytes on the structural properties

During OECT operation, polymer films are expected to undergo significant changes in their structure and morphology due to the uptake of ions and water. Therefore, the structural features observed for the as cast films may not provide sufficient information to understand any potential differences in mixed ionic and electronic transport. In order to understand the effect of aqueous electrolytes on the structure of each polymer, GIWAXS measurements were performed on thin films that had undergone ex situ electrolyte exposure or n-type doping. It should be noted that while EQCM-D allows for a quantitative determination of the bulk swelling behaviour of the polymer, in both ordered and disordered regions, GIWAXS only probes the ordered domains in the film.

Electrolyte exposure of the GIWAXS samples was carried out by covering the polymer film with a droplet of 0.1 M NaCl aqueous solution for approximately 30 min. A similar procedure was used to electrochemically dope the polymer film, with application of a bias of –0.65 V versus a Ag/AgCl pellet electrode immersed in the electrolyte. The samples were rinsed with deionised water to remove excess salt and dried with N_2 prior to measurement.

Figure 2.8 shows the GIWAXS line cuts and **Table 2.2** summarises the relevant peak parameters, whereas the 2D GIWAXS patterns are included in **Figure A5** in Appendix A. As shown in **Figure 2.8**, all polymers exhibit minimal changes in the out-of-plane π-stack scattering upon electrolyte exposure and electrochemical reduction. Due to the small differences in π-π spacing, comparisons could not be performed outside the experimental error in this crystallite direction.

Analysing the in-plane backbone scattering, **p(gNDI-gT2)** shows fairly steady coherence lengths across all film conditions. This was in contrast with a large expansion of the in-plane lamellar *d*-spacing from 24.7 Å to 25.9 Å (5%) and a decrease in coherence length by ~ 15%

upon electrolyte exposure. Electrochemical doping resulted in even more pronounced changes until the in-plane (100) peak diminished into the scattering background.

In the case of **p(C3-gNDI-gT2)**, both polymorphs showed minimal fluctuations (~ 1%) in the in-plane backbone *d*-spacings upon electrolyte exposure and reduction. Notably, lower expansions of the in-plane lamellar spacing are observed upon electrolyte exposure (0.4%) and electrochemical doping (3%) relative to **p(gNDI-gT2)**. The low expansion upon electrolyte exposure for **p(C3-gNDI-gT2)** suggests that the crystal lattice does not expand spontaneously in contact with the aqueous electrolyte and expands only upon electrochemical doping. Interestingly, a much higher decrease in the coherence length is observed in the direction of lamellar stacking, compared with the backbone direction upon electrochemical doping (42% versus 18% of the as-cast ξ).

The structure of **p(C6-gNDI-gT2)** functionalised with an extended alkyl spacer showed the lowest sensitivity to electrolyte exposure and electrochemical reduction. Notably, the in-plane lamellar scattering peak did not shift upon processing, indicating a constant *d*-spacing irrespective of ex situ conditions. The relative decrease in coherence length of ~ 18% between as cast and electrochemically reduced **p(C6-gNDI-gT2)** both along the lamellar and backbone directions indicated a more uniform increase in disorder, compared to **p(gNDI-gT2)** and **p(C3-gNDI-gT2)**.

Overall, the structural changes due to interactions with aqueous electrolytes agree with previous reports, where electrochemical doping leads to lamellar expansion as hydrated ions accumulate between the side chains to counterbalance the electronic charges along the polymer backbone.[96,140] Notably, the degree of distortion in the lattice spacings is influenced by the nature of the side chain, where introduction and extension of the alkyl spacer adjacent to the conjugated backbone leads to less pronounced structural changes.

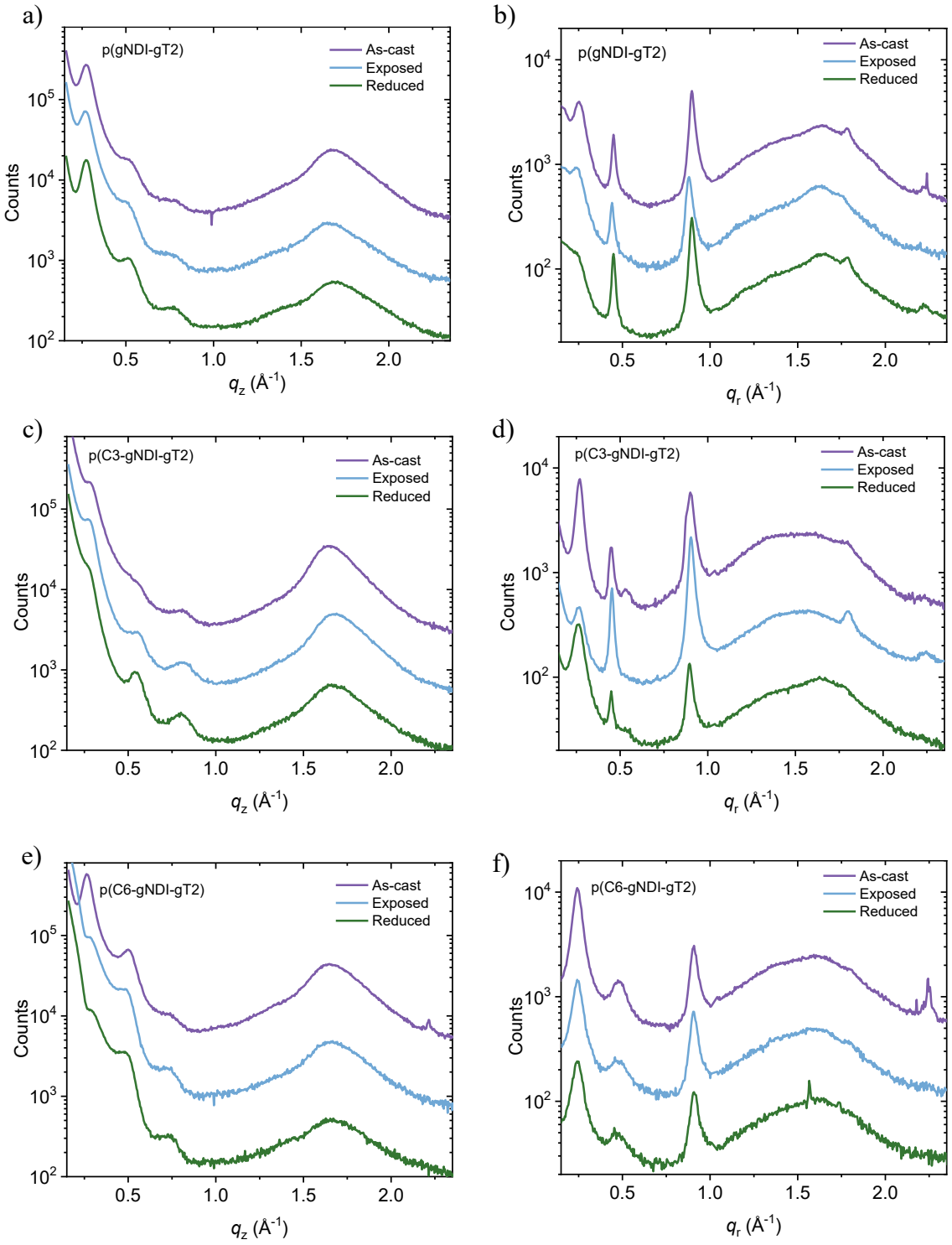


Figure 2.8. Ex situ GIWAXS: out-of-plane (q_z) and in-plane (q_r) line cuts for the polymer series as-cast (purple), exposed to electrolyte (blue) and electrochemically reduced (green), measured ex-situ for (a), (b) **p(gNDI-gT2)** (c), (d) **p(C3-gNDI-gT2)** (e), (f) **p(C6-gNDI-gT2)**.

Table 2.2. GIWAXS peak parameters across film conditions.

		π-π stacking[a]	lamellar stacking[b]		backbone stacking[c]	
		d (Å)	*d* (Å)	*ξ* (Å)	*d* (Å)	*ξ* (Å)
p(gNDI-gT2)	As-cast	3.76	24.7	112	7.00	303
	Exposed	3.78	25.9	95	7.13	278
	Reduced	3.72	–	–	7.00	307
p(C3-gNDI-gT2)	As-cast	3.82	23.4	213	6.99	345
	Exposed	3.74	23.5	155	6.94	311
	Reduced	3.75	24.0	123	7.00	284
p(C6-gNDI-gT2)	As-cast	3.81	25.8	164	6.92	254
	Exposed	3.76	25.7	144	6.92	293
	Reduced	3.76	25.8	134	6.90	208

[a] Out-of-plane π-stack scattering peak (010). [b] In-plane lamellar scattering peak (100). [c] In-plane backbone scattering associated with Form II (001)'.

2.7 Electrical characterisation

2.7.1 OFET performance

In order to assess the electronic transport properties of the polymers in dry state, OFET devices were fabricated with a bottom-gate (Si) bottom-contact (Ti/Au) architecture, using silicon dioxide as the dielectric. The polymer films were blade coated from chloroform solutions at 40 °C onto the substrates. The transfer characteristics were used to extract the OFET mobility in the linear regime (**Figure A6** in Appendix A). As previously reported for other NDI-T2 copolymers functionalised with EG side chains,[90,115] the OFET mobilities were found to be up to 4 orders of magnitude lower compared to their alkylated analogue, N2200.[106] Both polymers bearing alkyl spacers show a slight improvement in OFET mobility compared with the EG-only analogue. The derivative functionalised with a short C_3-alkyl spacer, **p(C3-gNDI-gT2)**, was found to have the highest electron mobility of 9.2×10^{-4} cm^2 V^{-1} s^{-1}, relative to **p(gNDI-gT2)** (2.2×10^{-4} cm^2 V^{-1} s^{-1}) and **p(C6-gNDI-gT2)** (6.3×10^{-4} cm^2 V^{-1} s^{-1}).

The higher OFET mobility of **p(C3-gNDI-gT2)** can be explained based on the structural characterisation of the neat polymer films using GIWAXS. In the as-cast form, **p(C3-gNDI-gT2)** displayed the largest π-stack scattering intensity and longest coherence length in both the backbone and lamellar directions within the polymer series. The enhanced coherence length along the backbone direction is likely to be a significant factor as NDI-T2 copolymers show anisotropic charge transport that favours the backbone direction over the lamellar direction.[157] In agreement with previous findings,[159] these results indicate that shorter side chains promote structural order in the pristine films, which is beneficial for charge transport in OFETs.

2.7.2 OECT performance

To assess the effect of alkyl spacers on the mixed ionic-electronic transport, OECT devices were measured in 0.1 M NaCl aqueous solutions in ambient conditions using a Ag/AgCl pellet electrode as the gate. The output and transfer characteristics are shown in **Figure 2.9** and device parameters are summarised in **Table 2.3**.

As expected, the source-drain current increases upon application of a positive bias at the gate, demonstrating n-type OECT operation in accumulation mode. The transfer characteristics show that **p(C6-gNDI-gT2)** bearing an extended spacer has a higher threshold voltage of 0.37 V than both **p(C3-gNDI-gT2)** and **p(C6-gNDI-gT2)** (0.25 and 0.26 V, respectively). This result is in accordance with the CV and spectroelectrochemistry findings and can be interpreted as a higher energy barrier for penetration of hydrated cations into the less hydrophilic film. Notably, both copolymers functionalised with alkyl spacers adjacent to the polymer backbone show a higher thickness-normalised peak transconductance g_m compared with **p(gNDI-gT2)** (**Figure 2.9**). The derived μC^* products follow the same trend, increasing from 0.06 to 0.13 and 0.16 F cm^{-1} V^{-1} s^{-1} when going from **p(gNDI-gT2)** without a spacer to **p(C3-gNDI-gT2)** and **p(C6-gNDI-gT2)**.

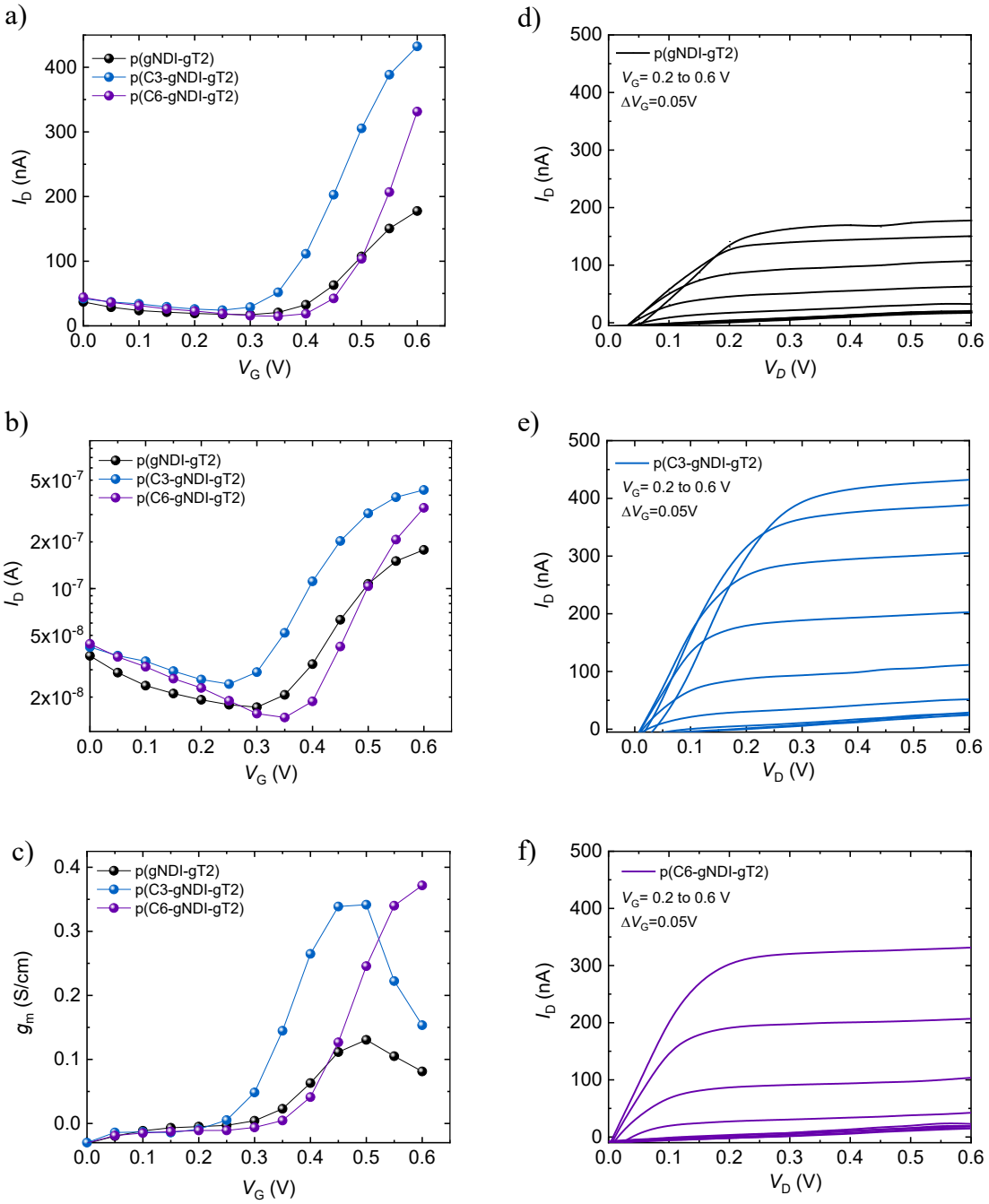


Figure 2.9. Performance of the OECT devices (W = 100 µm, L = 10 µm) in 0.1 M NaCl aqueous solution in ambient conditions showing (a) n-type transfer curve (V_D = 0.6 V) (b) current on a logarithmic scale (c) normalised transconductance (g_m) versus gate voltage (V_G). The transconductance was normalised by the thickness of the active layer. The output characteristics of the OECT devices fabricated with (d) **p(gNDI-gT2)** (e) **p(C3-gNDI-gT2)** (f) **p(C6-gNDI-gT2)**.

Table 2.3. OECT performance of polymers

Polymer	g_m (S/cm)[a]	V_T (V)[b]	$[\mu_{el} C^*]$ (F/cmVs)[c]	C^* (F/cm^3)[d]	μ_{el} OECT (cm^2/(Vs))[e]	μ_{el} OFET (cm^2/(Vs))[f]
p(gNDI-gT2)	0.13	0.26	0.06	221	1.28×10^{-6}	2.2×10^{-4}
p(C3-gNDI-gT2)	0.34	0.25	0.13	72	4.02×10^{-5}	9.2×10^{-4}
p(C6-gNDI-gT2)	0.37	0.37	0.16	59	1.52×10^{-4}	6.3×10^{-4}

[a] OECT peak transconductance measured at $V_G = 0.5$ V for **p(gNDI-gT2)** and **p(C3-gNDI-T2)** and $V_G = 0.6$ V for **p(C6-gNDI-T2)** normalized by thickness. [b] Threshold voltage. [c] $[\mu_{el}C^*]$ estimated from the transfer characteristics of the OECT device with known channel dimensions and biasing conditions. [d] Electrochemical impedance spectroscopy measurements of the polymers at the OECT gates in 0.1 M NaCl aqueous solution ($L = W = 500$ μm, $V = –0.6$ V versus Ag/AgCl). [e] Electron mobility extracted from bandwidth measurements. [f] OFET mobility extracted from bottom-gate bottom-contact transistors.

To investigate further the μC^* product of the polymer series, electrochemical impedance spectroscopy (EIS) and impedance matching measurements were performed to determine the volumetric capacitance (C^*) and electron mobility (μ) in turn. EIS measurements were carried out by spin coating the polymer solutions on gold electrodes and recording the changes in the impedance magnitude and phase (**Figure 2.10**). The phase behaviour in EIS is useful for identifying whether the film is dominated by a more resistive ($0° < \varphi < −45°$) or capacitive ($−45° < \varphi < −90°$) character.[160] As shown in **Figure 2.10b**, all polymers exhibit capacitive behaviour at low frequencies. The extracted capacitance (**Figure 2.10c**) shows a cut-off frequency after which the capacitance drops. The frequency cut-off appears to be affected by the nature of the side chain and decreases in the order **p(gNDI-gT2)** > **p(C3-gNDI-gT2)** > **p(C6-gNDI-gT2)**. This could be indicative of slower ionic charging for the polymers functionalised with alkyl spacers.[140]

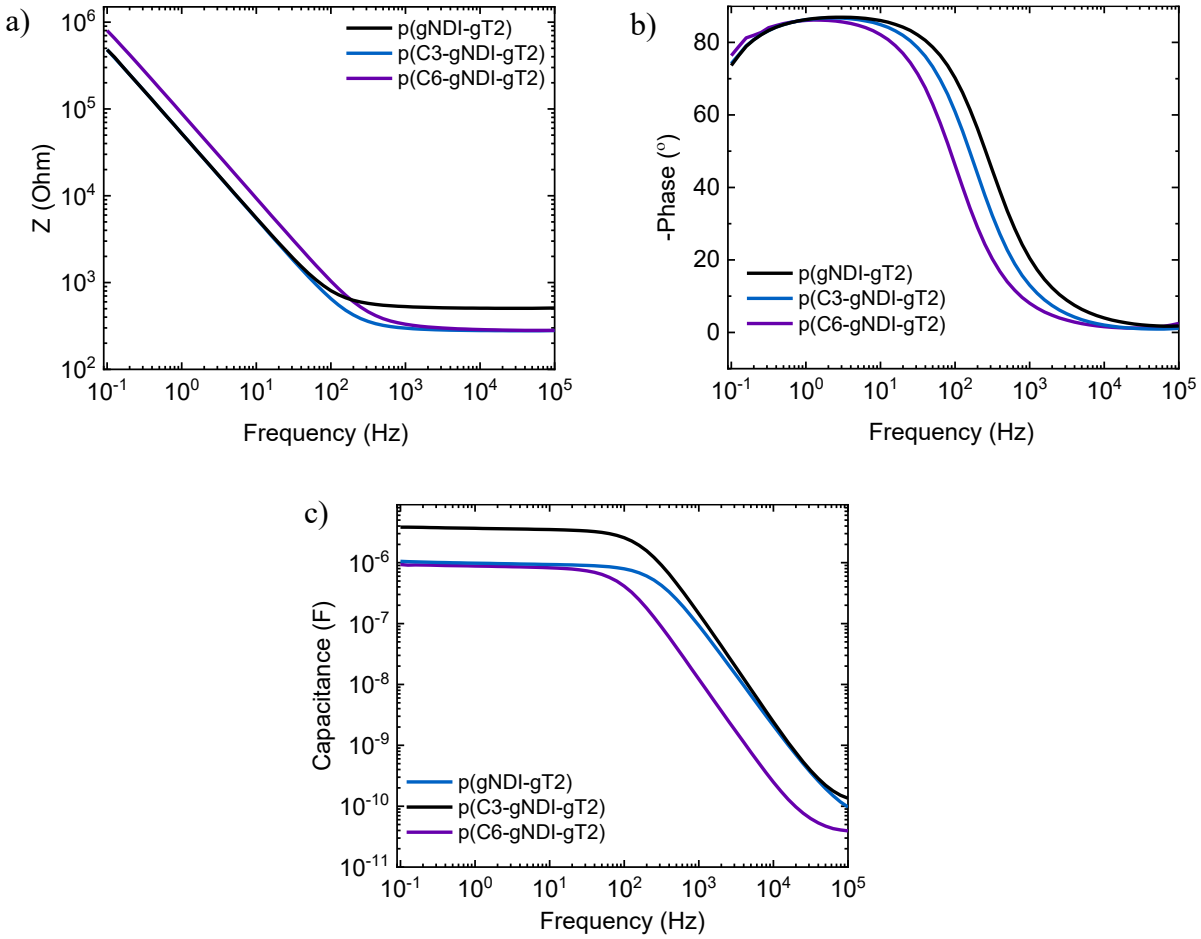


Figure 2.10. Electrochemical impedance spectroscopy of the polymers at the OECT gates in 0.1 M NaCl aqueous solution in ambient conditions (L = W = 500 µm, V = –0.6 V versus Ag/AgCl). (a) The impedance magnitude (b) phase and (c) the corresponding capacitance versus frequency plots.

The capacitance at 0.1 Hz for an offset voltage of –0.6 V versus Ag/AgCl was normalized by the volume of the film to calculate C^*. The polymer with the highest density of glycol units, **p(gNDI-gT2)**, shows the largest C^* of 221 F/cm^3. The C^* decreases for the polymers functionalised with alkyl spacers, with values of 72 F/cm^3 for **p(C3-gNDI-gT2)** and 59 F/cm^3 for **p(C6-gNDI-gT2)** (**Table 2.3**). According to the model proposed by Proctor et al., the volumetric capacitance is directly related to the density of cation/electron pairs within the bulk of the polymer.[114] The lower C^* of **p(C6-gNDI-gT2)** relative to **p(C3-gNDI-gT2)** could be

correlated with the presence of longer, electrically insulating side chains which lower the fraction of electroactive components (conjugated backbone). However, when comparing **p(C6-gNDI-gT2)** with **p(gNDI-gT2)**, the lengths of the side chains are similar and therefore cannot account for the large difference in C^*. Based on the EQCM-D findings, **p(C6-gNDI-gT2)** has a lower density of hydrophilic EG side chains and swelling ability. Therefore, in this case, the electronic states are presumably less accessible to the penetrated hydrated cations, giving a lower C^*.

The lower C^* of both polymers functionalised with alkyl spacers relative to **p(gNDI-gT2)** suggests that the higher μC^* product must be due to a higher electron mobility (μ). In order to verify these trends, the electron mobility was estimated from bandwidth measurements of the OECT channels using the impedance matching method.[94] As summarised in **Table 2.3**, **p(gNDI-gT2)** shows the lowest μ of 1.28×10^{-6} cm^2 V^{-1} s^{-1}. Introduction of alkyl spacers leads to an increase in μ to 4.02×10^{-5} cm^2 V^{-1} s^{-1} for **p(C3-gNDI-gT2)** and 1.52×10^{-4} cm^2 V^{-1} s^{-1} for **p(C6-gNDI-gT2)**. Notably, μ varies over a much larger range than C^* across the polymer series. At the expense of a small decrease in the volumetric capacitance, the introduction of alkyl spacers adjacent to the backbone leads to a larger increase in electron mobility, giving a larger μC^* product and normalised g_m overall.

It should be noted that the product between the independently measured values for μ and C^* and the μC^* product derived from the device transconductance deviate from an exact match. This has also been observed for p-type OECT materials such as **PTHS**.[93] Although the independently derived μC^* product appears to be underestimated, the trends are maintained across the polymer series.

Overall, the degree of swelling and mass uptake was inversely correlated with OECT performance, suggesting that the susceptibility of the polymer to structural disruption by ion

and water uptake played a limiting role. The structural benefits that seemed to impart improved electron mobility in OFETs did not necessarily result in improved electron mobility and performance in OECTs. While **p(C3-gNDI-gT2)** showed the highest OFET electron mobility, its OECT performance was lower than **p(C6-gNDI-gT2)** as assessed by μC^* product and normalised g_m. Similar findings have been recently reported by Flagg et al., where increasing the crystallinity of the polymer through annealing led to a higher OFET mobility, whilst the OECT mobility decreased.[139]

Polymer **p(C6-gNDI-gT2)** functionalised with an extended alkyl spacer showed the smallest changes in crystallite lattice spacings upon electrolyte exposure and after electrochemical doping (particularly in the lamellar direction), but also the lowest swelling ability and mass uptake from EQCM analysis. While the pristine film of **p(C3-gNDI-gT2)** showed structural features indicative of more efficient charge transport, these were presumably not preserved in the hydrated state due to more swelling and morphological changes. As a result, its OECT mobility was found to be more than one order of magnitude lower than its OFET mobility.

2.7.3 Stability measurements

An important requirement for bioelectronics applications based on OECTs is long-term stability during operation. Stability measurements were carried out for all polymers by monitoring the I_D upon the application of gate voltage steps alternating between 0 and 0.5 V (ΔV_G = 0.5 V) or 0 and 0.6 V (ΔV_G = 0.6 V) over 150 min.

The current response of **p(gNDI-gT2)** and **p(C3-gNDI-gT2)** was first recorded at ΔV_G = 0.5 V, which represents the gate voltage at which the peak g_m is measured. The ON current of **p(gNDI-gT2)** decreased by ~ 7% after the first 60 min of operation, after which it recovers

partially towards the end of the measurement. Polymer **p(C3-gNDI-gT2)** shows a steady increase in the ON current, with a total increase of ~ 19% over 150 min.

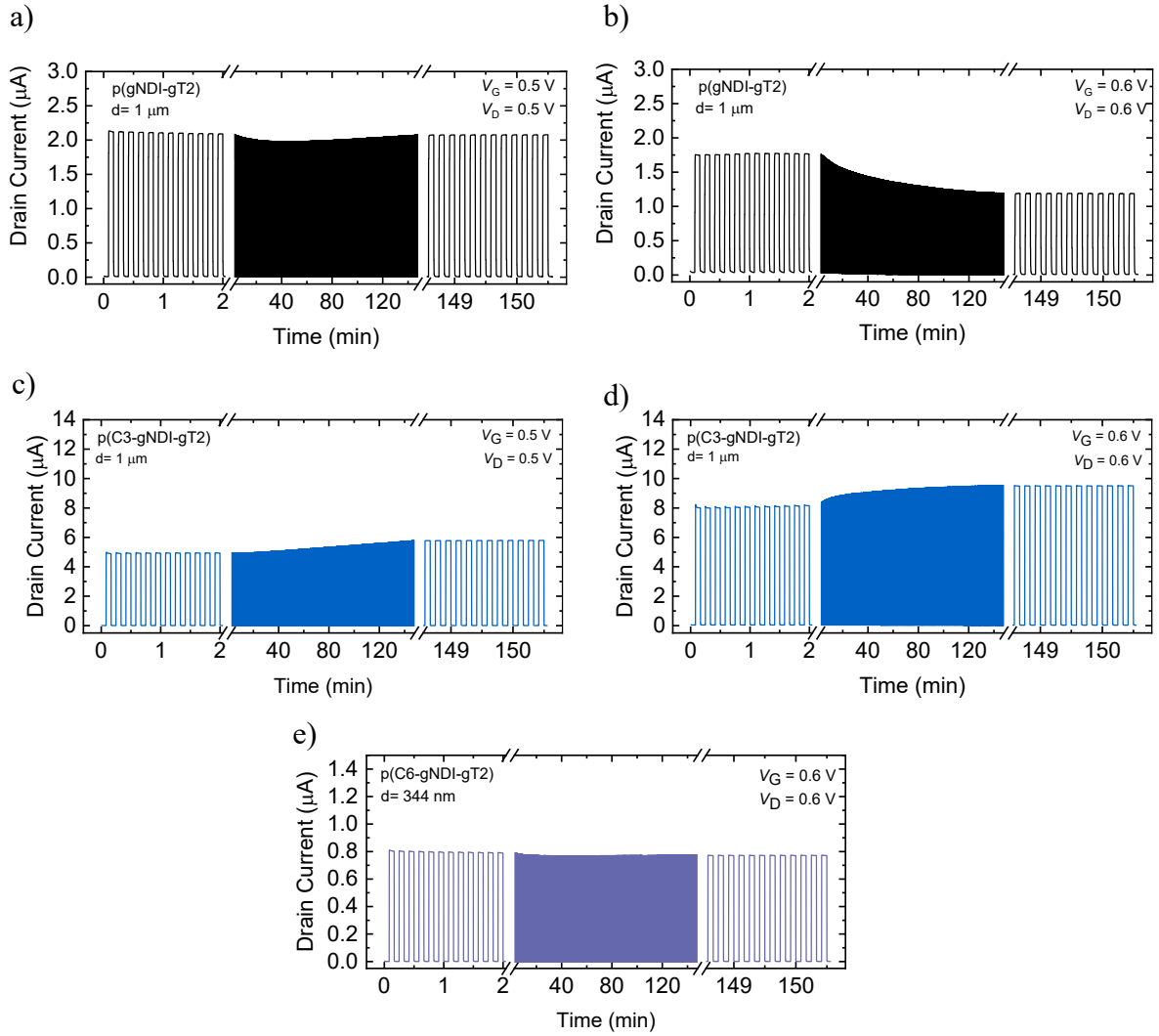


Figure 2.11. Stability pulsing experiment by alternating the gate potentials between $V_G = 0$ V and $V_G = 0.5$ V for (a) **p(gNDI-gT2)** ($d = 1$ µm), (b) **p(C3-gNDI-gT2)** ($d = 1$ µm) and between $V_G = 0$ V and $V_G = 0.6$ V for (b) **p(gNDI-gT2)** ($d = 1$ µm), (d) **p(C3-gNDI-gT2)** ($d = 1$ µm) and (e) **p(C6-gNDI-gT2)** ($d = 344$ nm) with a pulse duration of 5 s at $V_D = 0.6$ V for OECT channels in 0.1 M NaCl aqueous solution.

When the gate voltage is increased to $\Delta V_G = 0.6$ V, **p(gNDI-gT2)** shows much lower operational stability, retaining only 67% of the ON current after 2 h. The current response of **p(C3-gNDI-gT2)** at $\Delta V_G = 0.6$ V is similar to the recordings at $\Delta V_G = 0.5$ V, showing a total

increase of ~ 19%. The changes in ON current that **p(gNDI-gT2)** and **p(C3-gNDI-gT2)** show at both $\Delta V_G = 0.5$ V and $\Delta V_G = 0.6$ V could hinder their use for long-term sensing applications, where these fluctuations could interfere with changes in current in response to biological events or detection of analytes.

Remarkably, **p(C6-gNDI-gT2)** shows very stable operation, with no decrease in the original current for over 2 h of on-off switching at $\Delta V_G = 0.6$ V, corresponding to the bias at which peak g_m is observed. The improved long-term stability of **p(C6-gNDI-gT2)** is attributed to its lower extent of swelling and structural deformation during charging. These results demonstrate that optimisation of the length of the alkyl spacer within the polymer side chains is a useful strategy for improving the long-term operational stability of OECT materials.

2.8 Conclusions

A series of NDI-T2 copolymers functionalised with hybrid alkyl-glycol chains, where the conjugated backbone is segregated from the EG units by either a C_3- (**p(C3-gNDI-gT2)**) or C_6-alkyl spacer (**p(C6-gNDI-gT2)**), was synthesised. Their properties were studied with respect to the analogue **p(gNDI-gT2)** bearing EG-only side chains, which was the first reported n-type OECT material.[115] By studying the interactions of the copolymers with aqueous electrolytes and their performance in OECTs, it was possible to derive structure-property relationships for n-type materials used in aqueous-based electrochemical devices.

The chosen hybrid alkyl-glycol side chains allow electrochemically reversible reduction at low onsets (< –0.2 V versus Ag/AgCl), while limiting detrimental swelling of the polymers in the aqueous environment. The polymer functionalised with a C_6-alkyl spacer showed the lowest extent of water and ion uptake, swelling 70% less upon exposure and taking up half as much mass upon charging and discharging as **p(gNDI-gT2)**.

Introduction of alkyl spacers adjacent to the backbone led to a slight increase in the OFET mobility, in line with the design strategy this study was based on.[145] Both polymers functionalised with alkyl spacers showed a simultaneous decrease in C^* and increase in OECT mobility, which overall resulted in a higher μC^* and normalised g_m compared with **p(gNDI-gT2)**. The polymer bearing an extended alkyl spacer, **p(C6-gNDI-gT2)**, shows remarkable long-term stability in OECT devices, with no decrease in the original current for over 2 h of operation.

Using GIWAXS analysis, the OECT performance and stability were correlated with the extent of disruption of the crystallite lattice parameters due to ion/water uptake. The C_6-alkyl spacer which imparted the least sensitivity to electrolyte exposure and doping also led to improved OECT performance and stability. Further in operando GIWAXS measurements could provide more insight into the structural changes that each polymer undergoes during OECT operation.

Overall, these results highlight the importance of side chain engineering for preventing excessive swelling of the active material and achieving high stability and balanced mixed ionic-electronic transport properties during operation in aqueous electrolytes.

CHAPTER 3

Increasing the backbone coplanarity of naphthalene diimide-copolymers with mixed ionic and electronic conduction

3.1 General information and attributions

Polymers **P3gNDI** and **P3gNDTI** were synthesised in collaboration with Sophie Griggs (McCulloch Group, Imperial College London) as part of an undergraduate research project. OECT and EIS measurements were carried out during a research visit at Northwestern University under the supervision of Dr Bryan Paulsen (Rivnay Group, Northwestern University). DFT calculations were carried out by Dr Karl Thorley (Anthony Group, University of Kentucky). GPC measurements in chloroform were performed by Dr Rawad Hallani (McCulloch Group, KAUST) and PESA measurements were performed by Dr Craig Combe (KAUST). QCM and EQCM measurements were performed by Jokubas Surgailis (Inal Group, KAUST). GIWAXS measurements were performed and analysed by Dr Bryan Paulsen (Rivnay Group, Northwestern University).

3.2 Introduction

Previous studies have shown that functionalisation of n-type backbone motifs with hydrophilic ethylene glycol-based side chains is an effective strategy to allow stable n-type operation in aqueous electrolytes. Tuning of the ethylene glycol side chain density and its relative position (Chapter 2) for NDI-T2 copolymers proved to be a useful strategy to control swelling and increase the OECT mobility and the μC^* product. However, their μC^* and thickness-normalised g_m remain low compared to their p-type counterparts. When decoupling the μC^* terms, it becomes apparent that the low charge carrier mobility of n-type materials is still a limiting factor, with values of 3–4 orders of magnitude lower than those of p-type polymers (~ 0.00015 *vs.* ~ 1 $cm^2\,V^{-1}\,s^{-1}$ for **p(C6-gNDI-gT2)** and **p(gT2-TT)**,[86] respectively).

A strategy often adopted to increase the charge carrier mobility is to use rigid π-frameworks which favour intermolecular π-π stacking.[17] In this context, Takimiya and co-workers reported

the synthesis of naphthodithiophene diimide (NDTI, **Figure 3.1**), a core-extended NDI bearing fused thiophene rings with a highly planar molecular structure and small reorganisation energies.[161] Asymmetric derivatives with only one fused thiophene ring, known as naphtho[2,3-b]thiophene diimide (NTI, **Figure 3.1**), have also been developed as terminal building blocks for n-type small molecules.[162] Investigations of the electronic properties of NDI, NTI and NDTI units functionalised with *N,N*'-dioctyl side chains showed that extension of the core leads to an increase in electron affinity by *ca.* 0.1 V per each fused thiophene ring. Despite the electronic-rich nature of the thiophene rings, the stabilisation of the LUMO was attributed to extension of the π-conjugation. Conjugated NDTI-based polymers containing various comonomers such as vinylene, thiophene, bithiophene, thienothiophene, dithieno[3,2-b:2',3'-d]thiophene or naphtho[1,2-b:5,6-b']dithiophene have shown electron affinities between 4.0–4.2 eV and stable n-type operation in air, with electron mobilities up to 0.31 $cm^2 V^{-1} s^{-1}$ in OFET devices.[163–165] The attractive features conferred by the NDTI units in these cases motivated their choice as building blocks for n-type OECT materials.

Several studies have alluded to an inherent conflict between ionic and electronic transport in organic mixed conductors: while loosely packed chains are beneficial for ionic transport, electronic transport is supported by more ordered polymer backbones with π-stacked crystallites.[48,106,118] However, with an appropriate choice of side chains, p-type polymers with enhanced backbone coplanarity demonstrated high charge carrier mobilities, whilst maintaining efficient ion transport and storage.[86] For example, substitution of the thiophene unit with more rigid thienothiophene (TT) units from **p(g2T-T)** to **p(g2T-TT)** (Section 1.3.1) led to shorter π–π stacking distances and a three-fold increase in hole mobility, but also overall OECT performance of the material, as judged by the μC^* product.[86,93,118]

In search of n-type materials with higher charge carrier mobilities, this chapter investigates the effect of enhanced backbone coplanarity on the electrochemical activity and n-type OECT performance in aqueous electrolytes. Specifically, polymers containing core-extended NDTI units were synthesised for a comparative study versus the NDI-T2 backbones used for previously reported n-type OECT materials[90,115] and Chapter 2. A series of both linear and branched EG-based side chains were investigated to ensure both optimum performance and solubility of the resulting polymer.

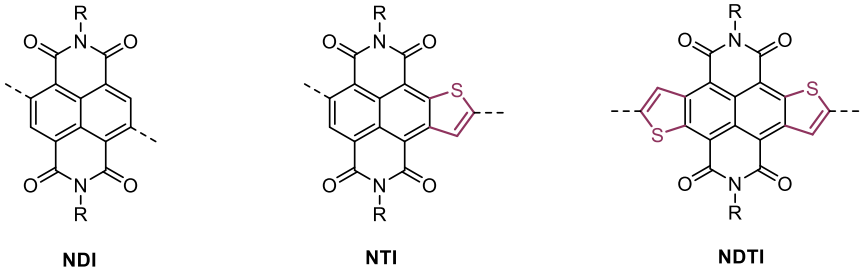


Figure 3.1. Structure of NDI and thiophene-annulated units, NTI and NDTI.

3.3 Density Functional Theory calculations

Density Functional Theory (DFT) calculations of methyl-functionalised NDI-T2 and NDTI-T2 tetramers were carried out at the ωB97XD/6-31G* level of theory to investigate the backbone conformation of the polymers and the frontier orbital wave function distribution (**Figure 3.2**). As previously reported,[166–168] the NDI backbone shows a significant twist and dihedral angles of 49-59° between the NDI and bithiophene moieties. In contrast, the NDTI backbone adopts a highly coplanar geometry with small dihedral angles of 3–5° for the NDTI-T2 linkage. Introduction of NDTI units also leads to a low dihedral angle of 12–14° for the bithiophene unit, while a twist of up to 31° is observed when coupled with NDI units. The increase in backbone coplanarity does not appear to influence the distribution of the LUMO wave function and both tetramers show strong localisation on the acceptor units. Conversely, the HOMO of

the NDI-T2 backbone is localised on the bithiophene moiety, whereas the NDTI-T2 analogue shows a slight delocalisation on the neighbouring NDTI units.

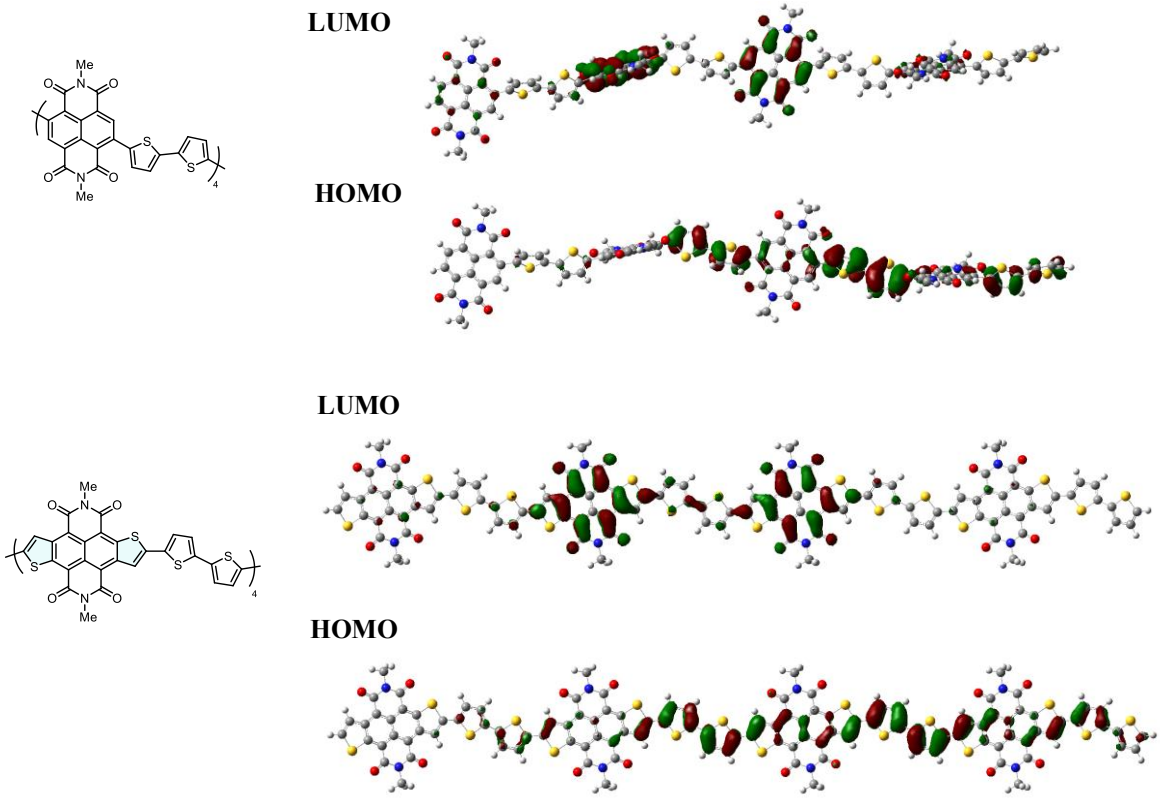


Figure 3.2. DFT calculations of methyl-substituted NDI-T2 and NDTI-T2 tetramers at the ωB97XD/6-31G* level of theory showing the energy-minimised structures and HOMO and LUMO wave function distributions.

To investigate further the backbone conformation, the torsional energy profiles were calculated using B3LYP-D3/6-31G* in gas phase along the dihedral coordinate connecting a thiophene ring with either NDI or NDTI units. The resulting profile and the atoms defining the torsion are shown in **Figure 3.3**. In agreement with previous reports,[169] the NDI-T unit shows a double well potential with stable conformations at ~ 50° and ~ 130° and high barriers for planarisation of 3.3 kcal/ mol. In sharp contrast, the NDTI-T unit shows a stable planar conformation at 180° and a barrier for rotation of 5.3 kcal/ mol. When compared to a rotatable bond between the two thiophene rings, the NDTI-T linkage shows a larger barrier for rotation, indicating that the

planar conformation is more stabilised. The DFT calculations therefore corroborate the enhanced backbone coplanarity upon lateral extension of the NDI core with thiophene units.

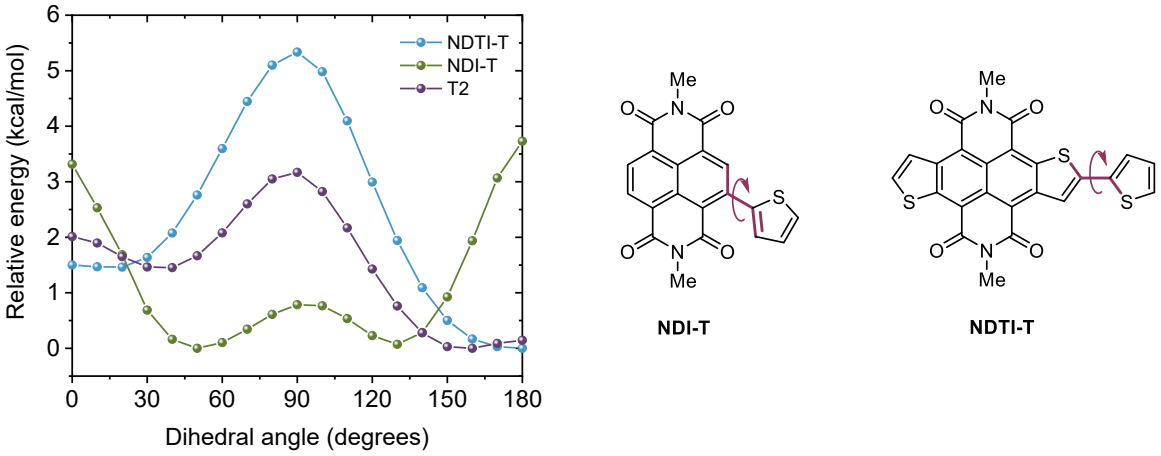
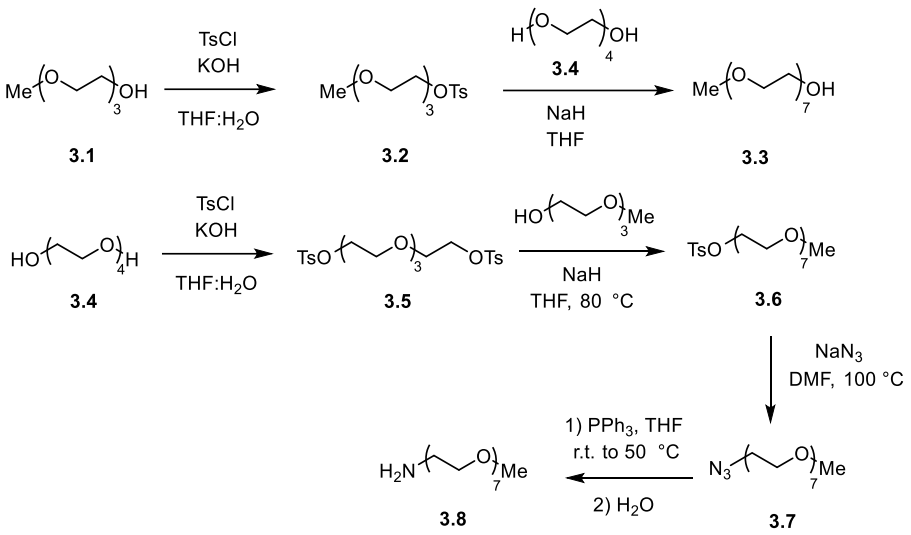


Figure 3.3. Torsional energy profile of the NDI-T and NDTI-T units calculated using B3LYP-D3/6-31G* in gas phase. The rotatable bonds are highlighted in red for the 0° conformer.

3.4 Synthesis

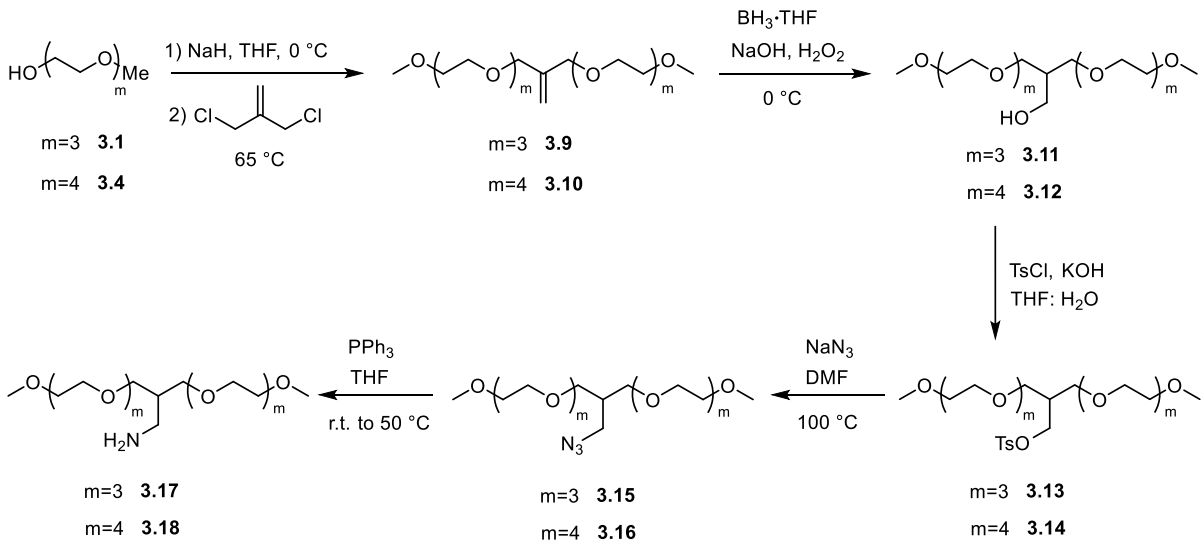
3.4.1 Synthesis of the side chains

Efforts towards the NDI and NDTI monomers began with the synthesis of a series of EG-based side chains containing either a hydroxyl or an amine pendant group. The linear heptakis(ethyleneglycol) **3.3** with a hydroxyl group was prepared using a two-step procedure[170] in an overall yield of 57%, involving tosylation of **3.1** and a S_N2 reaction with tetraethylene glycol to extend its chain length (**Scheme 3.1**). A similar series of substitution reactions was employed to synthesise the heptakis(ethylene glycol) monomethyl ether tosylate **3.6** from commercially available materials. Conversion of the tosyl end group to an azide, followed by Staudinger reduction in the presence of triphenylphosphine gave the heptakis(ethylene glycol) side chain **3.8** with a pendant amine group in an overall yield of 20% (4 steps).



Scheme 3.1. Synthesis of the linear heptakis(ethyleneglycol) side chains.

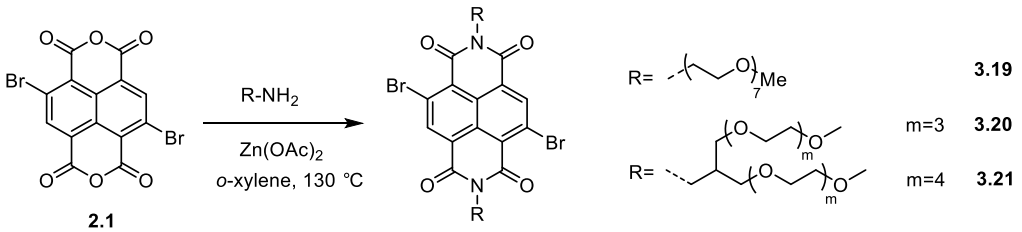
The branched side chains with a pendant hydroxyl group, containing either triethylene glycol (**3.11**) or tetraethylene glycol units (**3.12**) were synthesised according to literature[171] as shown in **Scheme 3.2**. Triethylene glycol monomethyl either **3.1** was deprotonated with sodium hydride and treated with methallyl dichloride to give the olefin **3.9**. The olefin was then subjected to a hydroboration-oxidation reaction to give **3.11** in an overall yield of 70% (2 steps). Following the same protocol, the analogue **3.12** containing tetraethylene glycol units was synthesised in an overall yield of 62% (2 steps). The branched side chains functionalised with hydroxyl groups were advanced to the amine derivatives using a sequence of tosylation, conversion to azide and Staudinger reduction as shown in **Scheme 3.2**. Accordingly, the side chains **3.17** and **3.18** were obtained in overall yields of 31% and 17%, respectively (5 steps). Although a shorter route involving Gabriel synthesis has been reported,[172] the chosen route avoided the use of highly toxic hydrazine hydrate. Moreover, the amine derivatives could be readily purified using a series of aqueous extractions, which removed the triphenylphosphine oxide obtained as a by-product after the Staudinger reaction.



Scheme 3.2. Synthesis of the branched ethylene glycol-based alcohols **3.11** and **3.12** and amines **3.17** and **3.18**.

3.4.2 Synthesis of the NDI monomers

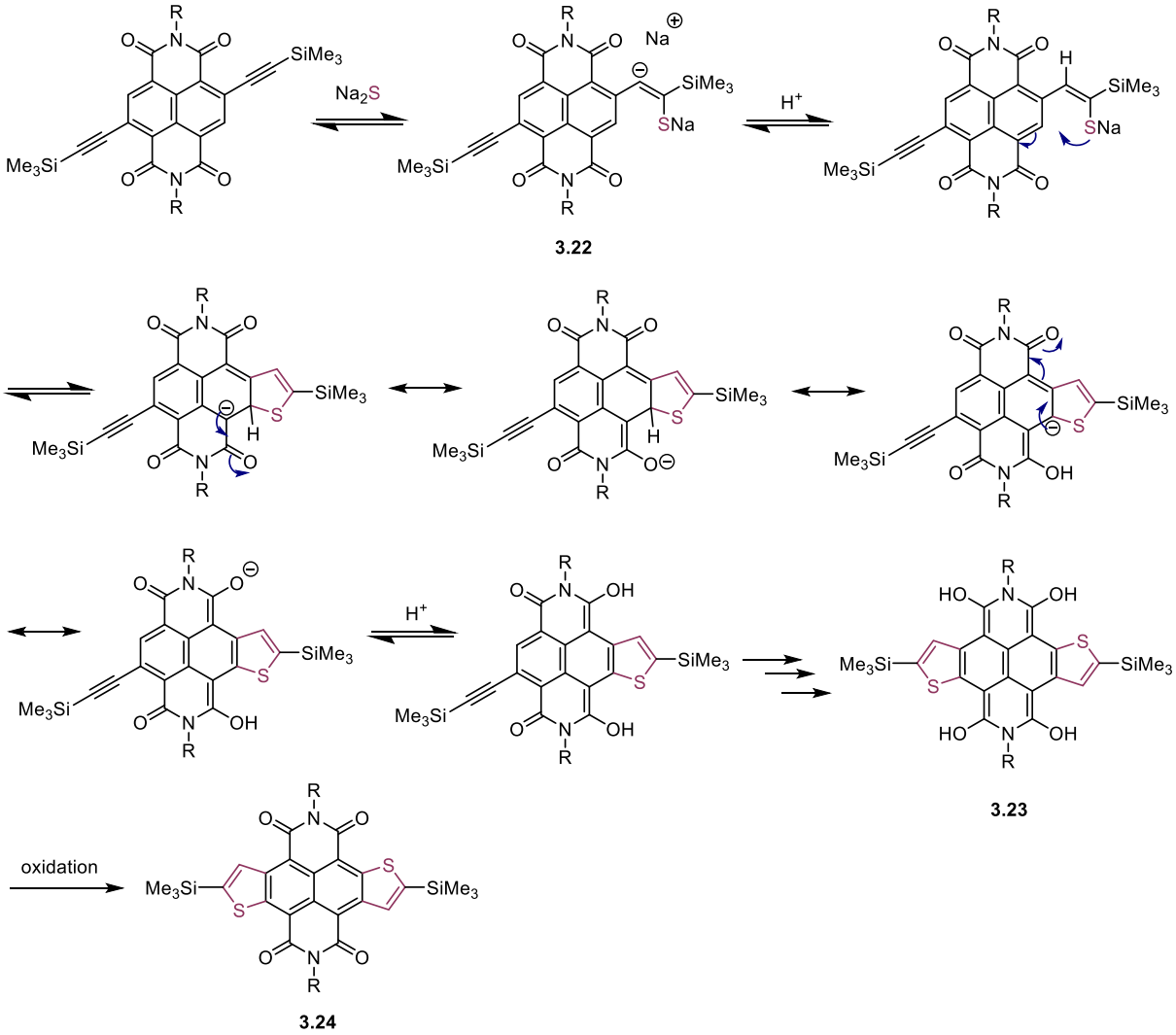
The NDI monomers functionalised with either a linear (**3.8**) or branched (**3.17** and **3.18**) EG-based side chain were obtained via an imidisation reaction from 2,6-dibromonaphtalene-anhydride (**2.1**) with the corresponding primary amine in yields of 27–37% (**Scheme 3.3**). Following an optimised protocol,[90] the reaction was carried out in *o*-xylene in the presence of anhydrous zinc acetate as a Lewis acid catalyst, which suppresses the formation of core-substituted side-products. Although the reaction appeared to have proceeded with the required selectivity, the highly polar solvent systems required for chromatography led to poor separation and therefore low isolated yields.



Scheme 3.3. Synthesis of the NDI monomers.

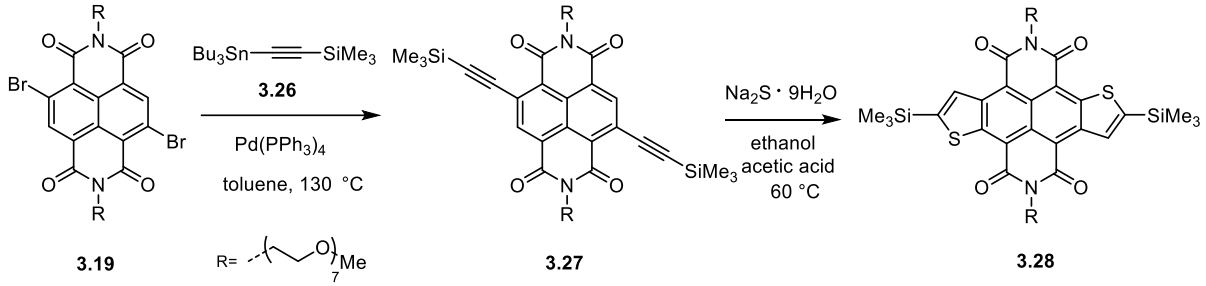
3.4.3 Synthesis of the NDTI monomers

Previous studies on substrates functionalised with *N*,*N*'-alkyl substituents suggest that the core of the NDI monomers can be readily extended to a NDTI unit *via* a Na_2S-promoted annulation of their ethynyl(trimethyl)silane derivative. While the mechanism is not completely elucidated, a plausible pathway involves addition of the sulfide anion to the ethyne moiety to give a vinylthiolate (**3.22**), followed by intramolecular Michael-like addition and oxidative aromatisation of **3.23**, as shown in **Scheme 3.4**.[161]



Scheme 3.4. Proposed mechanism of sodium sulfide-promoted annulation (adapted from literature).[161]

The annulation conditions were first trialled for monomer **3.19** as shown in **Scheme 3.5.** The 2,6-di((trimethylsylil)ethynyl)-derivative **3.27** was synthesised via Stille coupling of **3.19** and **3.26**, which proceeded in a yield of 85%. It should be noted that all attempts to convert the NDI monomer into **3.27** under Sonogashira coupling conditions,[173] led to a complex mixture containing only trace amounts of the desired product. This is presumably due to homocoupling of the organosilane product to form butadiynlyne-NDI species, which has been reported to proceed in the presence of Cu(I) salts.[174] The annulation reaction was attempted by stirring a suspension of the 2,6-bis((trimethylsylil) ethynyl)-derivative **3.27** and sodium sulfide nonahydrate in ethanol at 60 °C in the presence of acetic acid. In line with the proposed reaction mechanism,[161] the nucleophilic hydrogen substitution (S_NH) reaction with sodium sulfide was carried out under inert conditions, after which the reaction mixture was exposed to air for subsequent oxidative aromatisation. Under these conditions, product **3.28** was obtained as a mixture containing several other aromatic species, where the mono-thiophene-fused NTI derivative was identified as the major component by NMR analysis. Due to the high polarity of the species, separation of the mixture by column chromatography was not possible.



Scheme 3.5. Attempted route for the synthesis of the NDTI unit.

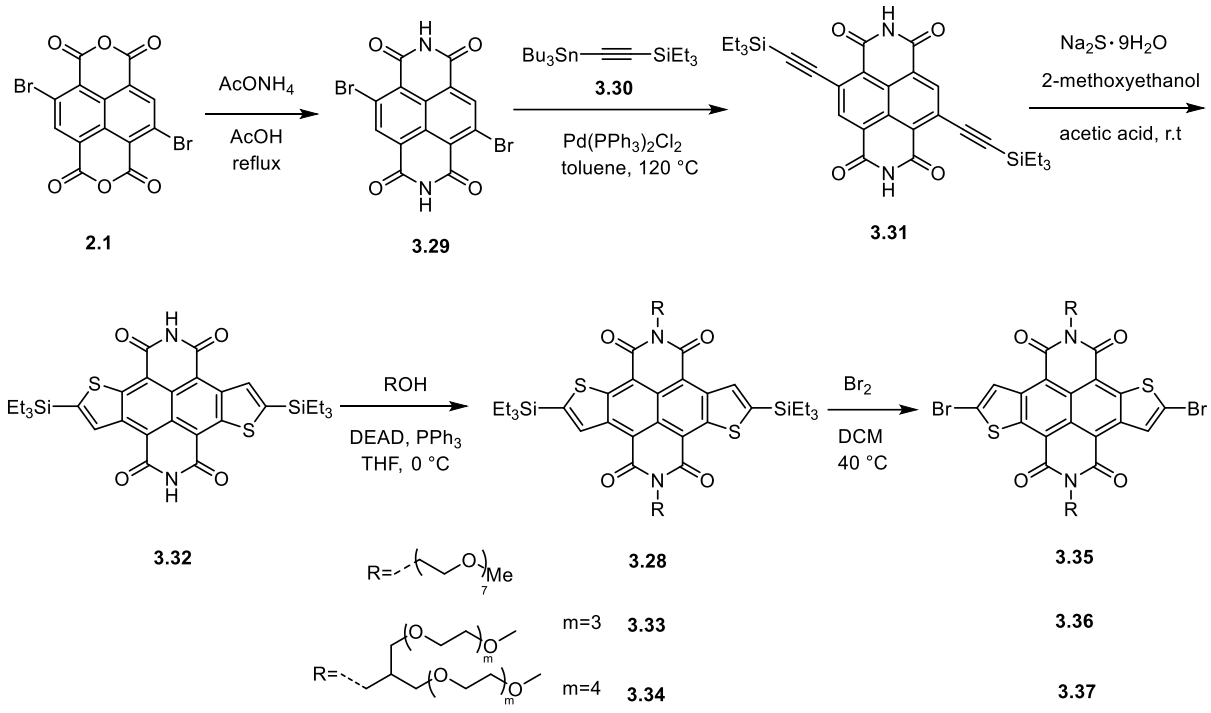
Due to the low conversion of the reaction and purification challenges, it was reasoned that a viable alternative would be to carry out the thiophene-annulation before functionalisation with

EG chains. Moreover, by carrying out the alkylation on the imide nitrogen in the late stages of the synthesis, NDTI derivatives with various substituents can be accessed much more readily.

Based on previous literature,[28] the synthetic route was redesigned such that the key intermediate was the *N*,*N*'-unsubstituted NDTI **3.32**, which could be subsequently functionalised with EG chains via a Mitsunobu reaction with the corresponding alcohol (**Scheme 3.6**). Naphthalene dianhydride **2.1** was converted into the diimide analogue **3.29** using ammonium acetate under acidic conditions in almost quantitative yields.[175] Subsequent Stille coupling with the stannylated ethynyl(triethyl) silane **3.30** gave the annulation precursor **3.31** in 93% yield. In this case, triethylsilyl groups were chosen instead of trimethylsilyl groups in order to improve the solubility of **3.31** in the solvent required for the annulation step.[28] Upon treatment with sodium sulfide nonahydrate, **3.31** was converted to the NDTI unit **3.32** at room temperature. Despite a modest yield of 22%, no extensive work-up or purification procedures were needed. Both ES and spectroscopic analysis were consistent with formation of the desired product, showing a proton signal at δ 9.10 ppm and δ 9.00 ppm attributable to the thiophene β-hydrogen and imide hydrogen, respectively.[28]

Having successfully synthesised the NDTI unit, the next step was a Mitsunobu reaction to introduce the EG substituents at the imide positions. Accordingly, the NDTI core **3.32** was treated in turn with alcohols **3.3**, **3.11**, **3.12** and a mixture of diethylazodicarboxylate and triphenylphosphine. The NDTI derivatives **3.28**, **3.33** and **3.34** were obtained in good yields ranging from 66% to 90%. It should be noted that a large excess of both diethylazodicarboxylate and triphenylphosphine (4 equivalents) was needed for full conversion to product. The final step in the synthesis of the NDTI monomers involved bromination of the triethylsilyl groups, which proceeded with yields between 40–51%. Notable NMR features of

the monomers included the presence of a singlet at ~ δ 9.05 attributable to the thiophene β-hydrogen and its corresponding carbon signal at ~ δ 127.0 ppm.

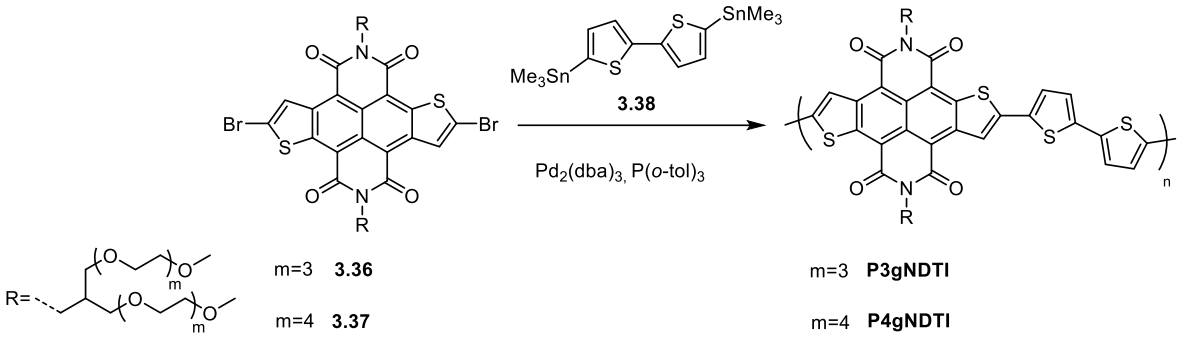


Scheme 3.6. Synthesis of the NDTI monomers.

3.4.4 Synthesis of the polymers

In order to synthesise the target NDTI-T2 copolymers, the Stille coupling between the dibromo-NDTI derivatives and bis(trimethylstannyl)-3,3'-dimethoxy-2,2'-bithiophene **3.38** was undertaken, as shown in **Scheme 3.7**. As a first attempt, the reaction was carried out in chlorobenzene at 135 °C using monomer **3.35** functionalised with linear EG-based side chains. However, the resulting polymer proved to be insoluble in common organic solvents, even at a high temperature. In an attempt to limit the molecular weight and increase the solubility of the polymer, the polymerisation was repeated at 80 °C in DMF and end-capped after 1 h of reaction. However, these conditions led to similar results, affording an insoluble dark-green solid. It was therefore reasoned that the linear EG side chains are not able to provide enough

solubility to the polymer, most likely due to enhanced rigidity of the NDTI-T2 backbone and stronger π-stacking interactions.



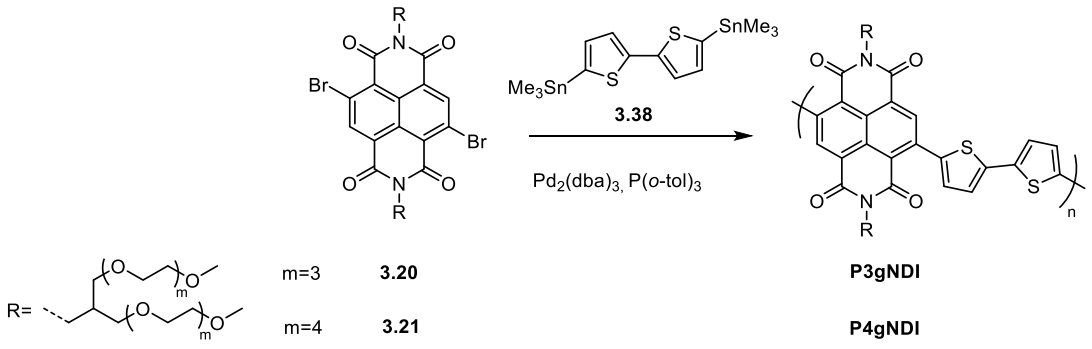
Scheme 3.7. Synthesis of the NDTI copolymers.

The polymerisation conditions were next trialled using the NDTI derivative functionalised with a branched triethylene glycol side chain (**3.36)** to afford **P3gNDTI** (**Scheme 3.7**). Stille coupling of **3.36** and **3.38** in chlorobenzene at 135 °C resulted in trace amounts of polymer that could be dissolved in hot chloroform, whereas most of the material was insoluble. Notably, when the reaction was carried out at 80 °C in DMF, a larger fraction of **P3gNDTI** (83%) could be extracted in hot chloroform. However, GPC analysis in chloroform at 40 °C indicated a low number average molecular weight (M_n) of 13.0 kDa ($Đ$ 1.57). In addition, a bimodal molecular weight distribution was observed, suggesting that the determined M_n is most likely overestimated. The molecular weight was also analysed by MALDI-ToF measurements, however the results were inconclusive and no identifiable peaks could be observed.

Similar conditions were employed for the polymerisation of the NDTI derivative functionalised with branched tetraethylene glycol side chains (**3.37**) with **3.38**. Coupling in DMF at 80 °C afforded polymer **P4gNDTI** in a yield of 80% and a M_n of 21.3 kDa ($Đ$ 1.48) for the chloroform fraction. The higher molecular weights obtained under the same conditions compared to **P3gNDTI** are due to the longer branched side chains of **P4gNDTI**, which provide greater

solubility in the polymerisation solvent and allow formation of more extended polymer chains. Notably, the M_n of the chloroform fraction was increased to 59.4 kDa ($Đ$ 4.54) when the polymerisation was carried out at 135 °C in chlorobenzene, while maintaining a good yield of 58%.

Having successfully synthesised **P3gNDTI** and **P4gNDTI**, their NDI analogues were synthesised for comparison by Stille coupling of the NDI monomers with **3.28** in chlorobenzene at 135 °C (**Scheme 3.8**). Polymers **P3gNDI** and **P4gNDI** were obtained in yields of 88% and 48%, respectively. Both polymers showed good solubility in chloroform at room temperature. GPC analysis indicated relatively high molecular weights and narrow dispersity, with M_n of 40.7 kDa ($Đ$ 1.79) and 22.0 kDa ($Đ$ 1.63) for **P3gNDI** and **P4gNDI**, respectively.



Scheme 3.8. Synthesis of the NDI polymers.

3.5 Physical and optoelectronic properties

The thermal and optoelectronic properties of the polymers, along with the determined molecular weights are summarised in **Table 3.1**. Thermogravimetric analysis (TGA) was carried out to investigate the thermal stability of the polymers series (**Figure B1**, Appendix B). Polymers **P4gNDTI**, **P3gNDI**, **P4gNDI** displayed good thermal stability with 5% weight-loss temperature in the range 381–391 °C under nitrogen flow. In contrast, **P3gNDTI** showed less robust thermal properties, with a low decomposition temperature of 202 °C.

Table 3.1. Optical and electronic properties of the polymers

Polymer	M_n [$Đ$] (kDa)[a]	T_d (°C)[b]	E_g^{opt} (V)[c]	soln λ_{max} abs (nm)[d]	EA (eV)[e]	IP (eV)[f]
P3gNDTI	13.0 [1.57]*	202	1.34	741	4.21	5.12
P4gNDTI	59.4 [4.54]*	381	1.30	793	4.17	5.14
P3gNDI	40.7 [1.79]	385	1.45	610	4.02	5.39
P4gNDI	22.0 [1.63]	391	1.39	612	4.04	5.40

[a] Number-average molecular weight and dispersity (GPC vs polystyrene standards in chloroform). [b] Temperature for 5% weight-loss from thermogravimetric analysis. [c] Optical band gap estimated from thin film absorption onset. [d] Solution absorption spectra (chloroform). [e] Cyclic voltammetry of polymer thin films on glassy carbon electrodes in acetonitrile with 0.1 M tetrabutylammonium hexafluorophosphate as the supporting electrolyte. [f] Measured by photoelectron spectroscopy in air. *Bimodal distribution observed.

The UV-Vis absorption spectra of the polymer series in dilute chloroform solution and as a thin film are shown in **Figure 3.4** and the corresponding optical parameters are summarised in **Table 3.1**. As expected,[151] the NDI-T2 copolymers show two absorption features, with a high energy band, ascribed to the π–π* transition and a lower energy band, due to intramolecular charge transfer. While the absorption spectra in solution are virtually identical for both NDI-T2 copolymers, **P4gNDI** exhibits a larger bathochromic shift (106 nm) of the absorption maximum from solution to thin-film compared to **P3gNDI** (77 nm). This results in a smaller optical band gap for **P4gNDI** (1.39 eV) relative to **P3gNDI** (1.45 eV), as determined from the absorption onset of the thin film absorption spectra.

The NDTI-based polymers show an additional weak band between 500–590 nm and markedly red-shifted absorption features compared to their NDI analogues, extending into the near-IR region. Replacing the NDI acceptors with NDTI units led to a reduction of the optical band gap to ~ 1.30 eV, consistent with increased effective π-conjugation. Due to the significant differences in molecular weight between **P3gNDTI** and **P4gNDTI**, the effect of extending the length of the side chain on their optical properties could not be determined with certainty.

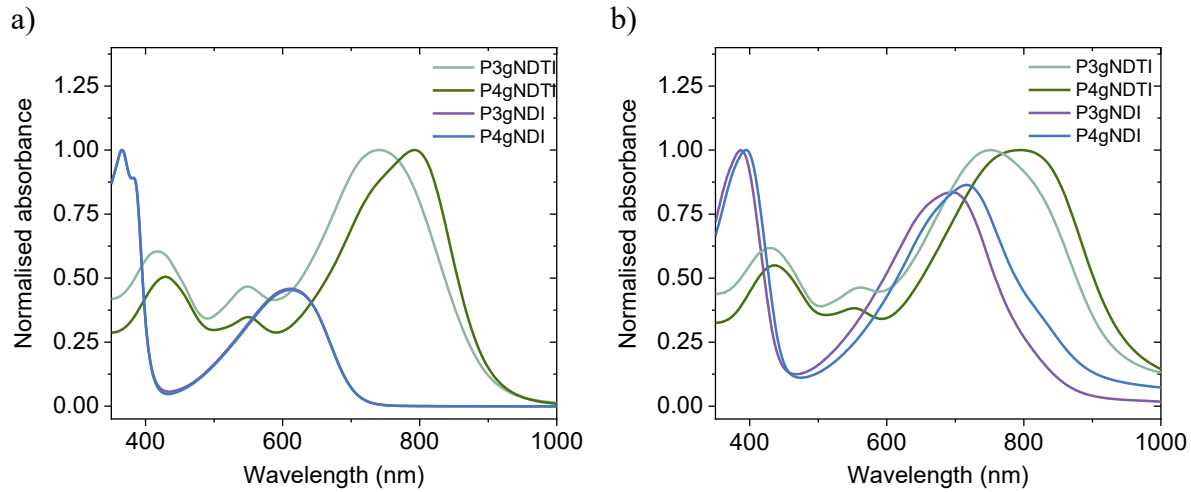


Figure 3.4. UV-Vis Spectra of the polymers (a) in chloroform solution and (b) as thin films on glass substrates.

The increased effective conjugation of NDTI-based copolymers is also reflected in their electronic properties. Both **P3gNDTI** and **P4gNDTI** show a lower ionisation potential than their NDI analogues, as determined by photoelectron spectroscopy in air (PESA) measurements (**Table 3.1**). The electron affinities of the polymer series were estimated using cyclic voltammetry of the thin films in 0.1 M tetrabutylammonium hexafluorophosphate ($TBAPF_6$) in acetonitrile (**Table 3.1**, **Figure B2** in Appendix B). In line with previous reports,[161,176] introduction of NDTI units led to a stabilisation of the LUMO levels by 0.1–0.2 eV in comparison to those of the NDI analogues. With high electron affinities of approximately 4.20 eV, **P3gNDTI** and **P4gNDTI** are therefore promising candidates for stable n-type operation in ambient conditions.[87]

3.6 GIWAXS analysis of the polymer films

Grazing incidence wide-angle X-ray scattering (GIWAXS) measurements were carried out to study the structural organisation of the **P3gNDI**, **P4gNDI** and **P4gNDTI** thin films. The effect of backbone coplanarity on the microstructure of the polymer was investigated through comparison of **P4gNDTI** and **P4gNDI**. The structural features of **P4gNDI** were also compared

to those of **P3gNDI** in order to identify any structural changes induced by extension of the side chain length. The two-dimensional GIWXAS patterns and line cuts taken along the out-of-plane and in-plane scattering directions are shown in **Figure 3.5** and the relevant peak parameters are summarised in **Table 3.2**.

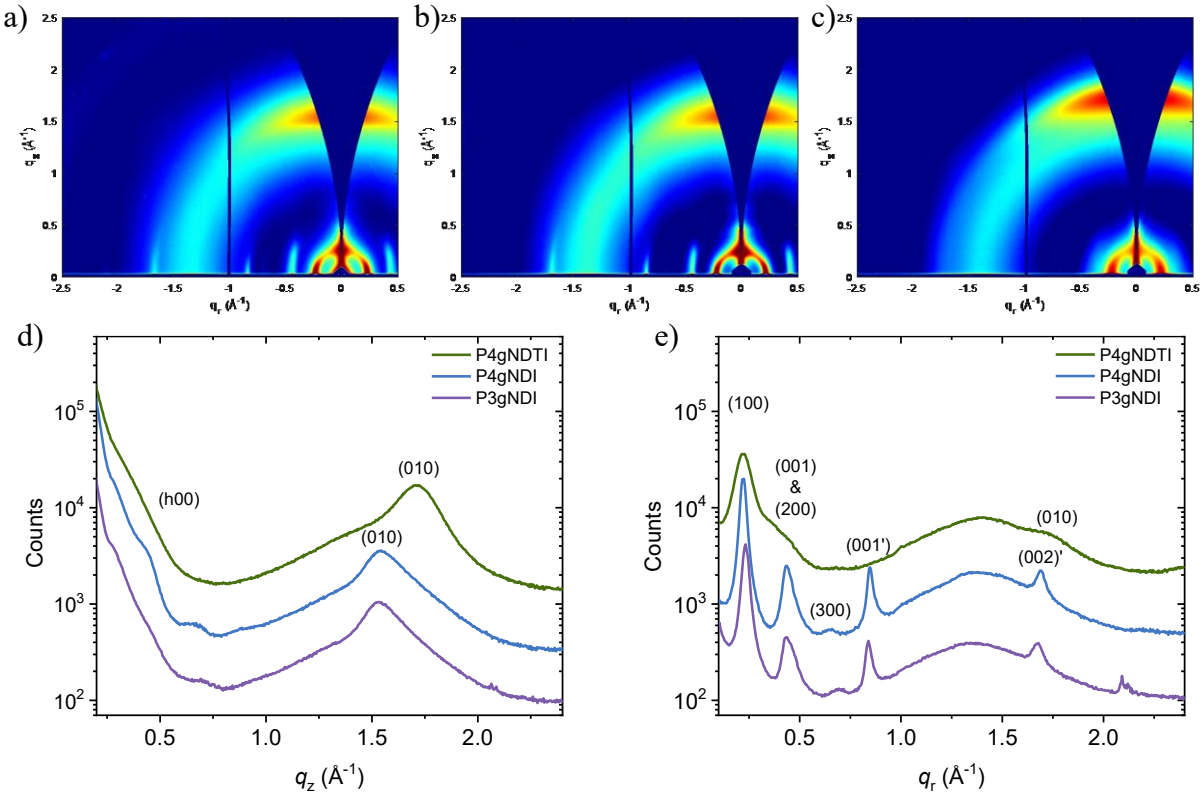


Figure 3.5. GIWAXS of neat as-cast films: q_r-q_z maps of scattered X-ray intensity from thin films of (a) **P3gNDI** (b) **P4gNDI** and (c) **P4gNDTI** polymers and (d) out-of-plane (q_z) and (e) in-plane (q_r) line cuts of each polymer.

All polymers adopt a predominantly face-on orientation, with enhanced out-of-plane π-stack scattering and in-plane backbone scattering. The in-plane π-stack scattering peaks are weak for **P4gNDTI** (q ~ 1.73 Å^{-1}) and indistinguishable for both NDI-based polymers. Introduction of NDTI units led to a significant contraction of the out-of-plane π-stack *d*-spacing (~ 0.40 Å) of **P4gNDTI** relative to both **P4gNDI** and **P3gNDI**. In line with the DFT calculations and optoelectronic properties, this is indicative of enhanced coplanarity and stronger intermolecular interactions for **P4gNDTI**.

Both **P3gNDI** and **P4gNDI** show evidence of three orders of in-plane lamellar scattering, while **P4gNDTI** shows a clear first order lamellar peak, followed by a broad shoulder. The nature of the polymer backbone does not appear to affect side chain ordering, with both **P4gNDI** and **P4gNDTI** displaying a lamellar *d*-spacing of 28.4 Å. Decreasing the length of the side chain branches by one ethylene glycol unit from **P4gNDI** to **P3gNDI** led to a contracted lamellar *d*-spacing of 27.0 Å, as judged by the (100) peak. Interestingly, the lamellar spacing of these NDI-T2 copolymers was more sensitive to the length of the EG side chain branches than previously reported NDI-T backbones. NDI-T copolymers with similar branched EG side chains showed only a ~ 0.5 Å increase in lamellar *d*-spacing when the side chain branches were extended by one EG unit,[159] compared to the ~ 1.4 Å increase observed herein.

Table 3.2. GIWAXS peak parameters

d-spacings (Å)	In-plane					Out-of-plane
	(100)	(001)	(001)'	(002)'	(010)	(010)
P3gNDI	27.0	14.6	7.48	7.50	–	4.07
P4gNDI	28.4	14.5	7.41	7.43	–	4.09
P4gNDTI	28.4	–	–	–	3.62	3.67

As previously demonstrated for NDI-T2 polymers,[156] **P3gNDI** and **P4gNDI** display in-plane backbone scattering peaks associated with two distinct polymorphs: Form I (noted as (001)) and Form II (noted as (001)' and (002)'). In contrast, **P4gNDTI** displayed no clear in-plane (001) peak, and (001)' and (002)' peaks were completely absent. From the **P4gNDTI** line cut (**Figure 3.5e**), the broad shoulder (0.3–0.5 $Å^{-1}$) may be due to overlapping (001) and (200) scattering, though this cannot be determined with certainty. This indicates significant loss of order along the backbone direction compared to **P3gNDI** and **P4gNDI**. Upon increasing the length of the branched side chain from **P3gNDI** to **P4gNDI**, the backbone *d*-spacing for both Form I and Form II polymorphs remained nearly identical.

Overall, the GIWAXS results indicate that substituting the NDI units with core-extended NDTI units promotes tighter π- π stacking of the polymer chains, however at the expense of structural order in the lamellar and backbone directions. Modifying the side chain branch length from **P3gNDI** to **P4gNDI** did not disrupt polymer ordering, with out-of-plane π−stack and in-plane backbone ordering remaining strong. Previous investigations have shown that the NDI-T2 copolymers show anisotropic charge transport that favours the backbone direction over the lamellar direction.[157]As the backbone ordering is maintained, functionalisation with longer tetraethylene glycol side chains is not expected to have a dramatic effect on the charge transport properties in dry state.

3.7 Electrochemical activity in aqueous electrolytes

3.7.1 Cyclic voltammetry of the polymer films

The electrochemical doping processes were screened in conditions more relevant to OECT operation by carrying out cyclic voltammetry of the polymer films in 0.1 M NaCl aqueous solutions. **Figure 3.6a** shows the reduction behaviour of the polymer series for three consecutive doping cycles, where the first cycle was disregarded to eliminate any differences due to reorganisation of the polymer chains and break-in effects.[177,178]

P3gNDI showed stable, reversible reduction with a low onset of ~ –0.15 V versus the Ag/AgCl reference electrode. In contrast, its NDTI analogue **P3gNDTI** quickly delaminated and showed a weak and featureless current response by the third doping cycle. Attempts to vary the film thickness through different spin- or drop-casting conditions onto both ITO substrates and glassy carbon electrodes failed to improve the stability of the **P3gNDTI** in aqueous electrolytes. The poor redox stability is most likely a result of its low molecular weight and indicates that **P3gNDTI** is not compatible with OECT operation in water-based electrolytes.

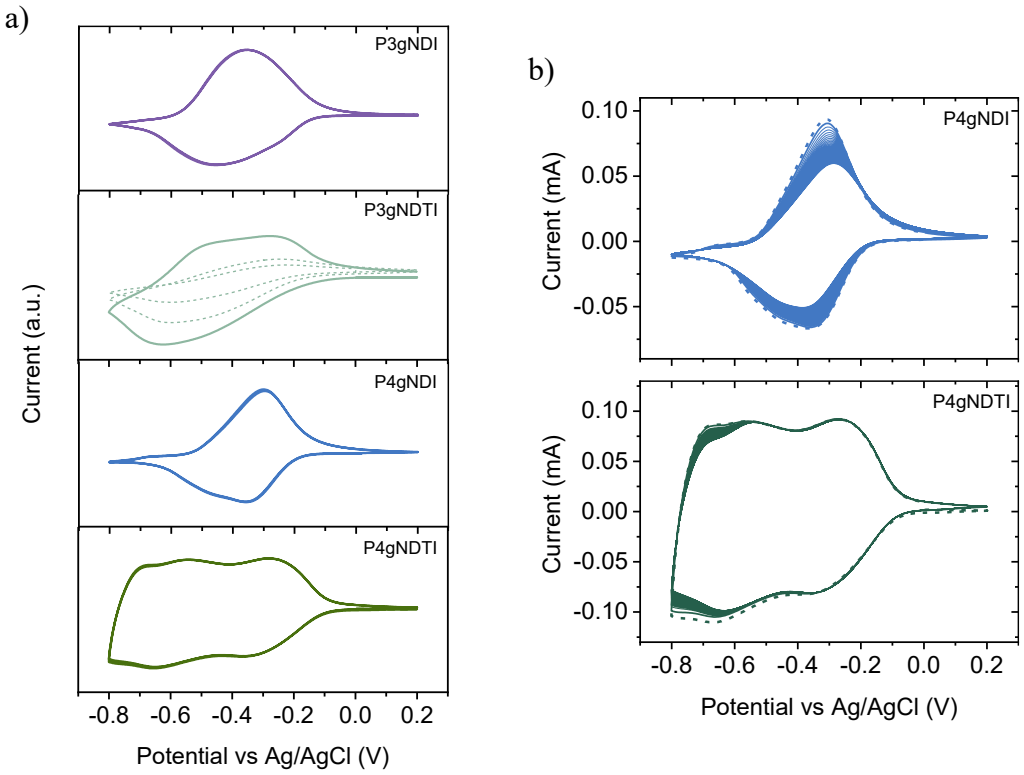


Figure 3.6. (a) Cyclic voltammetry of **P3gNDI**, **P3gNDTI**, **P4gNDI** and **P4gNDTI** on glassy carbon electrodes in degassed 0.1 M NaCl aqueous solution with a scan rate of 100 mV s^{-1} and a Ag/AgCl reference electrode (2nd, 3rd and 4th cycles). The 3rd and 4th cycles for **P3gNDTI** are shown are dashed lines (b) Cycling stability (50 scans) of **P4gNDI** (top) and **P4gNDTI** (bottom) films on glassy carbon electrodes in degassed 0.1 M NaCl aqueous solution with a scan rate of 100 mV s^{-1} and a Ag/AgCl reference electrode. The dashed lines show the first cycle.

Conversely, both **P4gNDI** and **P4gNDTI** showed reversible reduction features with constant current over the three doping cycles. Polymer **P4gNDI** shows a well-resolved reduction peak with an onset of –0.16 V. A lower reduction onset of –0.08 V is observed for **P4gNDTI**, which is attributed to its higher electron affinity. Notably, **P4gNDTI** displays broader reduction waves compared to its NDI analogue, suggesting that **P4gNDTI** allows more superposition of redox states and delocalization of the polaronic species over the extended π-system.[178,179]

Due to their ability to be reversibly (de)doped at low potentials, **P4gNDI** and **P4gNDTI** constitute a promising NDI/NDTI pair for studying the influence of backbone coplanarity on the OECT characteristics in aqueous electrolytes. Focusing on this system, the redox stability was further investigated during 50 charging and discharging cycles between 0 and 0.8 V versus Ag/AgCl (**Figure 3.6b**). While **P4gNDI** retains only 74% of the initial current, **P4gNDTI** exhibits stable current for the first reduction wave and retention of 94% of the initial current of the second wave, demonstrating improved stability during extended cycling.

3.7.2 Spectroelectrochemical measurements of the polymer films

To further investigate the electrochemical reduction behaviour of **P4gNDI** and **P4gNDTI**, their optical changes upon doping were monitored with spectroelectrochemical measurements in aqueous electrolytes. All experiments were conducted on thin films deposited on ITO electrodes by spin-coating, at potentials ranging from 0 to –0.8 V versus the Ag/AgCl reference electrode (**Figure 3.7**).

At biases between 0 to –0.6 V versus Ag/AgCl, **P4gNDI** shows a gradual decrease in the absorption of the π-π* and ICT bands with concomitant formation of a new feature at 500 nm and a shoulder at 791 nm, which is consistent with formation of a radical anion (polaron) species (**Figure 3.7a**).[179] In the case of **P4gNDTI**, the absorption of the bands with absorption maxima at 438, 552 and 794 nm gradually decreases, while a new feature emerges at 609 nm and the absorption in the sub-band gap region increases (**Figure 3.7b**). By monitoring the relative changes in the intensity of the ICT band as a function of applied bias, it can be observed that **P4gNDTI** undergoes larger spectral modulation relative to **P4gNDI** at the same doping potential (**Figure 3.7e**). The higher degree of electrochemical doping, as well as improved redox stability of **P4gNDTI**, are attributed to its higher EA, imparted by the extended π-conjugation.

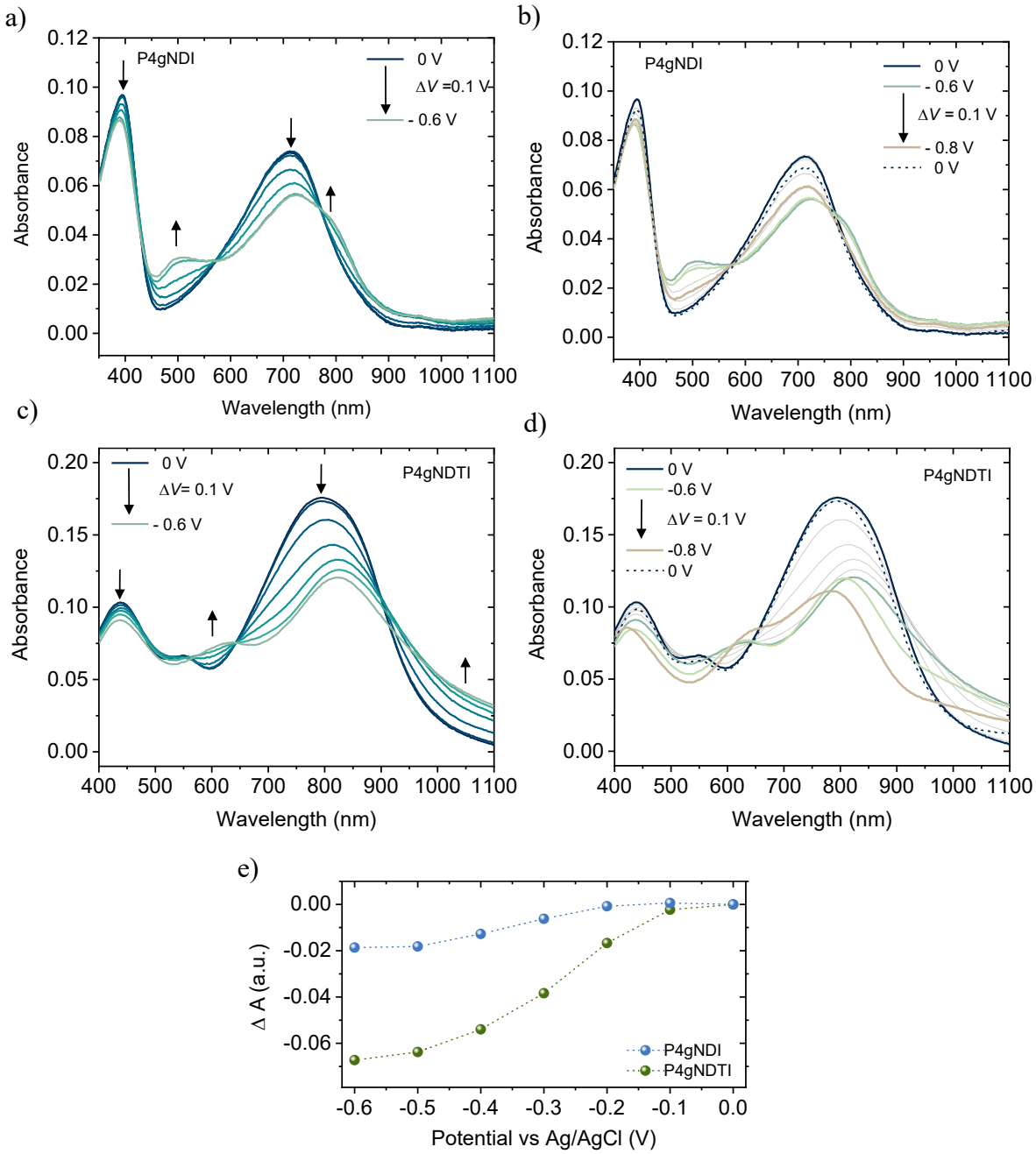


Figure 3.7. Evolution of the UV-Vis absorption spectrum during charging between 0 and –0.6 V for (a) **P4gNDI** and (c) **P4gNDTI** and between –0.6 and –0.8 V versus Ag/AgCl for (b) **P4gNDI** and (d) **P4gNDTI** in 0.1 M NaCl aqueous solution in steps of 100 mV. The dashed lines show the spectrum when the potential is reversed to 0 V after charging at –0.8 V versus Ag/AgCl. (e) Relative difference between the absorbance recorded with bias (0 V to –0.6 V versus Ag/AgCl) and the initial spectrum without bias of the ICT peak (696 nm for **P4gNDI** and 760 nm for **P4gNDTI**).

Figure 3.7b and **Figure3.7d** illustrate the spectral changes of the polymer thin films when the applied potential is decreased further to –0.8 V versus Ag/AgCl. Previous electrochemical investigations of NDI-T2 copolymers functionalised with alkyl side chains showed that the radical anion evolves into a dianion species (bipolaron) at more negative potentials.[179] Formation of the dianion species is typically evidenced by a decrease in the absorption of the radical anion bands and evolution of new features at 395 and 718 nm, red-shifted relative to the neutral polymer. However, in the case of **P4gNDI**, the characteristic features of the dianion species could not be identified in the applied potential range. This is in agreement with previous investigations of NDI-T2 copolymers functionalised with polar EG side chains in aqueous electrolytes,[115] as well as the copolymers studied in Chapter 2.

In contrast, **P4gNDTI** shows evidence of transformation into a distinct species with new absorption features at 422, 630 and 783 nm, when the applied potential is decreased to –0.8 V. When the potential is reversed to 0 V, the spectrum of the neutral polymer is restored in shape and intensity, demonstrating reversibility of the observed doping processes These results suggest that introduction of NDTI units may allow reversible formation of a dianion species at potentials within the electrochemical window of water. Calculations of the dianion spectral features using time-dependent density functional theory (TF-DFT)[54] are ongoing to support this assignment.

3.7.3 EQCM-D analysis

To study the effect of polymer backbone on the uptake of water and ions during electrochemical doping, electrochemical quartz crystal microbalance with dissipation monitoring (EQCM-D) measurements were performed for **P4gNDI** and **P4gNDTI**. The QCM-D sensors were first analysed prior to biasing in order to determine the extent of passive swelling when exposed to a 0.1 M NaCl aqueous solution (raw data shown in **Figure B3**, Appendix B). However, no

passive swelling could be extracted for the **P4gNDI** film (d = 78.8 nm) as the signals exceeded the measurement window, suggesting a surprisingly large mass uptake upon exposure to the electrolyte. On the other hand, the thin film of **P4gNDTI** with a comparable thickness (d = 91.8 nm) showed a detectable signal and was found to swell by 57% of its initial mass. Notably, the passive swelling of **P4gNDTI** is lower than that of NDI-T2 derivatives bearing linear side chains with a comparable number of EG units (*cf.* > 100% swelling for **P-100**).[90] These results indicate more controlled swelling upon substituting the NDI with NDTI units and enhancing the rigidity of the backbone.

At doping potentials, **P4gNDTI** shows further mass uptake with an additional 24% at –0.4 V and 218% at –0.7 V versus Ag/AgCl (**Figure 3.8a**) as more hydrated ions are injected into the film to stabilise the reduced species. Although the mass uptake of **P4gNDI** could not be quantified, it is reasonable to assume that its swelling would also increase further upon doping.

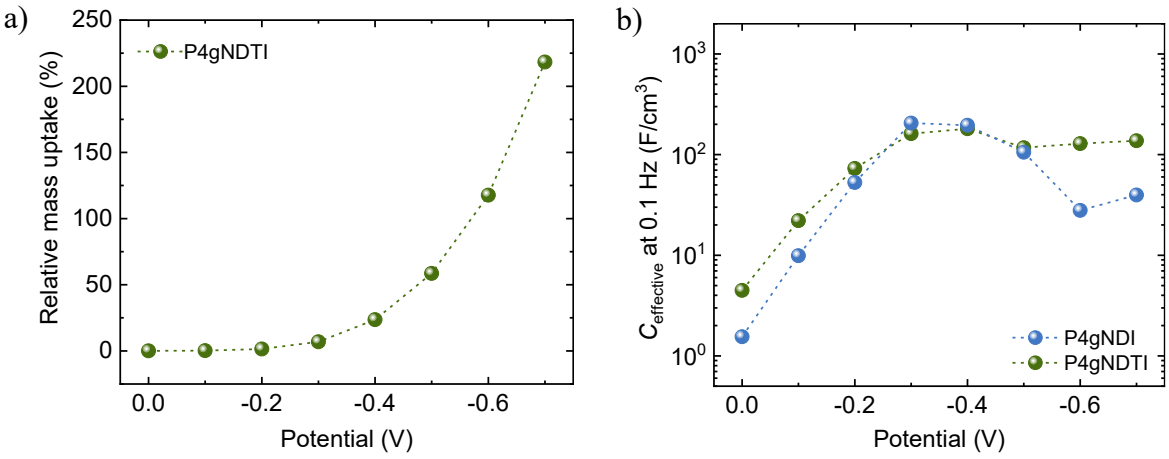


Figure 3.8. (a) Swelling percentage from QCM-D measurements with applied potentials between 0 and –0.7 V versus Ag/AgCl in 0.1 M NaCl aqueous solution for **P4gNDTI** (b) volumetric capacitance determined from electrochemical impedance spectra of the polymer-coated EQCM-D sensors for **P4gNDTI** and **P4gNDI** at a frequency of 0.1 Hz as a function of potential.

Following the swelling analysis, electrochemical impedance spectroscopy (EIS) was carried out on the polymer-coated EQCM-D sensors to extract the potential-dependant capacitance at low frequencies (0.1 Hz) (**Figure 3.8b**). Both **P4gNDI** and **P4gNDTI** show an increase in capacitance with increasing potential at a similar rate up to –0.3 V versus Ag/AgCl. The capacitance then passes through a peak value and decreases at more negative potentials. A similar voltage dependence of the capacitance has been observed for other OECT materials at low frequencies.[96,177]A possible explanation for this behaviour could be the large extent of hydration at doping potentials > –0.4 V (**Figure 3.8a**), which presumably increases the distance between electron/cation pairs and leads to a decrease in volumetric capacitance.[114] Consistent with more extreme levels of swelling, **P4gNDI** suffers a greater reduction in C^* than **P4gNDTI** at high doping potentials.

3.8 OECT performance

3.8.1 OECT performance of P3gNDI

A previous report by Wang et al. showed that functionalisation of p-type copolymers with branched EG side chains instead of linear ones leads to a decrease in the normalised transconductance and long-term stability of the OECT.[116] Therefore, a key question that had to be answered was whether the branched EG side chains required to solubilise the NDTI-T2 copolymers would have a detrimental effect on the n-type OECT characteristics. As the performance of NDI-T2 polymers with linear heptakis(ethylene glycol) side chains such as **P-100** had been investigated previously (**Table 1.1**, Section 1.3.2),[90] **P3gNDI** was used for preliminary measurements aimed at evaluating the effect of functionalisation with branched side chains on the performance of n-type materials.

OECT devices were fabricated as previously reported using **P3gNDI** as the channel material and gated using a Ag/AgCl electrode with a 0.1 M NaCl aqueous electrolyte solution in ambient

conditions.[83,93] The thin films were first deposited by drop casting the polymer solution in chloroform (5 mg/mL), which resulted in a channel thickness ranging from 1.5 to 2.0 µm. Representative output and transfer curves of **P3gNDI** are illustrated in **Figure 3.9**.

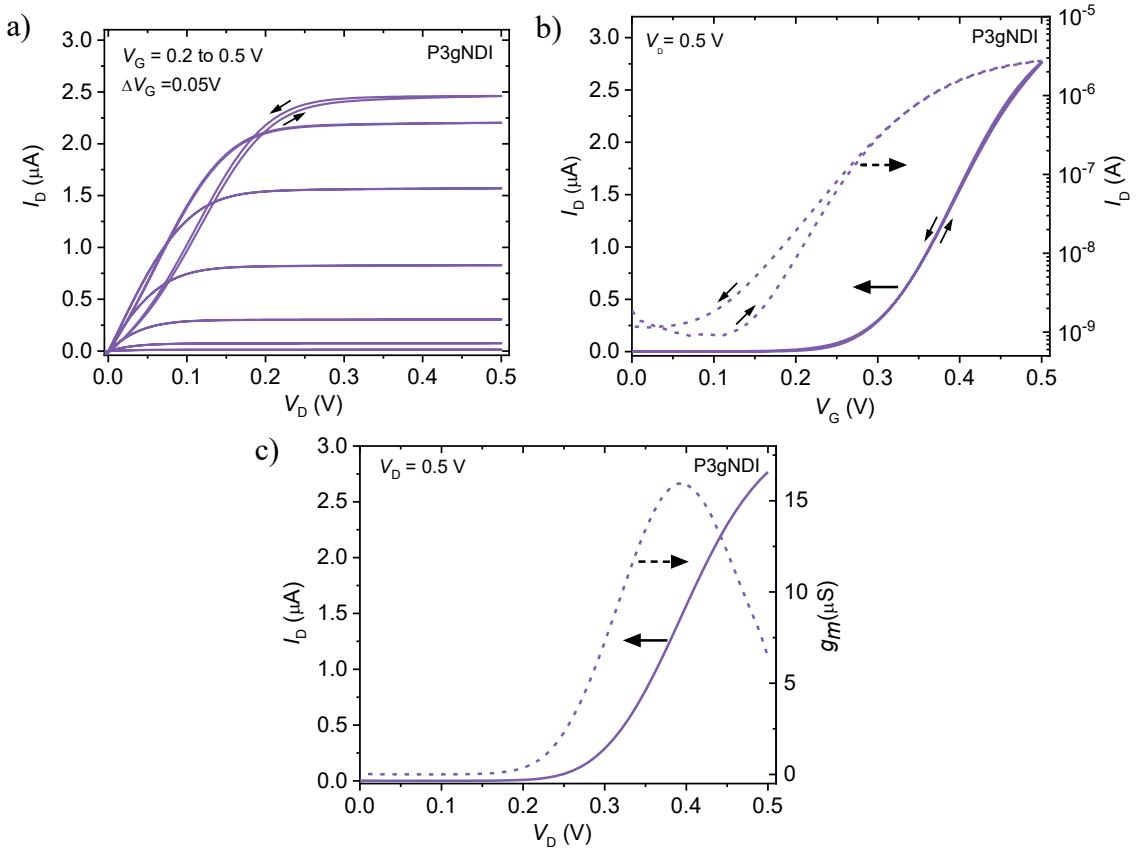


Figure 3.9. Performance of the **P3gNDI** OECT devices (W = 100 µm, L = 10 µm, d = 1.98 µm, 200 mV/s) in 0.1 M NaCl aqueous solution in ambient conditions showing (a) output curve for 0.2 < V_G < 0.5 V with ΔV_G = 0.05 V (b) transfer curve at V_D = 0.5 V and the corresponding transconductance (c) transfer curve at V_D = 0.5 V on a linear and logarithmic scale (dotted lines), showing hysteresis with direction indicated with arrows.

As the gate bias exceeds 0.2 V, the device turns on and reaches a peak drain current of ~ 2.6 µA at V_G = V_D = 0.5 V. As observed for other NDI copolymers bearing EG side chains,[90] **P3gNDI** shows hysteretic operation and a decrease in I_D at V_G = 0.5 V, however the origin of these non-idealities is not known (**Figure 3.9a**). The low threshold voltage (V_T) of 0.23 V is in good agreement with the onset of electrochemical reduction estimated by CV. Based on the

transfer characteristics, a thickness-normalised peak transconductance (g_m) of 0.08 S/cm was recorded at V_G = 0.4 V.

The OECT performance of **P3gNDI** was next evaluated as a thin active layer (130–140 nm) by changing the processing conditions from drop- to spin-casting. Although similar n-type characteristics were observed (**Figure B4**, Appendix B), the thickness-normalised g_m at V_G = 0.4 V decreased to 0.02 S/cm. Possible reasons for this discrepancy in the normalised g_m values include errors in measuring the thickness of thin spin-cast channels, differences in the efficiency of ionic-electronic coupling in thin versus thick films[180] or distinct microstructures of the polymers films upon changing the processing conditions.[91]

To allow a better comparison with **P-100**, the product of the material-dependent parameters (μC^*) was extracted based on the peak g_m of multiple channels with different thicknesses using equation (5) (Section 1.2.3) and was found to be 0.034 $\pm$ 0.007 F V^{-1} cm^{-1} s^{-1} (averaged over five devices). The volumetric capacitance (C^*) was determined via electrochemical impedance spectroscopy (EIS) measurements of polymer-coated gold electrodes immersed in a 0.1 M NaCl aqueous solution (**Figure B5**, Appendix B). The capacitance of **P3gNDI** was extracted by fitting the impedance data at a doping potential of V = –0.4 V versus Ag/AgCl to a Randles circuit[181] and normalising by the volume of the film to give a C^* of 137 F/cm^3. When comparing with the reported C^* of **P-100** (192.4 F/cm^3),[90] a slight decrease is observed upon replacing the linear EG side chains with branched ones. This is most likely a result of the increase in the overall length of the side chain by one EG unit and thereby lowering of the backbone to side chain ratio when going from **P-100** to **P3gNDI**. Although the impedance matching method[94] was applied to the OECT channels to independently measure the electron mobility (μ), no reliable values could be extracted. Nonetheless, the μC^* product of **P3gNDI** determined from the OECT measurements is comparable to the reported values for **P-100** (0.038 F cm^{-1} V^{-1} s^{-1}, **Table 1.1**).[90] Therefore, despite the slight decrease in C^*,

functionalisation of the NDI-T2 backbone with branched triethylene glycol side chains instead of linear heptakis(ethylene glycol) side chains ones has a minimal effect on the overall ionic-electronic transport properties.

3.8.2 OECT performance of P4gNDTI

To quantify the volumetric charging of **P4gNDTI**, EIS analysis of the polymer films was carried out on gold electrodes using a 0.1 M NaCl aqueous solution as the supportive electrolyte. It should be noted that all measurements in this section were carried out preliminarily with a sample of **P4gNDTI** with a M_n of 21.3 kDa ($Đ$ 1.79), rather than the higher M_n sample obtained after optimisation of the polymerisation conditions.

The Bode magnitude and phase angle plots when applying a voltage offset between 0.1 V and –0.5 V versus Ag/AgCl are presented in **Figure 3.10a** and **Figure 310b**. **P4gNDTI** behaves in a similar manner to high performing OECT materials,[86,90,125] showing a modulation in impedance of more than two orders of magnitude and more capacitive character at low frequencies upon increasing the offset voltage.

By fitting the impedance data at an offset voltage of –0.4 V (**Figure 3.10b**), the capacitance per area of **P4gNDTI** (1.43×10^{-2} F/cm^2) was found to be several orders of magnitude larger than that of alkylated NDI polymers in EG-OFETS (0.08×10^{-6} F/cm^2),[182] consistent with a volumetric doping regime. Considering the thickness of the polymer film (d = 2.16 μm), a volumetric capacitance (C*) of 66 F/cm^3 was obtained. EIS analysis of thinner polymer films (d = 133 nm) resulted in a similar C* of 70 F/cm^3 at a potential of –0.4 V versus Ag/AgCl. The C* of **P4gNDTI** is lower than the highest reported values for n-type OECT polymers functionalised with EG side chains (*cf.* 397 F/cm^3 for **p(gNDI-gT2)**),[115] but comparable to the NDI-T2 copolymers with optimised mixed ionic-electronic transport properties studied in Chapter 2 (*cf.* 59 F/cm^3 for **p(C6-gNDI-gT2)** and 72 F/cm^3 for **p(C3-gNDI-gT2)**).

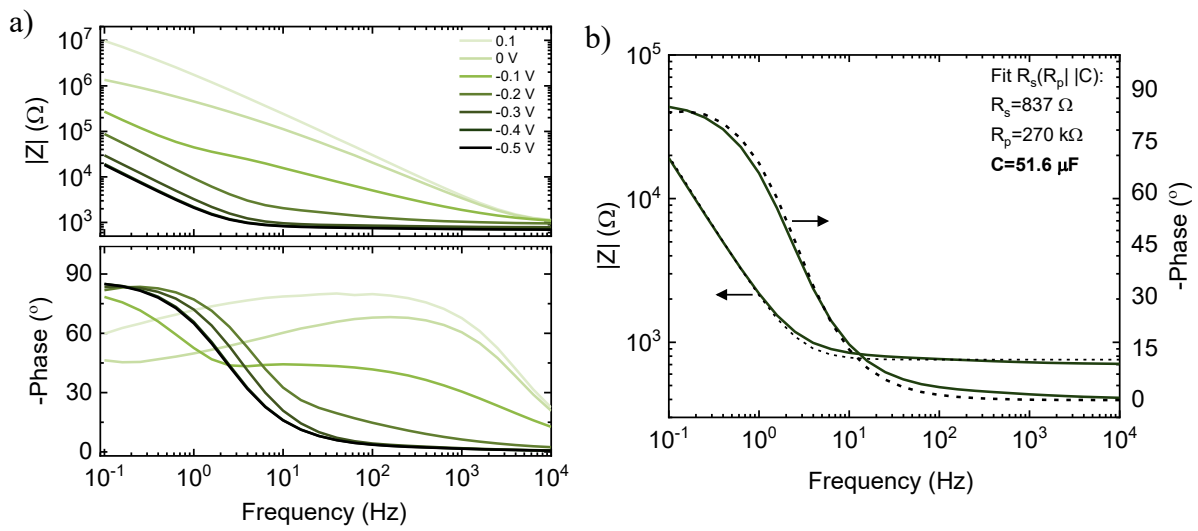


Figure 3.10. EIS measurements of **P4gNDTI** in an 0.1 M NaCl aqueous solution showing (a) impedance magnitude and phase and (b) impedance magnitude and phase at an offset bias of V = –0.4 V with the fits to a Randles circuit (dashed lines) versus frequency. The films were coated by drop casting on a gold electrode with $L = W = 600$ µm, $d = 2.16$ µm.

To gain further insight into the mixed conduction properties, OECT devices comprising **P4gNDTI** as the channel material were fabricated and analysed as described in Section 3.8.1. The output and transfer characteristics shown in **Figure 3.11** demonstrate accumulation mode n-type operation in aqueous electrolytes. Notably, **P4gNDTI** shows minimal hysteresis for forward and reverse biasing and negligible decrease in I_D at $V_G = 0.5$ V, as opposed to **P3gNDI** (**Figure 3.11a** *cf.* **Figure 3.9a**) and previously reported NDI copolymers with polar side chains, which typically show non-idealities at this potential.[90] The **P4gNDTI**-based device (d = 1.81 µm) is characterised by a low threshold voltage of 0.23 V and a peak g_m of 8.61µS, corresponding to a thickness-normalised g_m of 0.05 S/cm recorded at V_G = 0.43 V. Decreasing the thickness of the active layer (d = 122 nm, **Figure B6**, Appendix B) led to a similar OECT behaviour, with the device reaching a peak g_m of 0.30 µS at the same gate bias (V_G = 0.43 V). Based on the peak g_m of multiple channels with known dimensions and biasing conditions, the μC^* product was estimated to be 0.020 $\pm$ 0.001 F V^{-1} cm^{-1} s^{-1} (averaged over five devices).

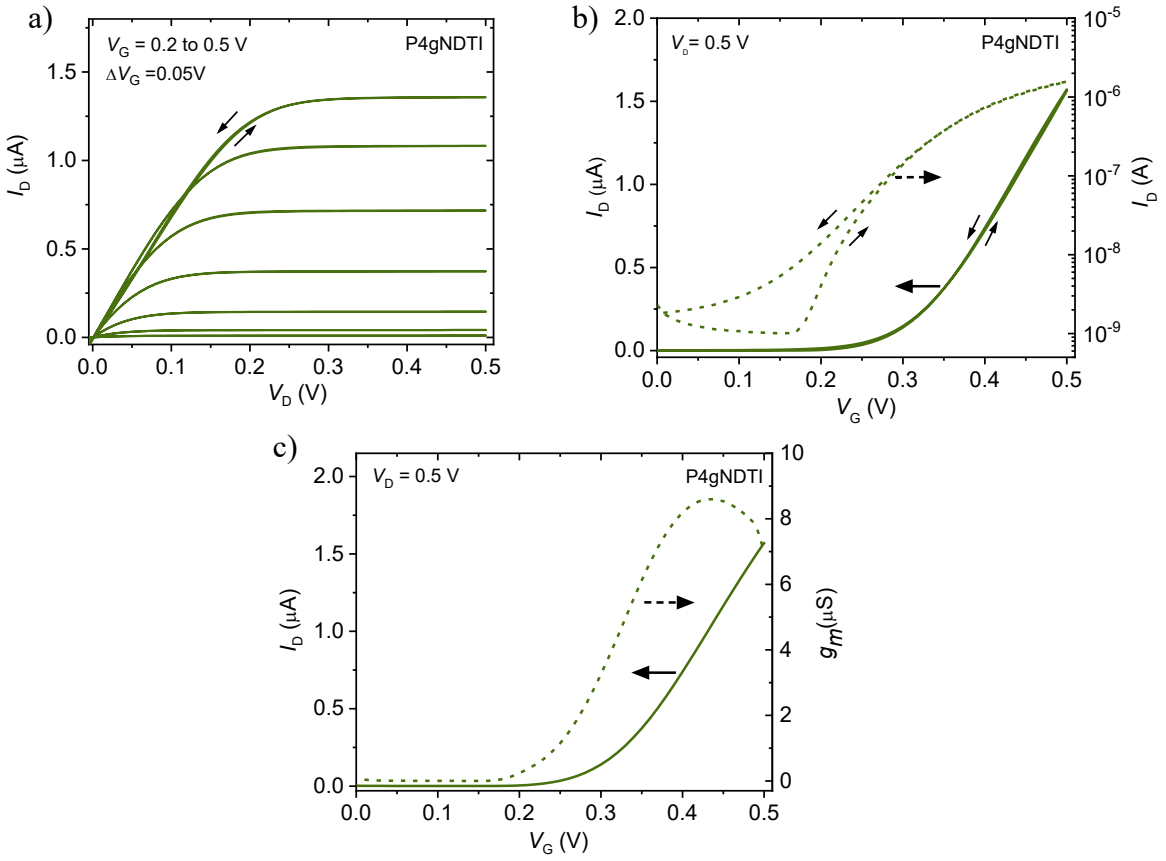


Figure 3.11. Performance of the **P4gNDTI** OECT devices (W = 100 µm, L = 10 µm, d = 1.81 µm, 200 mV/s) in 0.1 M NaCl aqueous solution in ambient conditions showing (a) output curve for 0.2 < V_G < 0.5 V with ΔV_G = 0.05 V (b) transfer curve at V_D = 0.5 V and the corresponding transconductance (c) transfer curve at V_D = 0.5 V on a linear and logarithmic scale (dotted lines), showing hysteresis with direction indicated with arrows.

Bandwidth measurements of both drop cast and spin cast OECT channels were also carried out to estimate the charge carrier mobility, as detailed by Rivnay et. al.[94] The OECT electron mobility was found to be 3.55 $\pm$ 0.99 × 10^{-5} $cm^2\ V^{-1}\ s^{-1}$ (averaged across six OECT channels), which is approximately one order of magnitude lower than the expected value based on the μC^* and C^* determined from OECT characteristics and EIS. This indicates an underestimation of the OECT mobility determined using the impedance matching method, most likely due to the low currents typically observed for n-type polymers (also seen in Chapter 2).

Overall, preliminary OECT analysis of **P4gNDTI** demonstrates n-type operation at low applied potentials with low hysteresis and a μC^* of 0.020 ± 0.001 F V^{-1} cm^{-1} s^{-1}. Due to the differences in the length of the branched EG side chains, a comparison between the OECT performance of **P4gNDTI** and **P3gNDI** would not clearly identify the effect of enhanced backbone coplanarity on mixed ionic-electronic transport. Analysis of the OECT performance of **P4gNDI**, as well as **P4gNDTI** with a higher molecular weight remain ongoing.

3.9 Conclusions

Naphthodithiophene diimide, a core-extended derivative of the widely used NDI unit, was explored as a building block for n-type materials with OECT operation in aqueous electrolytes. Theoretical analysis revealed that NDTI units promote a more coplanar geometry and reduce torsional disorder along the polymer backbone relative to NDI units. As linear side chains failed to provide enough solubility, the rigid NDTI-T2 motif was functionalised with branched side chains containing either triethylene glycol or tetraethylene glycol units. Consistent with enhanced backbone coplanarity and intermolecular interactions, **P3gNDTI** and **P4gNDTI** displayed a tighter π- π stacking of the polymer chains, as well as a narrower band gap (~ 1.30 eV) and higher EA (~ 4.2 eV) compared to their NDI analogues.

While **P3gNDTI** proved to be impractical for operation in aqueous electrolytes, **P4gNDTI** demonstrated improved stability during extended cycling and a higher degree of electrochemical doping than the NDI-based analogue, **P4gNDI**. Increasing the rigidity of the backbone also led to a more controlled swelling for **P4gNDTI** when exposed to aqueous electrolytes. Based on the findings in Chapter 2, the lower swelling ability could help preserve the structural order of the dry film to a larger extent and balance the mixed ionic and electronic transport properties.

Preliminary analysis of OECT devices fabricated with **P4gNDTI** revealed n-type accumulation mode operation with minimal forward-reverse hysteresis and less degradation of the drain current at gate biases > 0.45 V compared to NDI-based copolymers. Although the thickness-normalised g_m and μC^* are lower than the current highest performing n-type materials, increasing the molecular weight of **P4gNDTI** is expected to promote more ordering of the polymer chains and presumably improve the charge transport properties. Investigations of the mixed ionic-electronic transport properties of **P4gNDTI** with a higher molecular weight, as well as its NDI analogue **P4gNDI,** are currently ongoing.

CHAPTER 4

Tuning the electron affinity of isoindigo-based copolymers for n-type operation in OECTs

4.1 General information and attributions

OECT and EIS measurements were carried out during a research visit at Northwestern University under the supervision of Dr Bryan Paulsen (Rivnay Group, Northwestern University). Monomer **4.8** was provided by Dr Weiyuan Du (McCulloch Group, KAUST). GPC measurements in chloroform were performed by Dr Weiyuan Du (McCulloch Group, KAUST) and PESA measurements were performed by Dr Craig Combe (KAUST). QCM-D and EQCM-D measurements were performed by Jokubas Surgailis (Inal Group, KAUST). GIWAXS measurements were performed and analysed by Dr Bryan Paulsen (Rivnay Group, Northwestern University).

4.2 Introduction

High operational stability of organic mixed ionic-electronic conductors (OMIECs) in aqueous electrolytes at ambient conditions is crucial for their use in electrochemical devices that can interface with biological media. While several p-type OECT materials have found practical applications in bioelectronics, achieving a comparable performance and stability for n-type analogues has proven to be significantly more challenging. The key challenges for n-type operation in aqueous media are restriction of the applied potentials to the narrow electrochemical window of water[115,123] and stability of the polymer anion towards oxidation by atmospheric O_2 and H_2O.[87,131] Trapping or neutralisation of the polymer anion by these species are more likely to occur when the injected electrons are residing in a high energy LUMO, or, in other words, if the OMIEC has a low electron affinity (EA).[87,183] Similar challenges in other transistor technologies such as OFETs have inspired numerous synthetic efforts into lowering the LUMO levels of the polymer below –4.0 eV, often achieved by incorporating electron deficient units into the backbone.[37,128,130,135–137]

The limited number of reported n-type OECT polymers are based on either NDI or BBL units,[90,115,123] with a wide selection of electron deficient building blocks remaining unexplored. Amongst these, isoindigo (**II**) is a well-established acceptor unit for the design of copolymers with strong intermolecular interactions for OFET applications. Structural modification of either the isoindigo core or its comonomer allowed the design of polymers with either p-type, n-type or ambipolar transport properties in ambient conditons.[184–187] An efficient strategy to stabilise the LUMO levels and shift the charge transport polarity towards n-channel involves incorporation of pyridinic nitrogen atoms at the 7,7'-positions of the isoindigo core to form an azaisoindigo unit (**AII**).[188,189] This substitution of the benzene units with pyridine units simultaneously enhances the electron-deficient character of the polymer and minimises the steric effects between the co-repeat units, leading to OFET electron mobilities as high as 3.88 $cm^2\ V^{-1}\ s^{-1}$.[190] In the context of OECT applications, isoindigo units with EG-based chains have only recently been combined with electron rich bis(3,4-ethylenedioxythiophene) and bithiophene units to design a series of accumulation mode p-type materials.[116] However, isoindigo derivatives have not yet been explored as potential building blocks for n-type polymers with stable operation in aqueous-based OECTs.

This chapter focuses on design strategies to tune the electron affinity of isoindigo-based copolymers for n-type OECT operation in aqueous media. The frontier molecular orbital (HOMO/LUMO) energies were varied by systematically changing the nature of the key acceptor from isoindigo to azaisoindigo, as well as the choice of the comonomer. The investigated comonomers consist of bithiophene (**T2**), 5,6-difluoro-4,7-di(thiophen-2-yl)-benzothiadiazole (**T2FBT**) and 4,7-dithiazolyl-benzothia-diazole units (**TzBT**) units, yielding a series of six copolymers as illustrated in **Figure 4.1**. The presence of a highly electron deficient fluorinated benzothiadiazole (BT) core within the **T2FBT** unit is expected to increase the EA of the copolymer relative to the **T2** unit, as well as enhance the backbone coplanarity

through F···H nonbonding intramolecular interactions.[191] Similarly, the **TzBT** moiety contains a BT core, however it is flanked with more electron deficient thiazole units instead of thiophene units. In this case, the central BT unit was not functionalised with fluorine substituents due to the higher planarising effect of N···H interactions compared to F···N interactions.[192] All polymer backbones were functionalised with linear heptakis(ethylene glycol) side chains to facilitate penetration and transport of hydrated electrolyte ions. The polymer series allowed an investigation of the complex interplay between structural order, swelling ability and energetics in determining the electrochemical activity and OECT operation in aqueous electrolytes, extending the scope of present n-type OECT materials to isoindigo-based materials.

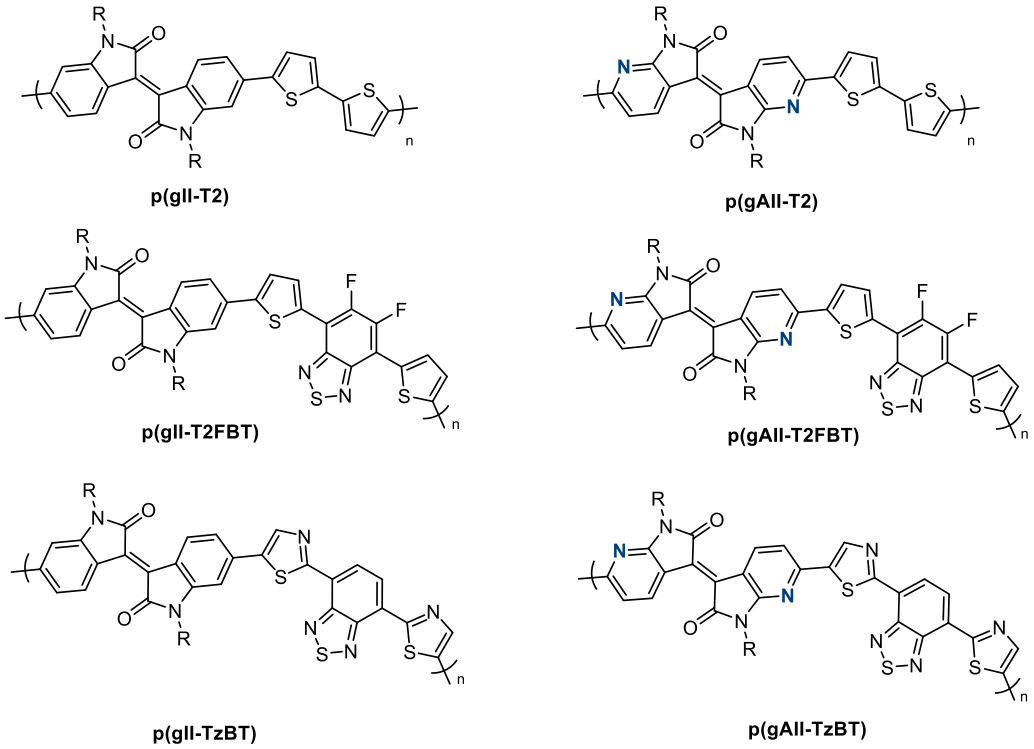
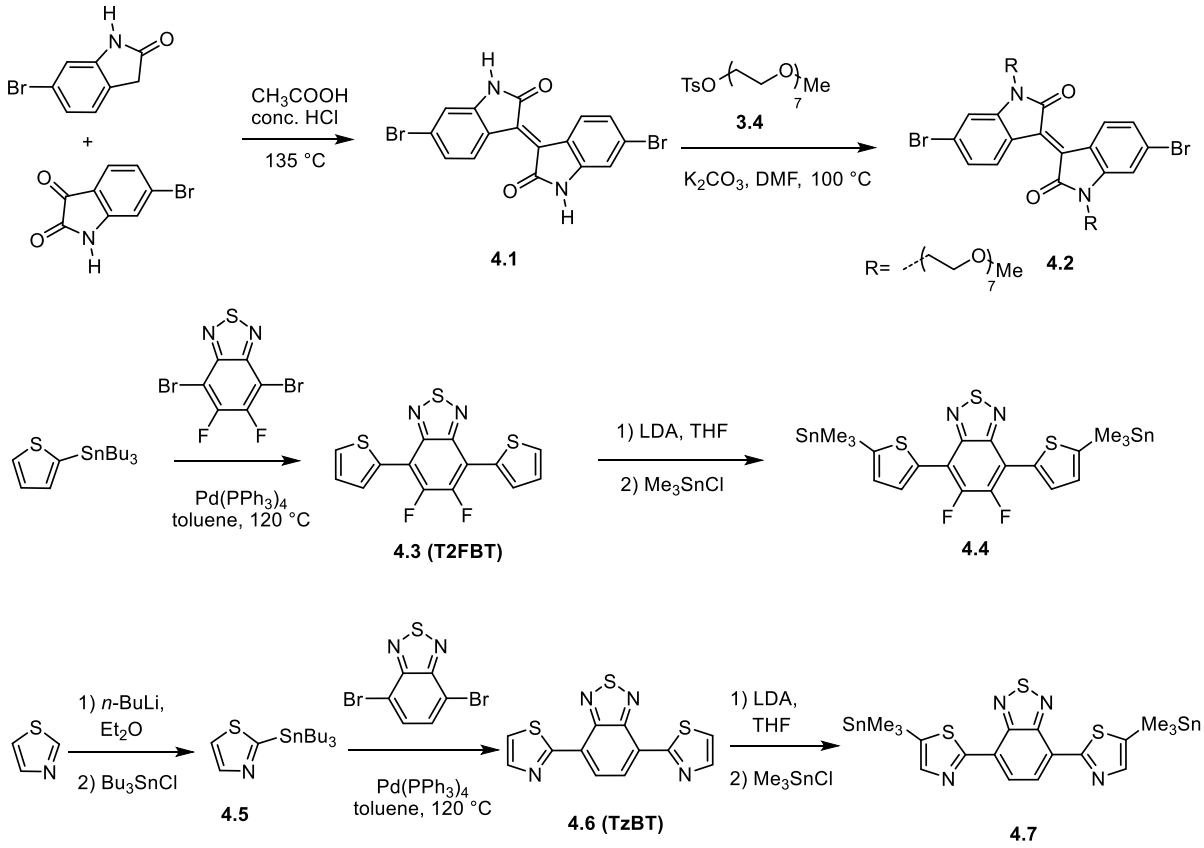


Figure 4.1. Structures of the isoindigo-based copolymers studied in this chapter. The polymers are functionalised with heptakis(ethylene glycol) side chains.

4.3 Synthesis of the polymers

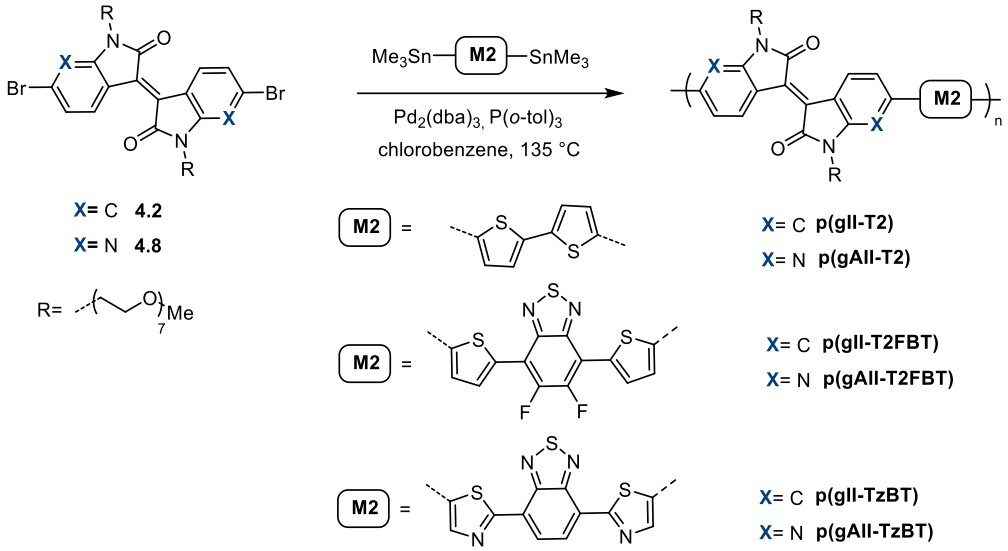
The synthesis of the heptakis(ethyleneglycol)-functionalised isoindigo monomer is outlined in **Scheme 4.1**. Adapting literature protocols,[193] the synthetic route involved condensation of 6-bromoisatin with 6-bromooxindole, followed by *N*-alkylation of the resulting 6,6'-dibromo-isoindigo **4.1** with the tosylate derivative **3.4** (Chapter 3), which afforded **4.2** in an overall yield of 36%.



Scheme 4.1. Synthesis of the isoindigo acceptor **4.2**, the distannylated **T2FBT** comonomer and the distannylated **TzBT** comonomer.

Having successfully synthesised the isoindigo acceptor, attention was next focused on the comonomers. 5,5′-Bis(trimethylstannyl)-2,2′-bithiophene was commercially sourced, while the distannylated **T2FBT** derivative (**4.4**) was synthesised in two steps according to previous literature, as shown in **Scheme 4.1**.[194] Adapting the method of Lee and co-workers,[195] the

TzBT unit (**4.6)** was obtained by stannylation of thiazole at the 2-position, followed by Stille coupling with 4,7-dibromo-2,1,3- benzothiadiazole. Lithiation at the 2-position of **4.6** with lithium diisopropylamide at –78 °C and quenching with trimethyl tin chloride afforded the distannylated monomer **4.7** in an overall yield of 38% (3 steps). Despite several attempts to increase the amount of lithium diisopropylamide or the reaction temperature, the stannylation reaction failed to proceed to completion, most likely due to the low solubility of the starting material and lithiated species at low temperature. Purification by both recrystallisation and preparative gel permeation chromatography was required prior to polymerisation to ensure correct stoichiometry and a high degree of polymerisation.



Scheme 4.2. Synthesis of the polymers using Stille polymerisation conditions.

The isoindigo **4.2** and azaisoindigo **4.8** units were co-polymerised in turn with each of the distannylated **T2**, **T2FBT** and **TzBT** units under Stille conditions[90] to afford six polymers, as illustrated in **Scheme 4.2**. All polymers were purified by Soxhlet extraction using hexane, methanol, ethyl acetate, acetone and collected in hot chloroform, with isolated yields ranging from 45 to 87%. The polymers containing **T2FBT** units were obtained in lower yields compared to the **T2** and **TzBT** analogues due to formation of insoluble residues with a

presumably a higher molecular weight, which accounted for a significant proportion of the mass balance.

4.4 Properties of the polymers

The number average molecular weights (M_n) of the polymers were estimated by gel permeation chromatography with chloroform as eluent at 40 °C and were found to vary between 5.9 and 27.7 kDa, as summarised in **Table 4.1**. The copolymers containing **T2FBT** units showed significantly lower M_n compared to the rest of the series, which was attributed to the low solubility of the higher molecular weight fractions. Thermogravimetric analysis indicated that all polymers have good thermal stability, with 5% weight-loss temperature in the 354–383 °C range under nitrogen flow (**Table 4.1**, **Figure C1** in Appendix C).

Table 4.1 Properties of the polymers

	M_n [$Đ$] (kDa)[a]	T_d (°C)[b]	E_g^{opt} (V)[c]	soln λ_{max} abs (nm)[d]	EA (eV)[e]	IP (eV)[e]	IP (eV)[f]
p(gII-T2)	10.7 [7.40]	359	1.52	724	3.65	4.94	5.13
p(gII-T2FBT)	5.90 [2.61]	362	1.58	701	3.69	5.16	5.40
p(gII-TzBT)	27.7 [1.31]	354	1.64	618	3.70	5.36	5.37
p(gAII-T2)	18.3 [1.99]	378	1.47	741	3.76	5.12	5.19
p(gAII-T2FBT)	6.24 [3.48]	383	1.56	708	3.98	5.44	5.38
p(gAII-TzBT)	22.4 [1.26]	364	1.66	619	3.94	5.58	5.50

[a] Number average molecular weight and polydispersity (GPC versus polystyrene standards in chloroform). [b] Decomposition temperature from thermogravimetric analysis. [c] Optical band gap estimated from thin film absorption onset. [d] Solution absorption spectra (chloroform). [e] Cyclic voltammetry of polymer thin films on glassy carbon electrodes in acetonitrile with 0.1 M tetrabutylammonium hexafluorophosphate as the supporting electrolyte. [f] Measured by photoelectron spectroscopy in air.

The absorption profiles of the polymer series as a thin film and in dilute chloroform solution are shown in **Figure 4.2** and the corresponding optical parameters are summarised in **Table**

4.1. All polymers display a broad absorption band with vibronic features (0–1 and 0–0) between 500–850 nm, which has been ascribed to intramolecular charge transfer.[196–198] Both copolymers containing **T2** units show an additional high energy band at 400–450 nm corresponding to the π–π* transition.[196] From solution to solid state, the absorption profiles are nearly identical with small red-shifts in the absorption maximum (< 15 nm), indicative of pre-aggregation in the chloroform solution for all polymers.

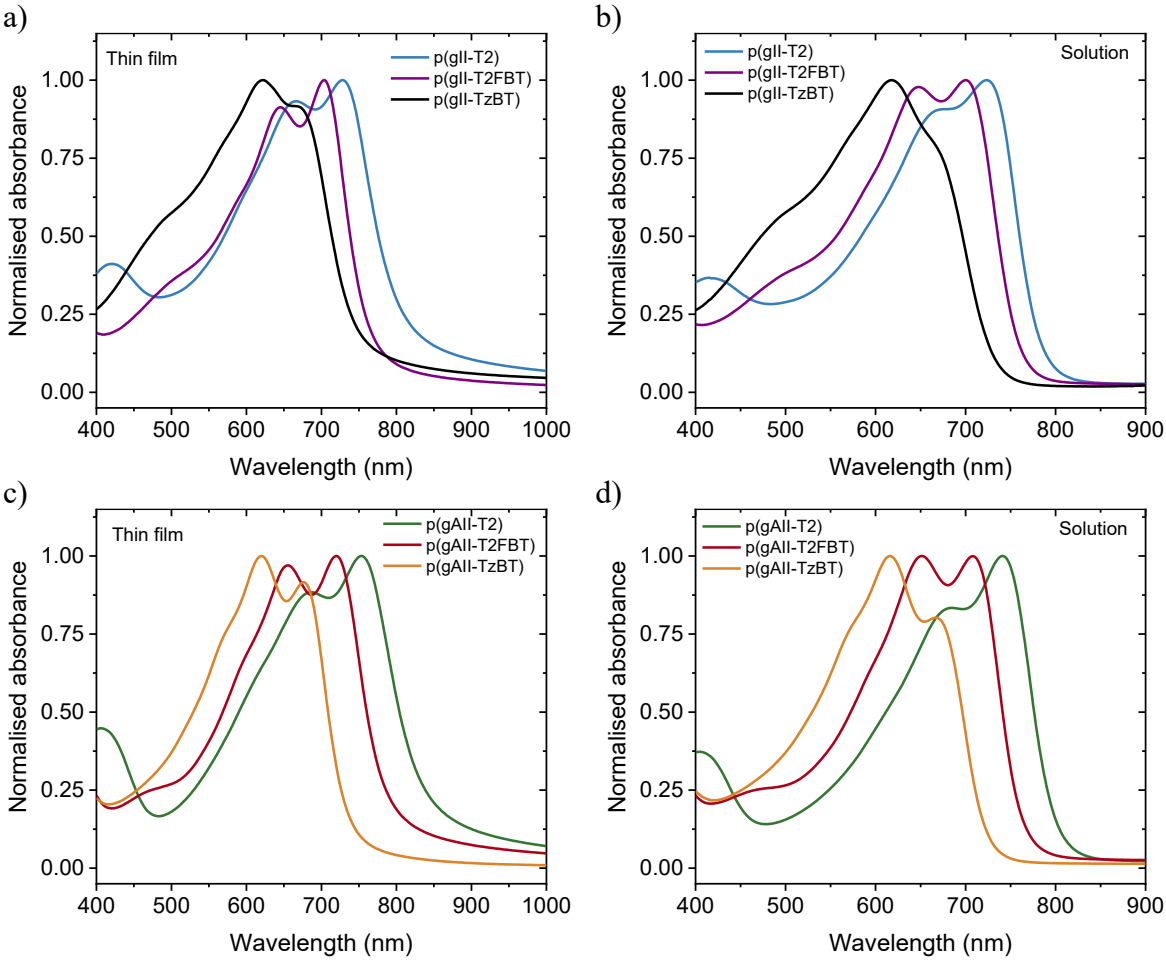


Figure 4.2. UV-Vis Spectra of the **II** and **AII** copolymers (a),(c) thin films on glass substrates and (b),(d) in chloroform solution.

The optical gaps were estimated from the absorption onset of the thin-film spectra, resulting in values between 1.47 to 1.66 eV. Introduction of electron deficient BT units from **p(gII-T2)** to **p(gII-T2FBT)** led to a blue-shift of the absorption maximum and an increase in the band gap.

A further blue shift is observed for the thiazole-containing copolymers, with band gaps of 1.58 and 1.64 eV for **p(gII-T2FBT)** and **p(gII-TzBT)**, respectively. The azaisoindigo-based copolymers display similar trends in the band gap upon varying the nature of the comonomer unit, increasing in the order **T2** < **T2FBT** < **TzBT** (**Figure 4.2c** and **Figure 4.2d**). When comparing the isoindigo and azaisoindigo-based polymers, introduction of pyridinic nitrogen atoms led to less evident changes in the absorption features and only slight red shifts in the absorption onset (< 0.05 eV).

To investigate the electronic properties, cyclic voltammetry measurements of the polymer thin films were carried out in 0.1 M $TBAPF_6$ acetonitrile solution (**Figure C2**, Appendix C). All electron affinities were determined from the onset of electrochemical reduction by calibrating against the ferrocene/ferrocenium redox couple. Similarly, the ionisation potentials (IP) were determined from the electrochemical oxidation onset, as well as photoelectron spectroscopy in air (PESA). The determined ionisation potentials and electron affinities of the polymer series are summarised in **Table 4.1**. The energy difference between the HOMO/LUMO levels and the Fermi level of the source electrode is expected to dictate the polarity of charge transport: while a high-lying HOMO (low IP) is preferred for hole injection and p-type operation, a low-lying LUMO (high EA) is desirable for electron injection and n-type operation.

The electron affinities vary from 3.65 eV for **p(gII-T2)** to 3.98 eV **for p(gAII-T2FBT)**, demonstrating that the chosen acceptor and donor units allow for systematic modulation of the EA across the polymer series. In line with previous DFT calculations,[189] the azaisoindigo-based copolymers show a larger electron affinity by approximately 0.1–0.3 V relative to their isoindigo analogues. Introduction of electron deficient BT units into the conjugated backbone led to an increase in the EA, with values of 3.76 eV to 3.98 eV for **p(gAII-T2)** and **p(gAII-T2FBT)**, respectively. In contrast, substitution of the **T2FBT** comonomer with **TzBT** units

resulted in negligible differences in the EA for both isoindigo- and azaisoindigo-based copolymers (< 0.04 eV).

The ionisation potentials of the polymer series measured electrochemically span a wider window than the electron affinities, with values ranging from 4.94 eV for **p(gII-T2)** to 5.58 eV for **p(gAII-TzBT)**. The larger ionisation potentials, as well as electron affinities, of **p(gAII-T2FBT)** and **p(gAII-TzBT)** are consistent with the stronger electron deficient character of their repeat units relative to the rest of the series.

4.5 GIWAXS analysis of the polymer thin films

Grazing incidence wide angle X-ray scattering (GIWAXS) measurements were performed to study the effect of varying the monomer units on the structural order of the polymer thin films. The two-dimensional GIWAXS patterns and line cuts along the out-of-plane and in-plane scattering directions are shown in **Figure 4.3** and the *d*-spacings calculated from peak fits are summarised in **Table 4.2**.

The microstructure of **p(gII-T2)** and **p(gII-T2FBT)** is evocative of previously reported isoindigo-based copolymers functionalised with alkyl chains.[191,199,200] Both polymers are strongly textured with predominantly edge-on orientated crystallites, with strong in-plane π-stack (010) scattering and multiple orders of out-of-plane lamellar (h00) scattering. A minority population of face-on crystallites can be also observed, with weak out-of-plane π-stack (010) scattering and in-plane lamellar (h00) scattering. The lamellar stacking of **p(gII-T2FBT)** is contracted (–1.9 Å) compared to **p(gII-T2)**, while the π-stack is barely contracted. The in-plane scattering for both **p(gII-T2)** and **p(gII-T2FBT)** showed an intermediate *q* peak tentatively assigned as (001), which is also present out-of-plane for **p(gII-T2FBT)**. A significant contraction of this (001) *d*-spacing (–0.24 Å) was observed from **p(gII-T2)** to **p(gII-T2FBT)**.

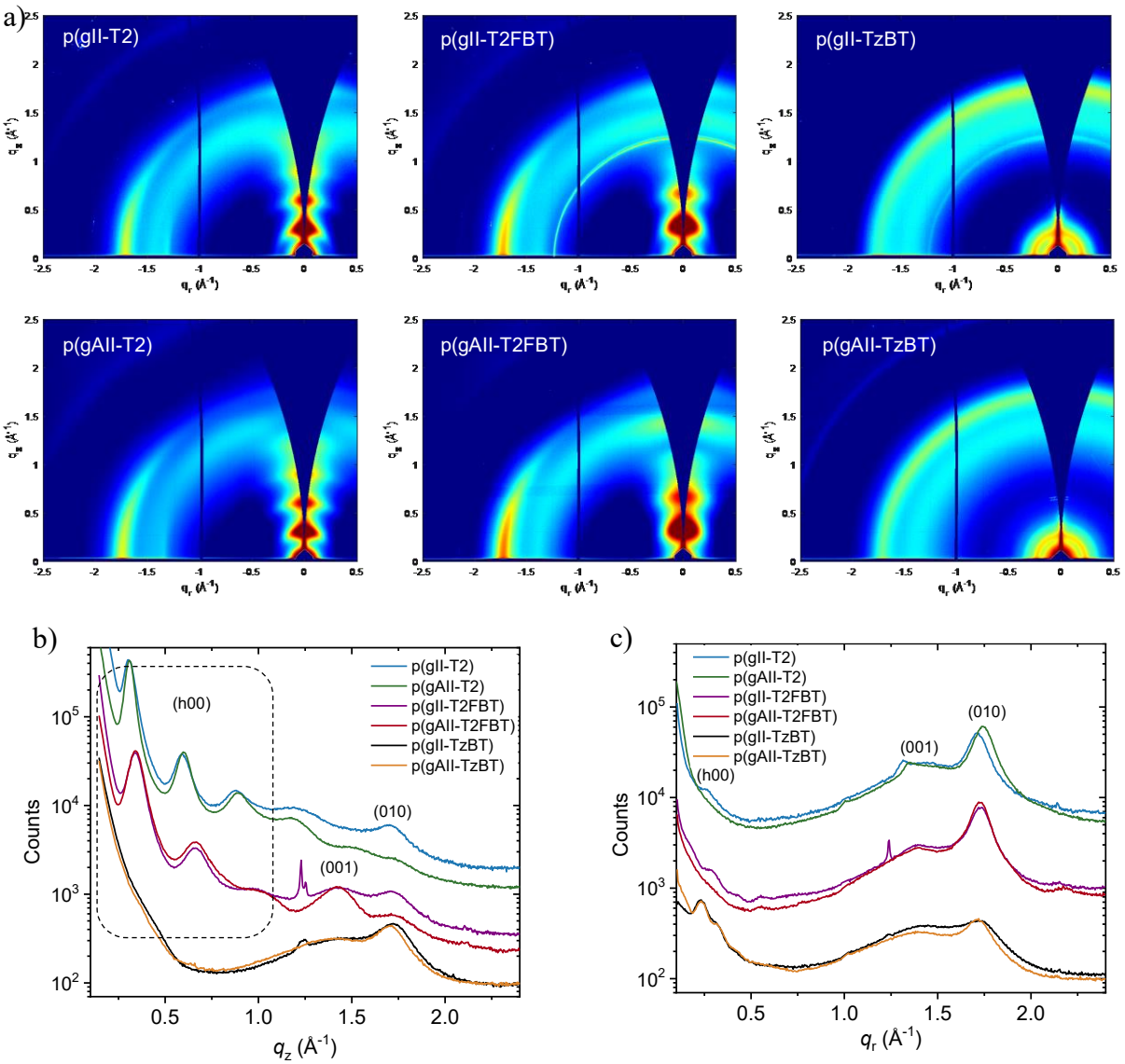


Figure 4.3. GIWAXS of neat as-cast films: (a) q_r-q_z maps of scattered X-ray intensity from thin films of the **II** and **AII** copolymers and (b) out-of-plane (q_z) and (c) in-plane (q_r) line cuts of each polymer.

The introduction of thiazole units within the polymer backbone led to a dramatic disruption of polymer chain ordering and crystallite orientation. In sharp contrast to the highly ordered and oriented **p(gII-T2)** and **p(gII-T2FBT)**, the scattering from **p(gII-TzBT)** was isotropic and much weaker. The out-of-plane lamellar scattering was unresolvable from the specular ridge

background and weak in-plane. The in-plane π-stack peak of **p(gII-TzBT)** showed a large decrease in intensity compared to **p(gII-T2)** and **p(gII-T2FBT)**.

Table 4.2 GIWAXS peak parameters

d-spacings (Å)	In-plane			Out-of-plane		
	(100)	(001)	(010)	(100)	(001)	(010)
p(gII-T2)	–	4.78	3.66	20.4	–	3.67
p(gII-T2FBT)	–	4.54	3.63	18.5	4.48	3.62
p(gII-TzBT)	27.0	–	3.63	–	5.07	3.64
p(gAII-T2)	–	4.66	3.60	20.3	–	3.66
p(gAII-T2FBT)	–	4.55	3.64	18.5	4.45	3.65
p(gAII-TzBT)	26.6	–	3.65	–	–	3.68

The azaisoindigo-based copolymers show very similar trends in terms of the general microstructure and *d*-spacings upon varying the nature of the comonomer. The **p(gAII-T2)** and **p(gAII-T2FBT)** polymers adopted a predominantly edge-on orientation with strong in-plane π-stack (010) scattering and multiple orders of out-of-plane lamellar (h00) scattering, while **p(gAII-TzBT)** scattering was weaker and isotropic.

Comparing the isoindigo and azaisoindigo-based polymers, the structural changes upon changing the nature of the key acceptor unit are much more subtle. The azaisoindigo-based copolymers containing **T2** and **T2FBT** units displayed less out-of-plane π-stack (010) scattering than their isoindigo counterparts, indicating a smaller proportion of face-on crystallites. The nature of the acceptor unit had little effect on the *d*-spacing as **T2** and **T2FBT** containing copolymers from both series had effectively identical lamellar d-spacings. Similarly, **p(gAII-TzBT)** and **p(gII-TzBT)** show a comparable lamellar *d*-spacing of 27.0 and 26.6 Å, respectively. While **p(gAII-T2)** exhibited a contracted π-stack spacing compared to

p(gII-T2), the rest of the azaisoindigo π-stack spacings were nearly identical to their isoindigo counterparts.

Overall, the GIWAXS analysis reveals a predominantly edge-on orientation of the **p(gII-T2), p(gII-T2FBT)**, **p(gAII-T2)** and **p(gAII-T2FBT)** domains, with subtle structural differences mostly dictated by the nature of the comonomer unit. In contrast, the thiazole-containing **p(gAII-TzBT)** and **p(gII-TzBT)** display a distinct isotropic microstructure with disrupted polymer chain ordering. The edge-on orientation of the **T2** and **T2BT** copolymers should be more advantageous for in-plane charge transport as required in the common configuration of an OECT.[201,202] In addition, several studies have demonstrated a strong correlation between the film microstructure and the mixed ionic-electronic conduction in aqueous environments.[106,118,139] Therefore, the structural differences between the two sets of materials are expected to contribute to some extent to their swelling and OECT behaviour.

To allow a more detailed investigation of the structure-property relationships, the polymer series was divided into two sets. The first set containing the highly oriented **p(gII-gT2)**, **p(gII-T2FBT)**, **p(gAII-T2)** and **p(gAII-T2FBT)** in Section 4.6 focuses on the effect of polymer energetics on the OECT characteristics, without major structural differences between the polymers. The second set containing the isotropic **p(gII-TzBT)** and **p(gAII-TzBT)** in Section 4.7 allows a study of the effect of disrupted structural ordering on the swelling ability and OECT operation.

4.6 Characterisation of the T2 and T2FBT copolymers

4.6.1 Electrochemical activity in aqueous electrolytes

Cyclic voltammetry measurements can provide a first indication of whether the polymers can undergo stable oxidation or reduction at a potential that is compatible with operation in an aqueous media. The polymer thin films were immersed in 0.1 M NaCl aqueous solutions and cycled in ranges between –0.7 V and 1.0 V versus Ag/AgCl, as shown in **Figure 4.4b**. The applied potentials were restricted to this range to ensure stability of the polymer films and prevent electrochemical reduction and oxidation of water.[87,103,115]

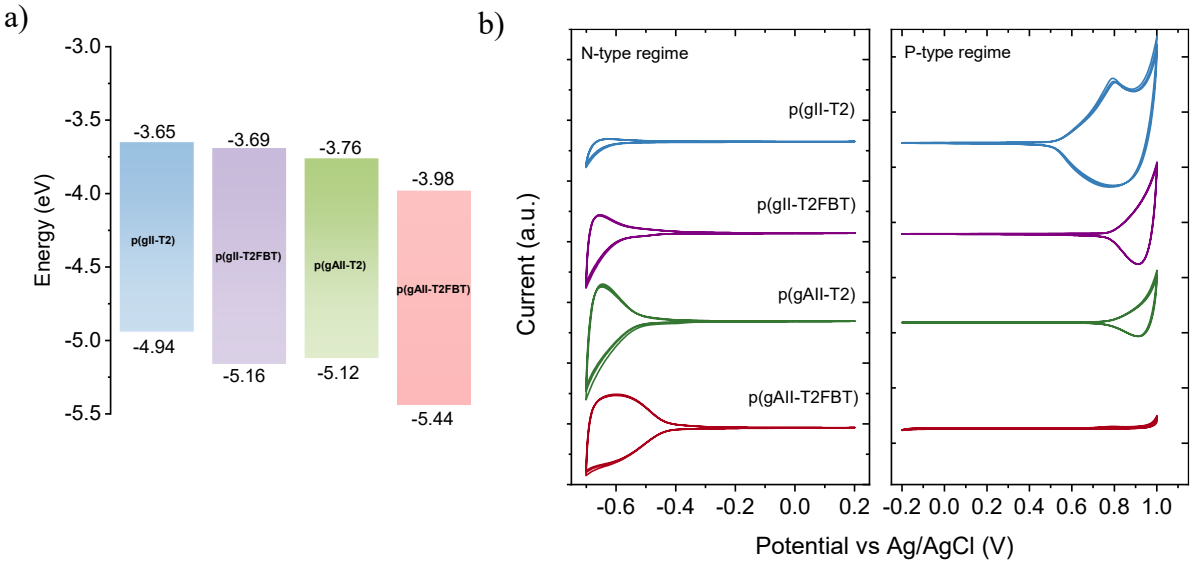


Figure 4.4. (a) Energy level diagram of the copolymers for reference, with values determined from the electrochemical oxidation and reduction onsets as described in Section 4.4 (b) Cyclic voltammetry of **p(gII-T2)**, **p(gII-T2FBT)**, **p(gAII-T2)** and **p(gAII-T2FBT)** films on glassy carbon electrodes in degassed 0.1 M NaCl aqueous solution with a scan rate of 100 mV s^{-1} and a Ag/AgCl reference electrode (2^{nd}, 3^{rd} and 4^{th} cycles). The first cycle was disregarded to eliminate any differences due to reorganisation of the polymer chains and break-in effects.

The n-type electrochemical activity in aqueous electrolytes was found to be strongly correlated to their electron affinity, where **p(gAII-T2FBT)** with the highest EA showed the earliest onset of electrochemical reduction (–0.46 V versus Ag/AgCl). The reduction onsets steadily shifted to more negative values with decreasing EA, with **p(gII-T2)** displaying the largest reduction onset of –0.64 V versus Ag/AgCl and almost negligible n-type electroactivity. An opposite trend was observed for the oxidation onsets, where **p(gII-T2)** showed reversible oxidation with an onset of 0.55 V versus Ag/AgCl, while **p(gAII-T2FBT)** could not be stably oxidised in the tested potential window. Based on their electroactivity in aqueous electrolytes, **p(gII-T2)** and **p(gAII-T2FBT)** are expected to behave as unipolar p-type and n-type semiconductors, respectively, in OECT configurations. Conversely, polymers **p(gII-T2FBT)** and **p(gAII-T2)** with intermediate LUMO levels showed relatively balanced reduction and oxidation waves, suggesting ambipolar operation in OECTs.

4.6.2 QCM-D analysis

The mixed ionic-electronic transport properties and OECT characteristics of the active material are strongly influenced by the extent of its swelling, as shown in Chapter 2 and previous reports.[95,140,141] To study the ability of the polymers to uptake hydrated ions, QCM-D measurements were carried out in a 0.1 M NaCl aqueous solution (**Figure C3**, Appendix C).

In contact with the aqueous electrolyte, polymer films are expected to swell due to passive diffusion of ions and water molecules, which has been previously correlated with the hydrophilicity[90,141,203] and microstructure of the polymer.[139] As the polymers comprise identical side chains and show similar structural features, no major differences in mass uptake were expected. The swelling ability was found to vary slightly across the series in an unsystematic manner, with values of 25% for **p(gII-T2FBT)**, 32% for **p(gAII-T2)**, 43% for **p(gII-T2)** and 49% for **p(gAII-T2FBT)**. The similar swelling ability for **p(gII-T2)** and

p(gAII-T2FBT) confirms that the shift in their reduction onsets in aqueous electrolytes is caused by the differences in LUMO energetics, rather than any significant differences in their ability to interact with hydrated ions.

4.6.3 OECT performance

To investigate the mixed ionic-electronic transport, OECT devices were fabricated as previously reported[93,204] and measured in 0.1 M NaCl aqueous solutions using a Ag/AgCl pellet electrode as the gate in ambient conditions. The OECT characteristics were acquired in turn at potentials corresponding to p-type (up to V_D = –0.8 V and V_G = –0.8 V) and n-type operation (up to V_D = 0.7 V and V_G = 0.7 V). Representative output and transfer curves are shown in **Figure 4.5** and **Figure 4.6** for p-type and n-type operation, respectively. The relevant OECT parameters for both p-type and n-type operation are summarised in **Table 4.3**.

Table 4.3. OECT parameters of **T2** and **T2FBT** copolymers

	p(gII-T2)	**p(gII-T2FBT)**	**p(gAII-T2)**	**p(gAII-T2FBT)**
n-type				
C^* (F/cm^3)[a]	–	–	48	151
g_m (S/cm)[b]	–	–	0.010	0.132
V_T (V)[c]	–	–	0.62	0.54
[μC^*] (F cm^{-1}V^{-1}s^{-1})[d]	–	–	0.031 ± 0.012	0.106 ± 0.012
p-type				
C^* (F/cm3)[a]	78	54	–	–
g_m (S/cm)[b]	60.10	0.129	0.077	–
V_T (V)[c]	–0.66	–0.72	–0.72	–
[μC^*] (F cm^{-1}V^{-1}s^{-1})[d]	44.36 ± 2.875	0.144 ± 0.017	0.097 ± 0.001	–

[a] Electrochemical impedance spectroscopy measurements of the polymers at the OECT gates (L = W = 600 µm) in 0.1 M NaCl aqueous solution at an offset bias of V = 0.8 V (p-type) or V = –0.7 V (n-type). [b] OECT peak transconductance measured at V_G = V_D = 0.7 V (p-type) and V_G = V_D = –0.8 V (n-type). [c] Threshold voltage. [d] Estimated from the transfer characteristics of the OECT device with known channel dimensions and biasing conditions (averaged over three devices).

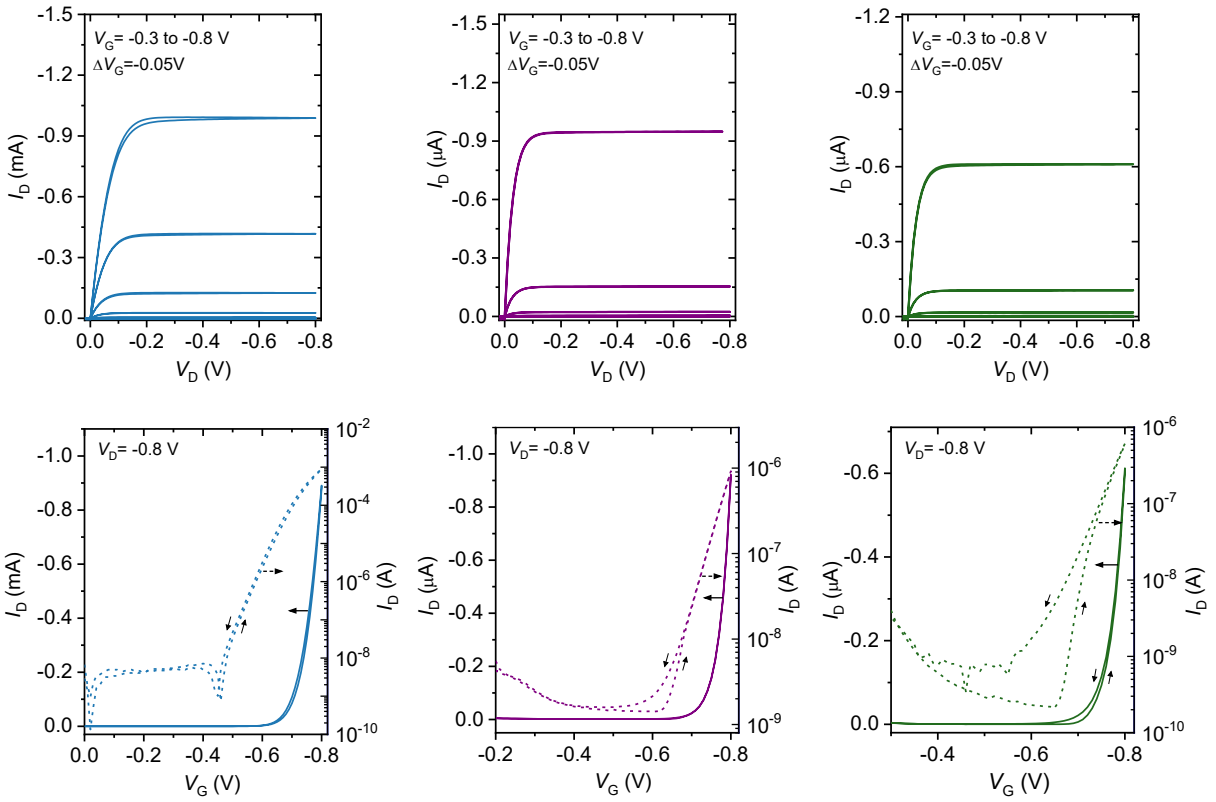


Figure 4.5. P-type performance of the **p(gII-T2)** (blue, d = 2.56 µm), **p(gII-T2FBT)** (purple, d = 2.14 µm) and **p(gAII-T2)** (green, , d = 2.48 µm) OECT devices (W = 100 µm, L = 10 µm, 200 mV/s) in 0.1 M NaCl aqueous solution in ambient conditions showing (top) output curves for –0.3 > V_G > –0.8 V with ΔV_G = –0.05 V and (bottom) transfer curves at V_D = –0.8 V on a linear and logarithmic scale (dashed lines), showing hysteresis with direction indicated with arrows.

In line with their high onsets for electrochemical reduction, **p(gII-T2)** and **p(gII-T2FBT)** showed no modulation of the source-drain current at positive biases and could not be operated as n-type materials. Instead, both polymers demonstrated p-type behaviour. As illustrated in **Figure 4.5**, **p(gII-T2)** devices turn on at a gate bias V_G > –0.45 V and reach a peak drain current of ~ 0.9 mA at V_D = V_G = –0.8 V, with almost no forward-reverse hysteresis. The thickness-normalised peak transconductance g_m was found to be 60.10 S/cm at V_G = –0.8 V. Notably, the normalised g_m of **p(gII-T2)** is ~ 5 times higher than the values recorded for other isoindigo-

based copolymers for OECT applications.[116] In the case of **p(gII-T2FBT)**, the peak drain current is approximately three orders of magnitude lower, resulting in a considerably lower thickness-normalised peak g_m under the same biasing conditions (0.129 S/cm at V_G = –0.8 V). Introduction of BT units also leads to an increase in the threshold voltage V_T from –0.66 V for **p(gII-T2)** to –0.72 V for **p(gII-T2FBT)**, consistent with its higher IP and oxidation onset in aqueous electrolytes. Therefore, in the case of **p(gII-T2FBT)**, the higher IP shifts the operation to higher potentials, leading to significantly lower I_D and thickness normalised g_m that can be achieved before degradation in the aqueous electrolyte.

Notably, both **p(gII-T2)** and **p(gII-T2BT)** show low OFF currents on the order of 10^{-9} to 10^{-8} A in ambient conditions, suggesting that faradaic noncapacitive side-reactions, such as the oxygen reductive reaction (ORR), are minimal during device operation. As demonstrated by Giovannitti et al., the ability to prevent ORR is due to their high IP ($\geq$ 4.9 eV) and represents an advantage over state-of-the-art materials such as **PEDOT:PSS** or **p(gT2-TT)** which undergo spontaneous electron transfer to molecular oxygen in ambient conditions.[120]

Substitution of the isoindigo core with azaisoindigo units from **p(gII-T2)** to **p(gAII-T2)** leads to a drop in the p-type OECT performance, with a thickness-normalised g_m of only 0.077 S/cm for **p(gAII-T2)**. However, owing to its higher EA, **p(gAII-T2)** also allows n-type operation, as illustrated by the output and transfer characteristics in **Figure 4.6**. The devices turn on at a gate bias V_G > 0.60 V and reach a thickness-normalised g_m of 0.010 S/cm at V_G = 0.7 V. Despite its low g_m in both directions, **p(gAII-T2)** shows a stable drain current upon successive sweeps to negative and positive biases, demonstrating ambipolar character. The relatively balanced p-n type characteristics make **p(gAII-T2)** a potential candidate for the development of complementary circuits based on OECTs containing a single channel material.[205]

Increasing both the EA and IP by inclusion of electron deficient BT units into the **p(gAII-T2)** backbone leads to unipolar n-type operation for **p(gAII-T2FBT)**. The **p(gAII-T2FBT)** devices show minimal forward-reverse hysteresis, indicating reversible ion insertion/injection processes. The OECT can be switched on at lower gate biases and the threshold voltage V_T was found to be nearly 0.1 V lower than that of **p(gAII-T2)**. Notably, **p(gAII-T2FBT)** reaches a peak thickness-normalised g_m of 0.132 S/cm at $V_G = 0.7$ V, considerably higher than **p(gAII-T2)** under the same device operation conditions.

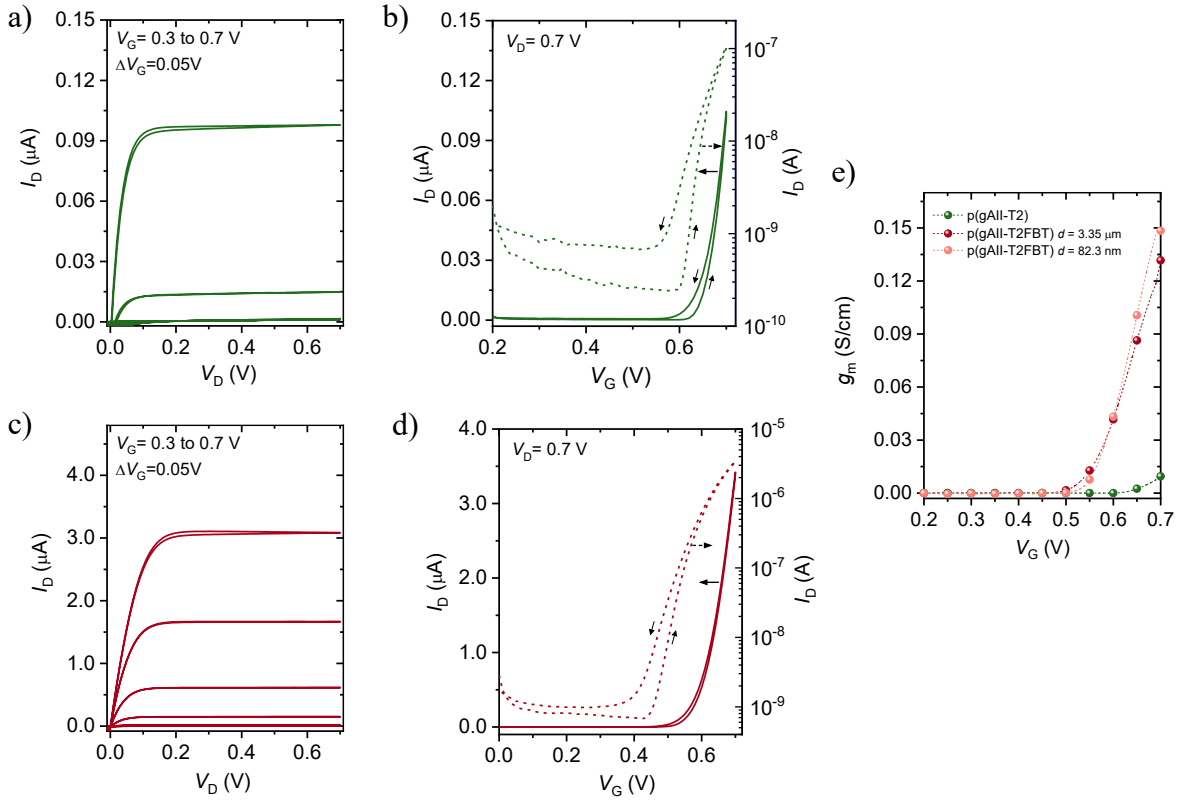


Figure 4.6. N-type performance of the **p(gAII-T2)** (green, d = 3.21 µm), **p(gAII-T2FBT)** (red, d = 3.35 µm) OECT devices (W = 100 µm, L = 10 µm, 200 mV/s) in 0.1 M NaCl aqueous solution in ambient conditions showing (a), (c) output curves for $0.3 < V_G < 0.7$ V with ΔV_G = 0.05 V (b), (d) transfer curves at $V_D = 0.7$ V on a linear and logarithmic scale (dashed lines), showing hysteresis with direction indicated with arrows and (e) thickness-normalised g_m as a function of V_G for **p(gAII-T2)** and **p(gAII-T2FBT)**, also showing the **p(gAII-T2FBT)** OECT fabricated by spin-coating with d = 82.3 nm.

Motivated by the superior performance of **p(gAII-T2FBT)** as a n-type channel material, the device preparation conditions were changed from drop- to spin-casting to deposit thinner active layers, which would allow a fair comparison with previously reported NDI-based OECTs.[90,91] Based on the transfer characteristics (**Figure C4**, Appendix C), the thickness-normalised g_m at $V_G = 0.7$ V was 0.148 S/cm, which is in good agreement with the g_m estimated from the drop-cast devices. Comparing with previously reported NDI-T2 based copolymers with identical EG side chains,[90] **p(gAII-T2FBT)** achieves a comparable peak $g_{m.}$, but requires operation at a higher bias of $V_G = 0.7$ V (*cf.* $g_m = 0.20$ S/cm at $V_G \sim 0.4$ V for **P-100**). Notably, the product of the material-dependent parameters (μC^*) of **p(gAII-T2FBT)** was found to be 0.106 $\pm$ 0.012 F V^{-1} cm^{-1} s^{-1} (averaged over three devices), which is also in the range of the highest reported values for NDI-T2 copolymers with EG side chains.[90,91,93]

As illustrated in **Figure 4.6e**, the transconductance of both **p(gAII-T2)** and **p(gAII-T2FBT)** OECT does not show the expected non-monotonic dependence on gate bias and does not appear to reach a peak value within the tested potential range (*cf.* polymers studied in Chapters 2 and 3). The bell-shaped transconductance is an intrinsic property of OECTs, which is suggested to be induced by material disorder.[206] This indicates that further backbone modifications to decrease the EA of the polymers could potentially shift the operational voltages to lower values and lead to higher transconductance values within the stable electrochemical window of the aqueous media.

To further investigate the mixed ionic-electronic transport properties across the series, electrochemical impedance measurements (EIS) were performed under a range of offset potentials. The Bode magnitude and phase angle plots are shown in **Figure 4.7**. The impedance data at an offset potential of either 0.8 V (p-type) or –0.7 V (n-type) versus Ag/AgCl were fit to a Randles circuit to extract the capacitance of the polymers, which was then normalized by the volume of the films to estimate the volumetric capacitance C^*.[181]

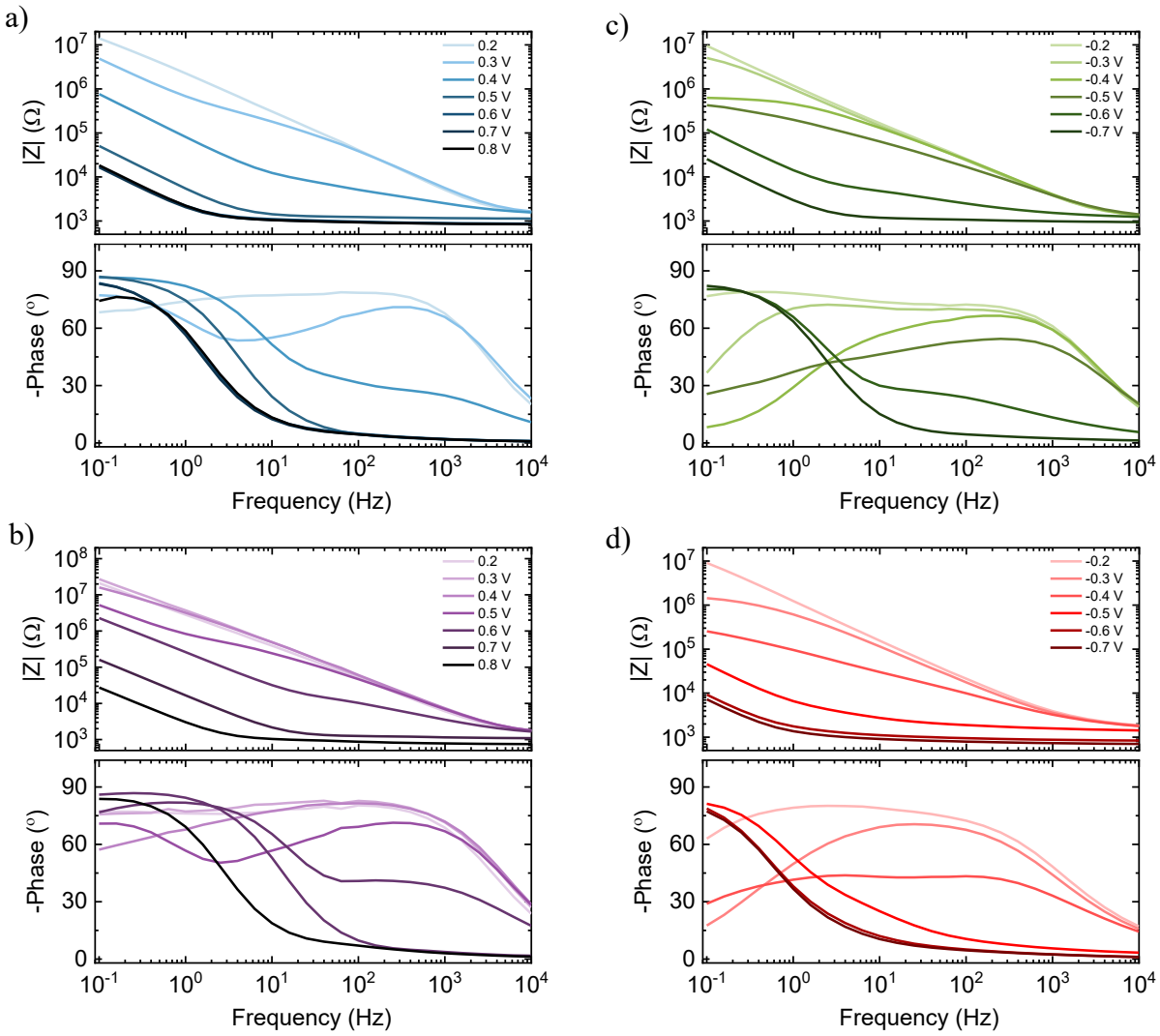


Figure 4.7. Electrochemical impedance spectroscopy measurements of (a) **p(gII-T2)** (d = 3.35 µm) (b) **p(gII-T2FBT)** (d = 2.89 µm) (c) **p(gAII-T2)** (d = 3.48 µm) (d) **p(gAII-T2FBT)** (d = 3.84 µm) in a 0.1 M NaCl aqueous solution showing impedance magnitude and phase versus frequency. The films were coated on a gold electrode with $L = W$ = 600 µm.

All polymers show a decrease of more than two orders of magnitude in the impedance upon application of doping potentials and a high capacitance per area ranging from 1.56×10^{-2} to 5.81×10^{-2} F/cm^2, indicative of volumetric charging of the polymer film.[86] Comparing the n-type materials, **p(gAII-T2)** requires higher applied potentials than **p(gAII-T2FBT)** to achieve a similar degree of doping, consistent with its lower EA and higher reduction onset from cyclic

voltammetry. Accordingly, **p(gAII-T2FBT)** shows a considerably higher C^* than **p(gAII-T2)** at an offset potential of –0.7 V versus Ag/AgCl, with values of 151 and 48 F/cm^3, respectively.

Interestingly, the C^* of **p(gAII-T2FBT)** is also considerably higher than the C^* of the p-type polymer **p(gII-T2)** (78 F/cm^3). However, based on the OECT characteristics, the estimated μC^* of **p(gAII-T2FBT)** is more than two orders of magnitude lower than the μC^* of **p(gII-T2)** (0.106 $\pm$ 0.012 versus 44.36 $\pm$ 2.875 F cm^{-1}V^{-1}s^{-1} for **p(gAII-T2FBT)** and **p(gII-T2)**, respectively). These results highlight the significant performance gap between p-type and n-type materials, where the OECT mobility of n-type materials is a clear limiting factor.

Overall, the device characteristics demonstrate that the backbone engineering strategy employed to tune the EA of isoindigo-based copolymers allows a gradual transition from unipolar p-type operation for **p(gII-T2)** to unipolar n-type OECT operation for **p(gAII-T2FBT)**. The comparable g_m and μC^* product of **p(gAII-T2FBT)** to previously reported n-type OECT polymers[90,91] confirms that the azaisoindigo core is a viable option for the design of high performing n-type OECT materials.

4.7 Characterisation of the TzBT copolymers

4.7.1 Interaction with aqueous electrolytes

The electrochemical redox activity of **p(gII-TzBT)** and **p(gAII-TzBT)** was investigated by cyclic voltammetry measurements of the thin films in 0.1 M NaCl aqueous solutions. Both polymers show switching between their neutral and reduced state within the tested potential range, as shown in **Figure 4.8**. Due to their relatively wide band gap and large IPs relative to the **T2** and **T2FBT** analogues, neither of the **TzBT** copolymers shows oxidative behaviour within the electrochemical window of water. The reduction onset shifts from –0.32 V versus

Ag/AgCl for **p(gAII-TzBT)** to –0.57 V versus Ag/AgCl for **p(gII-TzBT)**, consistent with the trends in electron affinities.

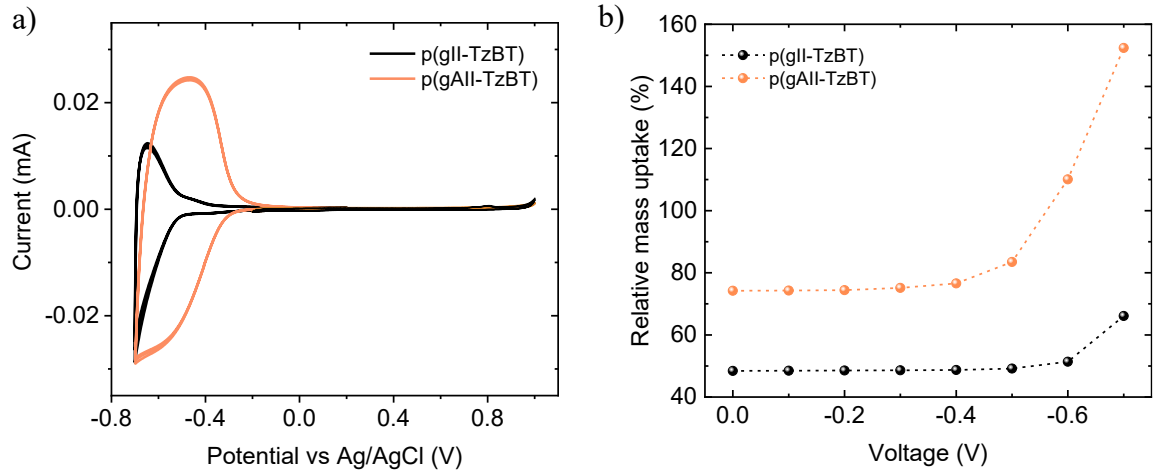


Figure 4.8. (a) Cyclic voltammetry of the polymer films on glassy carbon electrodes in degassed 0.1 M NaCl aqueous solution with a scan rate of 100 mV s^{-1} and a Ag/AgCl reference electrode (2^{nd}, 3^{rd} and 4^{th} cycles). (b) Total swelling determined from EQCM-D measurements of the polymer films upon exposure to a 0.1 M NaCl aqueous solution as a function of applied potential versus Ag/AgCl.

To further understand the interaction of **TzBT** copolymers with aqueous electrolytes, EQCM-D measurements were carried out both prior to biasing and at a potential of $V = -0.7$ V versus Ag/AgCl in 0.1 M NaCl aqueous solutions. Prior to biasing, the passive swelling of **p(gII-TzBT)** and **p(gAII-TzBT)** was found to be 48 and 74 %, respectively. As expected, upon applying a negative doping potential, both polymers show further mass uptake (**Figure 4.8b**). When electrochemical reduction occurs at the applied potential, the mass uptake increases further as cations migrate into the polymer film to counterbalance the negative electronic charges along the polymer backbone. The ability of **p(gAII-TzBT)** to undergo electrochemical reduction at lower potentials leads to an earlier onset for mass uptake and a significantly higher swelling throughout the potential range relative to **p(gII-TzBT)**. For instance, at a bias of –0.7 V, the total swelling was found to be 152% for **p(gAII-TzBT)** and 66% for **p(gII-TzBT)**. The

higher swelling ability of **p(gAII-TzBT)** is most likely due to fact that it can achieve a higher degree of doping at this potential and a larger amount of hydrated cations are injected from the electrolyte for charge compensation.

Comparing the electrochemical activity of the **TzBT** copolymers with their corresponding **T2FBT** derivatives (Section 4.6), the **TzBT** copolymers show considerably lower reduction onsets despite having nearly identical EAs (–0.52 V versus Ag/AgCl for **p(gII-T2FBT)** and –0.46 V versus Ag/AgCl for **p(gAII-T2FBT)**). This is attributed to more facile ion permeation for the **TzBT**-containing polymers, demonstrated by their higher swelling ability in the aqueous electrolyte. For instance, substitution of the **T2FBT** unit with a **TzBT** unit leads to an increase in the passive swelling from 49% for **p(gAII-T2FBT)** to 74% at **p(gAII-TzBT)**. Similarly, the mass accumulated within the **p(gII-TzBT)** film is almost double the mass accumulated within **p(gII-T2FBT)**, with a passive swelling of 48 and 25%, respectively.

Considering the structural features observed by GIWAXS (Section 4.5), the higher swelling ability of the **TzBT** copolymers could be a result of their more disrupted ordering and expanded lamellar spacings, which allow more percolation of ions within the hydrophilic polymer side chains.[96,140] These results demonstrate a complex interplay between the structural features and swelling ability, as well as HOMO and LUMO energetics of the polymers, in determining their electrochemical activity in aqueous electrolytes.

4.7.2 OECT performance

Having established that both **p(gII-TzBT)** and **p(gAII-TzBT)** show n-type behaviour in an aqueous environment at suitable applied potentials, OECT devices were fabricated and analysed as described in Section 4.6. The OECT characteristics were acquired at potentials up to V_D = 0.7 V and V_G = 0.7 V for **p(gII-TzBT)** and V_D = 0.6 V and V_G = 0.6 V for **p(gAII-TzBT)**. Representative output and transfer curves are illustrated in **Figure 4.9**, where both copolymers show some degree of hysteresis. The relevant OECT parameters are summarised in **Table 4.4**.

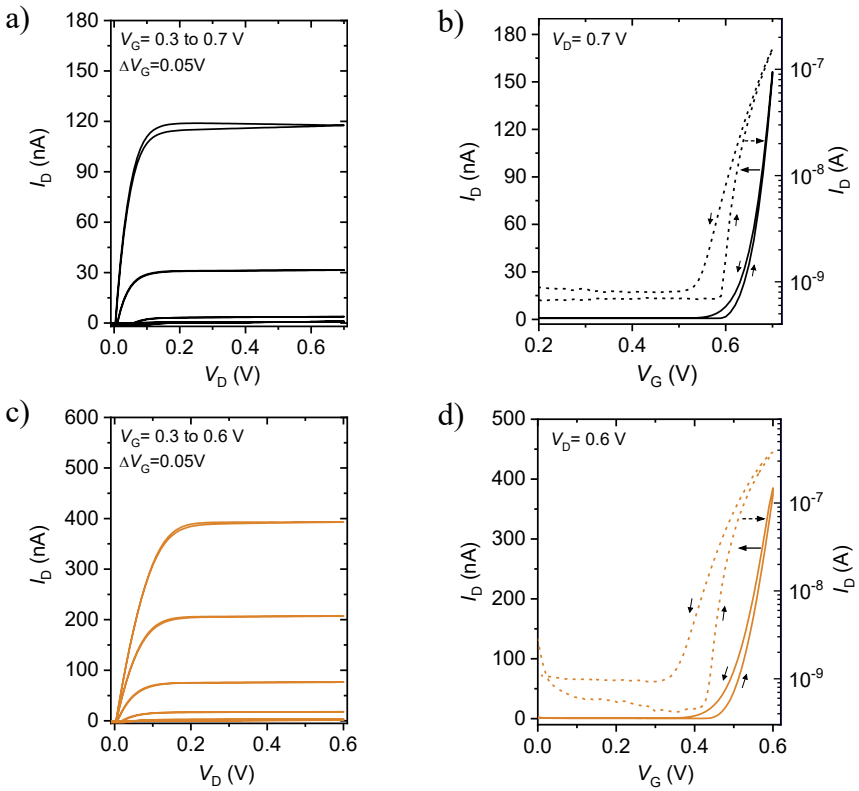


Figure 4.9. N-type performance of the **p(gII-TzBT)** (black, d = 1.20 µm), **p(gAII-TzBT)** (orange, d = 1.25 µm) OECT devices (W = 100 µm, L = 10 µm, 200 mV/s) in 0.1 M NaCl aqueous solution in ambient conditions showing (a), (c) output curves and (b), (d) transfer curves on a linear and logarithmic scale (dashed lines) at the indicated potentials.

The threshold voltages follow the trends in reduction onsets in aqueous electrolytes and shift from 0.61 to 0.44 V when going from **p(gII-TzBT)** to **p(gAII-TzBT)**. Based on the transfer characteristics, a thickness-normalised g_m of 0.030 S/cm was extracted for **p(gII-TzBT)** at V_G = 0.7 V. The azaisoindigo analogue **p(gAII-TzBT)** shows a comparable peak g_m of 0.041 S/cm, however at a lower gate bias of V_G = 0.6 V. Although a higher g_m might be reached at higher potentials, application of a gate bias > 0.6 V led to an irreversible decrease in drain current for all **p(gAII-TzBT)** devices.

Table 4.4. OECT parameters of **TzBT** copolymers

	C^* $(F/cm^3)^a$	g_m $(S/cm)^b$	V_T $(V)^c$	$[\mu C^*]$ $(F\ cm^{-1}\ V^{-1}\ s^{-1})^d$
p(gII-TzBT)	47	0.030	0.61	0.035 ± 0.006
p(gAII-TzBT)	44	0.041	0.44	0.030 ± 0.004

[a] Electrochemical impedance spectroscopy measurements of the polymers at the OECT gates (L = W = 600 μm) in 0.1 M NaCl aqueous solution at an offset bias of V = –0.7 V for **p(gII-TzBT)** or V = –0.6 V for **p(gAII-TzBT)**. [b] OECT peak transconductance measured at V_G= V_D = 0.7 V for **p(gII-TzBT)** and V_G = V_D = 0.6 V for **p(gAII-TzBT)**. [c] Threshold voltage. [d] Estimated from the transfer characteristics of the OECT device with known channel dimensions and biasing conditions (averaged over three devices).

To allow a comparison with the copolymers in the previous section, the product of the material-dependent parameters (μC^*) was calculated based on the OECT steady state performance using equation (5) (Section 1.2.3) and was found to be 0.035 ± 0.006 F V^{-1} cm^{-1} s^{-1} for **p(gII-TzBT)** and 0.030 ± 0.004 F V^{-1} cm^{-1} s^{-1} for **p(gAII-TzBT)** (averaged over three OECT devices). Next, the volumetric capacitance C^* was determined by electrochemical impedance spectroscopy as described in Section 4.6, with the Bode magnitude and phase angle plots shown in **Figure 4.10**. The volumetric capacitance was 47 F/cm^3 for **p(gII-TzBT)** at an offset potential of –0.7 V versus Ag/AgCl and 44 F/cm^3 for **p(gAII-TzBT)** at an offset potential of –0.6 V versus Ag/AgCl.

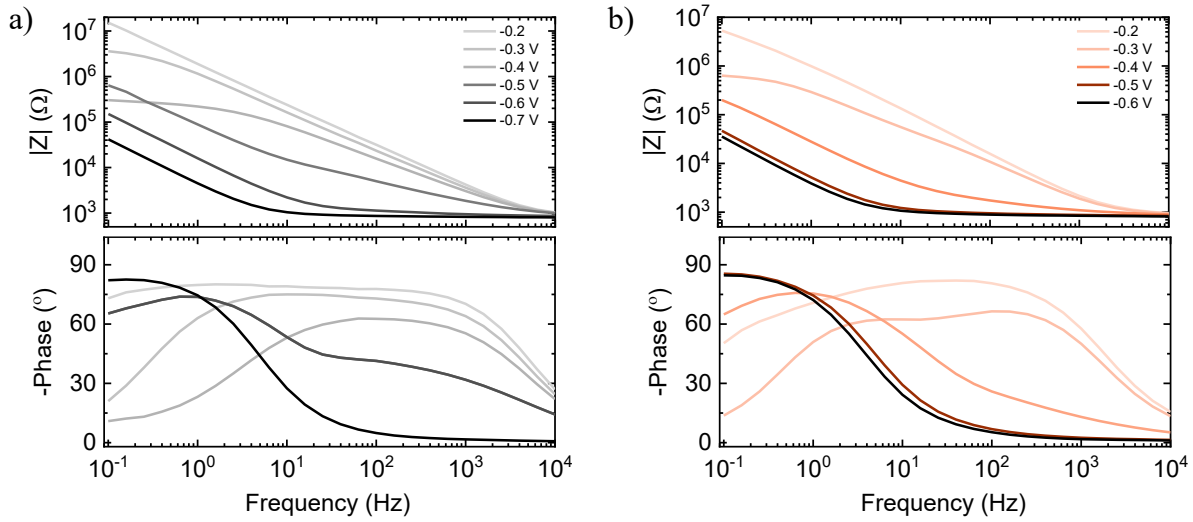


Figure 4.10. Electrochemical impedance spectroscopy measurements of (a) **p(gII-TzBT)** (d = 2.30 µm) (b) **p(gAII-TzBT)** (d = 2.39 µm) in an 0.1 M NaCl aqueous solution showing impedance magnitude and phase versus frequency. The films were coated on a gold electrode with $L = W = 600$ µm.

When comparing the OECT characteristics of **p(gII-TzBT)** with **p(gII-T2FBT)**, only **p(gII-TzBT)** allows n-type behaviour within the safe operational window, despite both polymers having nearly identical EA. The azaisoindigo derivatives show a similar trend, where the threshold voltage is decreased by 0.1 V when going from **p(gAII-T2FBT)** to **p(gAII-TzBT)**. This is attributed to the higher degree of swelling and ionic conduction of the **TzBT** polymers, which lowers the potential required to turn the device on.[90,141] Considering the material parameters, **p(gAII-TzBT)** shows a three-fold decrease in the μC^* product relative to **p(gAII-T2FBT)**. However, the μC^* product is determined from the maximum transconductance achieved before sample instability, which corresponds to a different V_G for the two copolymers (V_G = 0.6 V for **p(gAII-TzBT)** and V_G = 0.7 V for **p(gAII-T2FBT)**). Given that both $C^*$and μ can vary significantly with applied potential,[93] it is unclear whether the decrease in μC^* for **p(gAII-TzBT)** is due to structural differences or different device operation conditions. Based on the findings in Chapter 2, the lower operational stability of **p(gAII-TzBT)** at higher applied

potentials could be a result of its larger extent of swelling and therefore greater structural changes when charged at $V \geq -0.6$ V versus Ag/AgCl.

4.8 Conclusions

This chapter presents a backbone engineering study involving systematic introduction of electron deficient units to enable n-type OECT operation in aqueous environments. This concept is explicitly demonstrated using a series of isoindigo- and azaisoindigo-based copolymers containing comonomers with varying donor strength, which allowed a shift in the IP and EA over a range of 0.33 eV and 0.64 eV, respectively. GIWAXS analysis revealed a higher degree of structural order for **p(gII-T2)**, **p(gII-T2FBT)**, **p(gAII-T2)** and **p(gAII-T2FBT)** which all adopt a predominantly edge-on orientation, while the thiazole-containing **p(gAII-TzBT)** and **p(gII-TzBT)** display an isotropic microstructure with disrupted ordering.

The **T2** and **T2FBT** copolymers demonstrated a strong correlation between their LUMO energetics and ease of n-type doping, where **p(gAII-T2FBT)** with the highest EA showed the earliest onset for reduction in the aqueous electrolyte. The **TzBT** copolymers exhibited higher swelling ability and lower reduction onsets relative to the **T2FBT** analogues with similar EA, indicating that the ease of permeation of the hydrated ions into the polymer matrix also has a key role in determining the electrochemical activity of the active material.

Small modifications of the backbone of isoindigo-based copolymers allowed control of the polarity of device operation and led to the development of unipolar p-type, ambipolar and unipolar n-type OECT materials. The p-type material **p(gII-T2)** shows low OFF currents and a thickness-normalised g_m of 60.10 S/cm at $V_G = -0.8$ V, which rivals the performance of previously reported isoindigo-based copolymers for OECT applications.[116] The combined inclusion of electron deficient difluoro-BT units and pyridinic nitrogen atoms when going from **p(gII-T2)** to **p(gAII-T2FBT)** led to a transition from unipolar p-type to unipolar n-type OECT

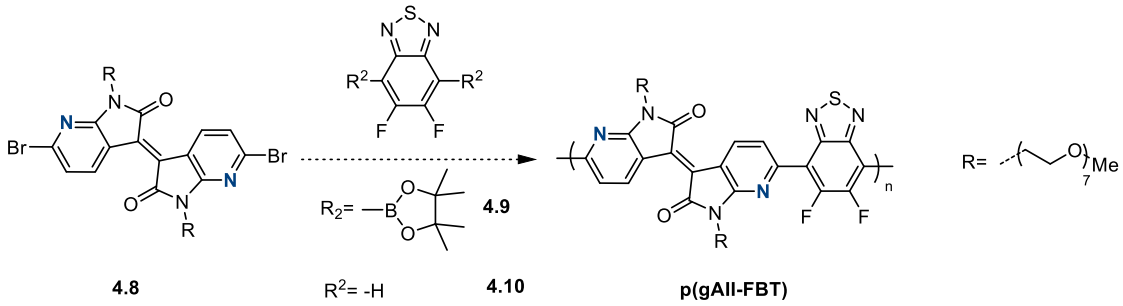
operation in the aqueous electrolyte. Polymer **p(gAII-T2FBT)** demonstrates a thickness-normalised g_m of 0.148 S/cm at $V_G = 0.7$ V and μC^* product of 0.106 $\pm$ 0.012 F V^{-1} cm^{-1} s^{-1} in accumulation mode n-type OECTs, which are comparable to those of previously reported NDI-based copolymers with identical side chains. In contrast, the thiazole-containing **p(gAII-TzBT)** with a similar EA exhibits lower performance and stability during device operation.

Although both the g_m and μC^* product of **p(gAII-T2FBT)** are lower compared to the copolymers studied in Chapter 2 or the previously reported polymer **BBL**,[123] this study introduces azaisoindigo derivatives as viable acceptor cores for the design of n-type OECT materials. More importantly, the polymer series provided a fundamental understanding of the effect of energy levels, structural features and swelling ability on the polarity of charge transport and device characteristics in OECTs.

Further engineering of the **p(gAII-T2FBT)** backbone to increase the EA to values similar to those observed for the NDTI-based copolymers studied in Chapter 3 could potentially lower the operational voltages and lead to higher transconductance values recorded within the stable potential window of the aqueous media.

4.9 Synthetic progress towards other AII copolymers

A previous study by Yue et al. demonstrated that alkylated acceptor-acceptor type polymers with alternating azaisondigo and benzothiazole (BT) units, where the backbone is composed exclusively of electron deficient units, show a higher electron affinity and more efficient n-type charge transport compared with their donor-acceptor analogues.[188] Motivated by these findings, it was reasoned that the electron affinity of **p(gAII-T2FBT)** could be further increased by removing the flanking thiophene units and synthesising its acceptor-acceptor analogue, **p(gAII-FBT)** (**Scheme 4.3**).



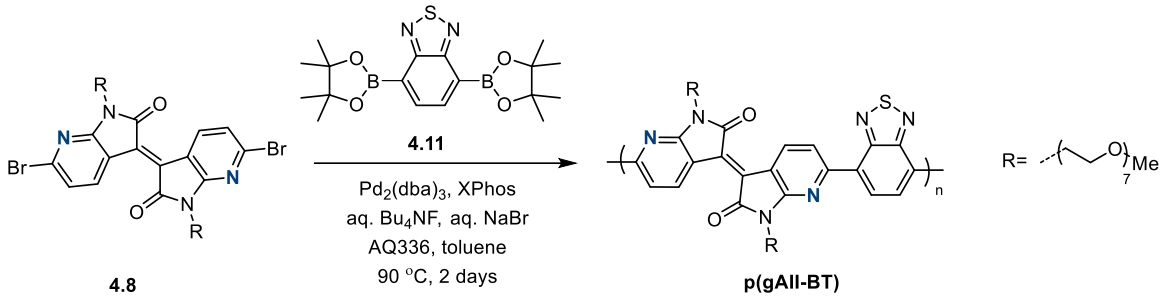
Scheme 4.3. Attempted synthesis of acceptor-acceptor copolymer **p(gAII-FBT)**.

Following the method of Yue et al.,[188] the synthesis of **p(gAII-FBT)** was first attempted by Suzuki cross-coupling of **4.8** and diboronic ester **4.9** in toluene at 110 °C, using a tris(dibenzylideneacetone)dipalladium(0)/ tris(*o*-tolyl)phosphine catalytic system and an aqueous solution of K_2CO_3 as the base (**Scheme 4.3**). These conditions failed to give the target polymer and led to rapid decomposition of the azaisoindigo monomer. Decomposition of isoindingo monomers with polar *N*,*N*'-substituents was previously observed under Suzuki conditions with K_2CO_3 and occurs most likely due to hydrolysis into brominated isatin and oxindole derivatives.[207] Using the method of Page et al.,[207] the reaction was repeated with tetra-*n*-butylammonium fluoride (TBAF) as an alternative mild base and at a lower temperature of

90 °C. However, only short oligomeric species were isolated, with a M_n of 1.8 kDa determined by GPC analysis (chloroform, 40 °C).

As Suzuki cross-coupling conditions were unsuccessful, direct arylation polymerisation (DArP) was tested as an alternative route. Marder and co-workers have recently shown that electron poor heterocycles such as dicyano[2,1,3]benzothiadiazole undergo DArP with various bromoarenes to form polymers with reasonably high molecular weights.[208] However, DArP of **4.8** and **4.10** using a palladium(II) acetate/ tris(*o*-methoxyphenyl)phosphine catalytic system with pivalic acid and caesium carbonate in 1,4-dioxane at 90 °C did not show any evidence of coupling. Increasing the reaction temperature to 120 °C led to formation of oligomers, with chains only up to 2 repeat units detected by MALDI-ToF.

These synthetic difficulties and the lack of literature reports of acceptor-acceptor copolymers incorporating fluorinated **BT** units led to the assumption that the presence of fluorine substituents lowers the coupling reactivity. Indeed, when monomer **4.8** was subjected to mild Suzuki cross-coupling conditions with the unsubstituted **BT** monomer **4.11**, the polymerisation reaction proceeded to give **p(gAII-BT)** in a yield of 21% (**Scheme 4.4**). The polymer was purified by Soxhlet extraction (hexane, ethyl acetate, methanol and acetone) to remove low molecular weight oligomers and collected in chloroform. The chloroform fraction showed a relatively high M_n of 24.6 kDa and dispersity ($Đ$) of 2.44, as determined by GPC using chloroform as the eluent at 40 °C.



Scheme 4.4. Synthesis of acceptor-acceptor copolymer **p(gAII-BT)**.

To investigate the effect of an all-acceptor backbone on the optoelectronic properties, **p(gAII-T2)** was analysed by UV-Vis spectroscopy and cyclic voltammetry in acetonitrile with 0.1 M tetrabutylammonium hexafluorophosphate as the supporting electrolyte (**Figure 4.11a** and **Figure 4.11b**). The UV-Vis absorption profile of **p(gAII-BT)** shows blue-shifted features and a wider band gap of 1.60 eV relative to **p(gAII-T2FBT)**. In addition to a less reversible doping process, **p(gAII-BT)** showed a very similar reduction onset to **p(gAII-T2FBT)**, resulting in nearly identical EA for the two polymers (3.96 eV for **p(gAII-BT)** *cf.* 3.98 for **p(gAII-T2FBT)**). The use of an acceptor-acceptor backbone containing unsubstituted BT units therefore did not prove to be an efficient strategy to increase the EA of **p(gAII-T2FBT)** and was not explored further. An alternative strategy could be replacement of the fluorine substituents with cyano groups, which has been shown to substantially increase the electron affinity of the polymer.[209]

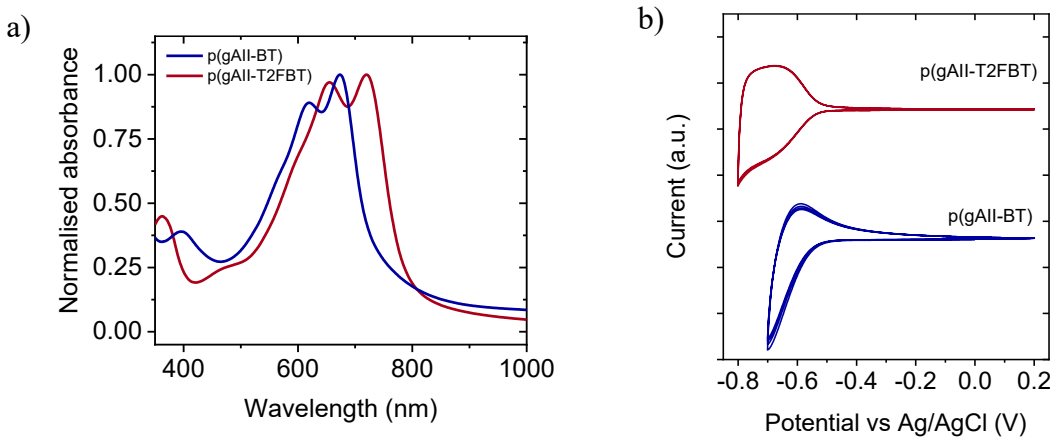


Figure 4.11. (a) UV-Vis Spectra of **p(gAII-BT)** as thin films on glass substrates (b) Cyclic voltammetry of **p(gAII-BT)** films on glassy carbon electrodes in degassed 0.1 M $TBAPF_6$ solution in acetonitrile with a scan rate of 100 mV s^{-1} and a Ag/AgCl reference electrode (2^{nd}, 3^{rd} and 4^{th} cycles). The data for **p(gAII-T2FBT)** is also shown for comparison.

CHAPTER 5

Experimental procedures

General experimental. All reactions were performed in oven-dried glassware under a nitrogen atmosphere using standard Schlenk techniques unless otherwise stated. Preparative gel permeation chromatography was performed using a LaboACE LC-5060 instrument with a separation line containing 2HR and 2.5HR columns. Column chromatography was performed on Geduran® silica gel, particle size 40–63 μm or with Biotage ZIP columns, using the indicated solvents. Reactions were monitored by analytical thin-layer chromatography with silica gel 60 F_{254} plates and visualised by either UV irradiation or staining with $KMnO_4$. All commercially available materials were used as received.

Materials characterisation. ^{1}H, ^{13}C and ^{19}F NMR spectra were recorded on a Bruker AV-400 (400 MHz) spectrometer at ambient temperature, unless otherwise stated. Chemical shifts are reported in units of parts per million (ppm, δ) for solutions in either chloroform-*d*, acetone-d_6 or dimethylsulfoxide-d_6 and coupling constants (J) are given in Hz. The chemical shifts were referenced using residual chloroform (^{1}H NMR: 7.26 ppm, ^{13}C NMR: 77.36 ppm), acetone (^{1}H NMR: 2.09 ppm, ^{13}C NMR: 30.60 ppm), dimethylsulfoxide (^{1}H NMR: 2.54 ppm, ^{13}C NMR: 40.45 ppm) or methanol (^{1}H NMR: 3.34 ppm, ^{13}C NMR: 49.86 ppm) peaks as an internal standard. UV-Vis absorption spectra were recorded on UV-1601 (λ_{max} 1100 nm) and a UV-2600 (λ_{max} 1400 nm) Shimadzu UV-Vis spectrometers. Electrospray (ES-ToF) mass spectrometry was performed using a Micromass LCT Premier. MALDI-ToF measurements were carried out in negative linear mode with DTCB as the matrix on a Micromass MALDImxTOF. Thermogravimetric analysis (TGA) analysis was carried out on a Mettler Toledo instrument, heating from 30.0°C to 105.0 °C (34.99 K/min), keeping the temperature at 105.0 °C for 10.0 min and heating from 105.0 to 800.0 °C (10.0 K/min) under nitrogen flow (50 mL/min). Number average (M_n) and weight average (M_w) molecular weights in chloroform at 40 °C were determined using an Agilent Technologies 1260 infinity GPC at 40 °C, using two PLgel 10 micrometer Mixed-B columns in series (300 × 7.5 mm), and calibrated against

narrow weight-average dispersity ($Đ$ < 1.10) polystyrene standards. Number average (M_n) and weight average (M_w) molecular weights in dichlorobenzene at 80 °C were determined using an Agilent Technologies 1200 series GPC, using two PL mixed B columns in series, and calibrated against narrow weight-average dispersity ($Đ$ < 1.10) polystyrene standards. Photoelectron spectroscopy in air (PESA) was carried out on a Riken-Keiki AC-2 PESA Spectrometer. GIWAXS was carried out at the Advanced Photon Source at Argonne National Laboratory.

Cyclic voltammetry. Cyclic voltammograms were recorded using an Autolab PGSTAT101 with a standard three-electrode setup with a working electrode, a platinum mesh counter electrode (active area 25 × 35 mm) and a Ag/AgCl reference electrode calibrated against the ferrocene/ferrocenium redox couple (Fc/Fc^+). The polymers were deposited by spin-coating chloroform solutions (5 mg/mL) at 1500 rpm on ITO-coated glass substrates (Chapter 2) or drop-casting chloroform solutions (5 mg/mL) on glassy carbon electrodes (Chapter 3 and Chapter 4). The measurements were carried out in either an anhydrous 0.1 M acetonitrile solution of tetrabutylammonium hexafluorophosphate ($TBAPF_6$) or a 0.1 M NaCl aqueous solution as the supporting electrolyte at a scan rate of 100 mV/s. The electrolyte solutions were degassed with nitrogen for 15 min prior to performing the measurement. Ionisation potentials were obtained using the equation $IP = (E_{ox} - E_{Fc} + 4.8\ V)$ and electron affinities using $EA = (E_{red} - E_{Fc} + 4.8\ V)$, where E_{Fc} was found to be 0.45 V versus Ag/AgCl.

Spectroelectrochemical analysis. The polymers were deposited by spin-coating chloroform solutions (5 mg/mL) at 1500 rpm on ITO-coated glass slides. The spectroelectrochemical measurements were performed in a 0.1 M NaCl aqueous solution using a standard three-electrode setup, with the ITO substrate as the working electrode, a platinum mesh counter electrode (active area 25 × 35 mm) and a Ag/AgCl reference electrode. For Chapter 2, the ITO substrates were immersed in a quartz cuvette filled with the electrolyte solution. The

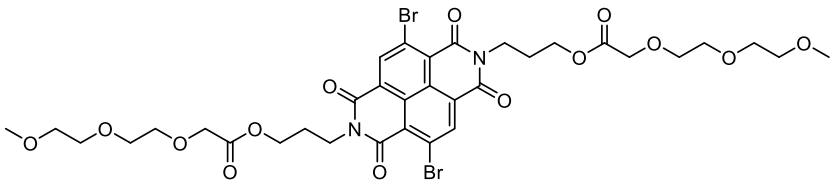
electrochemical measurements were performed while simultaneously recording the optical spectra using an OceanOptics USV 2000+ spectrometer, which collected the transmitted light through the cuvette from a tungsten lamp used as probe light source.[54] For Chapter 3, the measurements were performed in a custom-made cell positioned in the beam path of a UV-1601 Shimadzu UV-Vis spectrometer. Each potential was applied for 5 s before recording the optical spectra.

OECT fabrication and characterisation. All devices were fabricated using previously reported photolithographic procedures.[86,210] The polymer solutions were deposited by spin-coating at 500 rpm for 1 min (thin films) or drop-casting from chloroform solutions (5 mg/mL) before sacrificial peel off of Parylene C after drying. The samples were rinsed in deionised water and dried before testing, but no further annealing or cross-linking was carried out. All measurements were performed using an external Ag/AgCl pellet electrode as the gate in a 0.1 M NaCl aqueous solution in ambient conditions. The I-V characteristics were recorded on a National Instruments PXIe-1082 system using custom-made LabView scripts. The mobility of the OECT channel was determined by applying a sinusoidal voltage pulse at the gate electrode at varying frequencies. A custom MATLAB script was employed for impedance matching to extract the electron transit time as previously described.[94]

Electrochemical impedance spectroscopy. Electrochemical impedance spectroscopy was performed under ambient conditions in a 0.1 M NaCl aqueous solution with a potentiostat (Metrohm Autolab) and a three-electrode setup using a Ag/AgCl and Pt mesh as the reference and counter electrodes, respectively. The working electrode was a polymer-coated gold electrode, which was fabricated as described for the OECT channels above. The measurements were carried out with a 10 mV sine wave and frequencies from 0.1 Hz to 10 kHz. Analysis was performed with Metrohm NOVA software and custom MATLAB tools.

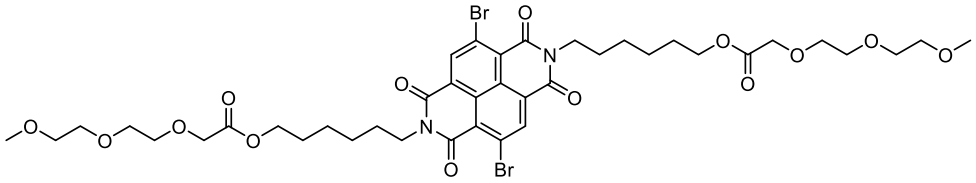
5.1 Synthetic procedures for Chapter 2

*(4,9-dibromo-1,3,6,8-tetraoxo-1,3,6,8-tetrahydrobenzo[lmn][3,8]phenanthroline-2,7-diyl)bis(propane-3,1-diyl) bis(2-(2-(2-methoxyethoxy)ethoxy)acetate) (**2.2**)*



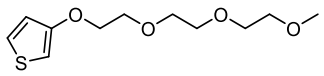
2,6-Dibromonaphthalene-1,4,5,8-tetracarboxylic dianhydride (0.50 g, 1.18 mmol, 1.0 equiv) and 3-amino-1-propanol (0.18 mL, 2.39 mmol, 2.0 equiv) were suspended in anhydrous *o*-xylene (25 mL) under argon. 2-[(2-Ethoxyethoxy)ethoxy]acetic acid (2.5 mL, 16.29 mmol, 13.8 equiv) was added and the reaction mixture was heated to 140 °C for 72 h. The mixture was allowed to reach room temperature and concentrated under reduced pressure. The resulting residue was dissolved in chloroform (50 mL) and washed with water (3 × 50 mL). The organic phase was dried over $MgSO_4$ and the solvent was removed under reduced pressure. The crude product was purified by preparative gel permeation chromatography in chloroform to give **2.2** (0.37 g, 36%) as a yellow solid. ^{1}H NMR (400 MHz, chloroform-*d*) δ 8.98 (s, 2H), 4.33 – 4.26 (m, 8H), 4.16 (s, 4H), 3.76 – 3.73 (m, 4H), 3.70 – 3.67 (m, 4H), 3.66 – 3.64 (m, 4H), 3.56 – 3.54 (m, 4H), 3.37 (s, 6 H), 2,14 (p, J = 6.5 Hz, 4H). ^{13}C NMR (100 MHz, chloroform-*d*) δ 170.6, 160.9, 139.2, 128.7, 127.9, 125.4, 124.2, 72.1, 71.1, 70.8, 70.7, 68.2, 62.4, 59.2, 38.7, 27.3. HRMS (ES-ToF): 859.0926 [M+H^{+}] (calc. 859.0924).

*(4,9-dibromo-1,3,6,8-tetraoxo-1,3,6,8-tetrahydrobenzo[lmn][3,8]phenanthroline-2,7-diyl)bis(hexane-6,1-diyl) bis(2-(2-(2-methoxyethoxy)ethoxy)acetate) (**2.3**)*



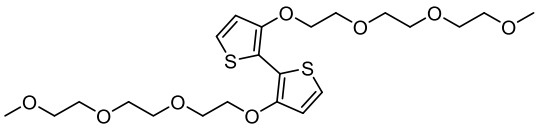
2,6-Dibromonaphthalene-1,4,5,8-tetracarboxylic dianhydride (0.35 g, 0.82 mol, 1.0 equiv) and 6-amino-1-hexanol (0.21 g, 1.81 mmol, 2.2 equiv) were suspended in anhydrous *o*-xylene (10 mL) under argon. 2-[(2-Ethoxyethoxy)ethoxy]acetic acid (2.5 mL, 16.29 mmol, 20.0 equiv) was added and the reaction mixture was heated to 140 °C for 16 h. The mixture was allowed to reach room temperature and concentrated under reduced pressure. The resulting residue was dissolved in chloroform (50 mL) and washed with water (3 × 50 mL). The organic phase was dried over $MgSO_4$ and the solvent was removed under reduced pressure. The crude product was purified by preparative gel permeation chromatography in chloroform, followed by recrystallization from ethyl acetate to give **2.3** (0.35 g, 44%) as a yellow solid. ^{1}H NMR (400 MHz, chloroform-*d*) δ 8.99 (s, 2H), 4.21 – 4.12 (m, 12H), 3.73 (m, 4H), 3.70 (m, 4H), 3.64 (m, 4H), 3.56 (m, 4H), 3.37 (s, 6H), 1.79 – 1.63 (m, 8H), 1.45 (m, 8H). ^{13}C NMR (100 MHz, chloroform-*d*) δ 170.9, 161.1, 161.1, 139.4, 128.7, 128.1, 125.7, 124.4, 72.3, 71.3, 71.0, 70.9, 69.0, 65.0, 59.4, 41.7, 28.8, 28.1, 27.0, 25.9. HRMS (ES-ToF): 965.1700 [M+Na^+] (calc. 965.1683).

*3-(2-(2-(2-Methoxyethoxy)ethoxy)ethoxy)thiophene (**2.5**)*[118]



p-Toluenesulfonic acid monohydrate (1.67 g, 8.78 mmol) was added to a solution of 3-methoxythiophene (10 g, 87.59 mmol) and triethylene glycol monomethyl ether (18.2 mL, 113. 85 mmol) in anhydrous toluene (150 mL) under a reverse flow of nitrogen. The resulting mixture was heated to reflux for 16 h. After cooling to room temperature, the mixture was quenched with water (100 mL) and extracted with ethyl acetate (3 × 200 mL). The combined organic fractions were washed with distilled water (3 × 200 mL), dried over anhydrous $MgSO_4$ and concentrated *in vacuo*. The crude material was filtered through a plug of silica (hexane: ethyl acetate, 99:1, then ethyl acetate) to give the desired product (9.35 g, 43%) as a dark brown oil. ^{1}H NMR (400 MHz, chloroform-*d*) δ 7.16 (dd, *J* = 5.3, 3.2 Hz , 1H), 6.77 (dd, *J* = 5.3, 1.6 Hz, 2H), 6.25 (dd, *J* = 3.2, 1.6 Hz, 2H), 4.15 – 4.07 (m, 2H), 3.86 – 3.80 (m, 2H), 3.75 – 3.71 (m, 2H), 3.70 – 3.64 (m, 4H), 3.58 – 3.52 (m, 2H), 3.38 (s, 3H). ^{13}C NMR (100 MHz, chloroform-*d*) δ 157.9, 125.0, 119.9, 97.9, 72.3, 71.1, 71.0, 70.9, 70.0, 69.9, 59.4.

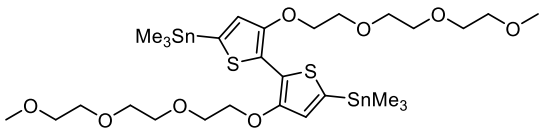
*3,3'-Bis(2-(2-(2-methoxyethoxy)ethoxy)ethoxy)-2,2'-bithiophene (**2.6**)*[118]



Adapting the method of Nielsen et al.,[118] *n*-BuLi (1.6 M in hexane, 13 mL, 20.8 mmol) was added dropwise to a solution of **2.5** (4.70 g, 19.1 mmol) in anhydrous THF (40 mL) at –10 °C. After stirring at –10 °C for 2 h, the reaction mixture was transferred to a solution of iron(III) acetylacetonate (6.71 g, 19.0 mmol) in anhydrous THF (100 mL) at 0 °C. The resulting mixture was then heated under reflux for 2 h. After cooling to room temperature, the mixture was concentrated under reduced pressure and filtered through a short silica plug (ethyl acetate: hexane, 3:1, then ethyl acetate) to remove inorganic residues. Column chromatography (ethyl

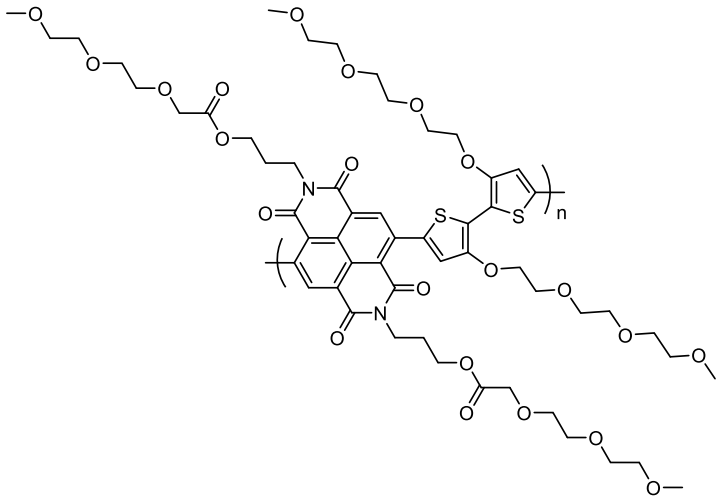
acetate: hexane, 3:1 to ethyl acetate) followed by recrystallisation from Et_2O afforded the title product (2.90 g, 62%) as a white crystalline solid. ^{1}H NMR (400 MHz, chloroform-*d*) δ 7.07 (d, J = 5.6 Hz, 2H), 6.85 (d, J = 5.6 Hz, 2H), 4.27 – 4.21 (m, 4H), 3.93 – 3.87 (m, 4H), 3.76 (m, 4H), 3.69 – 3.62 (m, 8H), 3.56 – 3.51 (m, 4H), 3.37 (s, 6H). ^{13}C (100 MHz, chloroform-*d*) δ 152.0, 122.2, 116.9, 115.1, 72.3, 71.7, 71.3, 71.0, 70.9, 70.3, 59.4.

*(3,3'-Bis(2-(2-(2-methoxyethoxy)ethoxy)ethoxy)-[2,2'-bithiophene]-5,5'diyl)bis(tri-methyl stannane) (**2.7**)*[54]



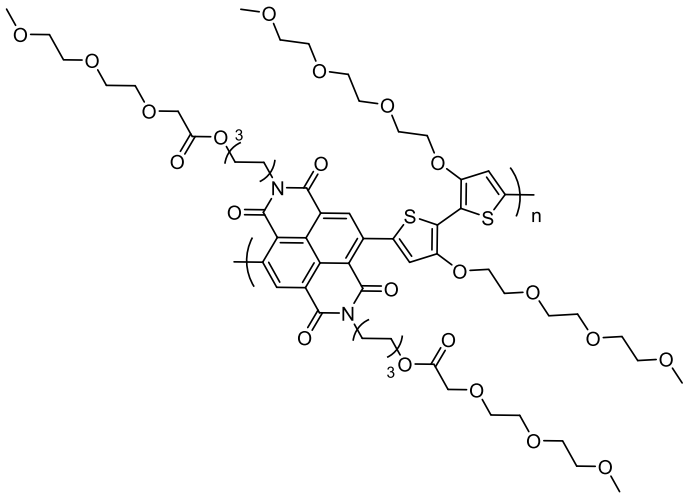
Adapting the method of Moia et al.,[54] *n*-BuLi (2.5 M in hexane, 3.25 mL, 8.15 mmol) was added dropwise to a solution of **2.6** (1.0 g, 2.04 mmol) in anhydrous THF (150 mL) at –78 °C. The resulting solution was stirred for 3 h at –78 °C. Trimethyltin chloride (1 M in hexane, 10.2 mL, 10.2 mmol) was added and the reaction mixture was allowed to warm to room temperature overnight. The mixture was diluted with diethyl ether (150 mL), washed with distilled water (3 × 150 mL) and dried over anhydrous Na_2SO_4. The resulting brown residue was dissolved in acetonitrile (100 mL) and washed thoroughly with hexane (3 × 100 mL) in order to remove tin by-products. The acetonitrile portion was concentrated under reduced pressure and subjected to preparative gel permeation chromatography in THF to remove small amounts of starting material and mono-substituted product. Recrystallisation from diethyl ether afforded the desired product (0.79 g, 48%) as a white crystalline solid, which was stored under nitrogen at 4 °C. ^{1}H NMR (400 MHz, acetone-d_6) δ 7.13 (s, 2H), 4.33 – 4.29 (m, 4H), 3.93 – 3.89 (m, 4H), 3.74 (m, 4H), 3.66 – 3.58 (m, 8H), 3.53 – 3.46 (m, 4H), 3.31 (s, 6H), 0.41 (s, 18H). ^{13}C NMR (100 MHz, acetone-d_6) δ 156.2, 131.6, 123.7, 117.6, 71.8, 71.3, 70.7, 70.5, 70.3, 70.0, 56.8, –9.3.

p(C3-gNDI-gT2)



A mixture of **2.2** (72.06 mg, 83.74 µmol, 1.0 equiv), **2.7** (68.35 mg, 83.74 µmol, 1.0 equiv) , $Pd_2(dba)_3$ (1.54 mg, 1.68 µmol, 0.02 equiv) and P(*o*-tol)$_3$ (2.00 mg, 6.57 µmol, 0.08 equiv) in anhydrous, degassed DMF (2.0 mL) was degassed for 10 min and heated to 80 °C for 4 h. 0.1 mL of a solution of 2-(tributylstannyl)thiophene (0.1 mL) and $Pd_2(dba)_3$ (1.15 mg, 1.26 µmol) in anhydrous, degassed DMF (0.5 mL) were added and the resulting mixture was stirred for 1 h at 90 °C. 0.1 mL of a solution of 2-bromothiophene (0.1 mL) in anhydrous, degassed DMF (0.5 mL) were subsequently added and stirring at 90 °C was maintained for a further 1 h. The dark green reaction mixture was cooled to room temperature and precipitated in ethyl acetate, followed by the addition of hexane. The solid was collected in a glass thimble and Soxhlet extraction was carried out with hexane, ethyl acetate, acetone, THF and chloroform. The polymer was dissolved in hot chloroform and re-precipitated in ethyl acetate, followed by the addition of hexane. Polymer **p(C3-gNDI-gT2)** was obtained as a dark green solid in a yield of 83% (83.0 mg, 69.79 µmol). ^{1}H NMR (400 MHz, chloroform-*d*) δ 8.89 – 8.75 (br s, 2H), 7.22 – 7.20 (br s, 1H, overlapped with residual solvent peak), 4.48 – 4.43 (m, 4H), 4.36 – 4.13 (m, 12H), 4.04 – 3.94 (m, 4H), 3.83 – 3.52 (m, 32H), 3.40 – 3.34 (br s, 6H), 3.33 – 3.27 (br s, 6H), 2.17-2.06 (m, 4H). GPC (chloroform, 40 °C): M_n=32.4 kDa, M_w=73.6 kDa.

p(C6-gNDI-gT2)

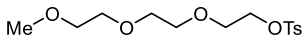


A mixture of **2.3** (45.95 mg, 48.64 µmol, 1.0 equiv), **2.7** (39.71 mg, 1.0 equiv), $Pd_2(dba)_3$ (0.89 mg, 0.97 µmol, 0.02 equiv) and P(*o*-tol)$_3$ (1.18 mg, 3.88 µmol, 0.08 equiv) in anhydrous, degassed DMF (1.5 mL) was degassed for 10 min and heated to 80 °C for 2 h. 0.1 mL of a solution of 2-(tributylstannyl)thiophene (0.1 mL) and $Pd_2(dba)_3$ (1.15 mg, 1.26 µmol) in anhydrous, degassed DMF (0.5 mL) were added and the resulting mixture was stirred for 1 h at 90 °C. 0.1 mL of a solution of 2-bromothiophene (0.1 mL) in anhydrous, degassed DMF (0.5 mL) were subsequently added and stirring at 90 °C was maintained for a further 1 h. The dark green reaction mixture was cooled to room temperature and precipitated in ethyl acetate, followed by the addition of hexane. The solid was collected in a glass thimble and Soxhlet extraction was carried out with hexane, ethyl acetate, MeOH, acetone and chloroform. The polymer was dissolved in hot chloroform and re-precipitated in ethyl acetate, followed by the addition of hexane. Polymer **p(C6-gNDI-gT2)** was obtained as a dark green solid in a yield of 70% (88.63 mg, 83.23 µmol). ^{1}H NMR (400 MHz, chloroform-*d*) δ 8.86 – 8.81 (br s, 2H), 7.25 – 7.20 (br s, 1H, overlapped with residual solvent peak), 4.46 – 4.37 (m, 4H), 4.21 – 4.10 (m, 12H), 4.02 – 3.95 (m, 4H), 3.82 – 3.77 (m, 4H), 3.76 – 3.59 (m, 24H), 3.57 – 3.53 (m, 4H), 3.51 – 3.45 (m, 4H), 3.40 – 3.35 (br s, 6H), 3.33 – 3.27 (br s, 6H), 1.78 – 1.65 (m, 8H), 1.51 – 1.39 (m, 8H). GPC (chloroform, 40 °C): M_n=20.2 kDa, M_w=54.0 kDa.

5.2 Synthetic procedures for Chapter 3

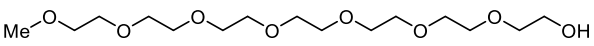
5.2.1 Synthesis of the linear side chains

*Triethylene Glycol Methyl Ether Tosylate (**3.2**)*[170]



Modifying the procedure of Tanaka et al.,[170] a solution of triethylene glycol monomethyl ether (6 mL, 37.5 mmol) in THF (40 mL) was added dropwise to a solution of KOH (4.2 g, 74.9 mmol) in distilled water (15 mL) at 0 °C. A solution of *p*-toluenesulfonyl chloride (7.9 g, 41.4 mmol) in THF (20 mL) was added dropwise to the mixture at 0 °C and the resulting suspension was stirred overnight at room temperature. The mixture was poured over an ice-water mixture and extracted thoroughly with dichloromethane (3 × 250 mL). The organic fractions were washed with water (3 × 250 mL) and dried over anhydrous $MgSO_4$. Removal of the solvent under reduced pressure afforded the product (11.2 g, 95%) as a pale yellow oil. The crude product was used in the next step without further purification. ^{1}H NMR (400 MHz, chloroform-*d*) δ 7.79 (d, J = 8.2 Hz, 2H), 7.34 (d, J = 8.2 Hz, 2H), 4.16 (t, J = 4.8 Hz, 2H), 3.70 – 3.66 (t, J = 4.8 Hz, 2H), 3.62 – 3.56 (m, 6H), 3.55 – 3.50 (m, 2H), 3.36 (s, 3H), 2.44 (s, 3H). ^{13}C NMR (100 MHz, chloroform-*d*) δ 145.1, 132.8, 130.8, 128.3, 72.2, 71.1, 70.9, 70.9, 69.6, 69.0, 59.4, 21.3.

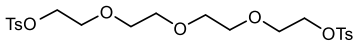
*Heptaethylene Glycol Monomethyl Ether (**3.3**)*[170]



Modifying the procedure of Tanaka et al.,[170] tetraethylene glycol (14.0 g, 72.1 mmol) was added in 3 portions to a mixture of sodium hydride (60% dispersion in mineral oil, 2.90 g, 72.5 mmol) in anhydrous THF (80 mL) at 0 °C and the mixture was heated to 55 °C until gas evolution stopped (*ca.* 1 h). The resulting mixture was allowed to reach room temperature and a solution of **3.2** (7.66 g, 24.1 mmol) in anhydrous THF (20 mL) was added dropwise. The

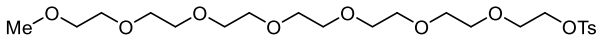
reaction mixture was heated under reflux overnight. After cooling to 0 °C, the mixture was quenched with methanol (10 mL) and diluted with chloroform (100 mL). The organic fractions were washed with distilled water (3 × 100 mL) and dried over anhydrous $MgSO_4$. The solvent was removed *in vacuo* and the crude oil was filtered through a plug of silica (chloroform, then chloroform: methanol, 90:10) to give the title product (4.92 g, 60%) as a colourless oil. ^{1}H NMR (400 MHz, chloroform-*d*) δ 3.74 – 3.70 (m, 2H), 3.68 – 3.58 (m, 24H), 3.56 – 3.52 (m, 2H), 3.37 (s, 3H). ^{13}C NMR (100 MHz, chloroform-*d*) δ 72.9, 72.3, 70.9 (multiple peaks), 70.7, 62.1, 59.4.

*Tetraethylene glycol di(p-toluenesulfonate) (**3.5**)*[211]



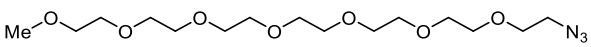
Modifying the procedure of Tanaka et al.,[170] a solution of tetraethylene glycol (18.9 g, 97.5 mmol) in THF (150 mL) was added dropwise to a solution of KOH (21.9 g, 390.3 mmol) in distilled water (60 mL) at 0 °C. A solution of *p*-toluenesulfonyl chloride (39.0 g, 204.8 mmol) in THF (100 mL) was added dropwise to the mixture at 0 °C and the resulting suspension was stirred overnight at room temperature. The mixture was poured over an ice-water mixture and extracted thoroughly with dichloromethane (3 × 400 mL). The organic fractions were washed with water (3 × 400 mL) and dried over anhydrous $MgSO_4$. Removal of the solvent under reduced pressure afforded the product (41.2 g, 84%) as a pale yellow oil. The crude product was used in the next step without further purification. ^{1}H NMR (400 MHz, chloroform-*d*) δ 7.76 (d, J = 8.3 Hz, 4H), 7.32 (d, J = 8.3 Hz, 4H), 4.16 – 4.10 (t, J = 4.8 Hz, 4H), 3.67 – 3.63 (m, 4H), 3.57 – 3.50 (m, 8H), 2.42 (s, 6H). ^{13}C NMR (100 MHz, chloroform-*d*) δ 145.1, 133.2, 130.1, 128.2, 70.9, 70.8, 69.5, 68.9, 21.9. HRMS (ES-ToF): 503.1395 [M+H$^+$] (calc. 503.1404).

*Heptaethylene Glycol Monomethyl Ether Tosylate (**3.6**)*[170]



Triethylene glycol monomethyl ether (5.6 mL, 35.0 mmol) was added dropwise to a solution of NaH (60% dispersion in mineral oil, 2.13 g, 53.3 mmol) in dry THF (50 mL) at 0 °C and the mixture was stirred for 1 h at 55 °C. After allowing to reach room temperature, a solution of **3.5** (17.6 g, 35.0 mmol) in dry THF (50 mL) was added and the resulting suspension was stirred at 80 °C overnight. The reaction mixture was subsequently cooled to 0 °C and slowly treated with isopropanol (20 mL), followed by the addition of water (50 mL). The mixture was extracted with dichloromethane and the combined organic phase was dried over anhydrous $MgSO_4$ and concentrated *in vacuo*. The crude product was purified by column chromatography (ethyl acetate, then ethyl acetate: methanol, 95:5) to give product **3.6** (5.5 g, 32%) as an yellow oil. ^{1}H NMR (400 MHz, chloroform-*d*) δ 7.82 – 7.76 (d, J = 8.3 Hz, 2H), 7.36 – 7.30 (d, J = 8.3 Hz, 2H), 4.17 – 4.13 (t, 4.8 Hz, 2H), 3.71 – 3.52 (m, 26H), 3.37 (s, 3H), 2.45 (s, 3H); ^{13}C NMR (100 MHz, chloroform-*d*) δ 145.0, 133.3, 130.1, 128.2, 72.2, 71.0 – 70.8 (multiple peaks), 69.5, 68.9, 59.3, 21.9.

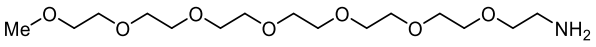
*22-Azido-2,5,8,11,14,17,20-heptaoxadocosane (**3.7**)*[212]



According to modified procedures of Dreaden et al.[213] and Wandrey et al.,[214] sodium azide (0.52 g, 8.00 mmol) was added in one portion to a solution of **3.6** (2.62 g, 5.30 mmol) in dry DMF (20 mL). The mixture was stirred for 2 h at 100 °C and allowed to reach room temperature overnight. After diluting with ethyl acetate (30 mL), the resulting precipitate was filtered. The solvent was removed *in vacuo* and the crude mixture was subsequently filtered through a silica plug, eluting with ethyl acetate. Removal of solvent under reduced pressure afforded product **3.7** (1.73 g, 89%) as a yellow oil, which was used in the next step without

further purification: ^{1}H NMR (400 MHz, chloroform-*d*) δ 3.69 – 3.61 (m, 24H), 3.56 – 3.52 (m, 2H), 3.38 (m, 2H), 3.37 (s, 3H); ^{13}C NMR (100 MHz, chloroform-*d*) δ 72.3, 71.1 – 70.8 (multiple peaks), 70.4, 59.4, 51.0. HRMS (ES-ToF): 366.2252 [M+H^{+}] (calc. 366.2240).

*2,5,8,11,14,17,20-Heptaoxadocosan-22-amine (**3.8**)*[212]



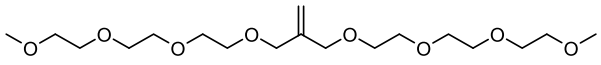
Adapting the method of Wandrey et al.,[214] PPh_3 (1.83 g, 6.98 mmol) was added in small portions to a solution of **3.7** (1.7 g, 4.65 mmol) in dry THF (30 mL) at 0 °C. After stirring for 4 h at room temperature, the reaction mixture was heated to 50 °C for 1 h. The resulting mixture was allowed to reach room temperature and quenched with water (0.3 mL). After stirring at room temperature overnight, the solvent was removed under reduced pressure and water was added (100 mL). The aqueous portion was washed with Et_2O (3 × 50 mL) and the solvent was removed *in vacuo* to give the title compound (1.29 g, 82%) as a yellow oil. The crude product was used in the next step without further purification. ^{1}H NMR (400 MHz, chloroform-*d*) δ 3.74 – 3.57 (m, 24H), 3.54 (m, 2H), 3.50 (m, 2H), 3.37 (s, 3H), 2.86 (t, J = 5.2 Hz, 2H); ^{13}C NMR (100 MHz, chloroform-*d*) δ 73.8, 72.3, 71.1 – 70.8 (multiple peaks), 70.4, 59.4, 51.0. HRMS (ES-ToF): 340.2347 [M+H^{+}] (calc. 340.2335).

5.2.2 Synthesis of the branched side chains

General procedure for the synthesis of the branched olefins. Modifying the method of Wu et al.,[171] the appropriate ethylene glycol monomethyl ether (3 equiv) was added dropwise to a suspension of sodium hydride (60% dispersion in mineral oil, 3.4 equiv) in anhydrous THF (2 mL/mmol) at 0 °C. When gas evolution ceased, methallyl dichloride (1 equiv) was added dropwise and the resulting mixture was stirred for 15 min at 0 °C. The mixture was allowed to reach room temperature and subsequently heated to 65 °C overnight. After cooling to 0 °C, the reaction mixture was quenched with distilled water (1.5 mL/mmol) to quench excess sodium

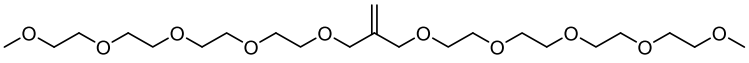
hydride and extracted with dichloromethane. The organic fractions were washed with distilled water, dried over anhydrous $MgSO_4$ and the solvent was removed *in vacuo*.

*13-Methylene-2,5,8,11,15,18,21,24-octaoxapentacosane (**3.9**)*[171]



Using the general procedure with triethylene glycol monomethyl ether (15.8 g, 96 mmol) and methallyl chloride (4.0 g, 32 mmol), the title product (12.0 g, 95%) was isolated as a pale yellow oil after column chromatography (ethyl acetate: hexane, 1:1). ^{1}H NMR (400 MHz, chloroform-*d*) δ 5.18 (br s, 2H), 4.02 (br s, 4H), 3.67 – 3.53 (m, 24H), 3.38 (s, 6H). ^{13}C NMR (100 MHz, chloroform-*d*) δ 142.6, 114.2, 72.1, 71.9, 70.8 – 70.7 (multiple peaks), 69.6, 59.2. HRMS (ES-ToF): 403.2295 [M+Na^+] (calc. 403.2308).

*16-Methylene-2,5,8,11,14,18,21,24,27,30-decaoxahentriacontane (**3.10**)*[215]

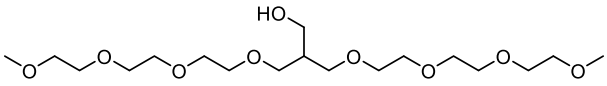


Using the general procedure with tetraethylene glycol monomethyl ether (20.9 g, 100.4 mmol) and methallyl chloride (4.18 g, 33.5 mmol), the title product (14.32 g, 91%) was isolated as a pale yellow oil after column chromatography (ethyl acetate: hexane, 3:2). ^{1}H NMR (400 MHz, chloroform-*d*) δ 5.17 (br s, 2H), 4.02 (br s, 4H), 3.68 – 3.51 (m, 32H), 3.37 (s, 6H). ^{13}C NMR (100 MHz, chloroform-*d*) δ 142.8, 114.4, 72.2, 72.1, 71.0, 70.9 – 70.8 (multiple peaks), 69.8, 59.4. HRMS (ES-ToF): 491.2817 [M+Na^+] (calc. 491.2827).

General procedure for the hydroboration-oxidation of the branched olefins. Borane tetrahydrofuran complex solution (1 M, 1.05 equiv) was added dropwise to a solution of the appropriate methylene precursor (1 equiv) in anhydrous THF (4 mL/mmol) at 0 °C. After stirring for 2 h at 0 °C, an aqueous solution of sodium hydroxide (2 M, 1 mL/mmol) was added dropwise and the mixture was stirred for a further 15 min at 0 °C. The mixture was slowly treated with H_2O_2 (30%, 1 mL/mmol) at 0 °C and allowed to reach room temperature and stirred

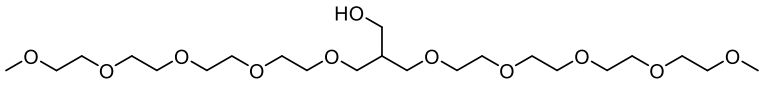
for 30 min. The reaction mixture was saturated with potassium carbonate and extracted with DCM. The organic fractions were washed with distilled water and dried over anhydrous $MgSO_4$. The solvent was removed *in vacuo* and the crude product was purified using column chromatography.

*13-(2,5,8,11-Tetraoxadodec-1-yl)-2,5,8,11-tetraoxatetradecan-14-ol (**3.11**)*[171]



Using the general procedure with **3.9** (4.91 g, 12.90 mmol), the title product (3.81 g, 74%) was isolated as a colourless oil after column chromatography (ethyl acetate). ^{1}H NMR (400 MHz, chloroform-*d*) δ 3.74 (d, J = 5.6 Hz, 2H), 3.65 – 3.53 (m, 28H), 3.37 (s, 6H), 2.17 – 2.08 (hept, J = 5.6 Hz, 1H). ^{13}C NMR (100 MHz, chloroform-*d*) δ 72.1, 71.1, 70.8 – 70.7 (multiple peaks), 70.6, 63.8, 59.3, 41.3. HRMS (ES-ToF): 421.2410 [M+Na$^+$] (calc. 421.2414).

*16-(2,5,8,11,14-Pentaoxapentadec-1-yl)-2,5,8,11,14-pentaoxaheptadecan-17-ol (**3.12**)*[215]

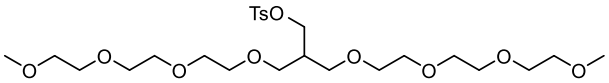


Using the general procedure with **3.10** (4.90 g, 10.46 mmol), the title product (3.81 g, 68%) was isolated as a colourless oil after column chromatography (ethyl acetate, then ethyl acetate: methanol, 90:10). ^{1}H NMR (400 MHz, chloroform-*d*) δ 3.71 (d, J = 5.6 Hz, 2H), 3.66 – 3.50 (m, 36H), 3.35 (s, 6H), 2.10 (hept, J = 5.6 Hz, 1H). ^{13}C NMR (100 MHz, chloroform-*d*) δ 72.2, 71.1, 70.9 (multiple peaks), 70.8, 63.6, 59.3, 41.5. HRMS (ES-ToF): 487.3115 [M+H$^+$] (calc. 487.3113).

General procedure for the tosylation of branched alcohols. The appropriate alcohol (1 equiv) was added dropwise to a solution of sodium hydroxide (6 equiv) in a mixture of distilled water and tetrahydrofuran (1:1 v/v, 1.2 mL/mmol) at 0 ^{o}C. The reaction mixture was slowly treated with a solution of *p*-toluenesulfonyl chloride (1.3 equiv) in THF (6 mL/mmol) and

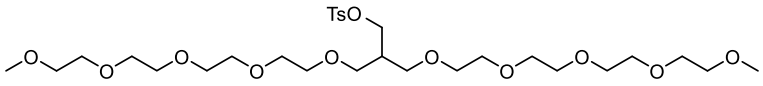
stirred for 2 h at 0 °C. The resulting suspension was stirred overnight at room temperature. The mixture was quenched with an aqueous HCl solution (2 M, 10 mL/mmol) and extracted with chloroform. The organic layers were washed with distilled water, dried over anhydrous $MgSO_4$ and concentrated *in vacuo*.

*2,5,8,11-Tetraoxatetradecan-14-ol, 13-(2,5,8,11-tetraoxadodec-1-yl)-, 14-(4-methylbenzene sulfonate) (**3.13**)*[171]



Using the general procedure with **3.11** (0.99 g, 2.49 mmol), the title product (0.84 g, 61%) was isolated as a pale yellow after column chromatography (ethyl acetate, then ethyl acetate: methanol, 90:10). ^{1}H NMR (400 MHz, chloroform-*d*) δ 7.82 – 7.73 (d, J = 8.3 Hz, 2H), 7.37 – 7.31 (d, J = 8.3 Hz, 2H), 4.11 (d, J = 5.5 Hz, 2H), 3.66 – 3.39 (m, 28H), 3.37 (s, 6H), 2.45 (s, 3H), 2.24 (hept, J = 5.5 Hz, 1H). ^{13}C NMR (100 MHz, chloroform-*d*) δ 145.0, 133.3, 130.0, 128.1, 72.1, 70.8 – 70.7 (multiple peaks), 70.5, 68.8, 68.5, 59.2, 39.6, 21.8. HRMS (ES-ToF): 553.2699 [M+H$^+$] (calc. 553.2683).

*2,5,8,11,14-Pentaoxaheptadecan-17-ol, 16-(2,5,8,11,14-pentaoxapentadec-1-yl)-, 17-(4-methyl benzenesulfonate) (**3.14**)*[215]

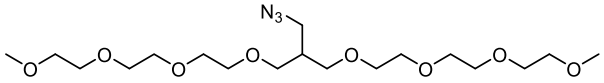


Using the general procedure with **3.12** (8.04 g, 16.52 mmol), the title product (4.15 g, 40%) was isolated as a pale yellow after column chromatography (ethyl acetate, then ethyl acetate: methanol, 90:10). ^{1}H NMR (400 MHz, chloroform-*d*) δ 7.78 (d, J = 8.3 Hz, 2H), 7.34 (d, J = 8.3 Hz, 2H), 4.11 (d, J = 5.5 Hz, 2H), 3.68 – 3.41 (m, 36H), 3.37 (s, 6H), 2.45 (s, 3H), 2.24 (hept, J = 5.5 Hz, 1H). ^{13}C NMR (100 MHz, chloroform-*d*) δ 145.0, 133.2, 130.1, 128.2, 72.1,

70.8 – 70.7 (multiple peaks), 70.6, 68.9, 68.6, 59.3, 39.8, 21.9. HRMS (ES-ToF): 641.3215 [M+H$^+$] (calc. 641.3207).

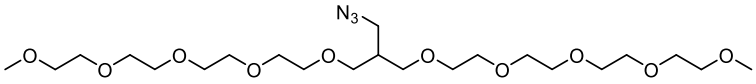
General procedure for the conversion into branched azides. Sodium azide (2.7 equiv) was added in one portion to a solution of the appropriate tosylate (1 equiv) in anhydrous DMF (10 mL/mmol). The mixture was stirred for 2 h at 100 ^{o}C and allowed to reach room temperature overnight. The mixture was diluted with ethyl acetate (70 mL/mmol) and the resulting precipitate was removed by filtration. The solvent was removed *in vacuo* and the crude mixture was filtered through a silica plug (ethyl acetate).

*13-(Azidomethyl)-2,5,8,11,15,18,21,24-octaoxapentacosane (**3.15**)*[171]



Using the general procedure with **3.13** (1.40 g, 2.87 mmol) the title product (0.99 g, 82%) was isolated as a brown oil. ^{1}H NMR (400 MHz, chloroform-*d*) δ 3.66 – 3.42 (m, 30H), 3.38 (s, 6H), 2.17 (hept, J = 6.3 Hz, 1H); ^{13}C NMR (100 MHz, chloroform-*d*) δ 72.1, 70.8 (multiple peaks), 70.7, 70.6, 67.9, 59.2, 50.4, 39.5. HRMS (ES-ToF): 446.2468 [M+Na$^+$] (calc. 446.2478).

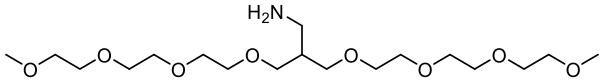
*16-(Azidomethyl)-2,5,8,11,14,18,21,24,27,30-decaoxahentriacontane (**3.16**)*



Using the general procedure with **3.14** (0.86 g, 1.37 mmol), the title product (0.59 g, 84%) was isolated as a brown oil. ^{1}H NMR (400 MHz, chloroform-*d*) δ 3.71 – 3.44 (m, 38H), 3.38 (s, 6H), 2.16 (hept, J = 6.3 Hz, 1H). ^{13}C NMR (100 MHz, chloroform-*d*) δ 73.0, 71.0 (multiple peaks), 70.9, 70.8, 69.3, 59.4, 50.6, 42.4. HRMS (ES-ToF): 534.2990 [M+Na$^+$] (calc. 534.3003).

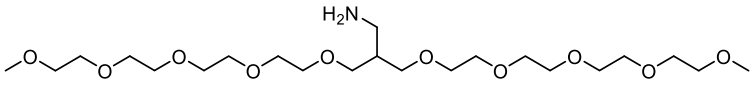
General procedure for the Staudinger reduction of the branched azides. Triphenyl phosphine (2.6 equiv) was added in small portions to a solution of the appropriate azide (1 equiv) in anhydrous THF (7 mL/mmol) at 0 °C. The mixture was allowed to reach room temperature and stirred for 6 h. The mixture was then heated to 50 °C for 1 h. After cooling to room temperature, the reaction mixture was quenched with distilled water (0.1 mL/mmol) and stirred overnight at room temperature. The solvent was removed *in vacuo* and the crude residue was suspended in distilled water (45 mL/mmol). The aqueous portion was thoroughly washed with diethyl ether and concentrated under reduced pressure.

*2-(2,5,8,11-tetraoxadodec-1-yl)-4,7,10,13-tetraoxatetradecan-1-amine (**3.17**)*[171]



Using the general procedure with **3.15** (0.95 g, 2.24 mmol), the title product (0.83 g, 88%) was isolated as a pale yellow oil. The crude product was used in the next step without further purification. ^{1}H NMR (400 MHz, chloroform-*d*) δ 3.66 – 3.43 (m, 28H), 3.38 (s, 6H), 2.79 (d, J = 6.0 Hz, 2H), 1.98 (hept, J = 6.0 Hz, 1H), 1.65 (s, 2H); ^{13}C NMR (100 MHz, chloroform-*d*) δ 72.1, 71.1, 70.8 (multiple peaks), 70.6, 59.2, 42.3, 42.1; HRMS (ES-ToF): 398.2766 [M+H^{+}] (calc. 398.2754).

*2-(2,5,8,11,14- Pentaoxapentadec -1-yl)-4,7,10,13,16-pentaoxaheptadecan-1-amine (**3.18**)*



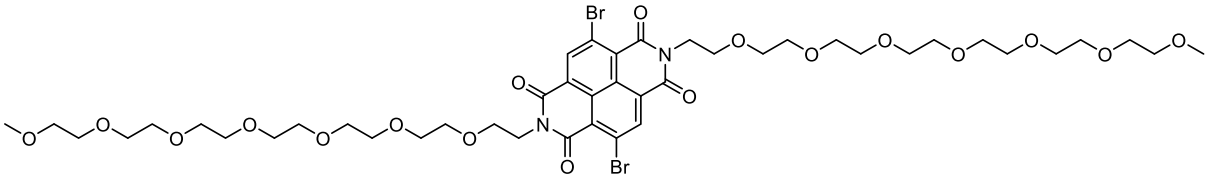
Using the general procedure with **3.16** (0.40 g, 0.78 mmol), the title product (0.31 g, 82%) was isolated as a pale yellow oil. The crude product was used in the next step without further purification. ^{1}H NMR (400 MHz, chloroform-*d*) δ 3.68 – 3.49 (m, 36H), 3.38 (s, 6H), 2.79 (d, J = 6.0 Hz, 2H), 2.25 (hept, J = 6.0 Hz, 1H). ^{3}C NMR (100 MHz, chloroform-*d*) δ 72.3, 71.2,

70.9 (multiple peaks), 70.8, 59.4, 42.5, 42.3. HRMS (ES-ToF): 486.3278 [M+H$^+$] (calc. 486.6230).

5.2.3 Synthesis of the NDI monomers

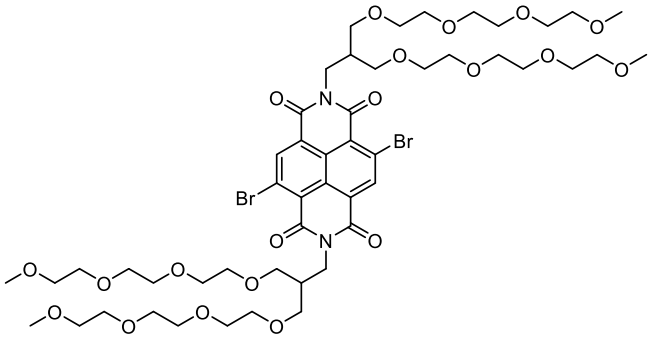
General procedure for the synthesis of the NDI monomers. A suspension of 2,6-dibromonaphthalene-1,4,5,8-tetracarboxydianhydride (1 equiv) and anhydrous zinc acetate (2 equiv) in anhydrous *o*-xylene (*ca.* 30 mL/mmol) was heated to 80 °C. The appropriate amine (2.2 equiv) was added dropwise. After heating to 130 °C for 2 h, the reaction mixture was diluted with chloroform and washed with water. The aqueous layer was further extracted with chloroform and the combined organic portions were washed with water and dried over anhydrous $MgSO_4$. The solvent was removed *in vacuo* and the resulting red residues were purified by column chromatography.

*4,9-dibromo-2,7-di(2,5,8,11,14,17,20-heptaoxadocosan-22-yl)benzo[lmn][3,8]phenanthroline-1,3,6,8(2H,7H)-tetraone (**3.19**)*



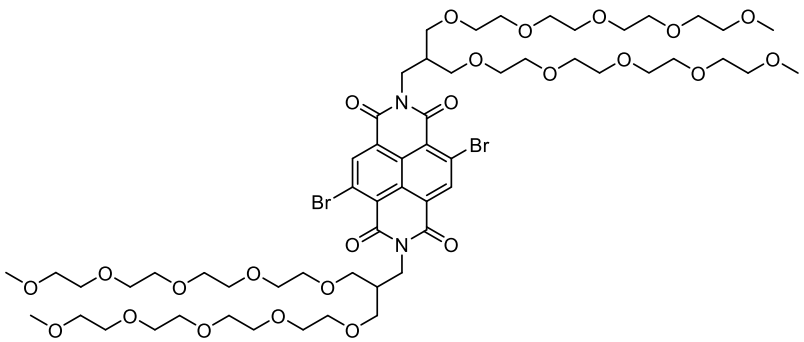
Using the general procedure with amine **3.8** (0.90 g, 2.65 mmol) and 2,6-dibromonaphthalene-1,4,5,8-tetracarboxydianhydride (0.51 g, 1.20 mmol) the title product (0.46 g, 36%) was isolated as a yellow solid after column chromatography (ethyl acetate, then ethyl acetate: methanol, 90:10) and recrystallisation from ethyl acetate. ^{1}H NMR (400 MHz, $CDCl_3$) δ 8.98 (s, 2H), 4.46 (t, J = 5.8 Hz, 4H), 3.84 (t, J = 5.8 Hz, 4H), 3.73 – 3.51 (m, 48H), 3.37 (s, 6H). ^{13}C NMR (100 MHz, $CDCl_3$) δ 161.2, 161.1, 139.4, 128.7, 128.2, 125.7, 124.5, 72.3, 70.9 (multiple peaks), 70.4, 67.9, 59.37, 40.4. HRMS (ES-ToF): 1067.2562 [M+H$^+$] (calc. 1067.2599).

*2,7-bis(13-(2,5,8,11-tetraoxadodecyl)-2,5,8,11-tetraoxatetradecan-14-yl)-4,9-dibromo-benzo[lmn][3,8]phenanthroline-1,3,6,8(2H,7H)-tetraone (**3.20**)*[159]



Using the general procedure with amine **3.17** (0.84 g, 2.11 mmol) and 2,6-dibromonaphthalene-1,4,5,8-tetracarboxydianhydride (0.41 g, 0.96 mmol), the title product (0.42 g, 37%) was isolated as a waxy yellow solid after column chromatography (ethyl acetate, then ethyl acetate: methanol, 90:10) and preparative gel permeation chromatography in chloroform . ^{1}H NMR (400 MHz, chloroform-*d*) δ 8.97 (s, 2H), 4.32 (d, J = 6.2 Hz, 4H), 3.65 – 3.43 (m, 56H), 3.36 (s, 12H), 2.56 – 2.50 (hept, J = 6.2 Hz, 2H). ^{13}C NMR (100 MHz, chloroform-*d*) δ 161.4, 161.3, 139.3, 128.5, 128.1, 125.7, 124.4, 72.2, 71.3, 70.9 – 70.8 (multiple peaks), 70.7, 59.4, 42.2, 38.6. HRMS (ES-ToF): 1183.3452 [M+H^{+}] (calc. 1183.3436).

*2,7-bis(16-(2,5,8,11,14-pentaoxapentadecyl)-2,5,8,11,14-pentaoxaheptadecan-17-yl)-4,9-dibromobenzo[lmn][3,8]phenanthroline-1,3,6,8(2H,7H)-tetraone (**3.21**)*

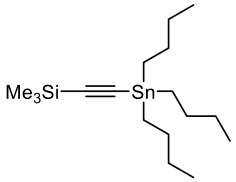


Using the general procedure with amine **3.18** (0.25 g, 0.51 mmol) and 2,6-dibromonaphthalene-1,4,5,8-tetracarboxydianhydride (0.10 g, 0.23 mmol), the title product (85 mg, 27%) was isolated as a waxy yellow solid after column chromatography (ethyl acetate, then ethyl acetate:

methanol, 90:10) and preparative gel permeation chromatography in chloroform. ^{1}H NMR (400 MHz, chloroform-*d*) δ 8.97 (s, 2H), 4.32 (d, J = 6.2 Hz, 4H), 3.66 – 3.46 (m, 72H), 3.37 (s, 12H), 2.52 (hept, J = 6.2 Hz, 2H). ^{13}C NMR (100 MHz, chloroform-*d*) δ 161.4, 161.3, 139.3, 128.5, 128.0, 125.7, 124.4, 72.2, 71.3, 70.9 – 70.8 (multiple peaks), 70.7, 59.4, 42.2, 38.6. HRMS (ES-ToF): 1361.4431 (calc. 1361.4459).

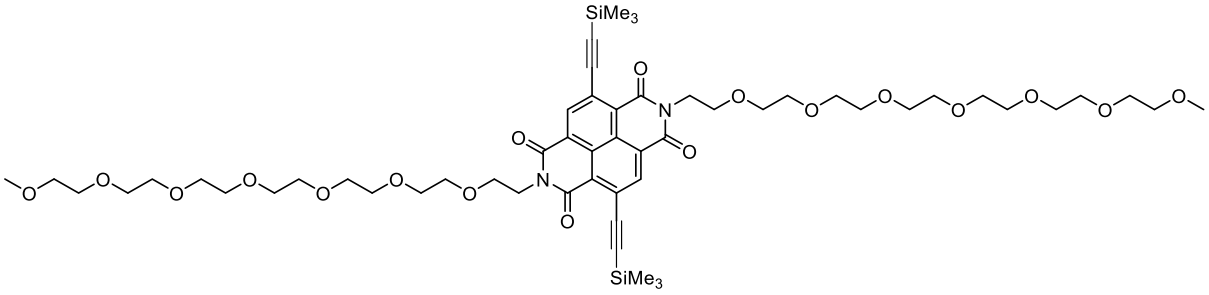
5.2.4 Synthesis of the NDTI monomers

*Tributyl(trimethylsilylethynyl)tin (**3.26**)*[216]



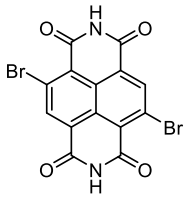
Following the procedure reported by Meana et al.,[216] *n*-BuLi (1.6 M in hexane, 1.26 mL, 2.02 mmol) was added dropwise to a solution of trimethylsilylacetylene (0.25 mL, 1.80 mmol) in anhydrous Et_2O (3.5 mL) at –78 °C. The reaction mixture was allowed to warm to 0 °C over 1 h. After cooling to –78 °C, tributyltinchloride (0.55 mL, 2.02 mmol) was added dropwise and the resulting mixture was allowed to reach room temperature overnight. The mixture was quenched with a saturated aqueous NH_4Cl solution (10 mL) and extracted with diethyl ether (3 × 20 mL). The combined organic layers were washed with distilled water and dried over anhydrous Na_2SO_4. Removal of the solvent *in vacuo* afforded the crude product (0.70 g, 98%) as a colourless oil. The crude product was used in the next step without further purification. ^{1}H NMR (400 MHz, chloroform-*d*) δ 1.60 – 1.51 (m, 6H), 1.38 – 1.31 (m, 6H), 1.06 – 0.94 (m, 6H), 0.90 (t, J = 7.3 Hz, 9H), 0.16 (s, 9H).

*2,7-di(2,5,8,11,14,17,20-heptaoxadocosan-22-yl)-4,9-bis((trimethylsilyl)ethynyl)benzo [lmn][3,8]phenanthroline-1,3,6,8(2H,7H)-tetraone (**3.27**)*



Tetrakis(triphenyl phosphine)palladium(0) (2.36 mg, 2.04 μmol) was added to a solution of **3.26** (30.00 mg, 77.47 μmol) and **3.19** (40.26 mg, 37.7 μmol) in anhydrous, degassed toluene (3.00 mL) under argon counterflow. The mixture was stirred overnight at 120 °C and after cooling, the solvent was removed *in vacuo*. The resulting brown residue was dissolved in acetonitrile (10 mL) and thoroughly washed with hexane (3 × 5 mL) in order to remove tin by-products. The acetonitrile portion was concentrated under reduced pressure and subjected to column chromatography (ethyl acetate, then ethyl acetate: methanol, 95:5) to give the desired product (35.30 mg, 85%) as a yellow waxy solid. ^{1}H NMR (400 MHz, chloroform-*d*) δ 8.78 (s, 2H), 4.44 (t, J = 6.0 Hz, 4H), 3.82 (t, J = 6.0 Hz, 4H), 3.75 – 3.50 (m, 48H), 3.37 (s, 6H), 0.36 (s, 18H). ^{13}C NMR (100 MHz, $CDCl_3$) δ 162.2, 161.5, 138.1, 127.3, 126.7, 126.5, 125.5, 111.1, 103.5, 72.3, 70.9 (multiple peaks), 68.0, 59.4, 39.8, 1.4. HRMS (ES-ToF): 1125.4988 [M+Na^+] (calc. 1125.4999).

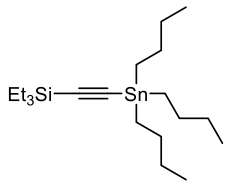
*2,6-dibromo-1,4,5,8-tetracarboxynaphthalenediimide (**3.29**)*[175]



Following the procedure reported by Dawson et al.,[175] a suspension of 2,6-dibromonaphthalene-1,4,5,8-tetracarboxydianhydride (5.0 g, 11.7 mmol) and ammonium

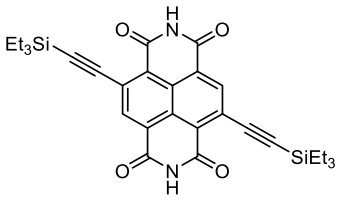
acetate (18.1 g, 235 mmol) in glacial acetic acid (100 mL) was heated under reflux for 2 h. After cooling to room temperature, the precipitate was collected by filtration and washed with acetic acid and methanol to afford the title product (4.79 g, 97%) as an orange solid: ^{1}H NMR (400 MHz, DMSO-d_6) δ 12.28 (br s, 2H), 8.65 (s, 2H); HRMS (ES-ToF): 420.8465 [M-H^{+}] (calc. 420.8640).

*Tributyl(triethylsilylethynyl)tin (**3.30**)*[217]



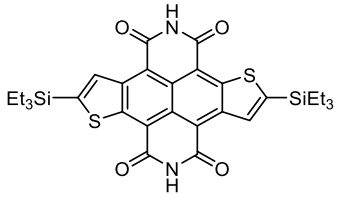
Following the procedure reported by Kinashi et al.,[217] *n*-BuLi (2.5 M in hexane, 10.3 mL, 25.8 mmol) was added dropwise to a solution of triethylsilylacetylene (4.4 mL, 24.6 mmol) in anhydrous THF (100 mL) at –78 °C. The reaction mixture was stirred for 1 h at –78 °C. Tributyltinchloride (6.7 mL, 24.6 mmol) was added dropwise and the resulting mixture was allowed to reach room temperature overnight. The mixture was quenched with a saturated aqueous NH_4Cl solution (20 mL) and extracted with hexane (3 × 200 mL). The combined organic layers were washed with distilled water, brine and dried over anhydrous Na_2SO_4. Removal of the solvent *in vacuo* afforded the crude product (9.97 g, 94%) as a colourless oil. The crude product was used in the next step without further purification. ^{1}H NMR (400 MHz, chloroform-*d*) δ 1.65 – 1.49 (m, 6H), 1.38 – 1.29 (m, 6H), 1.09 – 0.91 (m, 15H), 0.89 (t, J = 7.3 Hz, 9H), 0.58 (q, J = 7.3 Hz, 6H). ^{13}C NMR (100 MHz, chloroform-*d*) δ 117.1, 114.3, 28.9, 26.9, 14.4, 11.2, 7.5, 4.6.

*2,6-Bis(triethylsilylethynyl)-1,4,5,8-naphthalene tetracarboxylic acid diimide (**3.31**)*[28]



Modifying the method of Nakano et al.,[28] bis(triphenylphosphine)palladium (II) dichloride (0.31 g, 0.45 mmol) was added to a solution of **3.30** (8.46 g, 19.71 mmol) and **3.29** (3.80 g, 8.96 mmol) in anhydrous, degassed toluene (120 mL). The mixture was stirred overnight at 120 °C under an argon atmosphere and after cooling, the solvent was removed *in vacuo*. Recrystallisation from tetrahydrofuran-methanol afforded the title compound (4.54 g, 93%) as a yellow solid: ^{1}H NMR (400 MHz, DMSO-d_6) δ 12.12 (br s, 2H), 8.40 (s, 2H), 1.09 (t, J = 7.9 Hz, 18H), 0.74 (q, J = 7.9 Hz, 12H). HRMS (ES-ToF): 541.1987 [M-H$^+$] (calc. 541.1979).

*2,7-Bis(triethylsilyl)naphtho[2,3-b:6,7-b']dithiophene-4,5,9,10-tetracarboxylic acid diimide (**3.32**)*[28]

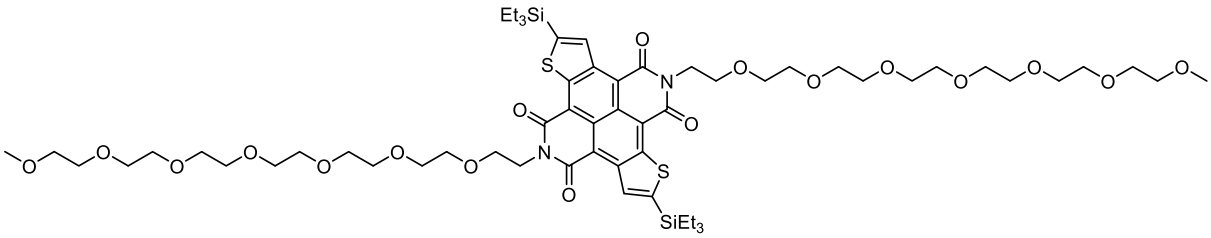


Modifying the procedure of Nakano et al.,[28] sodium sulfide nonahydrate (3.72 g, 15.49 mmol) was added in small portions to a suspension of **3.31** (1.40 g, 2.58 mmol) in anhydrous, degassed 2-methoxyethanol (250 mL) and acetic acid (8.7 mL) at 0 °C. The suspension was allowed to reach room temperature and stirred overnight under nitrogen. The mixture was then exposed to atmospheric conditions and compressed air was continuously bubbled into the stirred reaction mixture for 72 h at room temperature. A gradual colour change from brown to maroon was observed. The reaction mixture was cooled to 0 °C and poured over distilled water (200 mL). The resulting precipitate was collected under vacuum and thoroughly washed with

distilled water and methanol. The solid was suspended in hot chloroform (60 mL) and the insoluble residues were removed by filtration. The filtrate was concentrated under reduced pressure and the resulting solid was recrystallised two times from chloroform-methanol to give the title product (0.35 g, 22%) as a maroon solid. ^{1}H NMR (400 MHz, chloroform-*d*) δ 9.10 (s, 2H), 9.00 (s, 2H), 1.13 – 1.03 (m, 30H). ^{13}C NMR (100 MHz, chloroform-*d*) δ 163.3, 163.2, 158.2, 148.6, 143.7, 131.2, 124.5, 118.8, 116.9, 7.8, 4.4. HRMS (ES-ToF): 606.1509 (calc. 606.1499).

General procedure for the Mitsunobu reaction. Diethylazodicarboxylate (40 wt. % in toluene, 4 equiv) was added dropwise to a solution of **3.32** (1 equiv), appropriate alcohol (2.5 equiv) and triphenylphosphine (4 equiv) in degassed anhydrous THF (ca. 25 mL/mmol) at 0 °C. The solution was allowed to reach room temperature and stirred overnight. The solvent was removed under reduced pressure and the crude residues were subjected to column chromatography.

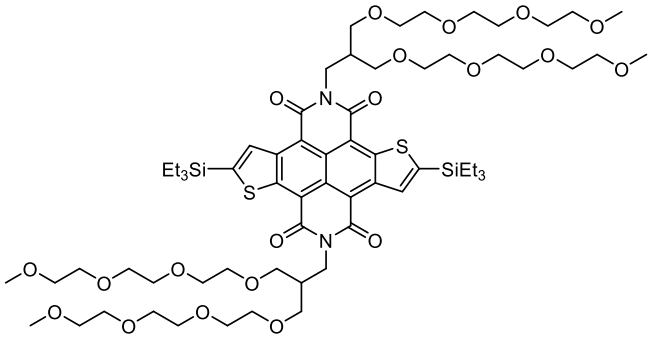
*2,8-di(2,5,8,11,14,17,20-heptaoxadocosan-22-yl)-5,11-bis(triethylsilyl)thieno[3',2':5,6] benzo[1,2,3,4-lmn]thieno[2,3-f][3,8]phenanthroline-1,3,7,9(2H,8H)-tetraone (**3.28**)*



Using the general procedure with **3.32** (250 mg, 0.41 mmol) and alcohol **3.3** (350 mg, 1.03 mmol), the title product (320 mg, 66%) was isolated as a maroon waxy solid after column chromatography (ethyl acetate, then ethyl acetate: methanol, 93:7) and preparative gel permeation chromatography in chloroform. ^{1}H NMR (400 MHz, chloroform-*d*) δ 9.15 (s, 2H), 4.63 (t, J = 6.2 Hz, 4H), 3.94 (t, J = 6.2 Hz, 4H), 3.76 – 3.72 (m, 4H), 3.68 – 3.50 (m, 44H), 3.36 (s, 6H), 1.14 – 1.08 (m, 18H), 1.06 – 0.99 (m, 12H). ^{13}C NMR (100 MHz, chloroform-*d*)

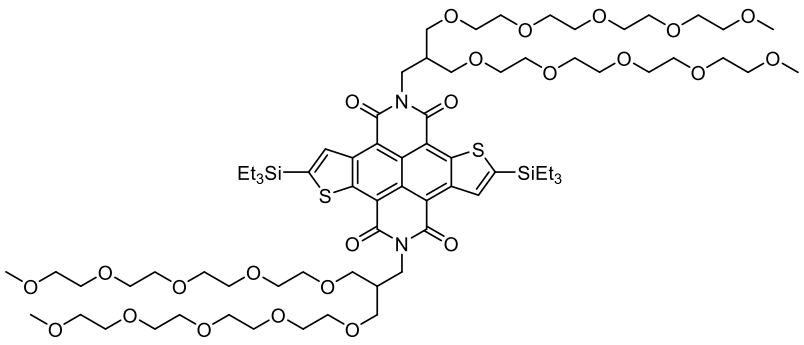
δ 163.9, 163.7, 157.2, 148.7, 144.4, 131.6, 123.0, 118.7, 117.5, 72.3, 70.9 (multiple peaks), 70.6, 68.2, 59.4, 40.2, 7.8, 4.4. HRMS (ES-ToF): 1251.5596 [M+H$^+$] (calc. 1251.5560).

*2,8-bis(13-(2,5,8,11-tetraoxadodecyl)-2,5,8,11-tetraoxatetradecan-14-yl)-5,11-bis(triethylsilyl)thieno[3',2':5,6]benzo[1,2,3,4-lmn]thieno[2,3-f][3,8]phenanthroline-1,3,7,9(2H,8H)-tetraone (**3.33**)*



Using the general procedure with **3.32** (170 mg, 0.27 mmol) and alcohol **3.11** (272 mg, 0.68 mmol), the title product (270 mg, 73%) was isolated as a maroon waxy solid after column chromatography (ethyl acetate, then ethyl acetate: methanol, 90:10). ^{1}H NMR (400 MHz, chloroform-*d*) δ 9.16 (s, 2H), 4.49 (d, J = 6.5 Hz, 4H), 3.73 – 3.39 (m, 56H), 3.33 (s, 12H), 2.70 (hept, J = 6.5 Hz, 2H), 1.17 – 1.06 (m, 18H), 1.06 – 0.97 (m, 12H). ^{13}C NMR (100 MHz, chloroform-*d*) δ 163.9, 163.7, 156.9, 148.6, 144.3, 131.7, 123.1, 118.9, 117.5, 72.3- 70.7 (multiple peaks), 59.3, 41.9, 38.8, 7.8, 4.4; HRMS (ES-ToF): 1367.6714 [M+H$^+$] (calc. 1367.6397).

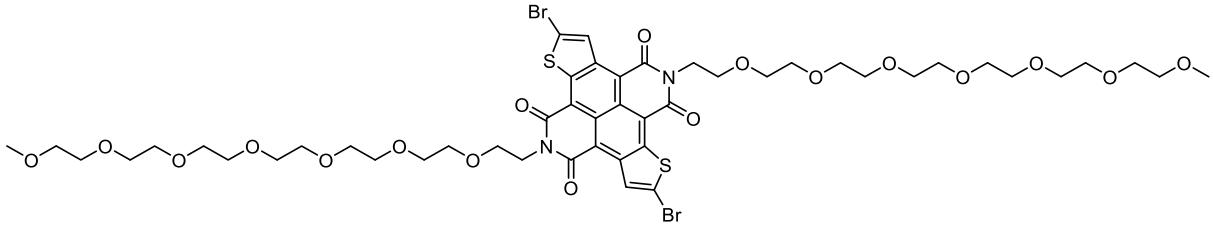
*2,8-bis(16-(2,5,8,11,14-pentaoxapentadecyl)-2,5,8,11,14-pentaoxaheptadecan-17-yl)-5,11-bis(triethylsilyl)thieno[3',2':5,6]benzo[1,2,3,4-lmn]thieno[2,3-f][3,8]phenanthroline-1,3,7,9(2H,8H)-tetraone (**3.34**)*



Using the general procedure with **3.32** (300 mg, 0.49 mmol) and alcohol **3.12** (600 mg, 1.23 mmol), the title product (690 mg, 90%) was isolated as a dark red viscous oil after column chromatography (ethyl acetate, then ethyl acetate: methanol, 90:10) and preparative gel permeation chromatography in chloroform. ^{1}H NMR (400 MHz, chloroform-*d*) δ 9.15 (s, 2H), 4.48 (d, J = 6.7 Hz, 4H), 3.65 – 3.45 (m, 72H), 3.34 (s, 12H), 2.69 (hept, J = 6.7 Hz, 2H), 1.18 – 0.94 (m, 30H). ^{13}C NMR (100 MHz, chloroform-*d*) δ 164.1, 163.9, 156.9, 148.6, 144.3, 131.7, 123.0, 118.8, 117.6, 72.2, 71.3, 70.9 – 70.8 (multiple peaks), 70.7, 59.3, 41.8, 38.8, 7.8, 4.4. HRMS (ES-ToF): 1543.7468 [M+H^{+}] (calc. 1543.7446).

General procedure for the bromination reaction. Bromine (5 equiv) was added to a solution of the appropriate triethylsilyl-functionalised NDTI (1 equiv) in degassed anhydrous DCM (ca. 40 mL/mmol) at 0 °C. The resulting solution was heated to 40 °C and stirred for 3 h. After cooling to room temperature, the solvent was removed under reduced pressure and the crude residues were subjected to column chromatography (ethyl acetate, then ethyl acetate: methanol, 90:10) and preparative gel permeating chromatography in chloroform.

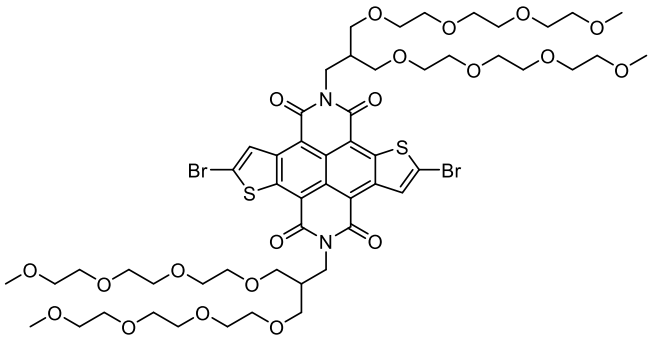
*5,11-dibromo-2,8-di(2,5,8,11,14,17,20-heptaoxadocosan-22-yl)thieno[3',2':5,6]benzo [1,2,3,4-lmn]thieno[2,3-f][3,8]phenanthroline-1,3,7,9(2H,8H)-tetraone (**3.35**)*



Using the general procedure with **3.28** (293 mg, 0.23 mmol), the title product (125 mg, 45%) was isolated as a maroon waxy solid. ^{1}H NMR (400 MHz, chloroform-*d*) δ) 9.05 (s, 2H), 4.58 (t, J = 5.9 Hz, 4H), 3.92 (t, J = 5.9 Hz, 4H), 3.73 (m, 4H), 3.65 – 3.52 (m, 44H), 3.37 (s, 6H). ^{13}C NMR (100 MHz, chloroform-*d*) δ 163.0, 162.7, 146.2, 142.2, 133.5, 126.9, 122.0, 117.5,

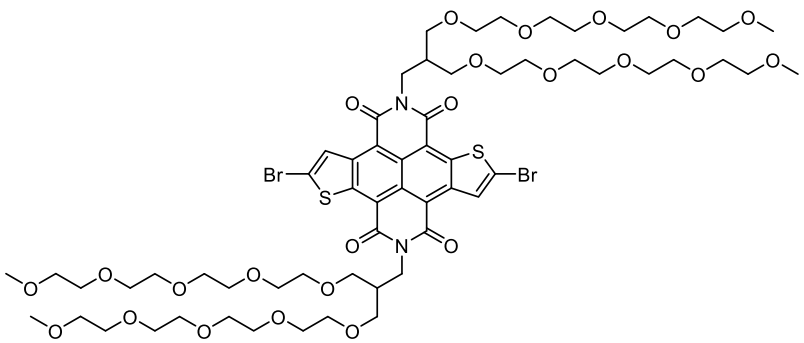
115.9, 72.3, 70.9, 70.9, 70.4, 68.0, 59.4, 40.2. HRMS (ES-ToF): 1203.1859 [M+Na^+] (calc. 1203.1840).

*2,8-bis(13-(2,5,8,11-tetraoxadodecyl)-2,5,8,11-tetraoxatetradecan-14-yl)-5,11-dibromo thieno[3',2':5,6]benzo[1,2,3,4-lmn]thieno[2,3-f][3,8]phenanthroline-1,3,7,9(2H,8H)-tetraone (**3.36**)*



Using the general procedure with **3.33** (270 mg, 0.20 mmol), the title product (100 mg, 40%) was isolated as a maroon waxy solid. ^{1}H NMR (400 MHz, chloroform-*d*) δ 9.05 (s, 2H), 4.43 (d, J = 6.7 Hz, 4H), 3.70 – 3.42 (m, 56H), 3.35 (s, 12H), 2.61 (hept, J = 6.7 Hz, 2H). ^{13}C NMR (100 MHz, $CDCl_3$) δ 163.8, 163.2, 146.4, 142.5, 133.6, 127.1, 121.8, 118.0, 116.4, 72.8, 72.2, 71.3, 70.9 – 70.8 (multiple peaks), 70.7, 59.4, 41.5, 38.3. HRMS (ES-ToF): 1317.2745 [M+Na^+] (calc. 1317.2697).

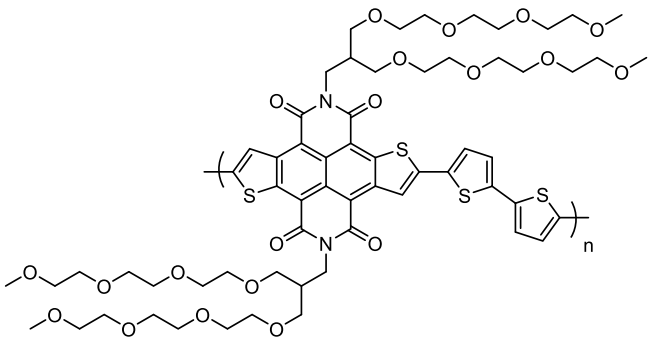
*2,8-bis(16-(2,5,8,11,14-pentaoxapentadecyl)-2,5,8,11,14-pentaoxaheptadecan-17-yl)-5,11-dibromothieno[3',2':5,6]benzo[1,2,3,4-lmn]thieno[2,3-f][3,8]phenanthroline-1,3,7,9(2H,8H)-tetraone (**3.37**)*



Using the general procedure with **3.34** (380 mg, 0.25 mmol), the title product (185 mg, 51%) was isolated as a dark red viscous oil. ^{1}H NMR (400 MHz, chloroform-*d*) δ 9.05 (s, 2H), 4.42 (d, J = 6.6 Hz, 4H), 3.70 – 3.40 (m, 72H), 3.35 (s, 12H), 2.60 (hept, J = 6.6 Hz, 2H). ^{13}C NMR (100 MHz, chloroform-*d*) δ 163.3, 163.0, 146.2, 142.3, 133.3, 127.0, 122.1, 117.8, 116.2, 72.2, 71.2, 70.8 – 70.6 (multiple peaks), 59.3, 41.8, 38.7. HRMS (ES-ToF): 1473.3893 [M+H^{+}] (calc. 1473.3900).

5.2.5 Synthesis of the polymers

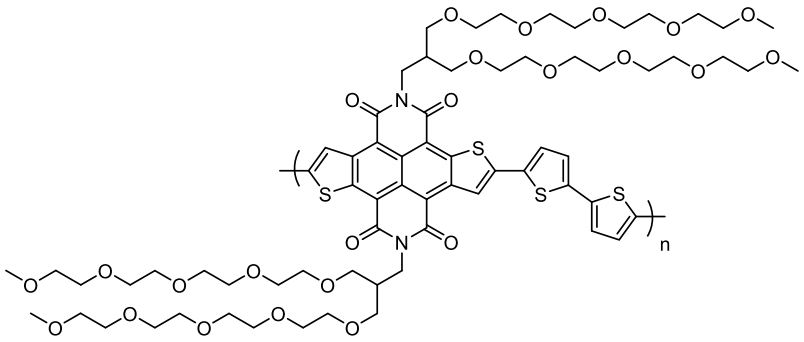
P3gNDTI



A mixture of **3.36** (27.03 mg, 21.0 µmol, 1.0 equiv), 5,5'-bis(trimethylstannyl)-2,2'-bithiophene (10.21 mg, 21.0 µmol, 1.0 equiv) , $Pd_2(dba)_3$ (0.38 mg, 0.42 µmol, 0.02 equiv) and P(*o*-tol)$_3$ (0.51 mg, 1.68 µmol, 0.08 equiv) in anhydrous, degassed DMF (1.5 mL) was degassed for 10 min and heated to 80 °C overnight. 0.1 mL of a solution of 2-(tributylstannyl)thiophene (0.1 mL) and $Pd_2(dba)_3$ (1.00 mg, 1.09 µmol) in anhydrous, degassed DMF (0.5 mL) were added and the resulting mixture was stirred for 1 h at 90 °C. 0.1 mL of a solution of 2-bromothiophene (0.1 mL) in anhydrous, degassed DMF (0.5 mL) were subsequently added and stirring at 90 °C was maintained for a further 1 h. The reaction mixture was cooled to room temperature and precipitated in ethyl acetate, followed by the addition of hexane. The solid was collected in a thimble and Soxhlet extraction was carried out with hexane, methanol, ethyl acetate, acetone and chloroform. The polymer was dissolved in hot chloroform and re-precipitated in ethyl

acetate, followed by the addition of hexane. Polymer **P3gNDTI** was obtained as a black green solid is a yield of 83% (22.6 mg, 17.36 μmol). ^{1}H NMR (500 MHz, 328 K, chloroform-*d*) δ 8.82 – 7.37 (broad), 4.57 – 4.53 (br s, 4H), 3.65 – 3.33 (m, 68H), 2.64 – 2.56 (br s, 2H). GPC (chloroform, 40 °C): M_n = 13.0 kDa, M_w = 20.4 kDa.

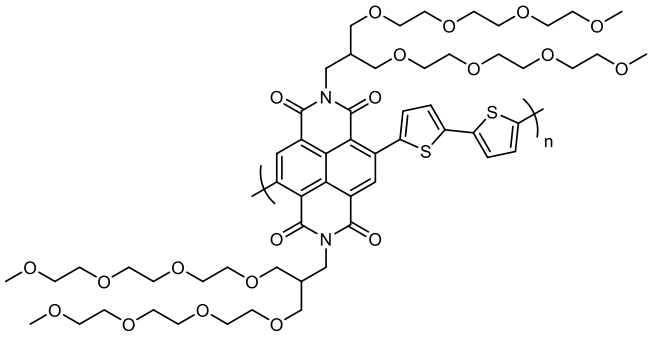
P4gNDTI



A mixture of **3.37** (71.75 mg, 48.70 μmol 1.0 equiv), 5,5'-bis(trimethylstannyl)-2,2'-bithiophene (23.95 mg, 48.70 μmol, 1.0 equiv) , $Pd_2(dba)_3$ (0.89 mg, 0.97 μmol, 0.02 equiv) and P(*o*-tol)$_3$ (1.18 mg, 3.89 μmol, 0.08 equiv) in anhydrous, degassed chlorobenzene (2.0 mL) was degassed for 10 min and heated to 135 °C overnight. 0.1 mL of a solution of 2-(tributylstannyl)thiophene (0.1 mL) and $Pd_2(dba)_3$ (1.00 mg, 1.09 μmol) in anhydrous, degassed chlorobenzene (0.5 mL) were added and the resulting mixture was stirred for 1 h at 135 °C. 0.1 mL of a solution of 2-bromothiophene (0.1 mL) in anhydrous, degassed chlorobenzene (0.5 mL) were subsequently added and stirring at 135 °C was maintained for a further 1 h. The reaction mixture was cooled to room temperature and precipitated in ethyl acetate, followed by the addition of hexane. The solid was collected in a thimble and Soxhlet extraction was carried out with hexane, methanol, ethyl acetate, acetone, THF and chloroform. The polymer was dissolved in hot chloroform and re-precipitated in ethyl acetate, followed by the addition of hexane. Polymer **P4gNDTI** was obtained as a black green solid is a yield of 58% (42 mg, 28.42 μmol). ^{1}H NMR (400 MHz, chloroform-*d*) δ 9.16 – 8.55 (broad), 4.57 –

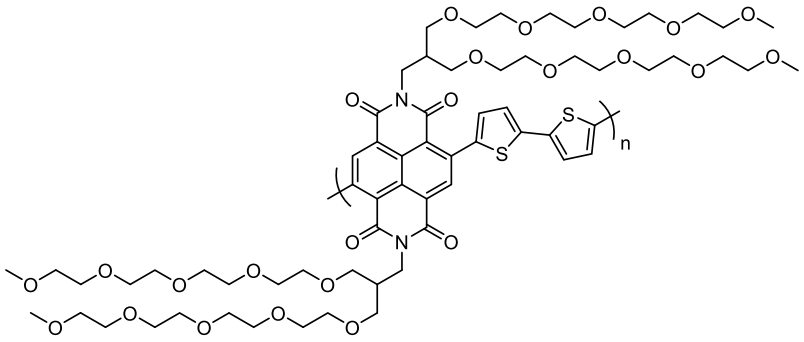
4.53 (br s), 3.92 – 3.31 (m), 2.78 – 2.51 (br s). GPC (chloroform, 40 °C): M_n = 59.4 kDa, M_w = 269.4 kDa.

P3gNDI[159]



A mixture of **3.20** (126.84 mg, 107.0 µmol, 1.0 equiv), 5,5'-bis(trimethylstannyl)-2,2'-bithiophene (52.65 mg, 107.0 µmol, 1.0 equiv) , $Pd_2(dba)_3$ (1.96 mg, 2.14 µmol, 0.02 equiv) and P(*o*-tol)$_3$ (2.61 mg, 8.56 µmol, 0.08 equiv) in anhydrous, degassed chlorobenzene (3.0 mL) was degassed for 10 min and heated to 135 °C overnight. 0.1 mL of a solution of 2-(tributylstannyl)thiophene (0.1 mL) and $Pd_2(dba)_3$ (1.00 mg, 1.09 µmol) in anhydrous, degassed chlorobenzene (0.5 mL) were added and the resulting mixture was stirred for 1 h at 135 °C. 0.1 mL of a solution of 2-bromothiophene (0.1 mL) in anhydrous, degassed chlorobenzene (0.5 mL) were subsequently added and stirring at 135 °C was maintained for a further 1 h. The reaction mixture was cooled to room temperature and precipitated in ethyl acetate, followed by the addition of hexane. The solid was collected in a thimble and Soxhlet extraction was carried out with hexane, methanol, ethyl acetate, acetone and chloroform. The polymer was dissolved in hot chloroform and re-precipitated in ethyl acetate, followed by the addition of hexane. Polymer **P3gNDI** was obtained as a deep blue solid is a yield of 88% (112.4 mg, 94.5 µmol). ^{1}H NMR (400 MHz, chloroform-*d*) δ 8.82 (br s, 2H), 7.37 (br s, 4H), 4.31 (br s, 4H), 3.62 – 3.49 (m, 56H), 3.35 (s, 12H), 2.56 (br s, 2H). GPC (chloroform, 40 °C): M_n = 40.7 kDa, M_w = 72.9 kDa.

P4gNDI

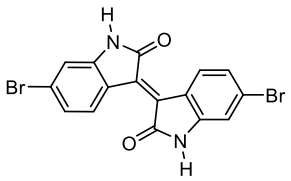


A mixture of **3.21** (49.62 mg, 36.45 µmol, 1.0 equiv), 5,5'-bis(trimethylstannyl)-2,2'-bithiophene (17.93 mg, 36.45 µmol, 1.0 equiv) , $Pd_2(dba)_3$ (0.67 mg, 0.73 µmol, 0.02 equiv) and P(*o*-tol)$_3$ (0.89 mg, 2.92 µmol, 0.08 equiv) in anhydrous, degassed chlorobenzene (1.5 mL) was degassed for 10 min and heated to 135 °C overnight. 0.1 mL of a solution of 2-(tributylstannyl)thiophene (0.1 mL) and $Pd_2(dba)_3$ (1.00 mg, 1.09 µmol) in anhydrous, degassed chlorobenzene (0.5 mL) were added and the resulting mixture was stirred for 1 h at 135 °C. 0.1 mL of a solution of 2-bromothiophene (0.1 mL) in anhydrous, degassed chlorobenzene (0.5 mL) were subsequently added and stirring at 135 °C was maintained for a further 1 h. The reaction mixture was cooled to room temperature and precipitated in a mixture of ethyl acetate: hexane (1:1, v/v). The solid was collected in a thimble and Soxhlet extraction was carried out with hexane and ethyl acetate. The polymer was dissolved in hot ethyl acetate and re-precipitated in ethyl acetate: hexane (1:1, v/v). Polymer **P4gNDI** was obtained as a deep blue solid is a yield of 48% (24 mg, 17.57 µmol). ^{1}H NMR (400 MHz, chloroform-*d*) δ 8.82 (br s, 2H), 7.40 (br s, 4H), 4.29 (br s, 4H), 3.66 – 3.47 (m, 72H), 3.35 (s, 12H), 2.56 (br s, 2H). GPC (chloroform, 40 °C): M_n = 22.0 kDa, M_w = 36.0 kDa.

5.3 Synthetic procedures for Chapter 4

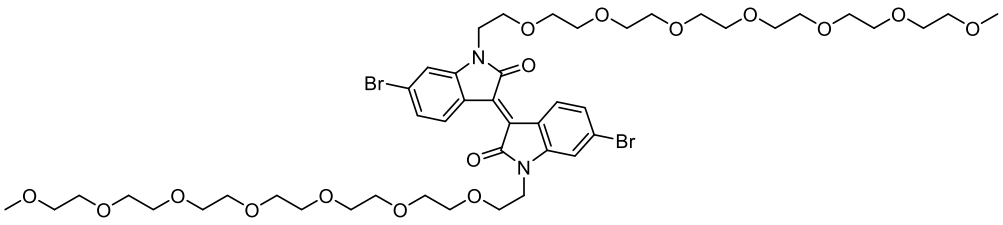
5.3.1 Synthesis of the monomers

*(E)-6,6'-Dibromo-[3,3'-biindolinylidene]-2,2'-dione (**4.1**)*[193]



Adapting the method of Dinçalp et al.,[193] 6-bromoisatin (2.15 g, 9.51 mmol) and 6-bromooxindole (2.01 g, 9.50 mmol) were suspended in glacial acetic acid (60 mL). Conc. HCl (0.4 mL) was added and the reaction mixture was heated to 135 °C for 36 h. After cooling to room temperature, the brown precipitate was collected by filtration and washed successively with distilled water, ethanol and ethyl acetate to give the title product (3.28 g, 82%) as a purple solid.^{1}H NMR (400 MHz, DMSO-d_6) δ 9.03 (d, J = 8.7 Hz, 2H), 7.22 (dd, J = 8.7, 2.0 Hz, 2H), 7.03 (d, J = 2.0 Hz, 2H).

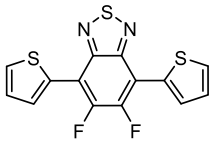
*(E)-6,6'-dibromo-1,1'-di(2,5,8,11,14,17,20-heptaoxadocosan-22-yl)-[3,3'-biindolinylidene]-2,2'-dione (**4.2**)*



3.6 (2.59 g, 5.24 mmol) was added dropwise to a suspension of **4.1** (1 g, 2.38 mmol) and potassium carbonate (1.65 g, 11.90 mmol) in anhydrous DMF (40 mL). The reaction mixture was heated to 100 °C overnight. After cooling to room temperature, the dark red solution was poured over an ice-water mixture and extracted with chloroform (3 × 100 mL). The organic layers were washed distilled water (3 × 100 mL) and dried over anhydrous $MgSO_4$. The solvent

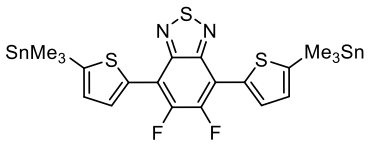
was removed in vacuo to give the crude product as a red oil. Purification by column chromatography (ethyl acetate to ethyl acetate: MeOH, 90:10) afforded the desired product (1.12 g, 44%) as a purple solid. ^{1}H NMR (400 MHz, acetone-d_6) δ 9.19 (d, J = 8.6 Hz, 2H), 7.39 (d, J = 2.0 Hz, 2H), 7.25 (dd, J = 8.6, 2.0 Hz, 2H), 4.07 (t, J = 5.4 Hz, 4H), 3.82 (t, J = 5.4 Hz, 4H), 3.66 – 3.47 (m, 48H), 3.32 (s, 6H). ^{13}C NMR (100 MHz, acetone-d_6) δ 168.1, 147.3, 132.8, 131.5, 126.7, 125.0, 120.9, 113.1, 72.3, 71.1, 71.0 – 70.9 (multiple peaks), 70.7, 69.0, 58.5, 40.8. HRMS (ES-ToF): 1065.2988 [M+H$^+$] (calc. 1065.2993).

*5,6-Difluoro-4,7-bis(thiophen-2-yl)-2,1,3-benzothiadiazole (**4.3**)*[194]



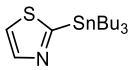
Tetrakis(triphenylphosphine)palladium (0) (175 mg, 0.15 mmol, 0.05 equiv) was added to a solution of 4,7-dibromo-5,6-difluoro-2,1,3-benzothiadiazole (1 g, 3.03 mmol, 1 equiv) and 2-(tributylstannyl)thiophene (2.2 mL, 6.93 mmol, 2.3 equiv) in degassed toluene (60 mL) under a reverse flux of nitrogen. The reaction mixture was heated to 120 ^{o}C overnight. The resulting yellow solution was concentrated *in vacuo* and ethanol (250 mL) was added to precipitate the product. The crude product was collected by filtration and recrystallised from hexane to afford the title product (0.72 g, 71%) as an orange crystalline solid. ^{1}H NMR (400 MHz, chloroform-*d*) δ 8.30 (d, J = 3.9, 2H), 7.62 (dd, J = 5.1, 3.9 Hz, 2H), 7.27 (d, J = 4.4 Hz, 2H). HRMS (ES-ToF): 335.9654 (calc. 335.9656).

*5,6-Difluoro-4,7-bis(5-(trimethylstannyl)thiophen-2-yl)-2,1,3-benzothiadiazole (**4.4**)*[194]



Lithium diisopropylamide (2 M in THF, 0.6 mL, 1.20 mmol, 2.5 equiv) was added dropwise to a solution of **4.3** (160 mg, 0.48 mmol, 1 equiv) in anhydrous THF (30 mL) at –78 °C. The resulting purple solution was stirred for 2 h at –78 °C. Trimethyltin chloride (1 M in THF, 1.25 mL, 1.25 mmol, 2.6 equiv) was added dropwise at –78 °C and the mixture was allowed to reach room temperature with stirring. The reaction mixture was quenched with distilled water (10 mL) and extracted with diethyl ether (3 × 50 mL). The combined organic layers were washed with distilled water (3 × 50 mL), dried over anhydrous $MgSO_4$ and concentrated *in vacuo*. Recrystallisation from methanol afforded the title product (253 mg, 80%) as a golden crystalline solid. ^{1}H NMR (400 MHz, chloroform-*d*) δ 8.34 (d, J = 3.7 Hz, 2H), 7.35 (d, J = 3.7 Hz, 2H), 0.45 (s, 18H). ^{19}F NMR (377 MHz, chloroform-*d*) δ –128.0. HRMS (ES-ToF): 661.8952 (calc. 661.8946).

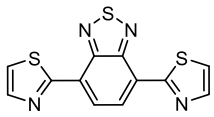
*2-(Tributylstannyl)thiazole (**4.5**)*[195]



Following the method of Lee et al.,[195] *n*-BuLi (2.5 M in hexane, 5.14 mL, 12.8 mmol) was added dropwise to a solution of thiazole (1 g, 11.7 mmol) in anhydrous diethyl ether (45 mL) at –50 °C. After stirring for 1 h at –50 °C, tributyltin chloride (4.16 g, 12.8 mmol) was added dropwise and the reaction mixture was stirred overnight at room temperature. A saturated aqueous $NaHCO_3$ solution was added (150 mL) and the mixture was extracted with diethyl ether (3 × 100 mL). The combined organic fractions were washed with distilled water (3 × 100 mL) and dried over anhydrous $MgSO_4$. Removal of the solvent *in vacuo* afforded the title

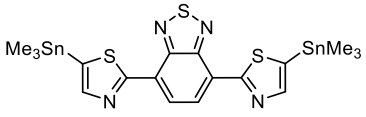
product (4.36 g, 99%) as a brown oil. The crude product was used in the next step without further purification. ^{1}H NMR (400 MHz, chloroform-*d*) δ 8.16 (d, J = 3.0 Hz, 1H), 7.53 (d, J = 3.0 Hz, 1H), 1.62 – 1.54 (m, 6H), 1.36 – 1.31 (m, 6H), 1.25 – 1.18 (m, 6H), 0.88 (t, J = 7.3 Hz, 9H). ^{13}C NMR (100 MHz, chloroform-*d*) δ 174.5, 145.6, 120.2, 29.2, 27.5, 14.0, 11.4.

*4,7-Di(thiazol-2-yl)benzo[c][1,2,5]thiadiazole (**4.6**)*[195]



Tetrakis(triphenylphosphine)palladium (0) (159 mg, 0.14 mmol, 0.05 equiv) was added to a solution of 4,7-dibromo-2,1,3-benzothiadiazole (0.81 g, 2.76 mmol, 1 equiv) and **4.5** (2.27 g, 6.07 mmol, 2.2 equiv) in degassed toluene (70 mL) under reverse flux of nitrogen. The reaction mixture was heated to 120 ^{o}C overnight. The resulting yellow solution was concentrated *in vacuo* and the crude product was recrystallised from methanol to afford the title product (0.69 g, 83%) as a crystalline orange solid. ^{1}H NMR (400 MHz, chloroform-*d*) δ 8.74 (s, 2H), 8.06 (d, J = 3.2 Hz, 2H), 7.63 (d, J = 3.2 Hz, 2H). ^{13}C NMR (100 MHz, chloroform-*d*) δ 162.3, 152.3, 143.7, 129.2, 126.1, 123.2. HRMS (ES-ToF): 302.9837 [M+H^{+}] (calc. 302.9833).

*4,7-Bis[5-(trimethylstannyl)-1,3-thiazol-2-yl]-2,1,3-benzothiadiazole (**4.7**)*



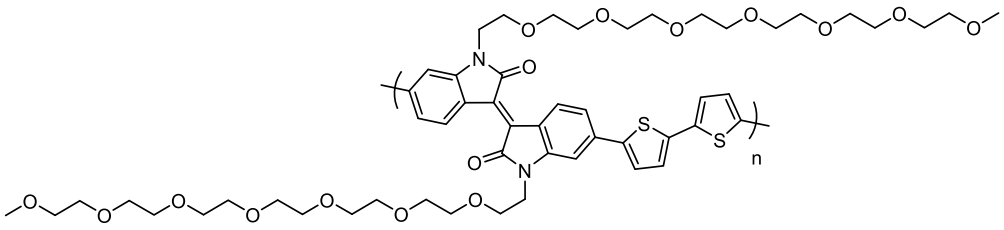
Lithium diisopropylamide (2 M in THF, 0.8 mL, 1.60 mmol, 2.4 equiv) was added dropwise to a solution of **4.6** (200 mg, 0.66 mmol, 1 equiv) in anhydrous THF (60 mL) at –78 °C. The resulting red solution was stirred for 2 h at –78 °C. Trimethyltin chloride (1 M in THF, 1.60 mL, 1.60 mmol, 2.4 equiv) was added dropwise at –78 °C and the mixture was allowed to reach room temperature with stirring. The reaction mixture was quenched with distilled water (10

mL) and extracted with diethyl ether (3 × 100 mL). The combined organic layers were washed with distilled water (3 × 100 mL), dried over anhydrous $MgSO_4$ and concentrated *in vacuo*. Recrystallisation from methanol, followed by gel permeation chromatography in THF gave the desired product (0.27 g, 46%) as an orange solid. ^{1}H NMR (400 MHz, acetone-d_6) δ 8.84 (s, 2H), 8.12 (s, 2H), 0.55 (s, 18H). HRMS (ES-ToF): 628.9121 [M+H+] (calc. 628.9117).

5.3.2 Synthesis of the polymers

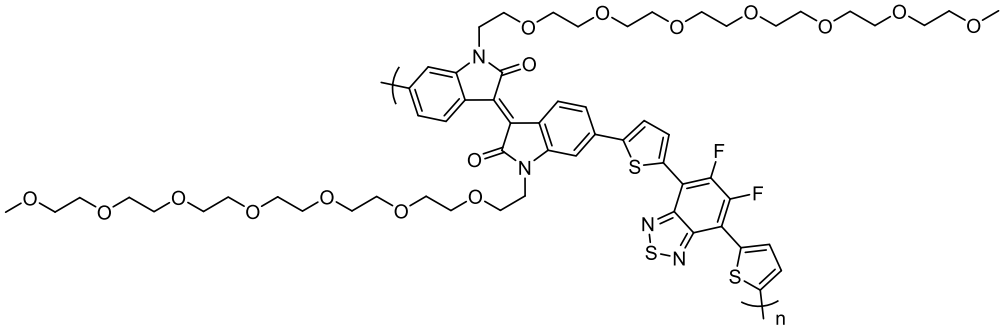
General procedure for the Stille polymerisation reaction. A mixture of the appropriate (aza)isoindigo monomer (1.0 equiv), appropriate bis(trimethylstannyl) monomer (1.0 equiv), $Pd_2(dba)_3$ (0.02 equiv) and P(*o*-tol)$_3$ (0.08 equiv) in anhydrous, degassed chlorobenzene (30 mL/ mmol) was degassed for 10 min and heated to 135 °C overnight. 0.1 mL of a solution of 2-(tributylstannyl)thiophene (0.1 mL) and $Pd_2(dba)_3$ (1.00 mg, 1.09 μmol) in anhydrous, degassed chlorobenzene (0.5 mL) were added and the resulting mixture was stirred for 1 h at 135 °C. 0.1 mL of a solution of 2-bromothiophene (0.1 mL) in anhydrous, degassed chlorobenzene (0.5 mL) were subsequently added and stirring at 135 °C was maintained for a further 1 h. The reaction mixture was cooled to room temperature and precipitated in ethyl acetate, followed by the addition of hexane. The solid was collected in a thimble and Soxhlet extraction was carried out with hexane, methanol, ethyl acetate, acetone and chloroform. The polymer was dissolved in hot chloroform and re-precipitated in ethyl acetate, followed by the addition of hexane.

p(gII-T2)



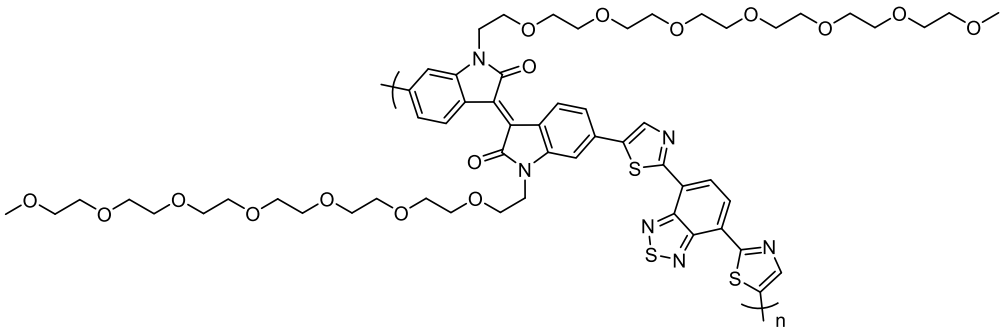
Using the general polymerisation procedure with **4.2** (70.14 mg, 65.87 μmol) and 5,5'-bis(trimethylstannyl)-2,2'-bithiophene (32.40 mg, 65.87 μmol), the title polymer (65 mg, 87%) was obtained as a metallic blue solid. ^{1}H NMR (500 MHz, 313 K, chloroform-*d*) δ 9.10 – 8.20 (br s), 7.51 – 6.45 (br s), 4.30 – 3.13 (m). GPC (chloroform, 40 °C): M_n = 10.7 kDa, M_w = 79.2 kDa.

p(gII-T2FBT)



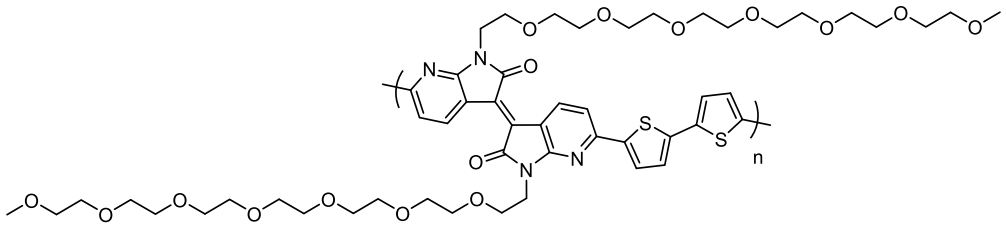
Using the general polymerisation procedure with **4.2** (72.54 mg, 68.12 μmol) and **4.4** (45.10 mg, 68.12 μmol), the title polymer (39 mg, 46%) was obtained as a metallic blue solid. ^{1}H NMR (500 MHz, 313 K, chloroform-*d*) δ 9.03 – 8.06 (br s), 7.50 – 6.49 (br s), 4.32 – 3.13 (m). GPC (chloroform, 40 °C): M_n = 5.9 kDa, M_w = 15.4 kDa.

p(gII-TzBT)



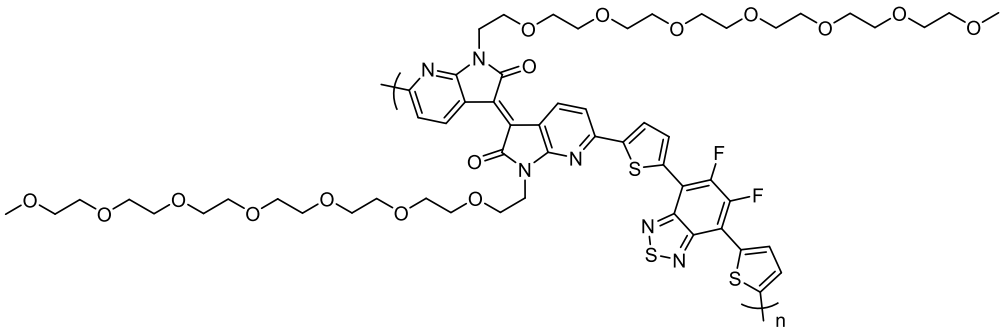
Using the general polymerisation procedure with **4.2** (32.86 mg, 30.86 μmol) and **4.7** (19.38 mg, 30.86 μmol), the title polymer (21 mg, 56%) was obtained as a dark blue solid. ^{1}H NMR (400 MHz, chloroform-*d*) δ 8.95 – 7.58 (br s), 7.23 – 6.44 (br s), 4.36 – 3.18 (m). GPC (chloroform, 40 °C): M_n = 27.7 kDa, M_w = 36.2 kDa.

p(gAII-T2)



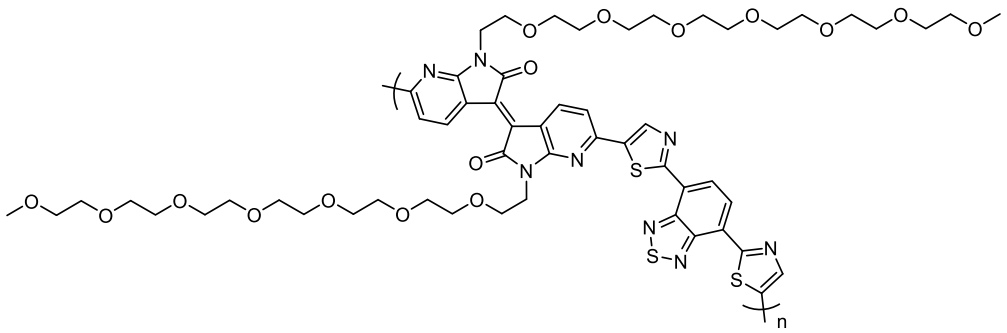
Using the general polymerisation procedure with **4.8** (71.08 mg, 66.63 μmol) and 5,5'-bis(trimethylstannyl)-2,2'-bithiophene (32.77 mg, 66.63 μmol), the title polymer (42 mg, 59%) was obtained as a dark blue solid. ^{1}H NMR (400 MHz, chloroform-*d*) δ 9.35 – 8.80 (br s), 4.13 – 3.24 (m). GPC (chloroform, 40 °C): M_n = 18.3 kDa, M_w = 36.4 kDa.

p(gAII-T2FBT)



Using the general polymerisation procedure with **4.8** (65.43 mg, 61.33 μmol) and **4.4** (40.60 mg, 61.33 μmol), the title polymer (34 mg, 45%) was obtained as a dark blue solid. ^{1}H NMR (500 MHz, 313 K, chloroform-*d*) δ 9.18 – 8.22 (br s), 7.37 – 6.24 (br s), 4.32 – 3.10 (m). GPC (chloroform, 40 °C): M_n = 6.24 kDa, M_w = 21.7 kDa.

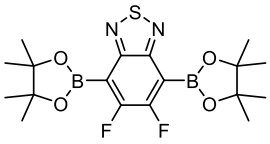
p(gAII-TzBT)



Using the general polymerisation procedure with **4.8** (57.13 mg, 53.55 μmol) and **4.7** (33.63 mg, 53.55 μmol), the title polymer (31 mg, 48%) was obtained as a dark blue solid. ^{1}H NMR (500 MHz, 313 K, chloroform-*d*) δ 9.15 – 8.23 (br s), 7.20 – 6.11 (br s), 4.38 – 3.11 (m). GPC (chloroform, 40 °C): M_n = 22.4 kDa, M_w = 28. 2 kDa.

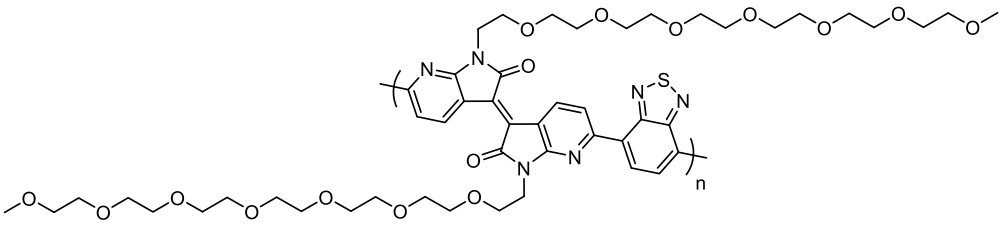
5.3.3 Synthesis of acceptor-acceptor polymers

5,6-Difluoro-4,7-bis(4,4,5,5-tetramethyl-1,3,2-dioxaborolan-2-yl)-2,1,3-benzothiadiazole ***(4.9)***



Potassium acetate (0.74 g, 7.54 mmol, 5 equiv) was dried under vacuum at 80 °C for 2 h with vigorous stirring. 4,7-Dibromo-5,6-difluoro-2,1,3-benzothiadiazole (0.5 g, 1.52 mmol, 1 equiv), bis(pinacolato)diboron (0.96 g, 3.78 mmol, 2.5 equiv) and anhydrous 1,4-dioxane (25 mL) were added and the reaction mixture was degassed for 1 h. [1,1′-Bis(diphenylphosphino)ferrocene] dichloropalladium(II) (110 mg, 0.15 mmol, 0.1 equiv) was added under reverse flow of nitrogen and the mixture was heated to 80 °C for 24 h. After removing the solvent *in vacuo*, the crude residue was suspended in hot hexane and filtered through a celite pad, washing thoroughly with hot hexane. Removal of solvent under reduced pressure and recrystallisation from hexane afforded the title product (315 mg, 49%) as a white crystalline solid. ^{1}H NMR (400 MHz, chloroform-*d*) δ 1.46 (s, 24 H). ^{13}C NMR (100 MHz, chloroform-*d*) δ 158.2 (dd, $^{1}J_{C\text{-}F}$ = 264.4 Hz, $^{2}J_{C\text{-}F}$ = 21.1 Hz), 153.4 (t, $^{2}J_{C\text{-}F}$ = 21.1 Hz), 110.8, 85.3, 25.2. ^{19}F NMR (377 MHz, chloroform-*d*) δ –117.0 (s, 2F). HRMS (ES-ToF): 425.1682 [M+H^{+}] (calc. 425.1684).

p(gAII-BT)



A mixture of **4.8** (54.70 mg, 51.27 µmol, 1.0 equiv), **4.9** (19.90 mg, 51.27 µmol, 1.0 equiv) $Pd_2(dba)_3$ (0.94 mg, 1.02 µmol, 0.02 equiv), XPhos (1.46 mg, 3.06 µmol, 0.06 equiv) and AQ336 (2 drops) were flushed with nitrogen and suspended in anhydrous, degassed toluene (1 mL). Tetrabutylammonium fluoride (75 wt. % in H_2O, 0.3 mL), followed by an aqueous NaBr solution (2 M, 0.2 mL), were added to the reaction mixture and the resulting suspension was degassed for 5 min. The mixture was heated to 90 °C for 2 days. After cooling to room temperature, the mixture was precipitated in hexane: ethyl acetate (6:1, v/v) and the solid was collected in a thimble. Soxhlet extraction was carried out with hexane, methanol and chloroform. The polymer was dissolved in hot chloroform and re-precipitated in hexane: ethyl acetate (6:1, v/v). Polymer **p(gAII-BT)** was obtained as a dark blue solid in a yield of 21%. (11.21 mg, 10.77 µmol). ^{1}H NMR (400 MHz, chloroform-*d*) δ 9.37 – 8.66 (br s), 4.21 – 3.19 (m). GPC (chloroform, 40 °C): M_n = 24.6 kDa, M_w = 60.1 kDa.

Conclusions and Outlook

Three polymer series based on n-type backbone motifs were developed to establish general structure-property relationships for mixed ionic and electronic transport in aqueous media. Investigations of their electrochemical activity, swelling behaviour and performance in organic electrochemical transistors (OECTs) provided further insight into the complex interactions between conjugated polymers, water and dopant ions.

The effect of segregating the polymer backbone from the ethylene-glycol (EG) side chain by an alkyl spacer was investigated as a strategy to improve the charge carrier mobility and OECT figures of merit. Naphthalene diimide-bithiophene (NDI-T2) copolymers bearing alkyl spacers showed improved OECT electron mobility and device performance when compared with the first known example of an n-type OECT material, **p(gNDI-gT2**). The polymer functionalised with an extended C_6-alkyl spacer also achieved remarkable stability and showed no fluctuations in the drain current for over 2 h of operation in OECTs, making it a promising candidate for long-term recordings in biological environments. The improved OECT mobility and stability imparted by the C_6-alkyl spacer were correlated with a lower extent of swelling and less detrimental changes in the crystallite lattice spacings upon electrolyte exposure and electrochemical doping. The results demonstrate that introduction of alkyl spacers and tuning of their length is an effective strategy to balance the electronic and ionic conduction and achieve high stability in aqueous-based electrochemical devices.

To improve further the electron mobility of NDI-T2 copolymers, the polymer backbone was structurally modified to enhance its rigidity and allow stronger interactions between neighbouring polymer chains. A thiophene-annulated derivative, the naphthodithiophene diimide (NDTI) unit, was chosen as the key acceptor unit due to its ability to planarise the backbone and minimise torsional disorder, as demonstrated by DFT calculations. It was found

that branched side chains containing tetraethylene glycol units provided sufficient solubility to achieve high molecular weights. As a result of its enhanced backbone coplanarity, **P4gNDTI** displayed a tighter π- π stacking of the polymer chains, a narrower band gap (~ 1.30 eV) and a higher electron affinity (~ 4.2 eV) compared to its NDI analogue, making it a good candidate for stable electron transport in ambient conditions. Indeed, **P4gNDTI** displayed improved stability during extended electrochemical cycling and less degradation of the drain current at gate biases > 0.45 V when operated as an n-type channel material in OECTs relative to the NDI derivatives. Although the effect of enhanced backbone planarity on the OECT figures of merit has not been elucidated yet, these results demonstrate the higher stability of **P4gNDTI** when electrochemically reduced in aqueous media. Ongoing investigations include OECT analysis of **P4gNDTI** of a higher molecular weight, as well as its NDI analogue, **P4gNDI**.

Given the promising results shown by the NDTI copolymers, a logical next step would be to modify the side chains and maximise the mixed conduction properties. The rigid NDTI-T2 backbone required a relatively long side chain to enhance its solubility, which in this case was based entirely on ethylene glycol units. Based on the findings of the first study, introduction of alkyl spacers before the branching point could be used to tune the ratio of hydrophilic and hydrophobic components and therefore modulate the swelling, while maintaining the overall length of the side chain.

Beyond applications in organic bioelectronics, polymers with high backbone planarity and polar side chains such as **P4gNDTI** are also desired in other fields such as thermoelectrics. Previous reports have demonstrated that ethylene glycol-based side chains enhance the miscibility of the n-type polymer with the dopant and improve the electrical conductivity at low doping concentrations.[142] In addition, the planar structure conferred by the NDTI unit could increase the polaron delocalisation length and consequently the electrical conductivity.[218]

The final study explored strategies to increase the electron affinity of isoindigo-based polymers, which had been previously employed only as p-type channel materials in OECTs. Systematic tuning of the energy levels by incorporation of electron deficient units and pyridinic nitrogen atoms led to a series of six copolymers with operation ranging from unipolar p-type to unipolar n-type in aqueous electrolytes. The p-type material **p(gII-T2)** achieved a thickness-normalised g_m of 60.10 S/cm (V_G = –0.8 V), which is ~ 5 times higher than the values recorded for other isoindigo-based copolymers for OECT applications.[116] Although its performance does not rival state-of-the-art p-type channel materials such as **PEDOT:PSS** or **p(gT2-TT)**, a notable advantage of **p(gII-T2)** is its higher ionisation potential, which disfavours the competing oxygen reduction reaction and leads to low OFF currents in ambient conditions.

At the opposite end of the series, the unipolar n-type material **p(gAII-T2FBT)** demonstrated a thickness-normalised g_m of 0.148 S/cm (V_G = 0.7 V) and μC^* of 0.106 $\pm$ 0.012 F V^{-1} cm^{-1} s^{-1}, which are in the range of the highest reported values for n-type OECT polymers based on donor-acceptor motifs. A limitation of **p(gAII-T2FBT)** is its large threshold voltage and operation at higher biases than the NDI or NDTI-based polymers. Although the threshold voltage was reduced by replacing the **T2BT** monomer with **TzBT** units, this led to disruption of the structural order, high levels of swelling upon doping and decreased performance in OECTs. A future strategy to shift the operation window of **p(gAII-T2BT)** to lower potentials could be replacement of the fluorine substituents of the **T2BT** unit with cyano groups, which have been shown to increase the electron affinity of the polymer.[209]

The structure-property relationships derived from this work could also be applied to tailor conjugated small molecules for n-type operation in OECTs, which would greatly simplify the synthetic routes and avoid the need for extensive optimisation of polymerisation conditions. Although recently introduced as accumulation mode p-type channel materials,[219] small

molecules suffer from low performance and no attempts have been yet made to tailor for n-type OECT applications.

Beyond polymers and small molecules, future directions in material design and optimisation for n-type OECTs could extend to two-dimensional or three-dimensional structures such as covalent organic frameworks (COFs).[220] COFs include ordered π-conjugated skeletons for efficient charge transport and open pores for ion transport, rendering them highly attractive for mixed conduction. Synthetic efforts could be centred around improving their solubility for solution processability[221] and tuning of the pore size for accommodating various analytes. The opportunities for material design to drive forward organic bioelectronics applications based on n-type materials are therefore vast.

Bibliography

1. Paterson, A. F. *et al.* Recent Progress in High-Mobility Organic Transistors: A Reality Check. *Adv. Mater.* **30**, 1801079 (2018).
2. Yang, J., Zhao, Z., Wang, S., Guo, Y. & Liu, Y. Insight into High-Performance Conjugated Polymers for Organic Field-Effect Transistors. *Chem* **4**, 2748–2785 (2018).
3. Kim, S. H. *et al.* Electrolyte-Gated Transistors for Organic and Printed Electronics. *Adv. Mater.* **25**, 1822–1846 (2013).
4. Li, Y., Xu, G., Cui, C. & Li, Y. Flexible and Semitransparent Organic Solar Cells. *Adv. Energy Mater.* **8**, 1701791 (2018).
5. Husain, A. A. F., Hasan, W. Z. W., Shafie, S., Hamidon, M. N. & Pandey, S. S. A review of transparent solar photovoltaic technologies. *Renew. Sustain. Energy Rev.* **94**, 779–791 (2018).
6. Lu, Y. & Chen, J. Prospects of organic electrode materials for practical lithium batteries. *Nat. Rev. Chem.* **4**, 127–142 (2020).
7. Bhosale, M. E., Chae, S., Kim, J. M. & Choi, J.-Y. Organic small molecules and polymers as an electrode material for rechargeable lithium ion batteries. *J. Mater. Chem. A* **6**, 19885–19911 (2018).
8. Goswami, S., Goswami, S. & Venkatesan, T. An organic approach to low energy memory and brain inspired electronics. *Appl. Phys. Rev.* **7**, 021303 (2020).
9. Ling, H. *et al.* Electrolyte-gated transistors for synaptic electronics, neuromorphic computing, and adaptable biointerfacing. *Appl. Phys. Rev.* **7**, 011307 (2020).
10. Rivnay, J., Owens, R. M. & Malliaras, G. G. The Rise of Organic Bioelectronics. *Chem. Mater.* **26**, 679–685 (2014).
11. Inal, S., Rivnay, J., Suiu, A.-O., Malliaras, G. G. & McCulloch, I. Conjugated Polymers in Bioelectronics. *Acc. Chem. Res.* **51**, 1368–1376 (2018).
12. Berggren, M. & Richter-Dahlfors, A. Organic Bioelectronics. *Adv. Mater.* **19**, 3201–3213 (2007).
13. Simon, D. T., Gabrielsson, E. O., Tybrandt, K. & Berggren, M. Organic Bioelectronics: Bridging the Signaling Gap between Biology and Technology. *Chem. Rev.* **116**, 13009–13041 (2016).
14. Pappa, A.-M. *et al.* Organic Electronics for Point-of-Care Metabolite Monitoring. *Trends Biotechnol.* **36**, 45–59 (2018).

15. Liao, C. *et al.* Flexible Organic Electronics in Biology: Materials and Devices. *Adv. Mater.* **27**, 7493–7527 (2015).
16. Bredas, J.-L. Mind the gap! *Mater. Horiz.* **1**, 17–19 (2013).
17. Bronstein, H., Nielsen, C. B., Schroeder, B. C. & McCulloch, I. The role of chemical design in the performance of organic semiconductors. *Nat. Rev. Chem.* **4**, 66–77 (2020).
18. Martin, R. E. & Diederich, F. Linear Monodisperse π-Conjugated Oligomers: Model Compounds for Polymers and More. *Angew. Chem. Int. Ed.* **38**, 1350–1377 (1999).
19. Bubnova, O. & Crispin, X. Towards polymer-based organic thermoelectric generators. *Energy Environ. Sci.* **5**, 9345–9362 (2012).
20. Schweicher, G. *et al.* Molecular Semiconductors for Logic Operations: Dead-End or Bright Future? *Adv. Mater.* **32**, 1905909 (2020).
21. Prins, P. *et al.* High Intrachain Hole Mobility on Molecular Wires of Ladder-Type Poly(p-Phenylenes). *Phys. Rev. Lett.* **96**, 146601 (2006).
22. Coropceanu, V. *et al.* Charge Transport in Organic Semiconductors. *Chem. Rev.* **107**, 926–952 (2007).
23. Fratini, S., Nikolka, M., Salleo, A., Schweicher, G. & Sirringhaus, H. Charge transport in high-mobility conjugated polymers and molecular semiconductors. *Nat. Mater.* **19**, 491–502 (2020).
24. Fratini, S. & Ciuchi, S. Dynamical localization corrections to band transport. *Phys. Rev. Res.* **2**, 013001 (2020).
25. Giannini, S., Carof, A. & Blumberger, J. Crossover from Hopping to Band-Like Charge Transport in an Organic Semiconductor Model: Atomistic Nonadiabatic Molecular Dynamics Simulation. *J. Phys. Chem. Lett.* **9**, 3116–3123 (2018).
26. Fratini, S., Mayou, D. & Ciuchi, S. The Transient Localization Scenario for Charge Transport in Crystalline Organic Materials. *Adv. Funct. Mater.* **26**, 2292–2315 (2016).
27. McCulloch, I. *et al.* Liquid-crystalline semiconducting polymers with high charge-carrier mobility. *Nat. Mater.* **5**, 328–333 (2006).
28. Nakano, M., Sawamoto, M., Yuki, M. & Takimiya, K. N,N′-Unsubstituted Naphthodithiophene Diimide: Synthesis and Derivatization via N-Alkylation and -Arylation. *Org. Lett.* **18**, 3770–3773 (2016).
29. Onwubiko, A. *et al.* Fused electron deficient semiconducting polymers for air stable electron transport. *Nat. Commun.* **9**, 1–9 (2018).
30. Thorley, K. J. & McCulloch, I. Why are S–F and S–O non-covalent interactions stabilising? *J. Mater. Chem. C* **6**, 12413–12421 (2018).

31. Naik, M. A., Venkatramaiah, N., Kanimozhi, C. & Patil, S. Influence of Side-Chain on Structural Order and Photophysical Properties in Thiophene Based Diketopyrrolopyrroles: A Systematic Study. *J. Phys. Chem. C* **116**, 26128–26137 (2012).
32. Noriega, R. *et al.* A general relationship between disorder, aggregation and charge transport in conjugated polymers. *Nat. Mater.* **12**, 1038–1044 (2013).
33. Gu, K. *et al.* Assessing the Huang–Brown Description of Tie Chains for Charge Transport in Conjugated Polymers. *ACS Macro Lett.* **7**, 1333–1338 (2018).
34. Onorato, J. W. & Luscombe, C. K. Morphological effects on polymeric mixed ionic/electronic conductors. *Mol. Syst. Des. Eng.* **4**, 310–324 (2019).
35. Himmelberger, S., Vandewal, K., Fei, Z., Heeney, M. & Salleo, A. Role of Molecular Weight Distribution on Charge Transport in Semiconducting Polymers. *Macromolecules* **47**, 7151–7157 (2014).
36. Tsumura, A., Koezuka, H. & Ando, T. Macromolecular electronic device: Field-effect transistor with a polythiophene thin film. *Appl. Phys. Lett.* **49**, 1210–1212 (1986).
37. Letizia, J. A. *et al.* n-Channel Polymers by Design: Optimizing the Interplay of Solubilizing Substituents, Crystal Packing, and Field-Effect Transistor Characteristics in Polymeric Bithiophene-Imide Semiconductors. *J. Am. Chem. Soc.* **130**, 9679–9694 (2008).
38. Facchetti, A. π-Conjugated Polymers for Organic Electronics and Photovoltaic Cell Applications. *Chem. Mater.* **23**, 733–758 (2011).
39. Lamport, Z. A., Haneef, H. F., Anand, S., Waldrip, M. & Jurchescu, O. D. Tutorial: Organic field-effect transistors: Materials, structure and operation. *J. Appl. Phys.* **124**, 071101 (2018).
40. Choi, H. H., Cho, K., Frisbie, C. D., Sirringhaus, H. & Podzorov, V. Critical assessment of charge mobility extraction in FETs. *Nat. Mater.* **17**, 2–7 (2018).
41. Liu, C. *et al.* Device Physics of Contact Issues for the Overestimation and Underestimation of Carrier Mobility in Field-Effect Transistors. *Phys. Rev. Appl.* **8**, 034020 (2017).
42. McCulloch, I., Salleo, A. & Chabinyc, M. Avoid the kinks when measuring mobility. *Science* **352**, 1521–1522 (2016).
43. Xia, Y., Cho, J. H., Lee, J., Ruden, P. P. & Frisbie, C. D. Comparison of the Mobility–Carrier Density Relation in Polymer and Single-Crystal Organic Transistors Employing Vacuum and Liquid Gate Dielectrics. *Adv. Mater.* **21**, 2174–2179 (2009).

44. Xue, Z., He, D. & Xie, X. Poly(ethylene oxide)-based electrolytes for lithium-ion batteries. *J. Mater. Chem. A* **3**, 19218–19253 (2015).
45. Smitha, B., Sridhar, S. & Khan, A. A. Solid polymer electrolyte membranes for fuel cell applications—a review. *J. Membr. Sci.* **259**, 10–26 (2005).
46. Stavrinidou, E. *et al.* Direct Measurement of Ion Mobility in a Conducting Polymer. *Adv. Mater.* **25**, 4488–4493 (2013).
47. Modarresi, M., Franco-Gonzalez, J. F. & Zozoulenko, I. Morphology and ion diffusion in PEDOT:Tos. A coarse grained molecular dynamics simulation. *Phys. Chem. Chem. Phys.* **20**, 17188–17198 (2018).
48. Giridharagopal, R. *et al.* Electrochemical strain microscopy probes morphology-induced variations in ion uptake and performance in organic electrochemical transistors. *Nat. Mater.* **16**, 737–742 (2017).
49. Nigrey, P. J., MacDiarmid, A. G. & Heeger, A. J. Electrochemistry of polyacetylene, (CH)x: electrochemical doping of (CH)x films to the metallic state. *J. Chem. Soc. Chem. Commun.* 594–595 (1979).
50. Bredas, J. L., Street, G. B. Polarons, bipolarons, and solitons in conducting polymers. *Acc. Chem. Res.* **18**, 309–315 (1985).
51. Beverina, L., A. Pagani, G. & Sassi, M. Multichromophoric electrochromic polymers: colour tuning of conjugated polymers through the side chain functionalization approach. *Chem. Commun.* **50**, 5413–5430 (2014).
52. Ponder, J. F., Österholm, A. M. & Reynolds, J. R. Conjugated Polyelectrolytes as Water Processable Precursors to Aqueous Compatible Redox Active Polymers for Diverse Applications: Electrochromism, Charge Storage, and Biocompatible Organic Electronics. *Chem. Mater.* **29**, 4385–4392 (2017).
53. Savagian, L. R. *et al.* Conjugated Polymer Blends for High Contrast Black-to-Transmissive Electrochromism. *Adv. Opt. Mater.* **6**, 1800594 (2018).
54. Moia, D. *et al.* Design and evaluation of conjugated polymers with polar side chains as electrode materials for electrochemical energy storage in aqueous electrolytes. *Energy Environ. Sci.* **12**, 1349–1357 (2019).
55. Malti, A. *et al.* An Organic Mixed Ion–Electron Conductor for Power Electronics. *Adv. Sci.* **3**, 1500305 (2016).
56. Österholm, A. M., Ponder, J. F., Kerszulis, J. A. & Reynolds, J. R. Solution Processed PEDOT Analogues in Electrochemical Supercapacitors. *ACS Appl. Mater. Interfaces* **8**, 13492–13498 (2016).

57. van de Burgt, Y. *et al.* A non-volatile organic electrochemical device as a low-voltage artificial synapse for neuromorphic computing. *Nat. Mater.* **16**, 414–418 (2017).
58. Maziz, A. *et al.* Knitting and weaving artificial muscles. *Sci. Adv.* **3**, e1600327 (2017).
59. Williamson, A. *et al.* Controlling Epileptiform Activity with Organic Electronic Ion Pumps. *Adv. Mater.* **27**, 3138–3144 (2015).
60. Jonsson, A. *et al.* Therapy using implanted organic bioelectronics. *Sci. Adv.* **1**, e1500039 (2015).
61. Braendlein, M., Lonjaret, T., Leleux, P., Badier, J.-M. & Malliaras, G. G. Voltage Amplifier Based on Organic Electrochemical Transistor. *Adv. Sci.* **4**, 1600247 (2017).
62. Pappa, A. M. *et al.* Direct metabolite detection with an n-type accumulation mode organic electrochemical transistor. *Sci. Adv.* **4**, eaat0911 (2018).
63. Venkatraman, V. *et al.* Subthreshold Operation of Organic Electrochemical Transistors for Biosignal Amplification. *Adv. Sci.* **5**, 1800453 (2018).
64. Ohayon, D. *et al.* Biofuel powered glucose detection in bodily fluids with an n-type conjugated polymer. *Nat. Mater.* **19**, 456–463 (2020).
65. Khodagholy, D. *et al.* Highly Conformable Conducting Polymer Electrodes for In Vivo Recordings. *Adv. Mater.* **23**, H268–H272 (2011).
66. Khodagholy, D. *et al.* In vivo recordings of brain activity using organic transistors. *Nat. Commun.* **4**, 1–7 (2013).
67. Leleux, P. *et al.* Organic electrochemical transistors for clinical applications. *Adv. Healthc. Mater.* **4**, 142–147 (2015).
68. Rivnay, J. *et al.* High-performance transistors for bioelectronics through tuning of channel thickness. *Sci. Adv.* 1–5 (2015).
69. Sessolo, M., Rivnay, J., Bandiello, E., Malliaras, G. G. & Bolink, H. J. Ion-Selective Organic Electrochemical Transistors. *Adv. Mater.* **26**, 4803–4807 (2014).
70. Xu, J. *et al.* Highly stretchable polymer semiconductor films through the nanoconfinement effect. *Science* **355**, 59–64 (2017).
71. Battista, E. *et al.* Enzymatic sensing with laccase-functionalized textile organic biosensors. *Org. Electron.* **40**, 51–57 (2017).
72. Gualandi, I. *et al.* Textile Organic Electrochemical Transistors as a Platform for Wearable Biosensors. *Sci. Rep.* **6**, 1–10 (2016).
73. Feig, V. R., Tran, H., Lee, M. & Bao, Z. Mechanically tunable conductive interpenetrating network hydrogels that mimic the elastic moduli of biological tissue. *Nat. Commun.* **9**, 1–9 (2018).

74. Hammock, M. L., Knopfmacher, O., Naab, B. D., Tok, J. B.-H. & Bao, Z. Investigation of Protein Detection Parameters Using Nanofunctionalized Organic Field-Effect Transistors. *ACS Nano* **7**, 3970–3980 (2013).
75. He, R.-X. *et al.* Detection of bacteria with organic electrochemical transistors. *J. Mater. Chem.* **22**, 22072–22076 (2012).
76. Owens, R. M. & Malliaras, G. G. Organic Electronics at the Interface with Biology. *MRS Bull.* **35**, 449–456 (2010).
77. Zeglio, E., Rutz, A. L., Winkler, T. E., Malliaras, G. G. & Herland, A. Conjugated Polymers for Assessing and Controlling Biological Functions. *Adv. Mater.* **31**, 1806712 (2019).
78. Fidanovski, K. & Mawad, D. Conjugated Polymers in Bioelectronics: Addressing the Interface Challenge. *Adv. Healthc. Mater.* **8**, 1900053 (2019).
79. White, H. S., Kittlesen, G. P. & Wrighton, M. S. Chemical derivatization of an array of three gold microelectrodes with polypyrrole: fabrication of a molecule-based transistor. *J. Am. Chem. Soc.* **106**, 5375–5377 (1984).
80. Rivnay, J. *et al.* Organic electrochemical transistors. *Nat. Rev. Mater.* **3**, 17086 (2018).
81. Sessolo, M. *et al.* Easy-to-Fabricate Conducting Polymer Microelectrode Arrays. *Adv. Mater.* **25**, 2135–2139 (2013).
82. Khodagholy, D. *et al.* High transconductance organic electrochemical transistors. *Nat. Commun.* **4**, 2133 (2013).
83. Rivnay, J. *et al.* Organic electrochemical transistors with maximum transconductance at zero gate bias. *Adv. Mater.* **25**, 7010–7014 (2013).
84. Inal, S. *et al.* A high transconductance accumulation mode electrochemical transistor. *Adv. Mater.* **26**, 7450–7455 (2014).
85. Zeglio, E., Eriksson, J., Gabrielsson, R., Solin, N. & Inganäs, O. Highly Stable Conjugated Polyelectrolytes for Water-Based Hybrid Mode Electrochemical Transistors. *Adv. Mater.* **29**, 1605787 (2017).
86. Giovannitti, A. *et al.* Controlling the mode of operation of organic transistors through side-chain engineering. *Proc. Natl. Acad. Sci.* **113**, 12017–12022 (2016).
87. de Leeuw, D. M., Simenon, M. M. J., Brown, A. R. & Einerhand, R. E. F. Stability of n-type doped conducting polymers and consequences for polymeric microelectronic devices. *Synth. Met.* **87**, 53–59 (1997).
88. Bernards, D. A. & Malliaras, G. G. Steady-State and Transient Behavior of Organic Electrochemical Transistors. *Adv. Funct. Mater.* **17**, 3538–3544 (2007).

89. Koutsouras, D. A. *et al.* Impedance Spectroscopy of Spin-Cast and Electrochemically Deposited PEDOT:PSS Films on Microfabricated Electrodes with Various Areas. *ChemElectroChem* **4**, 2321–2327 (2017).
90. Giovannitti, A. *et al.* The Role of the Side Chain on the Performance of N-type Conjugated Polymers in Aqueous Electrolytes. *Chem. Mater.* **30**, 2945–2953 (2018).
91. Savva, A. *et al.* Solvent Engineering for High-Performance n-Type Organic Electrochemical Transistors. *Adv. Electron. Mater.* **5**, 1900249 (2019).
92. Schmode, P. *et al.* The Key Role of Side Chain Linkage in Structure Formation and Mixed Conduction of Ethylene Glycol Substituted Polythiophenes. *ACS Appl. Mater. Interfaces* **12**, 13029–13039 (2020).
93. Inal, S., Malliaras, G. G. & Rivnay, J. Benchmarking organic mixed conductors for transistors. *Nat. Commun.* **8**, 1–7 (2017).
94. Rivnay, J. *et al.* Organic electrochemical transistors for cell-based impedance sensing. *Appl. Phys. Lett.* **106**, 043301 (2015).
95. Flagg, L. Q., Giridharagopal, R., Guo, J. & Ginger, D. S. Anion-Dependent Doping and Charge Transport in Organic Electrochemical Transistors. *Chem. Mater.* **30**, 5380–5389 (2018).
96. Cendra, C. *et al.* Role of the Anion on the Transport and Structure of Organic Mixed Conductors. *Adv. Funct. Mater.* **29**, 1807034 (2019).
97. Barthó, P. *et al.* Characterization of Neocortical Principal Cells and Interneurons by Network Interactions and Extracellular Features. *J. Neurophysiol.* **92**, 600–608 (2004).
98. Zeglio, E. *et al.* Conjugated Polyelectrolyte Blends for Electrochromic and Electrochemical Transistor Devices. *Chem. Mater.* **27**, 6385–6393 (2015).
99. Andersson, P., Forchheimer, R., Tehrani, P. & Berggren, M. Printable All-Organic Electrochromic Active-Matrix Displays. *Adv. Funct. Mater.* **17**, 3074–3082 (2007).
100. Zeglio, E. & Inganäs, O. Active Materials for Organic Electrochemical Transistors. *Adv. Mater.* **30**, 1800941 (2018).
101. Moser, M., Ponder, J. F., Wadsworth, A., Giovannitti, A. & McCulloch, I. Materials in Organic Electrochemical Transistors for Bioelectronic Applications: Past, Present, and Future. *Adv. Funct. Mater.* **29**, 1807033 (2019).
102. Paulsen, B. D., Tybrandt, K., Stavrinidou, E. & Rivnay, J. Organic mixed ionic–electronic conductors. *Nat. Mater.* **19**, 13–26 (2020).
103. Sun, H., Gerasimov, J., Berggren, M. & Fabiano, S. n-Type organic electrochemical transistors: materials and challenges. *J. Mater. Chem. C* **6**, 11778–11784 (2018).

104. Nilsson, D. *et al.* Bi-stable and Dynamic Current Modulation in Electrochemical Organic Transistors. *Adv. Mater.* **14**, 51–54 (2002).
105. De Keersmaecker, M., Lang, A. W., Österholm, A. M. & Reynolds, J. R. All Polymer Solution Processed Electrochromic Devices: A Future without Indium Tin Oxide? *ACS Appl. Mater. Interfaces* **10**, 31568–31579 (2018).
106. Rivnay, J. *et al.* Structural control of mixed ionic and electronic transport in conducting polymers. *Nat. Commun.* **7**, 11287 (2016).
107. Crispin, X. *et al.* The Origin of the High Conductivity of Poly(3,4-ethylenedioxythiophene)−Poly(styrenesulfonate) (PEDOT−PSS) Plastic Electrodes. *Chem. Mater.* **18**, 4354–4360 (2006).
108. Lang, U., Müller, E., Naujoks, N. & Dual, J. Microscopical Investigations of PEDOT:PSS Thin Films. *Adv. Funct. Mater.* **19**, 1215–1220 (2009).
109. Takano, T., Masunaga, H., Fujiwara, A., Okuzaki, H. & Sasaki, T. PEDOT Nanocrystal in Highly Conductive PEDOT:PSS Polymer Films. *Macromolecules* **45**, 3859–3865 (2012).
110. Rashid, R. B., Ciechowski, R. J. & Rivnay, J. Self-aligned, laser-cut organic electrochemical transistors. *Flex. Print. Electron.* **5**, 014007 (2020).
111. Inal, S. *et al.* Organic electrochemical transistors based on PEDOT with different anionic polyelectrolyte dopants. *J. Polym. Sci. Part B Polym. Phys.* **54**, 147–151 (2016).
112. Keene, S. T., Melianas, A., van de Burgt, Y. & Salleo, A. Mechanisms for Enhanced State Retention and Stability in Redox-Gated Organic Neuromorphic Devices. *Adv. Electron. Mater.* **5**, 1800686 (2019).
113. Keene, S. T. *et al.* Enhancement-Mode PEDOT:PSS Organic Electrochemical Transistors Using Molecular De-Doping. *Adv. Mater.* **32**, 2000270 (2020).
114. Proctor, C. M., Rivnay, J. & Malliaras, G. G. Understanding volumetric capacitance in conducting polymers. *J. Polym. Sci. Part B Polym. Phys.* **54**, 1433–1436 (2016).
115. Giovannitti, A. *et al.* N-type organic electrochemical transistors with stability in water. *Nat. Commun.* **7**, 1–10 (2016).
116. Wang, Y. *et al.* Hybrid Alkyl–Ethylene Glycol Side Chains Enhance Substrate Adhesion and Operational Stability in Accumulation Mode Organic Electrochemical Transistors. *Chem. Mater.* **31**, 9797–9806 (2019).
117. Savagian, L. R. *et al.* Balancing Charge Storage and Mobility in an Oligo(Ether) Functionalized Dioxythiophene Copolymer for Organic- and Aqueous- Based Electrochemical Devices and Transistors. *Adv. Mater.* **30**, 1804647 (2018).

118. Nielsen, C. B. *et al.* Molecular Design of Semiconducting Polymers for High-Performance Organic Electrochemical Transistors. *J. Am. Chem. Soc.* **138**, 10252–10259 (2016).
119. Giovannitti, A. *et al.* Redox-Stability of Alkoxy-BDT Copolymers and their Use for Organic Bioelectronic Devices. *Adv. Funct. Mater.* **28**, 1706325 (2018).
120. Giovannitti, A. *et al.* Energetic Control of Redox-Active Polymers toward Safe Organic Bioelectronic Materials. *Adv. Mater.* **32**, 1908047.
121. Chen, Z., Zheng, Y., Yan, H. & Facchetti, A. Naphthalenedicarboximide- vs Perylenedicarboximide-Based Copolymers. Synthesis and Semiconducting Properties in Bottom-Gate N-Channel Organic Transistors. *J. Am. Chem. Soc.* **131**, 8–9 (2009).
122. Yan, H. *et al.* A high-mobility electron-transporting polymer for printed transistors. *Nature* **457**, 679–686 (2009).
123. Sun, H. *et al.* Complementary Logic Circuits Based on High-Performance n-Type Organic Electrochemical Transistors. *Adv. Mater.* **30**, 1704916 (2018).
124. Liang, Y. *et al.* Tuning Channel Architecture of Interdigitated Organic Electrochemical Transistors for Recording the Action Potentials of Electrogenic Cells. *Adv. Funct. Mater.* **29**, 1902085 (2019).
125. Bischak, C. G., Flagg, L. Q., Yan, K., Li, C.-Z. & Ginger, D. S. Fullerene Active Layers for n-Type Organic Electrochemical Transistors. *ACS Appl. Mater. Interfaces* **11**, 28138–28144 (2019).
126. Tan, S. T. M. *et al.* Chemical to Electrical Transduction using Fuel Cell Powered Organic Electrochemical Transistors. (2020) doi:10.26434/chemrxiv.12071136.v1.
127. Pauliukaite, R., Malinauskas, A., Zhylyak, G. & Spichiger-Keller, U. E. Conductive Organic Complex Salt TTF-TCNQ as a Mediator for Biosensors. An Overview. *Electroanalysis* **19**, 2491–2498 (2007).
128. Jia, H. & Lei, T. Emerging research directions for n-type conjugated polymers. *J. Mater. Chem. C* **7**, 12809–12821 (2019).
129. Zhan, X. *et al.* Rylene and related diimides for organic electronics. *Adv. Mater.* **23**, 268–284 (2011).
130. Gao, X. & Hu, Y. Development of n-type organic semiconductors for thin film transistors: a viewpoint of molecular design. *J. Mater. Chem. C* **2**, 3099 (2014).
131. Di Pietro, R., Fazzi, D., Kehoe, T. B. & Sirringhaus, H. Spectroscopic Investigation of Oxygen- and Water-Induced Electron Trapping and Charge Transport Instabilities in n-type Polymer Semiconductors. *J. Am. Chem. Soc.* **134**, 14877–14889 (2012).

132. Brédas, J. L., Calbert, J. P., Filho, D. A. da S. & Cornil, J. Organic semiconductors: A theoretical characterization of the basic parameters governing charge transport. *Proc. Natl. Acad. Sci.* **99**, 5804–5809 (2002).
133. Sirringhaus, H. Reliability of Organic Field-Effect Transistors. *Adv. Mater.* **21**, 3859–3873 (2009).
134. Brixi, S. *et al.* Air and temperature sensitivity of n-type polymer materials to meet and exceed the standard of N2200. *Sci. Rep.* **10**, 1–10 (2020).
135. Jones, B. A., Facchetti, A., Wasielewski, M. R. & Marks, T. J. Tuning Orbital Energetics in Arylene Diimide Semiconductors. Materials Design for Ambient Stability of n-Type Charge Transport. *J. Am. Chem. Soc.* **129**, 15259–15278 (2007).
136. Usta, H. *et al.* Design, Synthesis, and Characterization of Ladder-Type Molecules and Polymers. Air-Stable, Solution-Processable n-Channel and Ambipolar Semiconductors for Thin-Film Transistors via Experiment and Theory. *J. Am. Chem. Soc.* **131**, 5586–5608 (2009).
137. Anthopoulos, T. D., Anyfantis, G. C., Papavassiliou, G. C. & de Leeuw, D. M. Air-stable ambipolar organic transistors. *Appl. Phys. Lett.* **90**, 122105 (2007).
138. Guardado, J. O. & Salleo, A. Structural Effects of Gating Poly(3-hexylthiophene) through an Ionic Liquid. *Adv. Funct. Mater.* **27**, 1701791 (2017).
139. Flagg, L. Q. *et al.* Polymer Crystallinity Controls Water Uptake in Glycol Side-Chain Polymer Organic Electrochemical Transistors. *J. Am. Chem. Soc.* **141**, 4345–4354 (2019).
140. Savva, A. *et al.* Influence of Water on the Performance of Organic Electrochemical Transistors. *Chem. Mater.* **31**, 927–937 (2019).
141. Savva, A. *et al.* Balancing Ionic and Electronic Conduction for High-Performance Organic Electrochemical Transistors. *Adv. Funct. Mater.* **30**, 1907657 (2020).
142. Kiefer, D. *et al.* Enhanced n-Doping Efficiency of a Naphthalenediimide-Based Copolymer through Polar Side Chains for Organic Thermoelectrics. *ACS Energy Lett.* **3**, 278–285 (2018).
143. Mei, J. & Bao, Z. Side Chain Engineering in Solution-Processable Conjugated Polymers. *Chem. Mater.* **26**, 604–615 (2014).
144. Dong, B. X. *et al.* Influence of Side-Chain Chemistry on Structure and Ionic Conduction Characteristics of Polythiophene Derivatives: A Computational and Experimental Study. *Chem. Mater.* **31**, 1418–1429 (2019).

145. Kim, R. *et al.* Oligo(ethylene glycol)-incorporated hybrid linear alkyl side chains for n-channel polymer semiconductors and their effect on the thin-film crystalline structure. *Chem. Commun.* **51**, 1524–1527 (2015).
146. Guo, X. & Watson, M. D. Conjugated Polymers from Naphthalene Bisimide. *Org. Lett.* **10**, 5333–5336 (2008).
147. He, Y., Guo, C., Sun, B., Quinn, J. & Li, Y. Branched alkyl ester side chains rendering large polycyclic (3 E ,7 E)-3,7-bis(2-oxoindolin-3-ylidene)benzo[1,2- b :4,5- b ′]difuran-2,6(3 H ,7 H)-dione (IBDF) based donor–acceptor polymers solution-processability for organic thin film transistors. *Polym. Chem.* **6**, 6689–6697 (2015).
148. Chen, X., Zhang, Z., Liu, J. & Wang, L. A polymer electron donor based on isoindigo units bearing branched oligo(ethylene glycol) side chains for polymer solar cells. *Polym. Chem.* **8**, 5496–5503 (2017).
149. Meng, B. *et al.* Replacing Alkyl with Oligo(ethylene glycol) as Side Chains of Conjugated Polymers for Close π–π Stacking. *Macromolecules* **48**, 4357–4363 (2015).
150. Langhals, H., Demmig, S. & Huber, H. Rotational barriers in perylene fluorescent dyes. *Spectrochim. Acta Part Mol. Spectrosc.* **44**, 1189–1193 (1988).
151. Steyrleuthner, R. *et al.* Aggregation in a High-Mobility n-Type Low-Bandgap Copolymer with Implications on Semicrystalline Morphology. *J. Am. Chem. Soc.* **134**, 18303–18317 (2012).
152. Gross, Y. M. & Ludwigs, S. P(NDI2OD-T2) revisited – Aggregation control as key for high performance n-type applications. *Synth. Met.* **253**, 73–87 (2019).
153. Molino, P. J. *et al.* Influence of Biodopants on PEDOT Biomaterial Polymers: Using QCM-D to Characterize Polymer Interactions with Proteins and Living Cells. *Adv. Mater. Interfaces* **1**, 1300122 (2014).
154. Lee, H.-S. *et al.* Reversible swelling of chitosan and quaternary ammonium modified chitosan brush layers: effects of pH and counter anion size and functionality. *J. Mater. Chem.* **22**, 19605–19616 (2012).
155. Rivnay, J. *et al.* Unconventional Face-On Texture and Exceptional In-Plane Order of a High Mobility n-Type Polymer. *Adv. Mater.* **22**, 4359–4363 (2010).
156. Brinkmann, M. *et al.* Segregated versus Mixed Interchain Stacking in Highly Oriented Films of Naphthalene Diimide Bithiophene Copolymers. *ACS Nano* **6**, 10319–10326 (2012).
157. Tremel, K. *et al.* Charge Transport Anisotropy in Highly Oriented Thin Films of the Acceptor Polymer P(NDI2OD-T2). *Adv. Energy Mater.* **4**, 1301659 (2014).

158. Rivnay, J., Mannsfeld, S. C. B., Miller, C. E., Salleo, A. & Toney, M. F. Quantitative Determination of Organic Semiconductor Microstructure from the Molecular to Device Scale. *Chem. Rev.* **112**, 5488–5519 (2012).
159. Lee, S. *et al.* Aqueous-Soluble Naphthalene Diimide-Based Polymer Acceptors for Efficient and Air-Stable All-Polymer Solar Cells. *ACS Appl. Mater. Interfaces* **11**, 45038–45047 (2019).
160. Larsson, O., Laiho, A., Schmickler, W., Berggren, M. & Crispin, X. Controlling the Dimensionality of Charge Transport in an Organic Electrochemical Transistor by Capacitive Coupling. *Adv. Mater.* **23**, 4764–4769 (2011).
161. Fukutomi, Y., Nakano, M., Hu, J.-Y., Osaka, I. & Takimiya, K. Naphthodithiophenediimide (NDTI): Synthesis, Structure, and Applications. *J. Am. Chem. Soc.* **135**, 11445–11448 (2013).
162. Chen, W., Nakano, M., Kim, J.-H., Takimiya, K. & Zhang, Q. Naphtho[2,3- b]thiophene diimide (NTI): a mono-functionalisable core-extended naphthalene diimide for electron-deficient architectures. *J. Mater. Chem. C* **4**, 8879–8883 (2016).
163. Nakano, M., Osaka, I. & Takimiya, K. Naphthodithiophene Diimide (NDTI)-Based Semiconducting Copolymers: From Ambipolar to Unipolar n-Type Polymers. *Macromolecules* **48**, 576–584 (2015).
164. Nakano, K. *et al.* Naphthodithiophene Diimide-Based Copolymers: Ambipolar Semiconductors in Field-Effect Transistors and Electron Acceptors with Near-Infrared Response in Polymer Blend Solar Cells. *Macromolecules* **49**, 1752–1760 (2016).
165. Wang, Y. *et al.* Naphthodithiophenediimide–Benzobisthiadiazole-Based Polymers: Versatile n-Type Materials for Field-Effect Transistors and Thermoelectric Devices. *Macromolecules* **50**, 857–864 (2017).
166. Schuettfort, T., Thomsen, L. & McNeill, C. R. Observation of a Distinct Surface Molecular Orientation in Films of a High Mobility Conjugated Polymer. *J. Am. Chem. Soc.* **135**, 1092–1101 (2013).
167. Schuettfort, T. *et al.* Surface and Bulk Structural Characterization of a High-Mobility Electron-Transporting Polymer. *Macromolecules* **44**, 1530–1539 (2011).
168. Szumilo, M. M. *et al.* Structure Influence on Charge Transport in Naphthalenediimide–Thiophene Copolymers. *Chem. Mater.* **26**, 6796–6804 (2014).
169. Olivier, Y. *et al.* 25th Anniversary Article: High-Mobility Hole and Electron Transport Conjugated Polymers: How Structure Defines Function. *Adv. Mater.* **26**, 2119–2136 (2014).

170. Tanaka, M. *et al.* Properties of modified surface for biosensing interface. *J. Colloid Interface Sci.* **497**, 309–316 (2017).
171. Wu, J. *et al.* Semiconducting Polymer Nanoparticles for Centimeters-Deep Photoacoustic Imaging in the Second Near-Infrared Window. *Adv. Mater.* **29**, 1703403 (2017).
172. Buendía, J. & Sánchez, L. Solvent-Dependent Disassembly of Amphiphilic OPE-Based Tricarboxamides. *Org. Lett.* **15**, 5746–5749 (2013).
173. Buckland, D., Bhosale, S. V. & Langford, S. J. A chemodosimer based on a core-substituted naphthalene diimide for fluoride ion detection. *Tetrahedron Lett.* **52**, 1990–1992 (2011).
174. Yue, W. *et al.* One-pot synthesis of well-defined oligo- butadiynylene-naphthalene diimides. *Org. Lett.* **12**, 3460–3 (2010).
175. Dawson, R. E. *et al.* Experimental evidence for the functional relevance of anion– π interactions. *Nat. Chem.* **2**, 533–538 (2010).
176. Yang, J. *et al.* Comparison among Perylene Diimide (PDI), Naphthalene Diimide (NDI), and Naphthodithiophene Diimide (NDTI) Based n-Type Polymers for All-Polymer Solar Cells Application. *Macromolecules* **50**, 3179–3185 (2017).
177. Österholm, A. M., Ponder, J. F., De Keersmaecker, M., Shen, D. E. & Reynolds, J. R. Disentangling Redox Properties and Capacitance in Solution-Processed Conjugated Polymers. *Chem. Mater.* **31**, 2971–2982 (2019).
178. Heinze, J., Frontana-Uribe, B. A. & Ludwigs, S. Electrochemistry of Conducting Polymers—Persistent Models and New Concepts. *Chem. Rev.* **110**, 4724–4771 (2010).
179. Trefz, D. *et al.* Electrochemical Investigations of the N-Type Semiconducting Polymer P(NDI2OD-T2) and Its Monomer: New Insights in the Reduction Behavior. *J. Phys. Chem. C* **119**, 22760–22771 (2015).
180. Savva, A., Wustoni, S. & Inal, S. Ionic-to-electronic coupling efficiency in PEDOT:PSS films operated in aqueous electrolytes. *J. Mater. Chem. C* **6**, 12023–12030 (2018).
181. Rivnay, J. *et al.* High-performance transistors for bioelectronics through tuning of channel thickness. *Sci. Adv.* **1**, e1400251 (2015).
182. Porrazzo, R. *et al.* Water-Gated n-Type Organic Field-Effect Transistors for Complementary Integrated Circuits Operating in an Aqueous Environment. *ACS Omega* **2**, 1–10 (2017).
183. Quinn, J. T. E., Zhu, J., Li, X., Wang, J. & Li, Y. Recent progress in the development of n-type organic semiconductors for organic field effect transistors. *J. Mater. Chem. C* **5**, 8654–8681 (2017).

184. Gao, Y. *et al.* Multifluorination toward High-Mobility Ambipolar and Unipolar n-Type Donor–Acceptor Conjugated Polymers Based on Isoindigo. *Adv. Mater.* **29**, 1606217 (2017).
185. Yang, J. *et al.* Isoindigo-Based Polymers with Small Effective Masses for High-Mobility Ambipolar Field-Effect Transistors. *Adv. Mater.* **29**, 1702115 (2017).
186. Wang, E., Mammo, W. & Andersson, M. R. 25th Anniversary Article: Isoindigo-Based Polymers and Small Molecules for Bulk Heterojunction Solar Cells and Field Effect Transistors. *Adv. Mater.* **26**, 1801–1826 (2014).
187. Stalder, R. *et al.* Ambipolar Charge Transport in Isoindigo-Based Donor–Acceptor Polymers. *Chem. Mater.* **28**, 1286–1297 (2016).
188. Yue, W. *et al.* Azaisoindigo conjugated polymers for high performance n-type and ambipolar thin film transistor applications. *J. Mater. Chem. C* **4**, 9704–9710 (2016).
189. Huang, J. *et al.* Diazaisoindigo-Based Polymers with High-Performance Charge-Transport Properties: From Computational Screening to Experimental Characterization. *Chem. Mater.* **28**, 2209–2218 (2016).
190. Chen, Z. *et al.* Multisubstituted Azaisoindigo-Based Polymers for High-Mobility Ambipolar Thin-Film Transistors and Inverters. *ACS Appl. Mater. Interfaces* **11**, 34171–34177 (2019).
191. Kim, M. *et al.* Controlling Ambipolar Charge Transport in Isoindigo-Based Conjugated Polymers by Altering Fluorine Substitution Position for High-Performance Organic Field-Effect Transistors. *Adv. Funct. Mater.* **29**, 1805994 (2019).
192. Jackson, N. E. *et al.* Controlling Conformations of Conjugated Polymers and Small Molecules: The Role of Nonbonding Interactions. *J. Am. Chem. Soc.* **135**, 10475–10483 (2013).
193. Dinçalp, H., Saltan, G. M., Zafer, C. & Mutlu, A. Synthesis and photophysical characterization of isoindigo building blocks as molecular acceptors for organic photovoltaics. *Spectrochim. Acta. A. Mol. Biomol. Spectrosc.* **202**, 196–206 (2018).
194. Hu, H. *et al.* Terthiophene-Based D–A Polymer with an Asymmetric Arrangement of Alkyl Chains That Enables Efficient Polymer Solar Cells. *J. Am. Chem. Soc.* **137**, 14149–14157 (2015).
195. Lee, J. Y., Song, K. W., Song, H. J. & Moon, D. K. Synthesis and photovoltaic property of donor–acceptor type conjugated polymer containing carbazole and 4,7-dithiazolylbenzothiadiazole moiety utilized as a promising electron withdrawing unit. *Synth. Met.* **161**, 2434–2440 (2011).

196. Estrada, L. A. *et al.* Understanding the Electronic Structure of Isoindigo in Conjugated Systems: A Combined Theoretical and Experimental Approach. *Macromolecules* **46**, 8832–8844 (2013).
197. Salvatori, P. *et al.* Computational Modeling of Isoindigo-Based Polymers Used in Organic Solar Cells. *J. Phys. Chem. C* **117**, 17940–17954 (2013).
198. Shin, E.-S. *et al.* Design of New Isoindigo-Based Copolymer for Ambipolar Organic Field-Effect Transistors. *ACS Appl. Mater. Interfaces* **10**, 13774–13782 (2018).
199. Lei, T. *et al.* Systematic Investigation of Isoindigo-Based Polymeric Field-Effect Transistors: Design Strategy and Impact of Polymer Symmetry and Backbone Curvature. *Chem. Mater.* **24**, 1762–1770 (2012).
200. Chen, M. S. *et al.* Control of Polymer-Packing Orientation in Thin Films through Synthetic Tailoring of Backbone Coplanarity. *Chem. Mater.* **25**, 4088–4096 (2013).
201. Sirringhaus, H. *et al.* Two-dimensional charge transport in self-organized, high-mobility conjugated polymers. *Nature* **401**, 685–688 (1999).
202. Osaka, I. & Takimiya, K. Backbone orientation in semiconducting polymers. *Polymer* **59**, A1–A15 (2015).
203. Schmode, P. *et al.* High-Performance Organic Electrochemical Transistors Based on Conjugated Polyelectrolyte Copolymers. *Chem. Mater.* **31**, 5286–5295 (2019).
204. Rivnay, J. *et al.* Organic Electrochemical Transistors with Maximum Transconductance at Zero Gate Bias. *Adv. Mater.* **25**, 7010–7014 (2013).
205. Khim, D. *et al.* Control of Ambipolar and Unipolar Transport in Organic Transistors by Selective Inkjet-Printed Chemical Doping for High Performance Complementary Circuits. *Adv. Funct. Mater.* **24**, 6252–6261 (2014).
206. Friedlein, J. T. *et al.* Influence of disorder on transfer characteristics of organic electrochemical transistors. *Appl. Phys. Lett.* **111**, 023301 (2017).
207. Page, Z. A., Liu, F., Russell, T. P. & Emrick, T. Tuning the energy gap of conjugated polymer zwitterions for efficient interlayers and solar cells. *J. Polym. Sci. Part Polym. Chem.* **53**, 327–336 (2015).
208. Shi, Q. *et al.* The Direct Arylation Polymerization (DArP) of Well-Defined Alternating Copolymers Based On 5,6-Dicyano[2,1,3]benzothiadiazole (DCBT). *Asian J. Org. Chem.* **7**, 1419–1425 (2018).
209. Casey, A. *et al.* Cyano substituted benzothiadiazole: a novel acceptor inducing n-type behaviour in conjugated polymers. *J. Mater. Chem. C* **3**, 265–275 (2014).

210. Khodagholy, D. *et al.* High transconductance organic electrochemical transistors. *Nat. Commun.* **4**, 2133 (2013).
211. Tamesue, S., Endo, T., Ueno, Y. & Tsurumaki, F. Sewing Hydrogels: Adhesion of Hydrogels Utilizing in Situ Polymerization of Linear Polymers inside Gel Networks. *Macromolecules* **52**, 5690–5697 (2019).
212. Liu, X. *et al.* Monitoring Fluorinated Dendrimer-Based Self-Assembled Drug-Delivery Systems with 19F Magnetic Resonance. *Eur. J. Org. Chem.* **2017**, 4461–4468 (2017).
213. Ec, D. *et al.* P-glycoprotein-dependent trafficking of nanoparticle-drug conjugates. *Small Weinh. Bergstr. Ger.* **10**, 1719–1723 (2014).
214. Mahou, R. & Wandrey, C. Versatile Route to Synthesize Heterobifunctional Poly(ethylene glycol) of Variable Functionality for Subsequent Pegylation. *Polymers* **4**, 561–589 (2012).
215. Allampally, N. K., Bredol, M., Strassert, C. A. & De Cola, L. Highly Phosphorescent Supramolecular Hydrogels Based on Platinum Emitters. *Chem. – Eur. J.* **20**, 16863–16868 (2014).
216. Meana, I., Albéniz, A. C. & Espinet, P. Selective Green Coupling of Alkynyltins and Allylic Halides to Trienynes via a Tandem Double Stille Reaction. *Adv. Synth. Catal.* **352**, 2887–2891 (2010).
217. Kinashi, N., Sakaguchi, K., Katsumura, S. & Shinada, T. Preparation of E-α-stannyl-β-trimethylsilylethynylacrylate, building block for polyconjugated ylidenebutenolide and its derivatives, by novel E-selective ethynylstannylation of propiolate. *Tetrahedron Lett.* **57**, 129–132 (2016).
218. Wang, S. *et al.* Thermoelectric Properties of Solution-Processed n-Doped Ladder-Type Conducting Polymers. *Adv. Mater.* **28**, 10764–10771 (2016).
219. Parr, Z. S. *et al.* Semiconducting Small Molecules as Active Materials for p-Type Accumulation Mode Organic Electrochemical Transistors. *Adv. Electron. Mater.* **n/a**, 2000215.
220. Sun, T., Xie, J., Guo, W., Li, D.-S. & Zhang, Q. Covalent–Organic Frameworks: Advanced Organic Electrode Materials for Rechargeable Batteries. *Adv. Energy Mater.* **10**, 1904199 (2020).
221. Wang, L. *et al.* A highly soluble, crystalline covalent organic framework compatible with device implementation. *Chem. Sci.* **10**, 1023–1028 (2019).

APPENDICES

APPENDIX A. Supplementary figures for Chapter 2

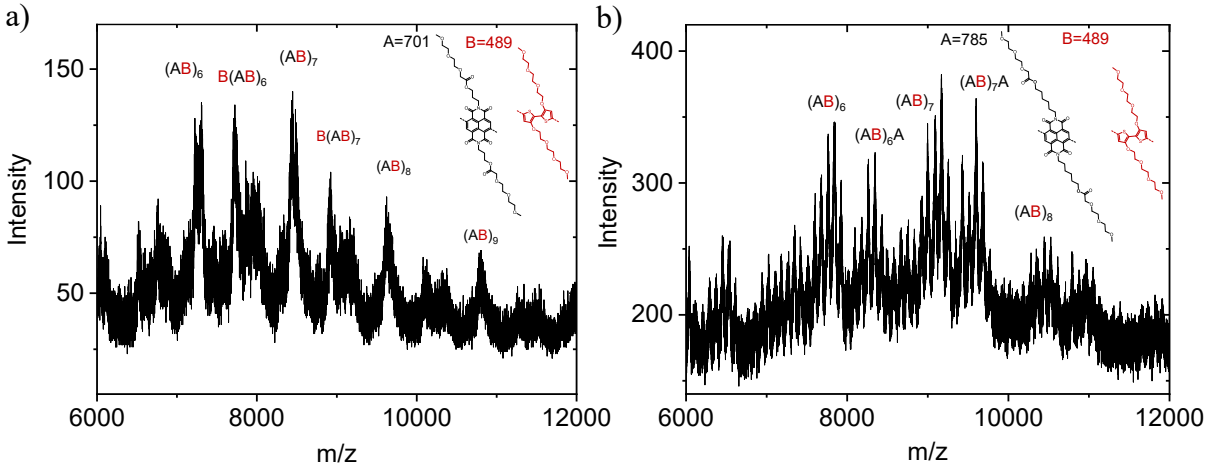


Figure A1. MALDI-ToF spectra of (a) **p(C3-gNDI-gT2)** and (b) **p(C6-gNDI-gT2)**.

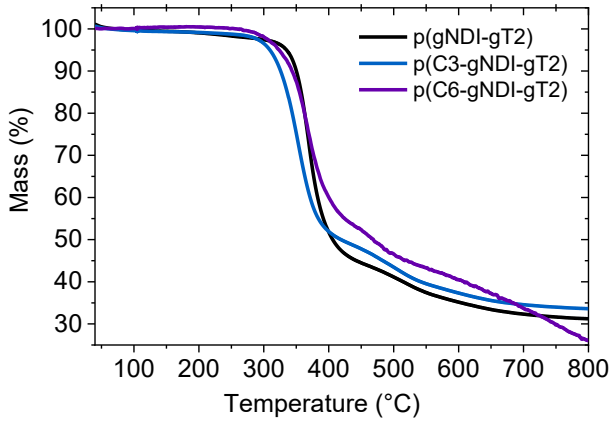


Figure A2. Thermogravimetric analysis of **p(gNDI-gT2)**, **p(C3-gNDI-gT2)** and **p(C6-gNDI-gT2)**. Polymers were heated under inert conditions (nitrogen flow) under the following conditions: [1] 30.0 to 105.0 °C, 34.99 K/min, N_2 50.0 ml/min, [2] 105.0 °C, 10.00 min, N_2 50.0 ml/min [3] 105.0 to 800.0 °C, 10.00 K/min, N_2 50.0 mL/min.

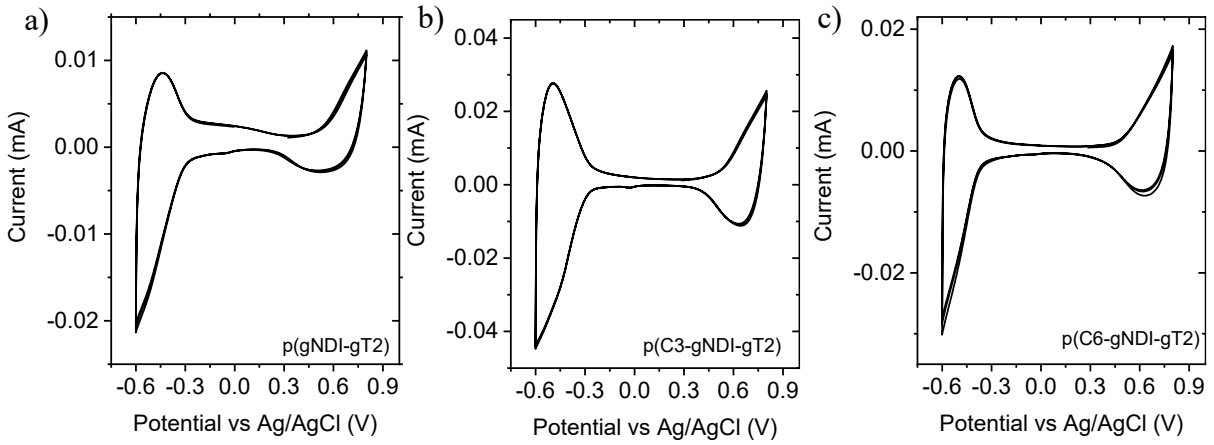


Figure A3. Cyclic voltammetry of (a) **p(gNDI-gT2)** (b) **p(C3-gNDI-gT2)** and (c) **p(C6-gNDI-gT2)** on ITO coated glass substrates in acetonitrile using $TBAPF_6$ as the supporting electrolyte (0.1 M) at 100 mV/s (2^{nd}, 3^{rd} and 4^{th} cycles).

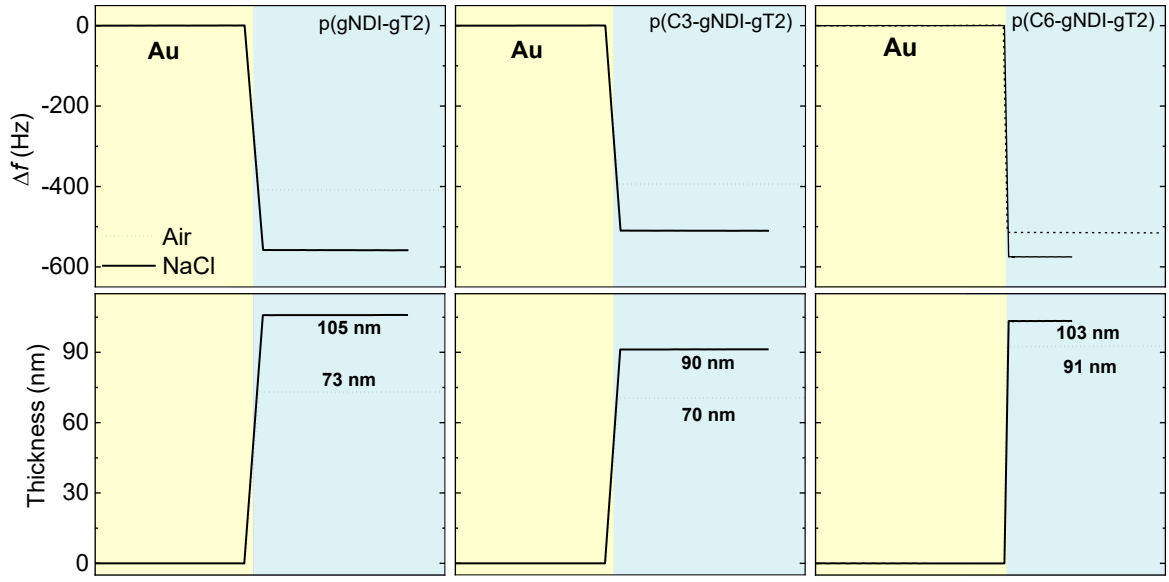


Figure A4. Frequency changes (Δf) and the corresponding calculated thicknesses of (left) **p(gNDI-gT2)** (middle) **p(C3-gNDI-gT2)** and (right) **(C6-gNDI-gT2)** films in air and in a 0.1 M NaCl aqueous solution using QCM measurements (7^{th} overtone shown for Δf).

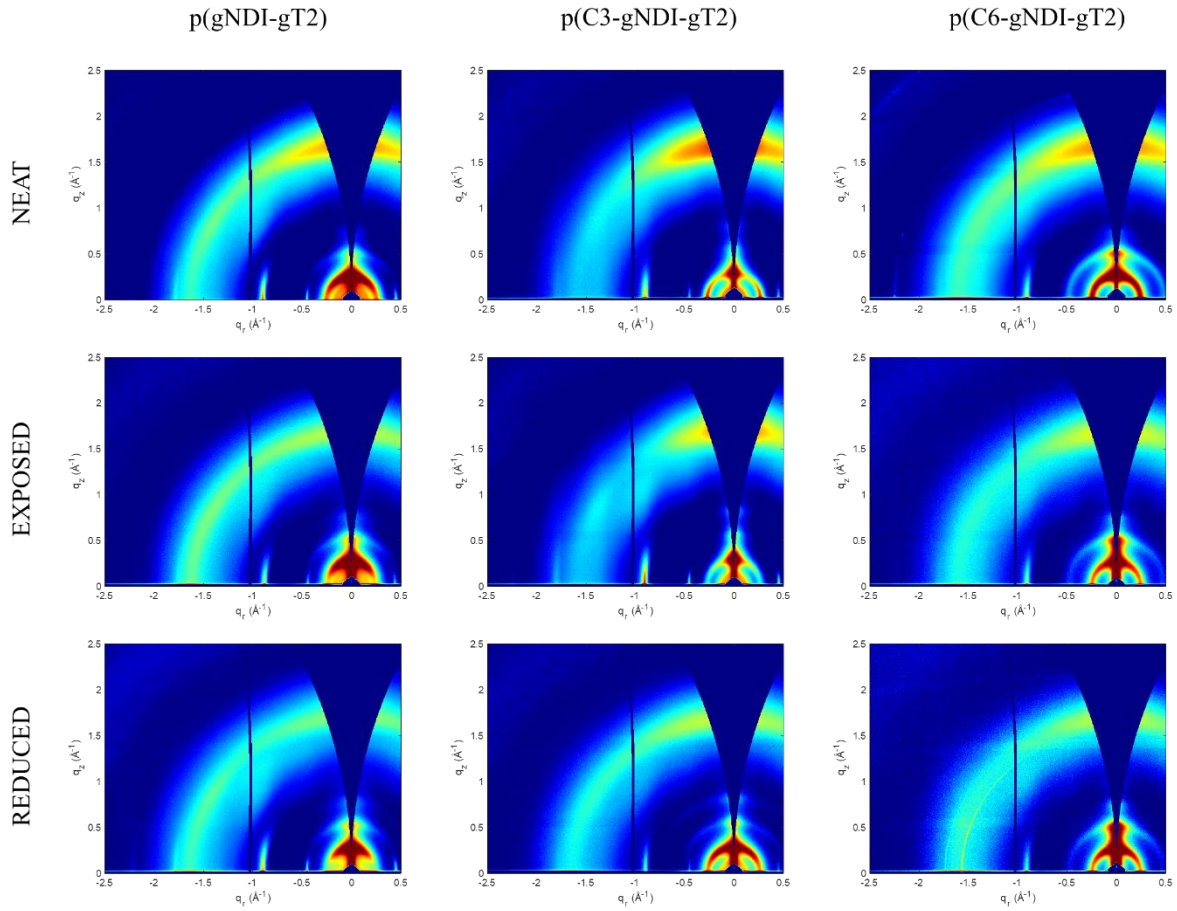


Figure A5. Ex situ GIWAXS: q_r-q_z plots of **p(gNDI-gT2)**, **p(C3-gNDI-gT2)** and **p(C6-gNDI-gT2)** neat (as cast), after ex situ electrolyte exposure and ex situ electrochemical reduction (n-type doping).

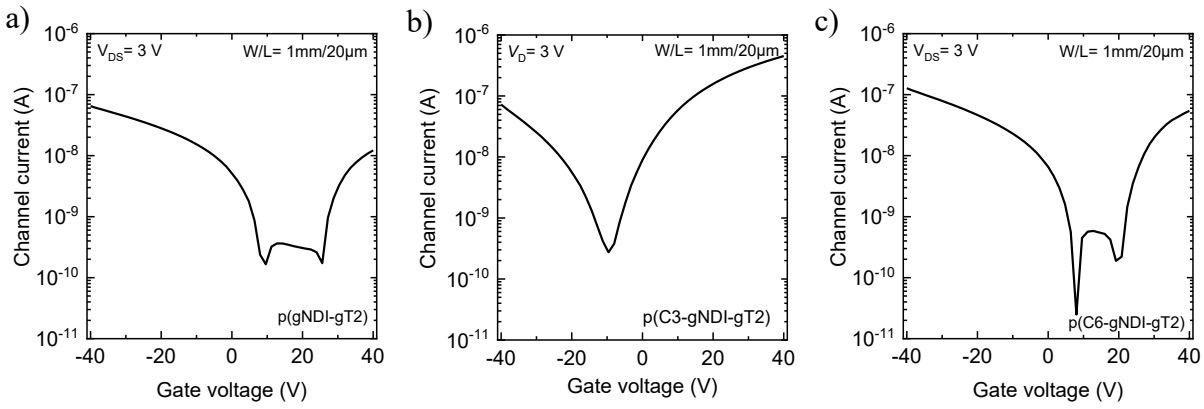


Figure A6. Transfer curves of (a) **p(gNDI-gT2)** (b) **p(C3-gNDI-gT2)** and (c) **p(C6-gNDI-gT2)** in OFETs with bottom-gate (Si) bottom-contact (Ti/Au) architecture, using silicon dioxide as the dielectric.

APPENDIX B. Supplementary figures for Chapter 3

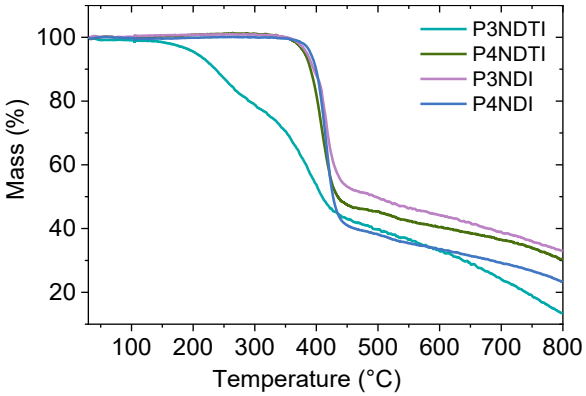


Figure B1. Thermogravimetric analysis of **P3gNDI**, **P4gNDI**, **P3gNDTI** and **P4gNDTI**. Polymers were heated under inert conditions (nitrogen flow) under the following conditions: [1] 30.0 to 105.0 °C, 34.99 K/min, N_2 50.0 ml/min, [2] 105.0 °C, 10.00 min, N_2 50.0 ml/min [3] 105.0 to 800.0 °C, 10.00 K/min, N_2 50.0 mL/min.

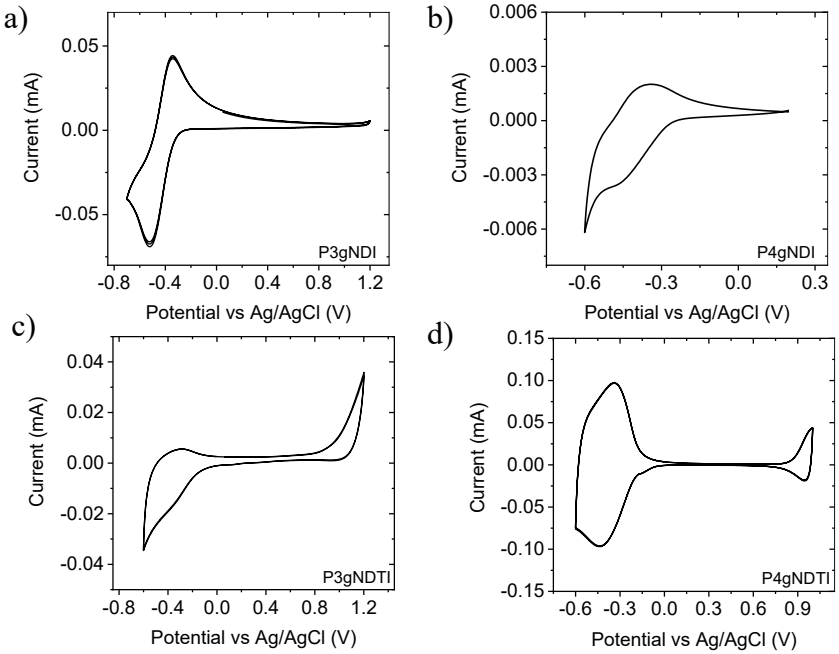


Figure B2. Cyclic voltammetry of (a) **P3gNDI** (b) **P4gNDI** (c) **P3gNDTI** and (d) **P4gNDTI** on glassy carbon electrodes in acetonitrile using $TBAPF_6$ as the supporting electrolyte (0.1 M) at 100 mV/s (2^{nd}, 3^{rd} and 4^{th} cycles shown, except for **P4gNDI** where only one cycle is shown as the polymer film is not stable in contact with acetonitrile).

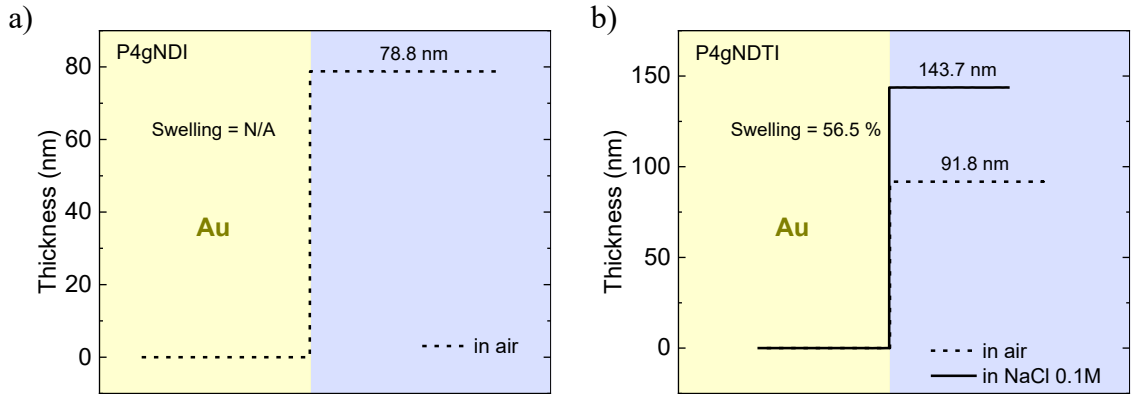


Figure B3. QCM-D measurements of (a) **P4gNDI** and (b) **P4gNDTI** showing calculated thicknesses and passive swelling of the polymer films in air and a 0.1 NaCl aqueous solution.

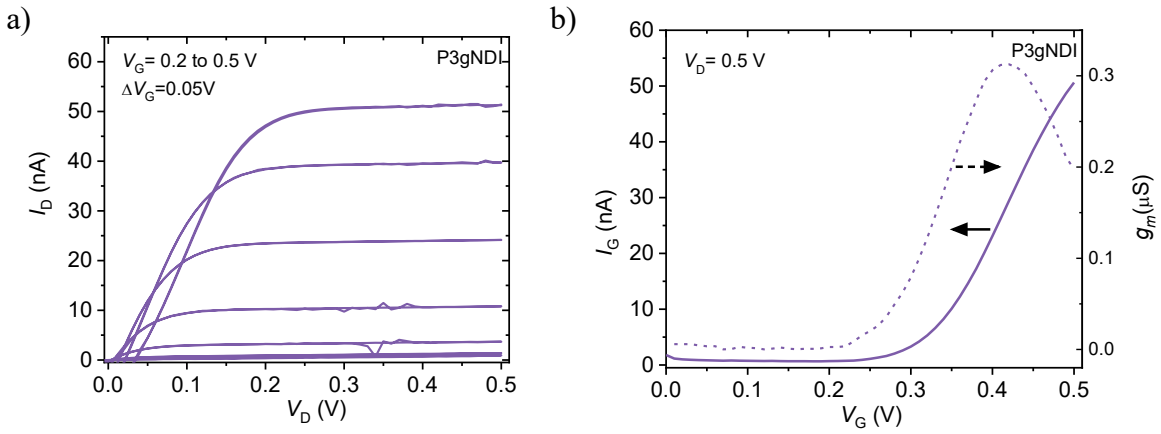


Figure B4. Performance of the **P3gNDI** OECT devices (W = 100 µm, L = 10 µm, d = 138 nm, 200 mV/s) in a 0.1 M NaCl aqueous solution in ambient conditions showing (a) output curve for 0.2 < V_G < 0.5 V with ΔV_G = 0.05 V (b) transfer curve at V_D = 0.5 V and the corresponding transconductance.

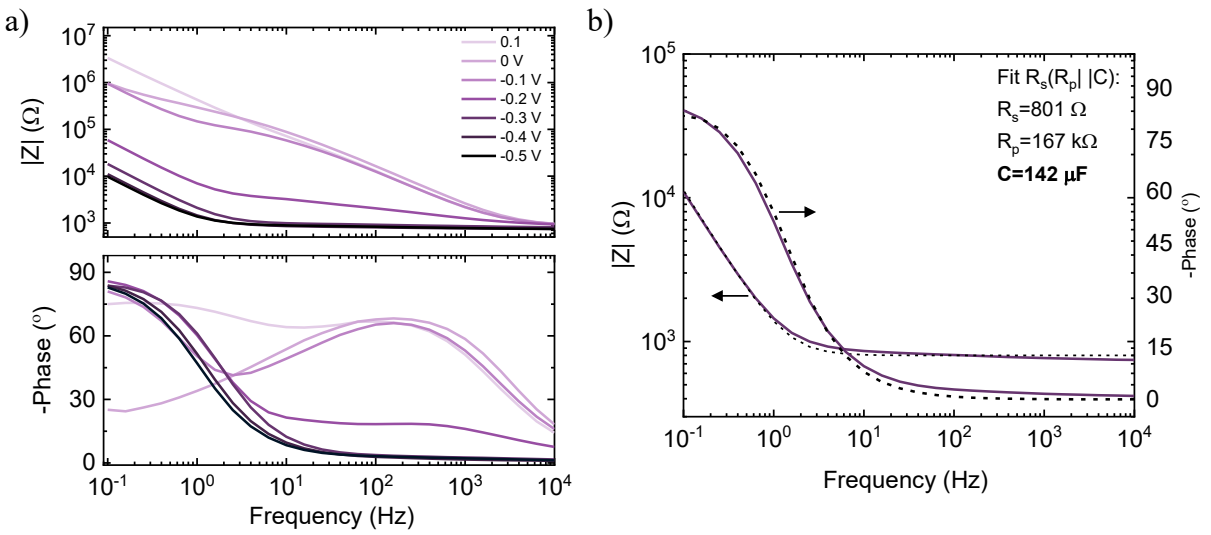


Figure B5. EIS measurements of **P3gNDI** in a 0.1 M NaCl aqueous solution in ambient conditions showing (a) impedance magnitude and phase and (b) impedance magnitude and phase at an offset bias of V = –0.4 V with the fits to a Randles circuit (dashed lines) versus frequency. The films were coated on a gold electrode with L = W = 600 µm, d = 2.88 µm.

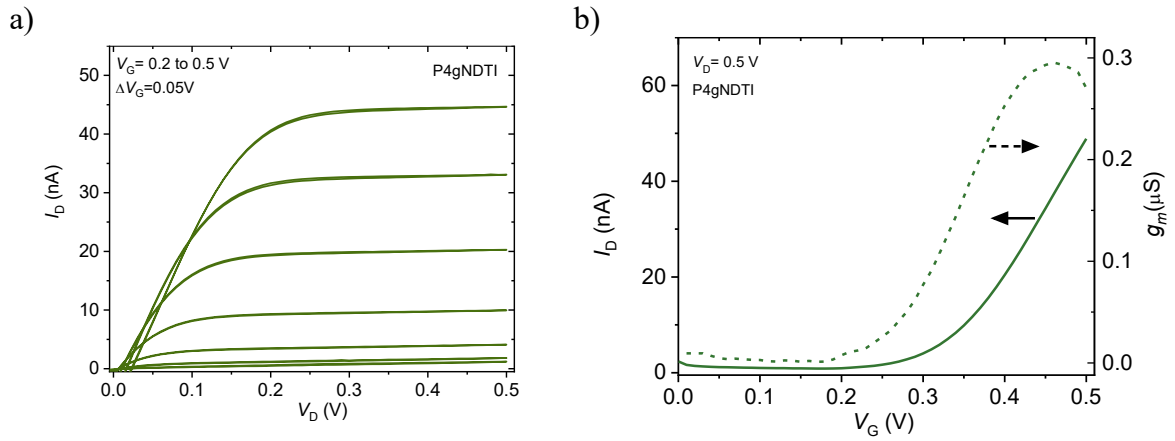


Figure B6. Performance of the **P4gNDTI** OECT devices (W = 100 µm, L = 10 µm, d = 122 nm, 200 mV/s) in a 0.1 M NaCl aqueous solution in ambient conditions showing (a) output curve for 0.2 < V_G < 0.5 V with ΔV_G = 0.05 V (b) transfer curve at V_D = 0.5 V and the corresponding transconductance.

APPENDIX C. Supplementary figures for Chapter 4

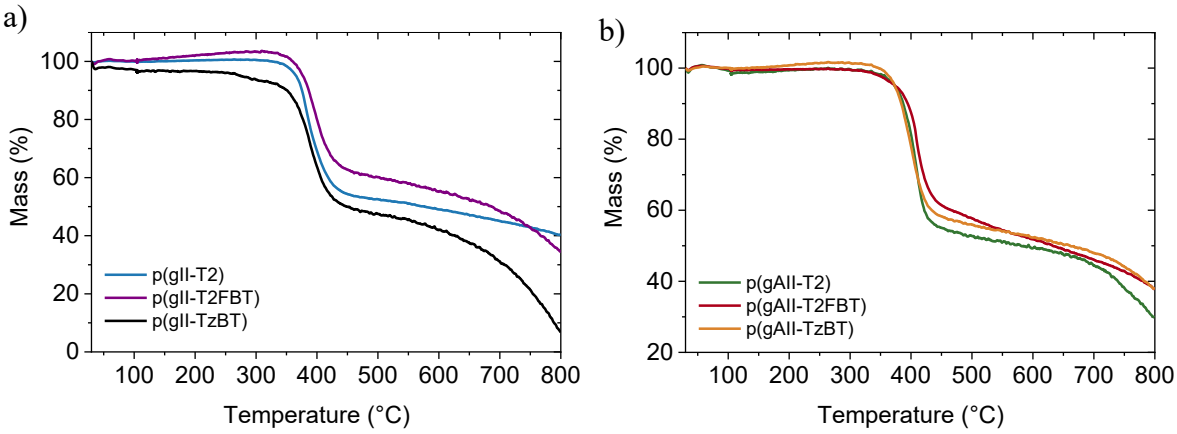


Figure C1. Thermogravimetric analysis of (a) isoindigo-based and (b) azaisoindigo-based polymers. Polymers were heated under inert conditions (nitrogen flow) under the following conditions: [1] 30.0 to 105.0 °C, 34.99 K/min, N_2 50.0 mL/min, [2] 105.0 °C, 10.00 min, N_2 50.0 ml/min [3] 105.0 to 800.0 °C, 10.00 K/min, N_2 50.0 mL/min.

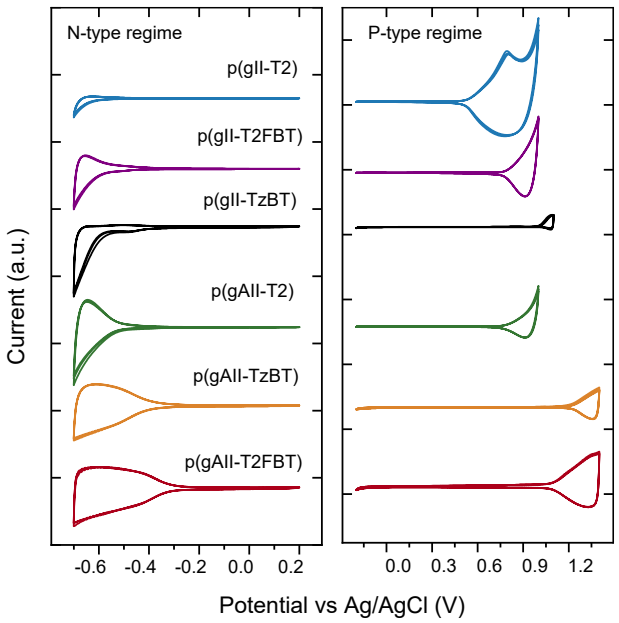


Figure C2. Cyclic voltammetry of (aza)isoindigo-based polymer films on glassy carbon electrodes in degassed 0.1 M $TBAPF_6$ solution in acetonitrile with a scan rate of 100 mV s^{-1} and a Ag/AgCl reference electrode (2^{nd}, 3^{rd} and 4^{th} cycles).

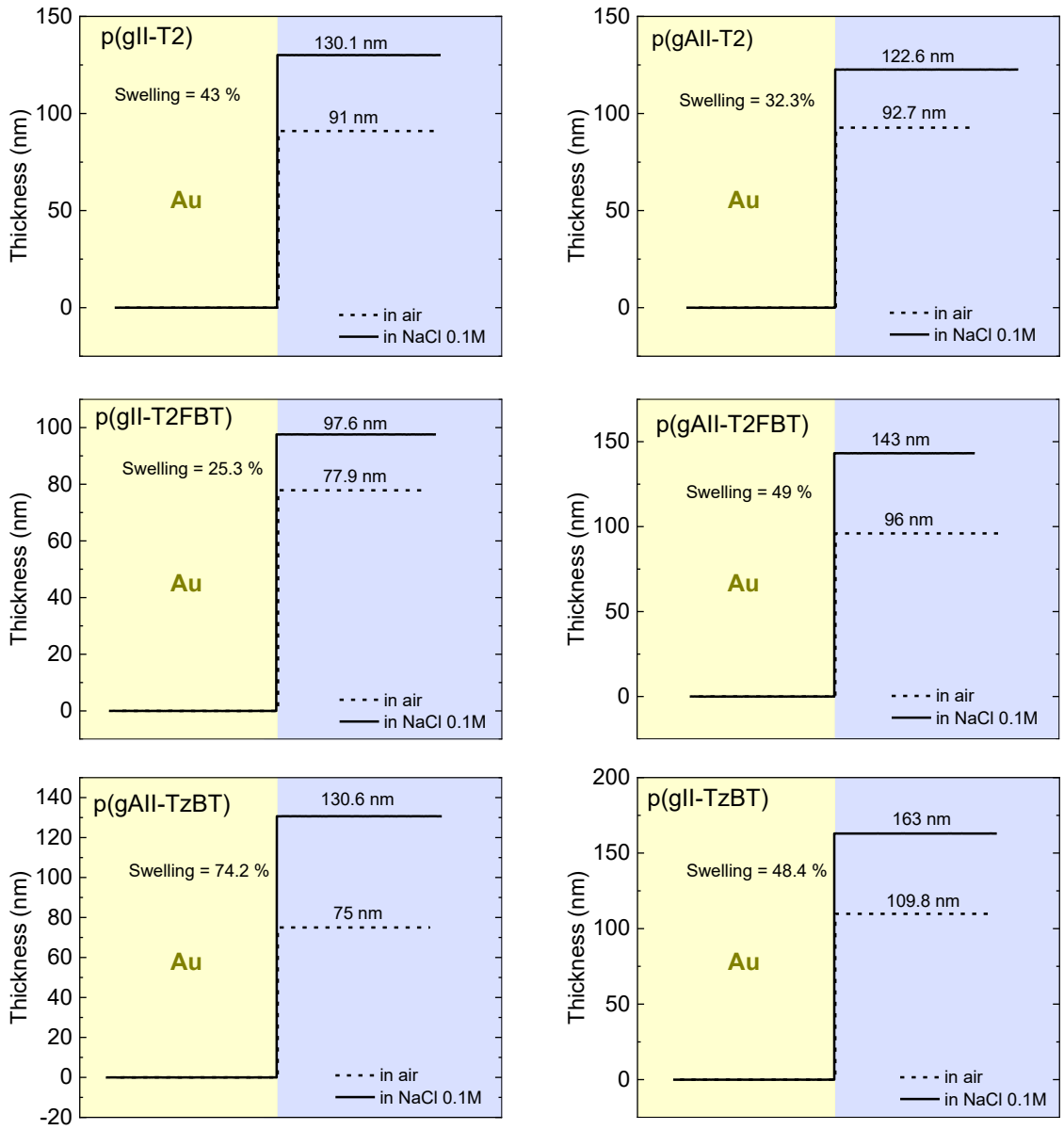


Figure C3. QCM-D measurements showing calculated thicknesses and passive swelling of (aza)isoindigo-based polymer films in air and a 0.1 NaCl aqueous solution.

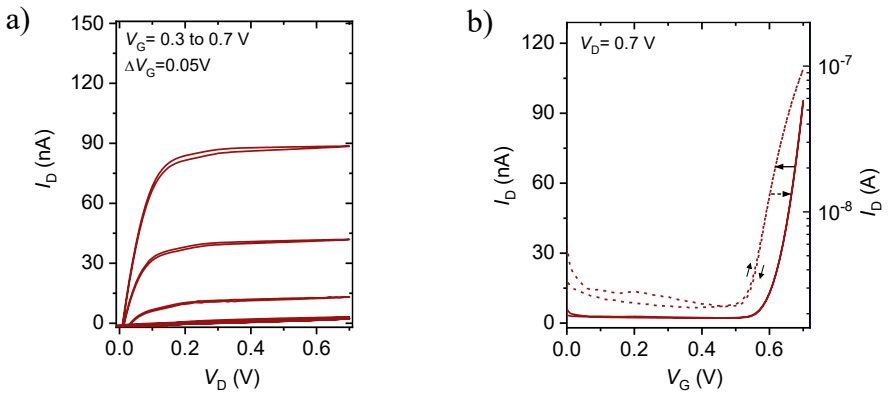


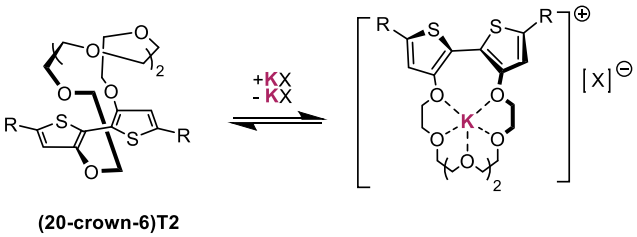
Figure C4. N-type performance of the **p(gAII-T2FBT)** (d = 82.3 nm) OECT devices (W = 100 µm, L = 10 µm, 200 mV/s) in a 0.1 M NaCl aqueous solution in ambient conditions showing (a) output curve for $0.3 < V_G < 0.7$ V with $\Delta V_G = 0.05$ V (b) transfer curve at V_D = 0.7 V on a linear and logarithmic scale (dashed lines), showing hysteresis with direction indicated with arrows.

APPENDIX D. K^+ ion sensors for plant monitoring

D1. Introduction

Potassium (K^+) is an essential macronutrient for plant growth and function, with crucial roles in nutrient transport, photosynthesis and stomata regulation.[1–3] Monitoring the distribution of K^+ ions in plants can advance the current understanding of how plants function and how their processes can be optimised. Stavrinidou and co-workers recently forged new directions in plant monitoring by manufacturing an organic electrochemical transistor (OECT) using plant tissue as the gating medium.[4] Remarkably, the plant was able to take up an aqueous solution of PEDOT-S:H and form conductive polymer wires embedded into its xylem, which served as the transistor channel, source and drain. This demonstration of employing organic electronic materials to introduce electronic functionality into plants inspired the search for more tailored π-conjugated systems that can act as K^+ ion sensors when interfaced with the plant.

Sensing of alkali metal cations in solution is often achieved using optical probes which undergo a change in absorbance or fluorescence properties upon analyte binding. These optical sensors typically consist of a chromophore that is covalently attached to an ion-binding macrocycle such as a crown ether,[5–7] cryptand[8] or calixarene.[9] An attractive detector unit that has been incorporated into conjugated polymers with high selectivity towards K^+ ions is the crown ether-functionalised bithiophene unit, **(20-crown-6)T2**, illustrated in **Scheme S1**.[5]



Scheme S1. Formation of complex and backbone twist upon binding of K^+ to **(20-crown-6)T2** (adapted from literature).[5]

Developed by Swager and co-workers,[6] the **(20-crown-6)T2** unit undergoes a reversible conformational twist upon complexation of K^+ ions, with an increase in the dihedral angle across the thiophene-thiophene bond from ~ 14.0° to 84.6° (**Scheme S1**).[5] When incorporated into conjugated polymers, the backbone twist of **(20-crown-6)T2** upon ion binding breaks the π-conjugation of the system and shifts its absorption maximum to shorter wavelengths, giving rise to a ratiometric colour change.[5] Despite their high selectivity and sensitivity for K^+ ions, these polymer sensors are not compatible with applications in plants as they can only be dissolved and probed in cytotoxic organic solvents such as acetonitrile and tetrahydrofuran.

To tailor for ion sensing applications in plants, **(20-crown-6)T2** was incorporated into a donor-acceptor template by coupling with electron deficient benzothiadiazole (BT) units as illustrated in **Figure S1**. The role of the flanking BT units is to decrease the band gap of the conjugated system and shift the absorption maximum of the detector unit after K^+ complexation (λ_{max} ~ 290 nm) to a wavelength range with lower interference from the absorption of chlorophyll pigments abundant in the plant (λ_{max} ~ 520–620 nm).[10] To ensure solubility in aqueous media, the small molecule was functionalised with polar imidazolium end groups attached via vinyl linkages. This section presents the synthetic routes towards **(20-crown6)T2BTI** and an investigation of its optical response upon binding of K^+ ions in organic and aqueous solutions.

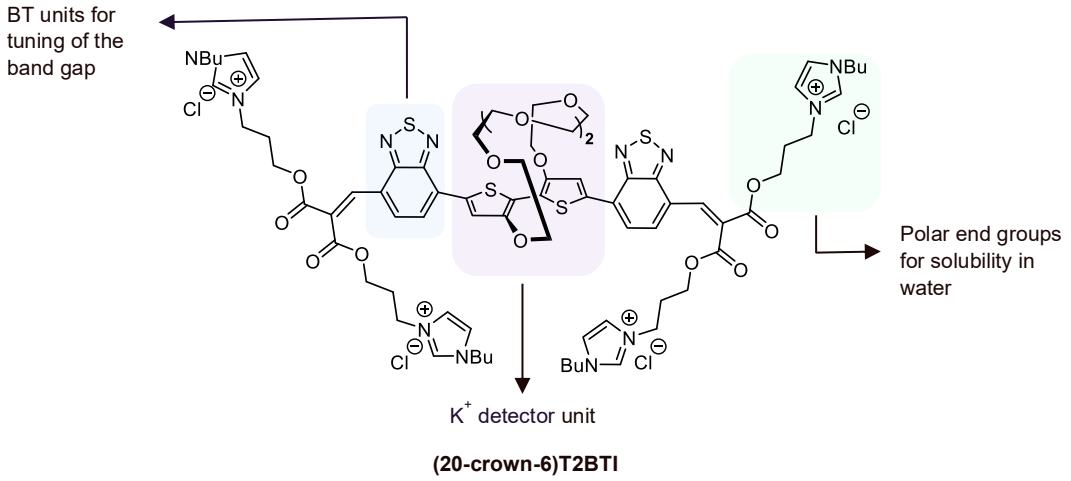
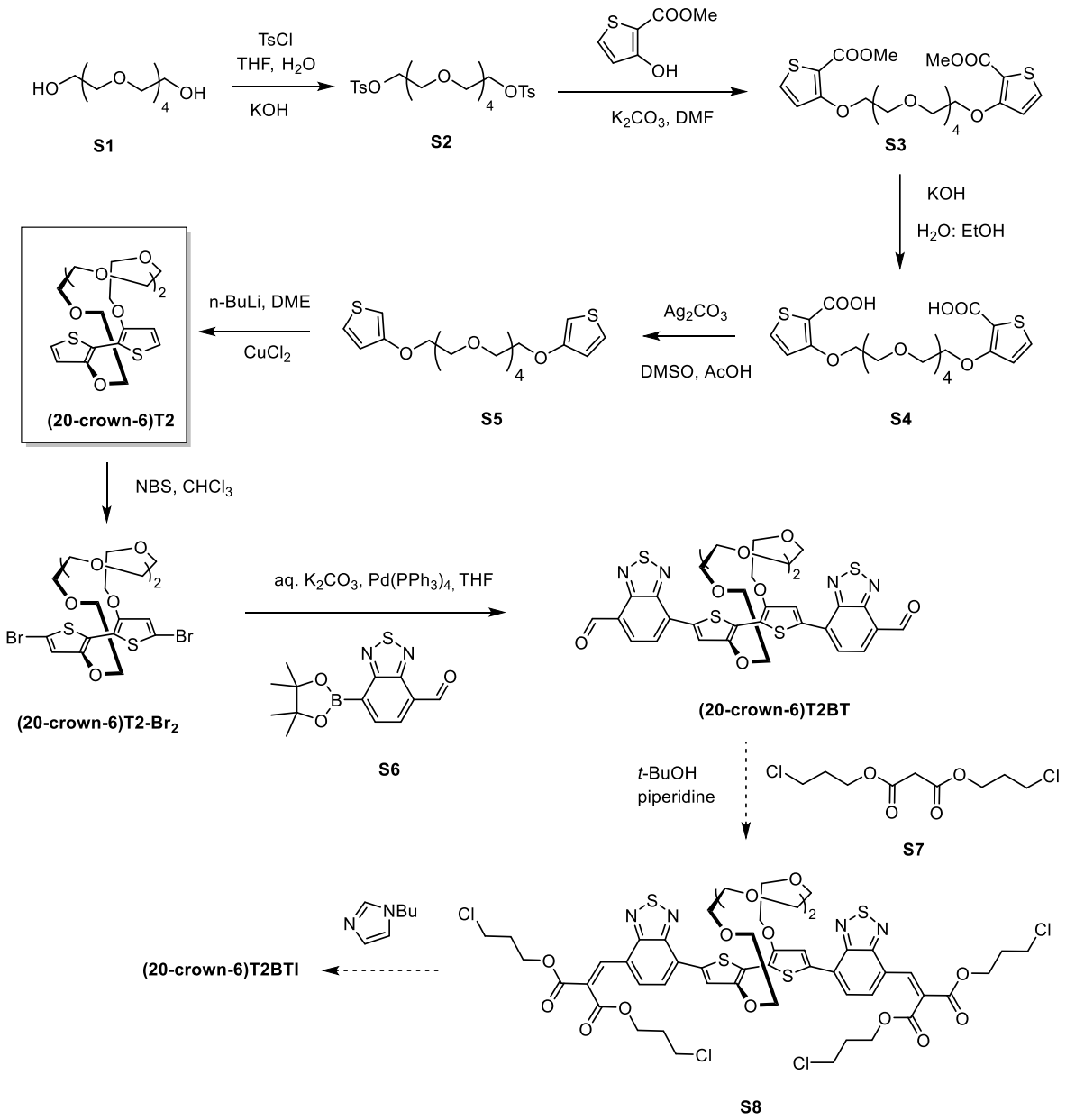


Figure S1. Design strategy of the small molecule ion sensor **(20-crown-6)T2BTI**.

D2. Synthesis of the small molecule

The synthetic route towards the detector unit **(20-crown-6)T2** was designed according to literature and commenced with preparation of the thiophene-flanked ethylene glycol derivative **S3 (Scheme S2)**.[5] Following hydrolysis of the ester at the thiophene 2-position, the resulting carboxylic acid **S4** was subjected to a protodecarboxylation reaction to generate **S5**. The protodecarboxylation reaction was modified to decrease the reaction time and increase the yield (76% versus 64% lit.)[5] by using a Ag_2CO_3/AcOH catalytic system.[11] A copper(II)-catalysed oxidative coupling was next employed to form the **(20-crown-6)T2** unit. To generate the donor-acceptor sensor, **(20-crown-6) T2** was brominated with NBS at –20 °C and subjected to a Suzuki cross coupling reaction with the boronic ester **S6**. Under Suzuki conditions, **(20-crown-6)T2BT** was obtained as a mixture containing unreacted starting material and mono-coupled product, which resulted in a low isolated yield of 21%.

Having successfully incorporated the detector unit into a donor-acceptor template, the next planned steps were attachment of end groups with a pendant chloride group and conversion into an imidazolium salt as shown in **Scheme S2**. Following a protocol by Zhou et al.,[12] Knoevenagel condensation of **(20-crown-6)T2BT** with bis(3-chloropropyl) malonate (**S7**) was attempted in the presence of catalytic amounts of piperidine. However, the starting materials were collected unreacted and these conditions failed to provide any of the desired product **S8**. Therefore, a screening of several conditions for the Knoevenagel condensation with the malonic ester **S7** was performed using 7-bromobenzo[c][1,2,5]thiadiazole-4-carbaldehyde (**S9**) as a model system. A summary of the results is presented in **Table S1**. Remarkably, a combination of catalytic amounts of $InCl_3$ as a Lewis acid and acetic anhydride[13] led to full conversion of the starting material into the Knoevenagel product **S10** and an isolated yield of 81%.

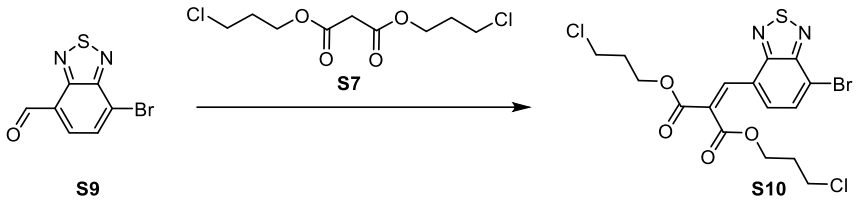


Scheme S2. Attempted route towards the synthesis of the small molecule ion sensor.

With **S10** in hand, it was reasoned that the synthetic route towards the small molecule ion sensor **(20-crown-6)T2BTI** could be greatly simplified by using C-H heteroarylation to couple **S10** with the detector unit **(20-crown-6)T2**.[14] As shown in **Scheme S3**, the product of the Knoevenagel condensation **S10** was subjected to a direct C-H heteroarylation using a $Pd(OAc)_2$/ P(*o*-anysyl)$_3$ catalyst system, which proceeded cleanly and afforded the product **S8** in a yield of 51%. Notably, this approach did not require bromination of the detector unit or synthesis of the boronic ester **S6** and resulted in a higher yield than the previous Suzuki

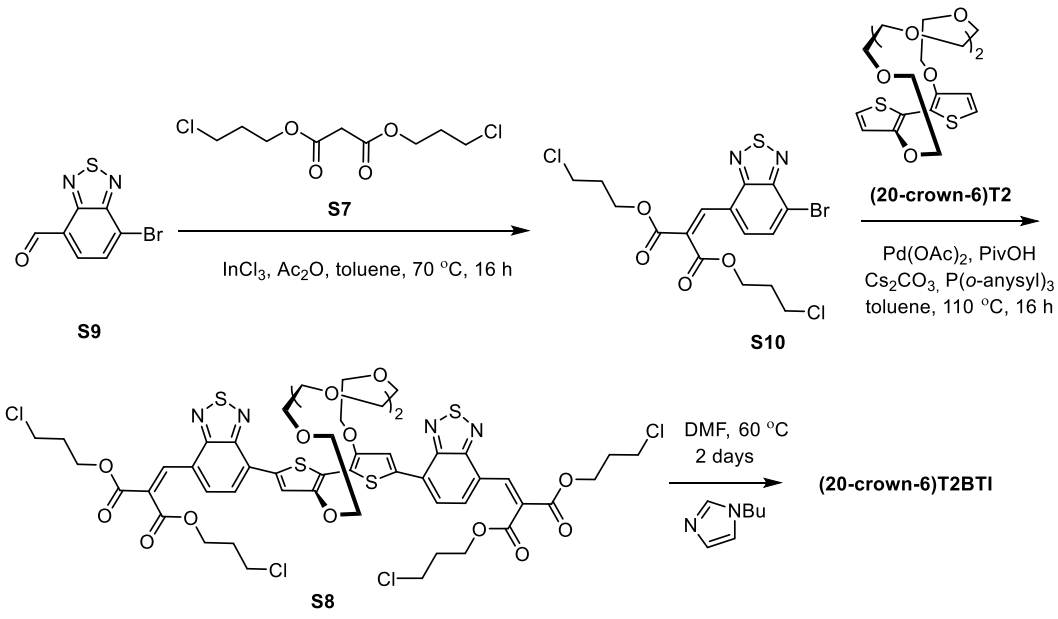
coupling. Adapting a protocol by Campisciano et al.,[15] **S8** was treated with 1-butylimidazole in DMF and heated to 60 °C for 2 days to afford the target small molecule ion sensor **(20-crown-6)T2BTI** in almost quantitative yields.

Table S1. Screening of reaction conditions for the Knoevenagel condensation.



Entry	Reaction conditions	% Product[a]
1	Piperidine, *t*-BuOH, 85 °C, 16 h	88%
2	Pyridine, *t*-BuOH, 85 °C, 16 h	–
3	Basic Al_2O_3, toluene, 70 °C, 16 h	5%
4	$InCl_3$, Ac_2O, toluene, 70 °C, 16 h	100%

[a] Conversion of starting material to product was estimated by ^{1}H NMR analysis.



Scheme S3. Optimised synthetic route towards the small molecule ion sensor.

Formation of the imidazolium salt was confirmed by NMR analysis, where **(20-crown-6)T2BTI** showed the expected 1-butylimidazole signals[15] and integration corresponding to

complete conversion into four charged end groups (**Figure E21**, Appendix E). Notably, the presence of the polar end groups endowed the small molecule with good solubility in water and methanol at room temperature.

D3. Optical response upon ion complexation

The ability of the detector unit to bind K^+ ions when incorporated into a donor-acceptor template was first investigated by titrations of its precursor **(20-crown-6)T2BT**. UV-Vis spectroscopy was used to monitor the optical changes of a solution of the sensor in acetonitrile upon successive additions of a solution of $KClO_4$, as illustrated in **Figure S2**.

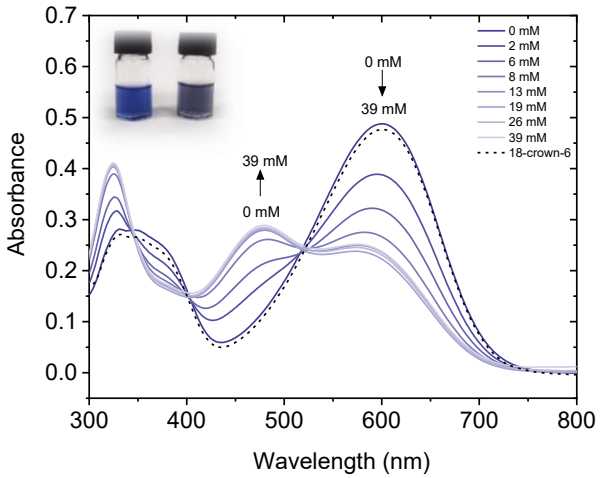


Figure S2. Evolution of the UV-Vis spectrum of **(20-crown-6)T2BT** upon titration with $KClO_4$ in acetonitrile (10 μM). The inset shows the colour change of the sensor solution before and after the titration.

In the unbound form, **(20-crown-6)T2BT** shows a dual-band absorption profile with an absorption maximum (λ_{max}) of 598 nm and appears blue in solution. Upon K^+ ion binding, the dominant absorption band is gradually quenched and a new feature emerges with a λ_{max} of 476 nm. The presence of three clear isosbestic points at ~344 nm, 400 nm and 520 nm indicates conversion of the small molecule into the K^+ complex with no competing side reactions. The formation of the complex in the presence of K^+ ions can be also detected visually, with a colour

change from blue to purple in the acetonitrile solution. The observed blue shift in λ_{max} is consistent with twisting of the bithiophene backbone upon K^+ complexation,[5] which disrupts the π-conjugation and increases the band gap of the small molecule. When 18-crown-6 is added to the solution after the complexation reaction, the initial spectrum is completely recovered, indicating that the backbone twisting upon ion binding is reversible.

Similar characterisation by UV-Vis spectroscopy was carried out for the small molecule ion sensor, **(20-crown-6)T2BTI**, by titrating in turn solutions of methanol and water with KCl (**Figure S3a**). In methanol, **(20-crown-6)T2BTI** shows the expected ratiometric response, with a blue-shift of the absorption maximum by ~125 nm, appearance of three isosbestic points at 351, 390 and 523 nm, as well as a colour change from blue to purple. The observed spectral changes are reversible and occur at low concentrations of K^+ between 0 to 133 mM, which matches the typical concentration range of K^+ ions in plants.[2] In sharp contrast, treatment of **(20-crown-6)T2BTI** as an aqueous solution with KCl only showed quenching of the absorption bands, with no indication of formation of a twisted complex. In addition, the features of the initial spectrum could not be recovered upon the addition of 18-crown-6, indicating that the quenching process is irreversible (**Figure S3b**).

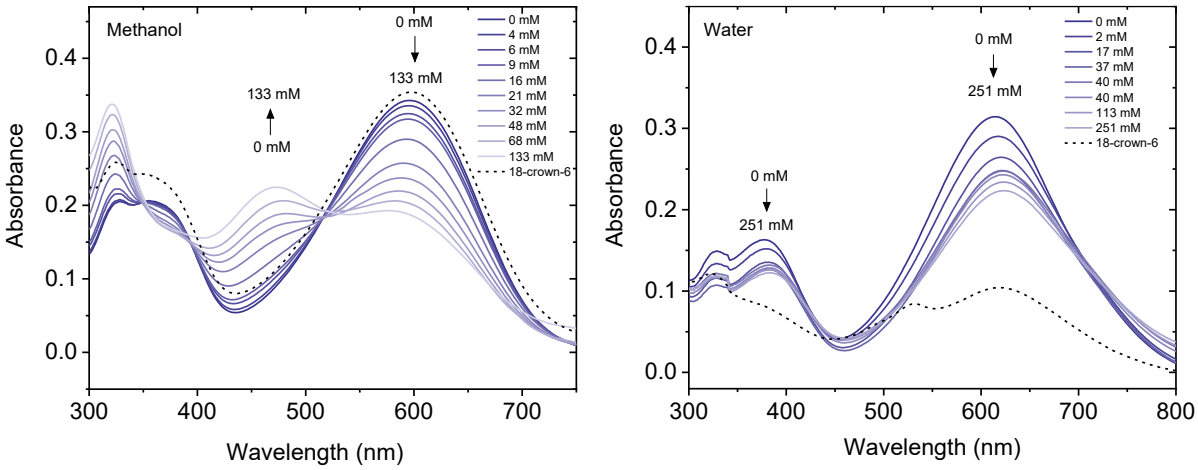


Figure S3. Evolution of the UV-Vis spectrum of **(20-crown-6)T2BTI** upon titration with KCl in (a) methanol (40 mM) and (b) in water (40 mM).

The optical responses of **(20-crown-6)T2BTI** indicate that despite its good sensing ability in organic solvents, the detector unit is not capable of binding aqueous cations at the investigated concentration ranges. Previous reports have suggested that crown ethers have weak ion binding properties in aqueous solutions, with a complex dissociation constant that can be up to three orders of magnitude higher in water versus organic solvents.[16,17] While a higher concentration might give the expected response, this would exceed the concentration range of K^+ ions relevant for plants.

D4. Conclusions and outlook

The ion selective unit **(20-crown-6)** was incorporated into a water soluble small molecule designed for K^+ ion sensing in plants by developing a modular synthetic route consisting of three steps. **(20-crown-6)T2BTI** shows ratiometric response upon binding of K^+ ions at concentrations on the order of mM in methanol solutions. However, the small molecule did not show any evidence of backbone twist and binding of ions when analysed in aqueous media. The lack of binding of aqueous ions precludes its use for biological applications, where organic solvents such as methanol would be toxic to living plant cells. Although not applicable to sensing applications in aqueous media, the design concept and synthetic protocols employed for **(20-crown-6)T2BTI** contributed to the development of a series of small molecule-based ion sensors with tuned absorption across the entire visible range.[18]

Alternative K^+ detector units based on phenyl aza-[18]-crown-6 moieties[19] with proven ratiometric response in aqueous media are currently being investigated (**Figure S4**). A challenge that remains unaddressed is tuning the band gap of the sensor such that the absorption of the complex has minimal overlap with chlorophyll pigments. To achieve this, functional groups with varying electron deficient character are currently being screened for functionalising the hemicyanine unit and tuning the strength of intramolecular charge transfer.

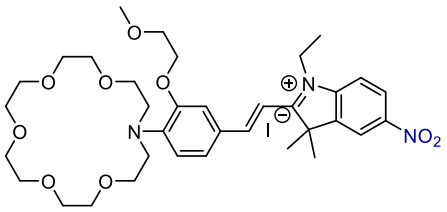
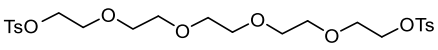


Figure S4. Proposed structure for alternative K^+ ion selective small molecule for plant monitoring.

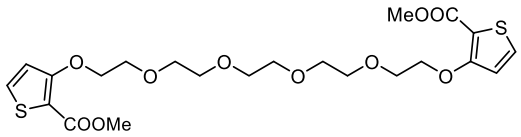
D5. Experimental procedures

*Pentaethylene glycol di(p-toluenesulfonate) (**S2**)*[20]



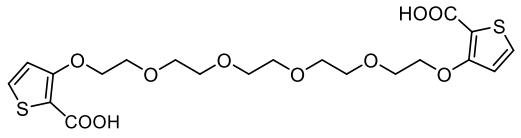
Adapting the procedure of Tanaka et al.,[21] a solution of pentaethylene glycol (6.0 mL, 28.4 mmol) in THF (30 mL) was added dropwise to a solution of KOH (6.27 g, 117.4 mmol) in distilled water (15 mL) at 0 °C. A solution of *p*-toluenesulfonyl chloride (11.46 g, 60.1 mmol) in THF (30 mL) was added to the mixture over 30 min at 0 °C and the resulting suspension was stirred overnight at room temperature. The mixture was poured over an ice-water mixture and extracted thoroughly with dichloromethane (3 × 200 mL). The organic fractions were washed with distilled water (3 × 100 mL) and dried over anhydrous $MgSO_4$. Removal of the solvent under reduced pressure afforded the product (15.2 g, 98%) as a pale-yellow oil. The crude product was used in the next step without further purification. ^{1}H NMR (400 MHz, chloroform-*d*) δ 7.80 (d, J = 8.3 Hz, 4H), 7.36 (d, J = 8.3 Hz, 4H), 4.22 – 4.12 (m, 4H), 3.70 – 3.59 (m, 16H), 2.46 (s, 6H). ^{13}C NMR (100 MHz, chloroform-*d*) δ 145.1, 133.3, 130.6, 128.33, 71.1, 71.0, 70.9, 69.6, 69.1, 22.0.

*Dimethyl-3,3'-((3,6,9,12-tetraoxatetradecane-1,14-diyl)bis(oxy))bis(thiophene-2-carboxylate) (**S3**)*[5]



Following the procedure of Giovannitti et al.,[5] **S2** (7.68 g, 14.05 mmol) was added dropwise to a solution of methyl 3-hydroxythiophene-2-carboxylate (4.44 g, 28.1 mmol) and potassium carbonate (3.88 g, 28.1 mmol) in anhydrous DMF (30 mL) at room temperature. The mixture was heated to 100 °C for 16 h. After cooling to room temperature, distilled water (50 mL) was added and the reaction mixture was extracted with diethyl ether (3 × 200 mL). The combined organic fractions were washed with distilled water (3 × 200 mL), dried over anhydrous $MgSO_4$ and concentrated *in vacuo* to give the title product (5.52 g, 76%) as a light brown oil. The crude product was used in the next step without further purification. ^{1}H NMR (400 MHz, chloroform-*d*) δ 7.38 (d, J = 5.5 Hz, 2H), 6.86 (d, J = 5.5 Hz, 2H), 4.30 – 4.25 (m, 4H), 3.90 – 3.86 (m, 4H), 3.82 (s, 6H), 3.77 – 3.73 (m, 4H), 3.65 (m, 8H). ^{13}C NMR (100 MHz, chloroform-*d*) δ 162.4, 161.5, 130.3, 117.8, 109.2, 72.0, 71.4, 71.0, 70.9, 70.0, 51.9.

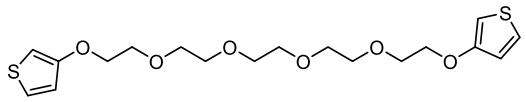
*3,3'-((3,6,9,12-Tetraoxatetradecane-1,14-diyl)bis(oxy))bis(thiophene-2-carboxylic acid) (**S4**)*[5]



Following the procedure of Giovannitti et al.,[5] potassium hydroxide (3.43 g, 61.1 mmol) was added in small portions to a suspension of **S3** (7.92 g, 15.3 mmol) in a mixture of EtOH: H_2O (1:4 v/v, 40 mL) at 0 °C. The resulting mixture was heated to 100 °C for 16 h. The solvent was removed under reduced pressure and an aqueous 2 M HCl solution was added until pH=1.0 was reached. The mixture was diluted with dichloromethane (100 mL) and the aqueous phase

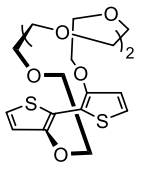
was separated and extracted with dicholoromethane (3 ×100 mL). The combined organic fractions were washed with distilled water (3 × 100 mL) and dried over anhydrous $MgSO_4$. Removal of the solvent under reduced pressure afforded the title product (7.26 g, 97%) as a light brown oil, which was used in the next step without further purification. ^{1}H NMR (400 MHz, chloroform-*d*) δ 7.50 (d, J = 5.5 Hz, 2H), 6.86 (d, J = 5.5 Hz, 2H), 4.36 – 4.31 (m, 4H), 3.90 (m, 4H), 3.77 (m, 4H), 3.70 (m, 8H). ^{13}C NMR (100 MHz, chloroform-*d*) δ 164.2, 160.2, 132.6, 117.0, 112.5, 72.4, 71.4, 71.0, 70.9, 69.4.

*1,14-Bis(thiophen-3-yloxy)-3,6,9,12-tetraoxatetradecane (**S5**)*[5]



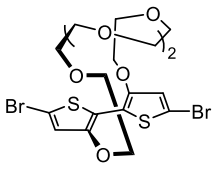
Adapting the method of Frontana et al.,[11] **S4** (2.06 g, 4.20 mmol) was added to a suspension of silver carbonate (0.46 g, 1.68 mmol) in degassed anhydrous DMSO (50 mL). Glacial acetic acid (13 mL) was added and the mixture was heated to 150 °C for 2 h 30 min. After cooling to 0 °C, the reaction mixture was quenched with an aqueous HCl solution (5 M, 10 mL) and the black precipitate was removed by filtration. The filtrate was extracted with ethyl acetate (3 × 50 mL), dried over anhydrous $MgSO_4$ and concentrated under reduced pressure. The crude residue was purified using column chromatography (toluene: ethyl acetate, 3:2) to afford the title product (1.28 g, 76%) as a yellow solid. ^{1}H NMR (400 MHz, chloroform-*d*) δ 7.16 (dd, J = 5.3, 3.1 Hz, 2H), 6.77 (dd, J = 5.3, 1.6 Hz, 2H), 6.25 (dd, J = 3.1, 1.6 Hz, 2H), 4.14 – 4.07 (m, 4H), 3.86 – 3.81 (m, 4H), 3.73 – 3.64 (m, 12H). ^{13}C NMR (100 MHz, chloroform-*d*) δ 157.9, 125.0, 119.9, 97.8, 71.1, 71.0, 70.0, 69.9.

(20-Crown-6)T2[5]



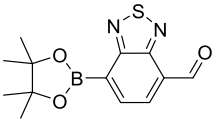
Following the method of Giovannitti et al.,[5] *n*-BuLi (2.5 M in hexane, 1.97 mL, 4.92 mmol) was added over 30 min to a solution of **S5** (0.9 g, 2.24 mmol) in anhydrous degassed DME (10 mL) at –20 °C. The brown suspension was stirred for 30 min at –20 °C and then allowed to reach 0 °C. The lithiated mixture was cannulated into a suspension of $CuCl_2$ (0.6 g, 4.46 mmol) in anhydrous degassed DME (10 mL) at 0 °C. The resulting green suspension was allowed to reach room temperature and stirred overnight. After quenching with distilled water (10 mL), the precipitate was filtered and washed with diethyl ether. The filtrate was extracted with diethyl ether (3 × 50 mL) and the combined organic fractions were washed with distilled water (3 × 50 mL), dried over anhydrous Na_2SO_4 and concentrated under reduced pressure. The crude residue was filtered through a silica plug (ethyl acetate: hexane, 50:50 to ethyl acetate) and recrystallised from diethyl ether to give the title product (0.30 g, 33%) as a pale yellow solid. ^{1}H NMR (400 MHz, acetone-d_6) δ 7.29 (d, J = 5.6 Hz, 2H), 7.02 (d, J = 5.6 Hz, 2H), 4.38 – 4.31 (m, 4H), 3.83 – 3.76 (m, 4H), 3.58 – 3.51 (m, 4H), 3.48 – 3.41 (m, 4H), 3.35 (s, 4H). ^{13}C NMR (100 MHz, acetone-d_6) δ 152.6, 122.3, 117.2, 113.5, 71.1, 70.9, 70.3, 70.2, 70.0.

(20-Crown-6)T2-Br$_2$[5]



Following the procedure of Giovannitti et al.,[5] NBS (0.17 g, 0.95 mmol) was added in two portions to a solution of **(20-crown-6)T2** (0.19 g, 0.46 mmol) in degassed anhydrous chloroform (12 mL) at –20 °C in the dark. The reaction mixture was stirred for 5 min at –20 °C, quenched with an aqueous $NaHCO_3$ solution (1 M, 10 mL) and diluted with chloroform (10 mL). The organic layer was separated, washed with distilled water (3 × 10 mL), dried over anhydrous Na_2SO_4 and concentrated under reduced pressure. The crude residue was purified by column chromatography (toluene: ethyl acetate, 1:1 with 3% triethylamine) and recrystallisation from a mixture of diethyl ether: THF (3:1) to afford the desired product (0.15 g, 58%) as yellow crystals. ^{1}H NMR (400 MHz, chloroform-*d*) δ 6.85 (s, 2H), 4.33 – 4.25 (m, 4H), 3.81 – 3.74 (m, 4H), 3.59 – 3.52 (m, 8H), 3.41 (s, 4H).

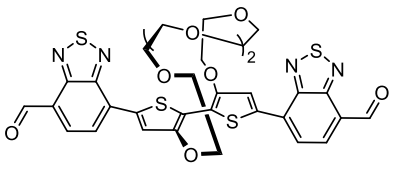
7-(4,4,5,5-Tetramethyl-1,3,2-dioxaborolan-2-yl)-2,1,3-benzothiadiazole-4-carboxaldehyde ***(S6)***



A mixture of 7-bromobenzo[c][1,2,5]thiadiazole-4-carbaldehyde (1.00 g, 4.11 mmol), bis(pinacolato)diboron (2.40 g, 9.46 mmol), potassium acetate (2.42 g, 24.66 mmol) and bis[(diphenylphosphino)ferrocene] dichloropalladium(II) (0.15 g, 0.21 mmol) was dried under vacuum for 2 h with vigorous stirring. Degassed anhydrous 1,4-dioxane (15 mL) was added and the reaction mixture was heated to 80 °C overnight. The reaction mixture was quenched with distilled water (5 mL) and extracted with ethyl acetate (3 × 50 mL). The combined organic

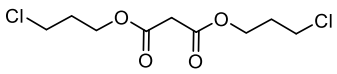
fractions were washed with saturated brine solution (3 × 50 mL), dried over anhydrous $MgSO_4$ and concentrated under reduced pressure. The crude residue was suspended in hot heptane and filtered through a celite pad, washing thoroughly with hot hexane. Removal of solvent under reduced pressure and recrystallisation from heptane afforded the title product (0.25 g, 21%) as a white solid. ^{1}H NMR (400 MHz, chloroform-*d*) δ 10.82 (s, 1H), 8.32 (d, J = 6.8 Hz, 1H), 8.19 (d, J = 6.8 Hz, 1H), 1.45 (s, 12H). ^{13}C NMR (400 MHz, chloroform-*d*) δ 189.8, 158.4, 152.9, 137.9, 130.9, 129.7, 85.2, 25.2. HRMS (ES-ToF): 291.0957 [M+H$^+$] (calc. 291.0957).

(20-Crown-6)T2BT



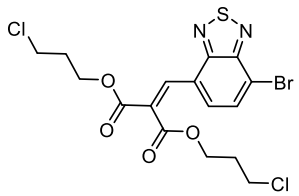
Degassed tetrahydrofuran (8 mL) was added to a mixture of **(20-crown-6)T2-Br$_2$** (68.3 mg, 0.12 mmol, 1 equiv), **S6** (82.0 mg, 0.28 mmol, 2.3 equiv) and tetrakis(triphenylphosphine) palladium (0) (8.5 mg, 7.4 μmol, 0.06 equiv) and the resulting mixture was flushed with nitrogen for 15 min. A degassed aqueous K_2CO_3 solution (1 M, 5 mL) was added and the resulting blue solution was stirred at 80 °C overnight. After allowing to reach room temperature, the mixture was extracted with DCM (3 × 50 mL). The combined organic fractions were washed with distilled water (3 × 50 mL), dried over anhydrous $MgSO_4$ and the solvent was removed *in vacuo*. The crude solid was purified by column chromatography (ethyl acetate:hexane, 1:1, then ethyl acetate) to give the title product (18.3 mg, 21%) as a dark blue solid. ^{1}H NMR (400 MHz, chloroform-*d*) δ 10.72 (s, 2H), 8.33 (s, 2H), 8.22 (d, J = 7.6 Hz, 2H), 7.99 (d, J = 7.6 Hz, 2H), 4.67 – 4.60 (m, 4H), 3.98 – 3.92 (m, 4H), 3.64 – 3.58 (m, 4H), 3.49– 3.43 (m, 4H), 3.25 (s, 4H). ^{13}C NMR (100 MHz, chloroform-*d*) δ 188.8, 154.9, 154.4, 152.7, 135.0, 133.3, 133.0, 125.5, 123.1, 120.0, 119.7, 72.3, 71.8, 71.1, 70.8, 70.5. HRMS (ES-ToF): 747.0709 [M+Na$^+$] (calc. 747.0688).

*Bis(3-chloropropyl) malonate (**S7**)*[15]



Modifying the procedure of Campisciano et al.,[16] malonyl dichloride (1.04 mL, 10.64 mmol) was added dropwise to a solution of 3-chloro-1-propanol (1.78 mL, 21.28 mmol) and pyridine (1.72 mL, 21.28 mmol) in anhydrous DCM (65 mL) at 0 °C. After stirring for a further 1 h at 0 °C, the mixture was allowed to reach room temperature overnight with stirring. The reaction mixture was diluted with DCM (60 mL) and the organic fractions were washed with aqueous HCl solution (2 M, 3 × 60 mL), aqueous saturated $NaHCO_3$ (3 × 60 mL), distilled water (3 × 50 mL) and dried over anhydrous Na_2SO_4. The solvent was removed under reduced pressure and the crude residue was purified by column chromatography (DCM: petroleum ether, 3:2) to give the title product (1.73 g, 63%) as a light-yellow oil. ^{1}H NMR (400 MHz, chloroform-*d*) δ 4.32 (t, J = 6.2 Hz, 4H), 3.62 (t, J = 6.2 Hz, 4H), 3.40 (s, 2H), 2.12 (p, J = 6.2 Hz, 4H). ^{13}C NMR (100 MHz, chloroform-*d*) δ 166.6, 66.2, 43.7, 41.3, 31.7. HRMS (ES-ToF): 257.0343 [M+H$^+$] (calc. 257.0342).

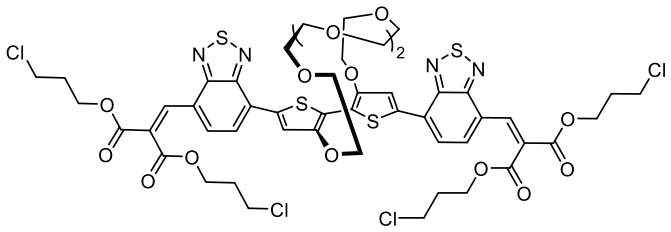
*Bis(3-chloropropyl)2-((7-bromobenzo[c][1,2,5]thiadiazol-4-yl)methylene)malonate (**S10**)*



Adapting the method of Ogiwara et al.,[13] 7-bromobenzo[c][1,2,5]thiadiazole-4-carbaldehyde (400 mg, 1.56 mmol, 1 equiv) and indium (III) chloride (34.4 mg, 0.156 mmol, 0.1 equiv) were suspended in anhydrous toluene (10 mL). **S7** (564.5 mg, 2.33 mmol, 1.5 equiv) and acetic anhydride (158.24 mg, 1.56 mmol, 1 equiv) were added to the reaction mixture and the resulting suspension was heated to 70 °C overnight. After cooling to room temperature, the brown solution was extracted with ethyl acetate (3 × 50 mL). The combined organic fractions

were washed with saturated aqueous $NaHCO_3$ (3 × 50 mL), distilled water (3 × 50 mL), dried over anhydrous $MgSO_4$ and concentrated under reduced pressure. Recrystallisation from hexane: ethyl acetate (95:5) afforded the title product (590 mg, 78%) as a yellow solid. ^{1}H NMR (400 MHz, chloroform-*d*) δ 8.38 (s, 1H), 7.88 (d, J = 7.6 Hz, 1H), 7.64 (dd, J = 7.6, 0.9 Hz, 1H), 4.47 (t, J = 6.1 Hz, 2H), 4.41 (t, J = 6.1 Hz, 2H), 3.66 (t, J = 6.2 Hz, 2H), 3.52 (t, J = 6.2 Hz, 2H), 2.22 (p, J = 6.2 Hz, 2H), 2.11 (p, J = 6.1 Hz, 2H). ^{13}C NMR (100 MHz, chloroform-*d*) δ 165.7, 163.4, 153.3, 153.1, 136.8, 132.0, 129.6, 128.4, 125.8, 117.3, 62.7, 62.4, 41.0, 40.8, 31.5, 31.1. HRMS (ES-ToF): 481.9297 (calc. 481.9292).

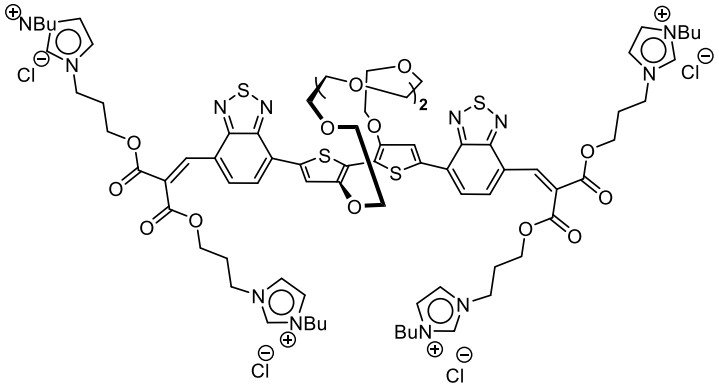
*Tetrakis(3-chloropropyl) 2,2'-(((5,6,8,9,11,12,14,15,17,18-decahydrodithieno[3,2-q:2',3'-s][1,4,7,10,13,16]hexaoxacycloicosine-2,21-diyl)bis(benzo[c][1,2,5]thiadiazole-7,4-diyl))bis(methaneylylidene))dimalonate (**S8**)*



Anhydrous degassed toluene (5 mL) was added to a mixture of **(20-crown-6)T2** (54.18 mg, 0.14 mmol,), **S10** (143.50 mg, 0.30 mmol, 2.2 equiv) palladium (II) acetate (0.63 mg, 2.80 µmol, 0.02 equiv), tris(*o*-methoxyphenyl)phosphine (1.76 mg, 5.60 µmol, 0.04 equiv), pivalic acid (14.30 mg, 0.14 mmol, 1 equiv) and cesium carbonate (136.84 mg, 0.42 mmol, 3.0 equiv) under nitrogen and the resulting blue solution was stirred overnight at 110 °C. After allowing to reach room temperature, the mixture was extracted with DCM (3 × 30 mL). The combined organic fractions were washed with distilled water (3 × 30 mL), dried over anhydrous $MgSO_4$ and the solvent was removed *in vacuo*. The crude solid was dissolved in dichloromethane and precipitated into methanol to give the title product (86 mg, 51%) as a dark blue solid. ^{1}H NMR (400 MHz, chloroform-*d*) δ 8.50 (s, 2H), 8.23 (s, 2H), 7.86 (d, J = 7.7 Hz, 2H), 7.79 (d, J = 7.7 Hz, 2H), 4.61-4.55 (m, 4H), 4.50-4.46 (m, 8H), 3.97-3.90 (m, 4H), 3.68 (t, J = 6.2 Hz, 4H),

3.65 – 3.60 (m, 4H), 3.56 (t, J = 6.1 Hz, 4H), 3.52 – 3.42 (m, 4H), 3.28 (s, 4H), 2.23 (p, 6.2 Hz, 4H), 2.15 (p, 6.1 Hz, 4H). ^{13}C NMR (100 MHz, chloroform-*d*) δ 166.7, 164.2, 154.9, 154.4, 152.1, 137.6, 135.1, 130.2, 130.0, 126.7, 124.1, 123.8, 119.1,118,5, 72.3, 71.8, 71.0, 70.7, 70.5, 62.8, 62.7, 41.4, 41.3, 31.9, 31.5.HRMS (ES-ToF): 1202.1135 (calc. 1202.0355).

(20-Crown-6)T2BTI



1-butylimidazole (1 mL) was added to a solution of **S8** (20.6 mg, 0.017 mmol) in anhydrous DMF (1 mL) and the resulting mixture was heated to 60 °C for 2 days. After allowing to cool to room temperature, the solvent was removed under reduced pressure. The crude product was suspended in distilled water (10 mL) and washed with dichloromethane (3 × 20 mL) and hexane (3 × 20 mL). The aqueous fraction was concentrated under reduced pressure to give the title product (26.0 mg, 98%) as a blue waxy solid. ^{1}H NMR (400 MHz, methanol-*d*) δ 8.40 (m, 2H), 8.28 (m, 2H), 8.10 – 7.61 (m, 12H), 4.63 (m, 4H), 4.55 – 4.16 (m, 20H), 3.97 (m, 4H), 3.62 (m, 4H), 3.43 (m, 4H), 2.48 (m, 4H), 2.31 (m, 4H), 1.90 (m, 8H), 1.38 (m, 4H), 0.99 (m, 12H).

D6. References

1. Gierth, M. & Mäser, P. Potassium transporters in plants – Involvement in K+ acquisition, redistribution and homeostasis. *FEBS Lett.* **581**, 2348–2356 (2007).
2. Wang, Y. i. & Wu, W.-H. Plant Sensing and Signaling in Response to K+-Deficiency. *Mol. Plant* **3**, 280–287 (2010).
3. Wang, Y. & Wu, W.-H. Potassium Transport and Signaling in Higher Plants. *Annu. Rev. Plant Biol.* **64**, 451–476 (2013).
4. Stavrinidou, E. *et al.* Electronic plants. *Sci. Adv.* **1**, e1501136 (2015).
5. Giovannitti, A. *et al.* Sodium and Potassium Ion Selective Conjugated Polymers for Optical Ion Detection in Solution and Solid State. *Adv. Funct. Mater.* **26**, 514–523 (2016).
6. Marsella, M. J. & Swager, T. M. Designing conducting polymer-based sensors: selective ionochromic response in crown ether-containing polythiophenes. *J. Am. Chem. Soc.* **115**, 12214–12215 (1993).
7. Qiu, J. *et al.* Rapid colorimetric detection of potassium ions based on crown ether modified Au NPs sensor. *Sens. Actuators B Chem.* **281**, 783–788 (2019).
8. Carpenter, R. D. & Verkman, A. S. Function-Oriented Synthesis of a Didesmethyl Triazacryptand Analogue for Fluorescent Potassium Ion Sensing. *Eur. J. Org. Chem.* **2011**, 1242–1248 (2011).
9. Kumar, R. *et al.* Revisiting Fluorescent Calixarenes: From Molecular Sensors to Smart Materials. *Chem. Rev.* **119**, 9657–9721 (2019).
10. Colmano, G. Visible Absorption Spectrum of Chlorophyll a , b , and β-Carotene Molecules mixed in Monolayers at a Water–Air Interface. *Nature* **193**, 1287–1288 (1962).
11. Cisneros-Pérez, P. A., Martínez-Otero, D., Cuevas-Yánez, E. & Uribe-Frontana, B. A. Diprotodecarboxylation Reactions of 3,4-Dialkoxythiophene-2,5-dicarboxylic Acids Mediated by Ag2CO3 and Microwaves. *Synth. Commun.* **44**, 222–230 (2014).
12. Zhou, J. *et al.* Small Molecules Based on Benzo[1,2-b:4,5-b′]dithiophene Unit for High-Performance Solution-Processed Organic Solar Cells. *J. Am. Chem. Soc.* **134**, 16345–16351 (2012).
13. Ogiwara, Y., Takahashi, K., Kitazawa, T. & Sakai, N. Indium(III)-Catalyzed Knoevenagel Condensation of Aldehydes and Activated Methylenes Using Acetic Anhydride as a Promoter. *J. Org. Chem.* **80**, 3101–3110 (2015).

14. Liu, C.-Y., Zhao, H. & Yu, H. Efficient Synthesis of 3,4-Ethylenedioxythiophene (EDOT)-Based Functional π-Conjugated Molecules through Direct C–H Bond Arylations. *Org. Lett.* **13**, 4068–4071 (2011).
15. Campisciano, V., La Parola, V., Liotta, L. F., Giacalone, F. & Gruttadauria, M. Fullerene–Ionic-Liquid Conjugates: A New Class of Hybrid Materials with Unprecedented Properties. *Chem. – Eur. J.* **21**, 3327–3334 (2015).
16. Schwarze, T., Müller, H., Schmidt, D., Riemer, J. & Holdt, H.-J. Design of Na+-Selective Fluorescent Probes: A Systematic Study of the Na+-Complex Stability and the Na+/K+ Selectivity in Acetonitrile and Water. *Chem. – Eur. J.* **23**, 7255–7263 (2017).
17. Minta, A. & Tsien, R. Y. Fluorescent indicators for cytosolic sodium. *J. Biol. Chem.* **264**, 19449–19457 (1989).
18. Moser, M. *et al.* Highly selective chromoionophores for ratiometric Na + sensing based on an oligoethyleneglycol bridged bithiophene detection unit. *J. Mater. Chem. C* **7**, 5359–5365 (2019).
19. Song, G., Sun, R., Du, J., Chen, M. & Tian, Y. A highly selective, colorimetric, and environment-sensitive optical potassium ion sensor. *Chem. Commun.* **53**, 5602–5605 (2017).
20. Shen, J.-C. *et al.* A rings-in-pores net: crown ether-based covalent organic frameworks for phase-transfer catalysis. *Chem. Commun.* **56**, 595–598 (2020).
21. Tanaka, M. *et al.* Properties of modified surface for biosensing interface. *J. Colloid Interface Sci.* **497**, 309–316 (2017).

APPENDIX E. NMR Spectra

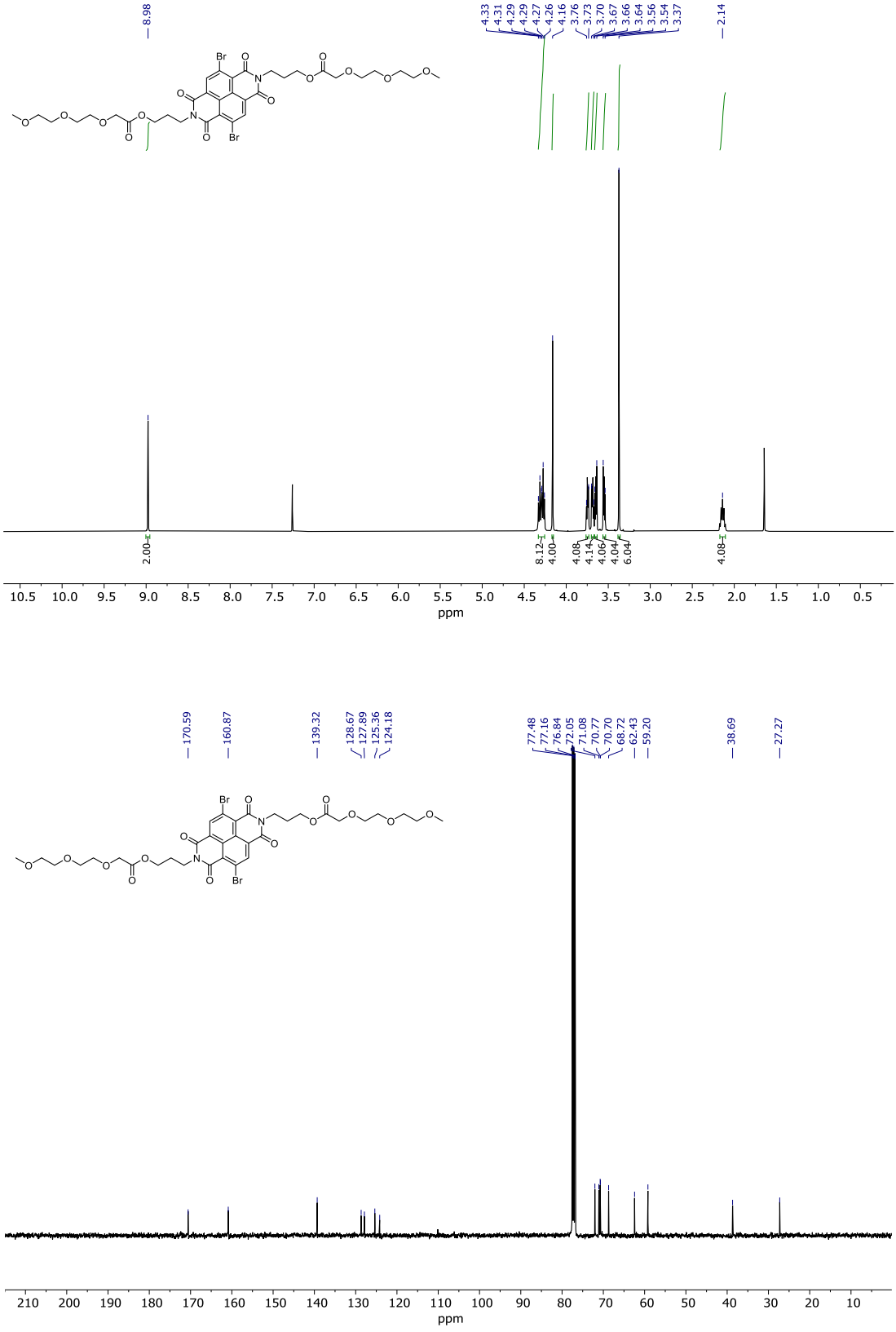


Figure E1. ^{1}H NMR (400 MHz) and ^{13}C NMR (100 MHz) spectra of **2.2** in $CDCl_3$.

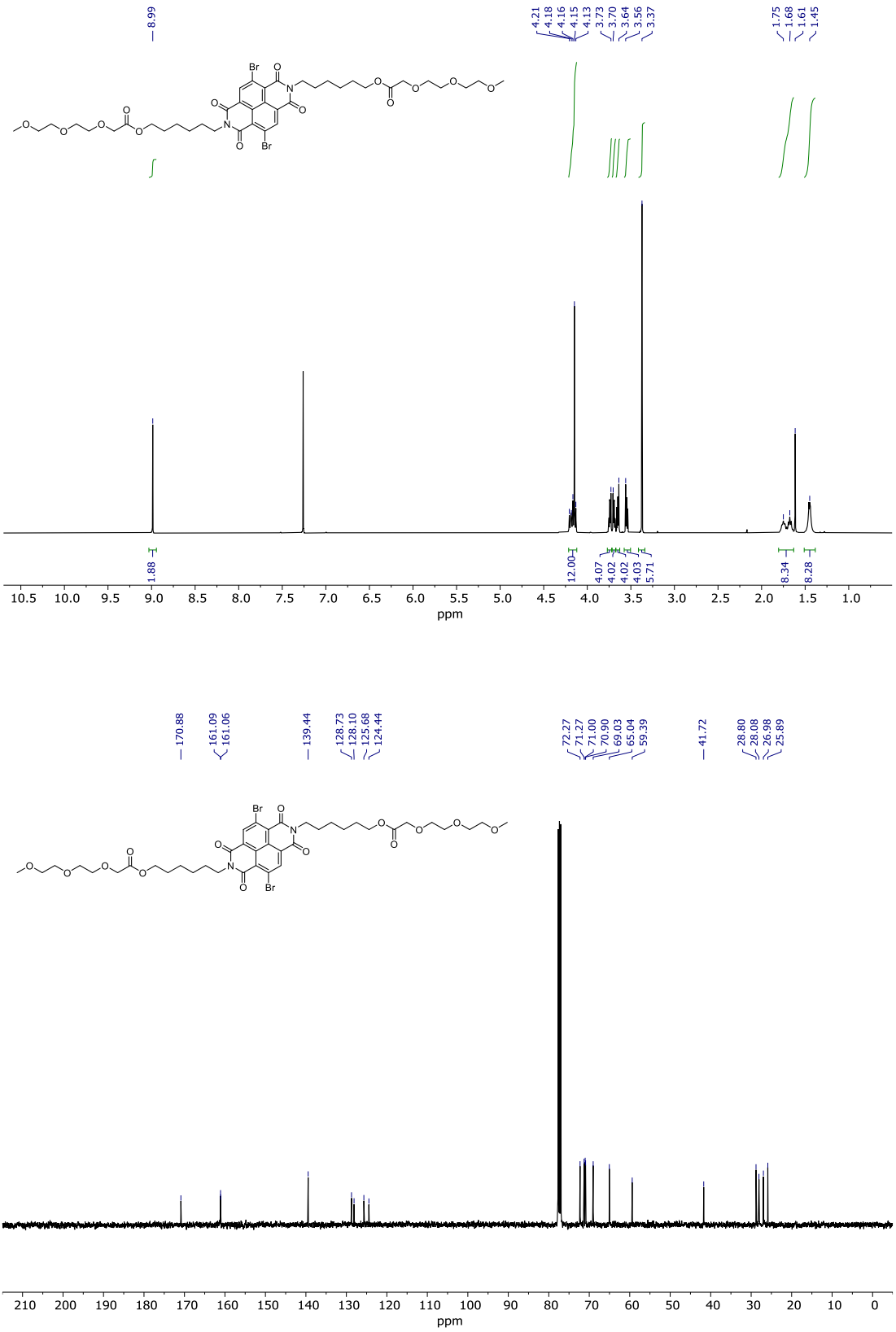


Figure E2. ^{1}H NMR (400 MHz) and ^{13}C NMR (100 MHz) spectra of **2.3** in $CDCl_3$.

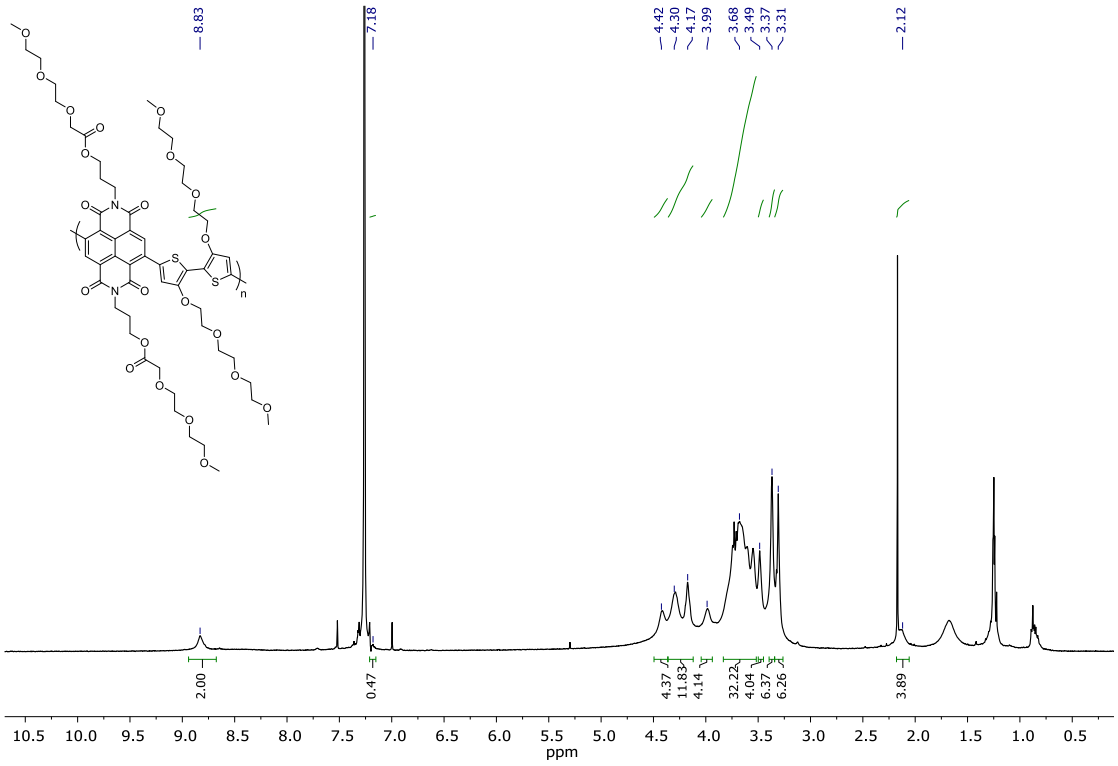


Figure E3. ^{1}H NMR (400 MHz) spectrum of **p(C3-gNDI-gT2)** in $CDCl_3$.

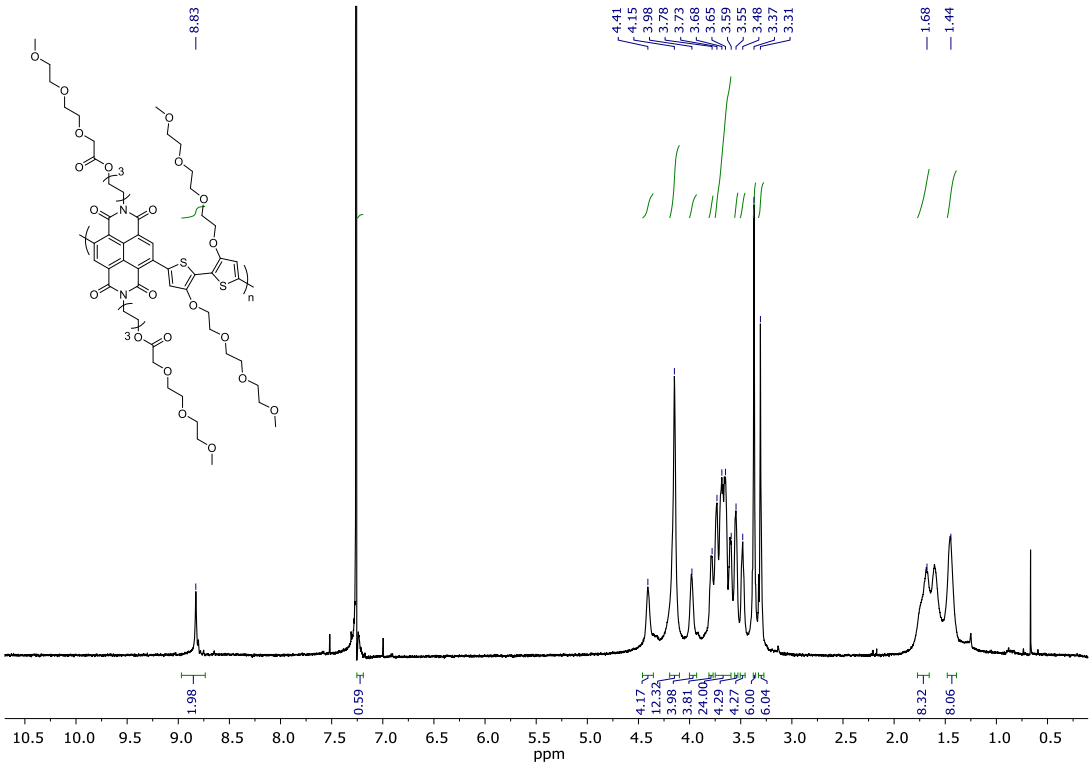


Figure E4. ^{1}H NMR (400 MHz) spectrum of **p(C6-gNDI-gT2)** in $CDCl_3$.

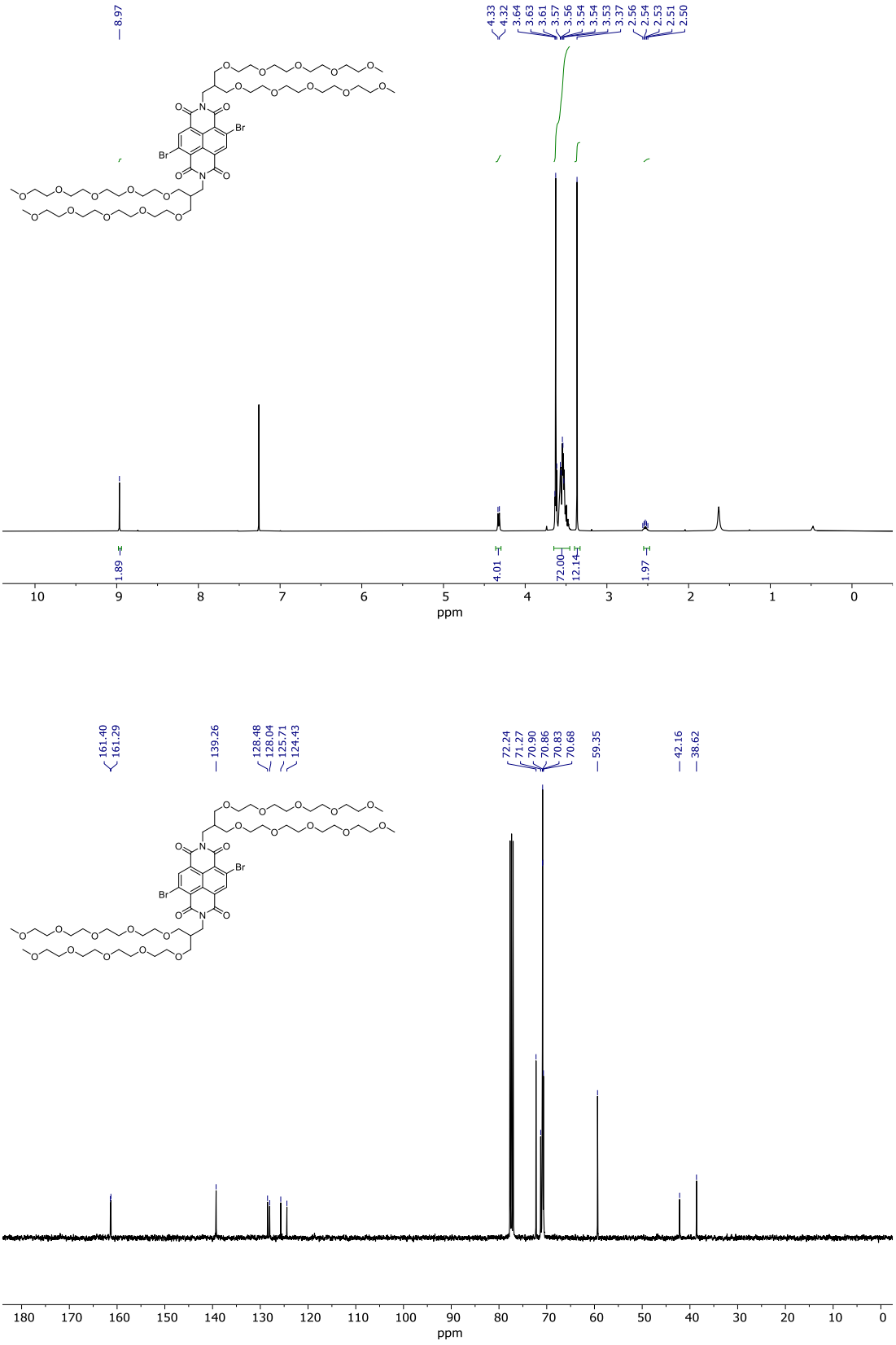


Figure E5. ^{1}H NMR (400 MHz) and ^{13}C NMR (100 MHz) spectra of **3.21** in $CDCl_3$.

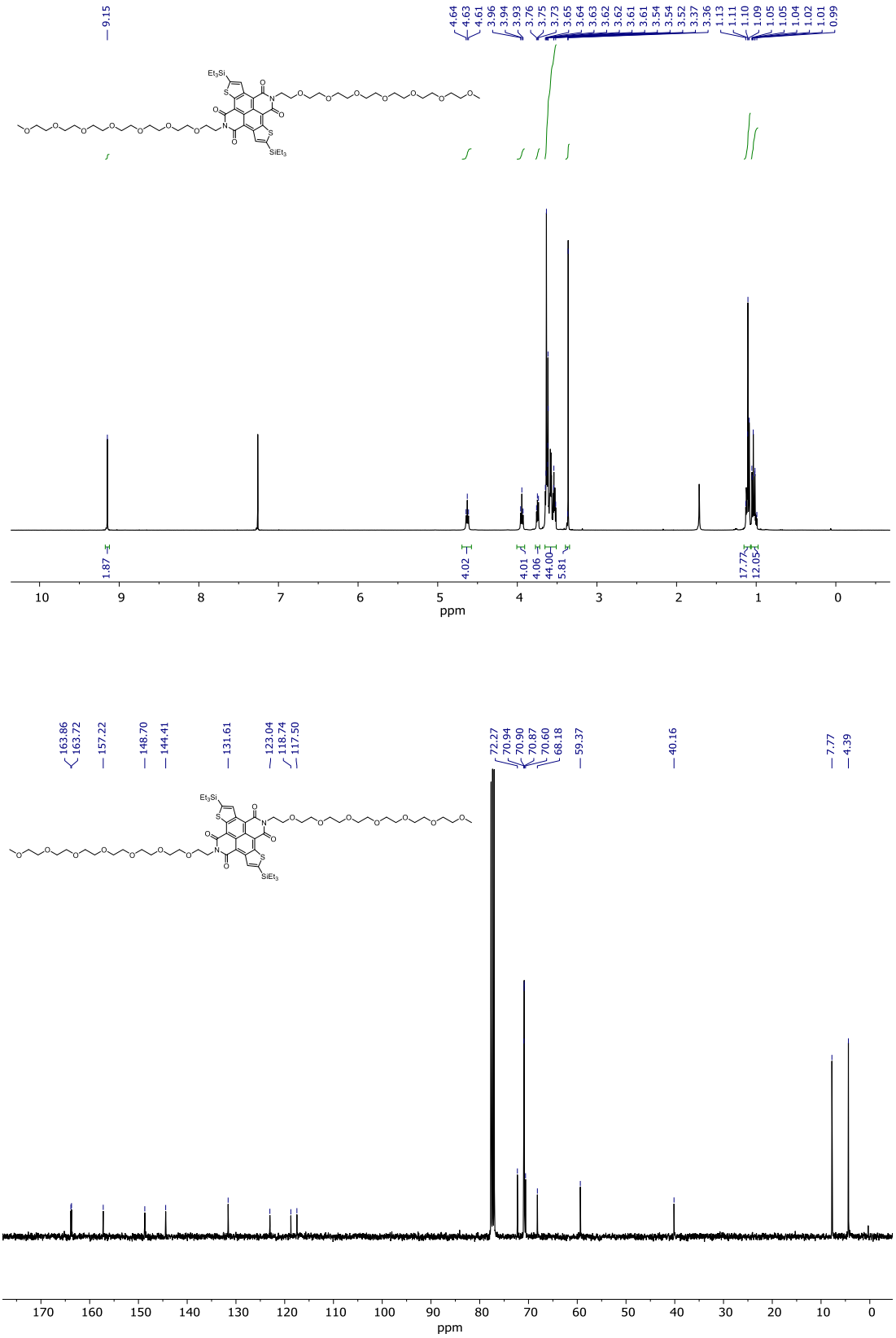


Figure E6. ^{1}H NMR (400 MHz) and ^{13}C NMR (100 MHz) spectra of **3.28** in $CDCl_3$.

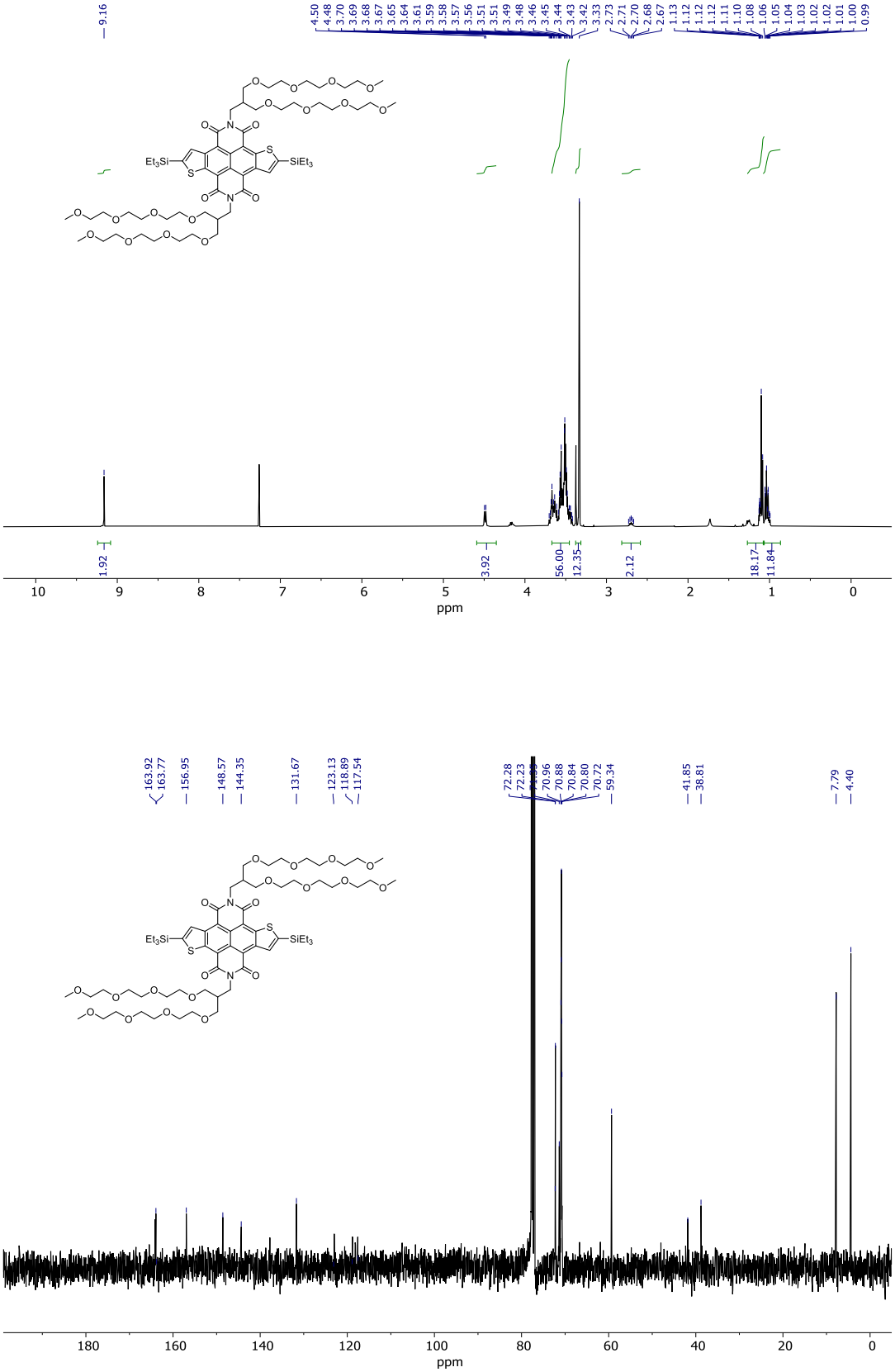


Figure E7. ^{1}H NMR (400 MHz) and ^{13}C NMR (100 MHz) spectra of **3.33** in $CDCl_3$.

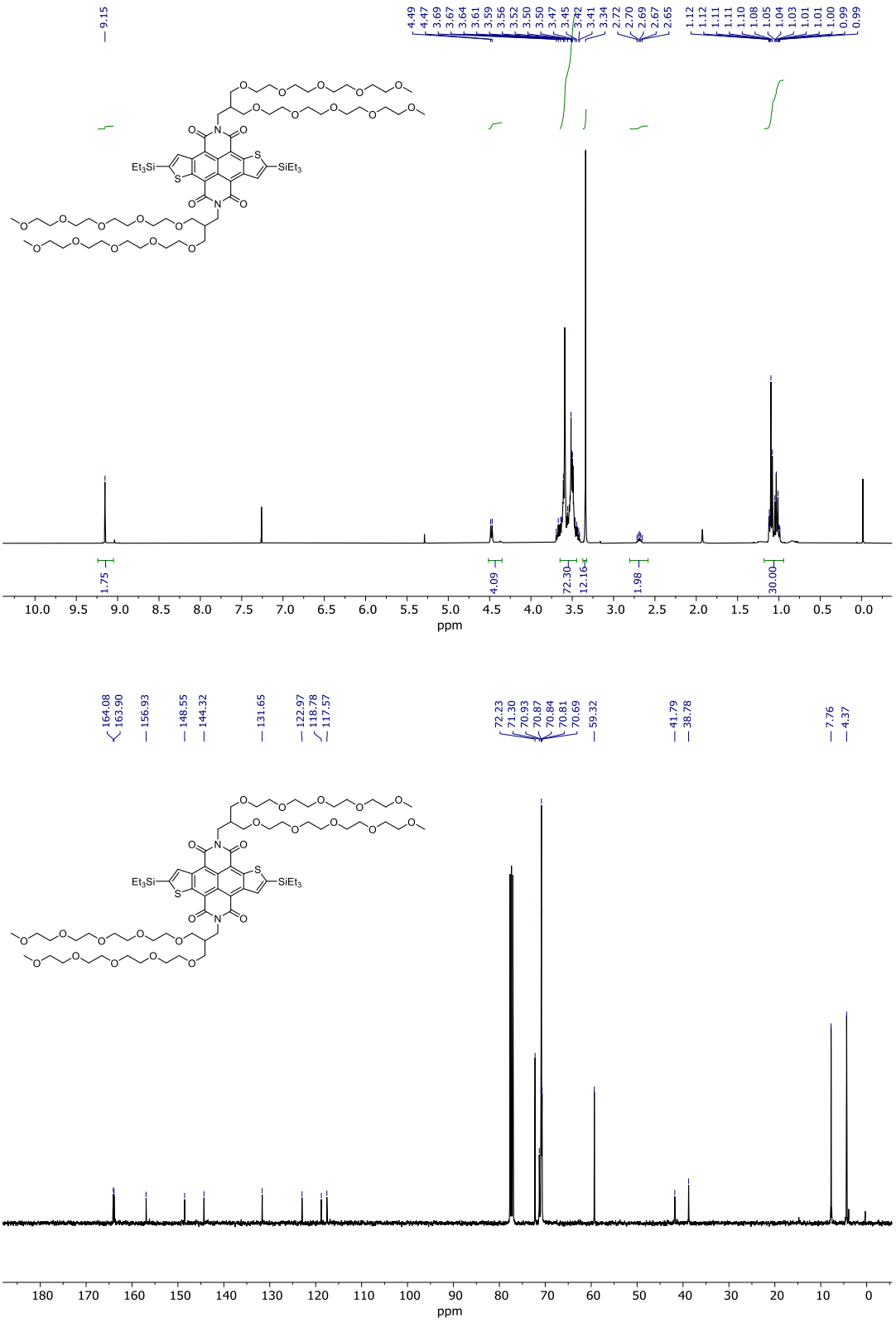


Figure E8. ^{1}H NMR (400 MHz) and ^{13}C NMR (100 MHz) spectra of **3.34** in $CDCl_3$.

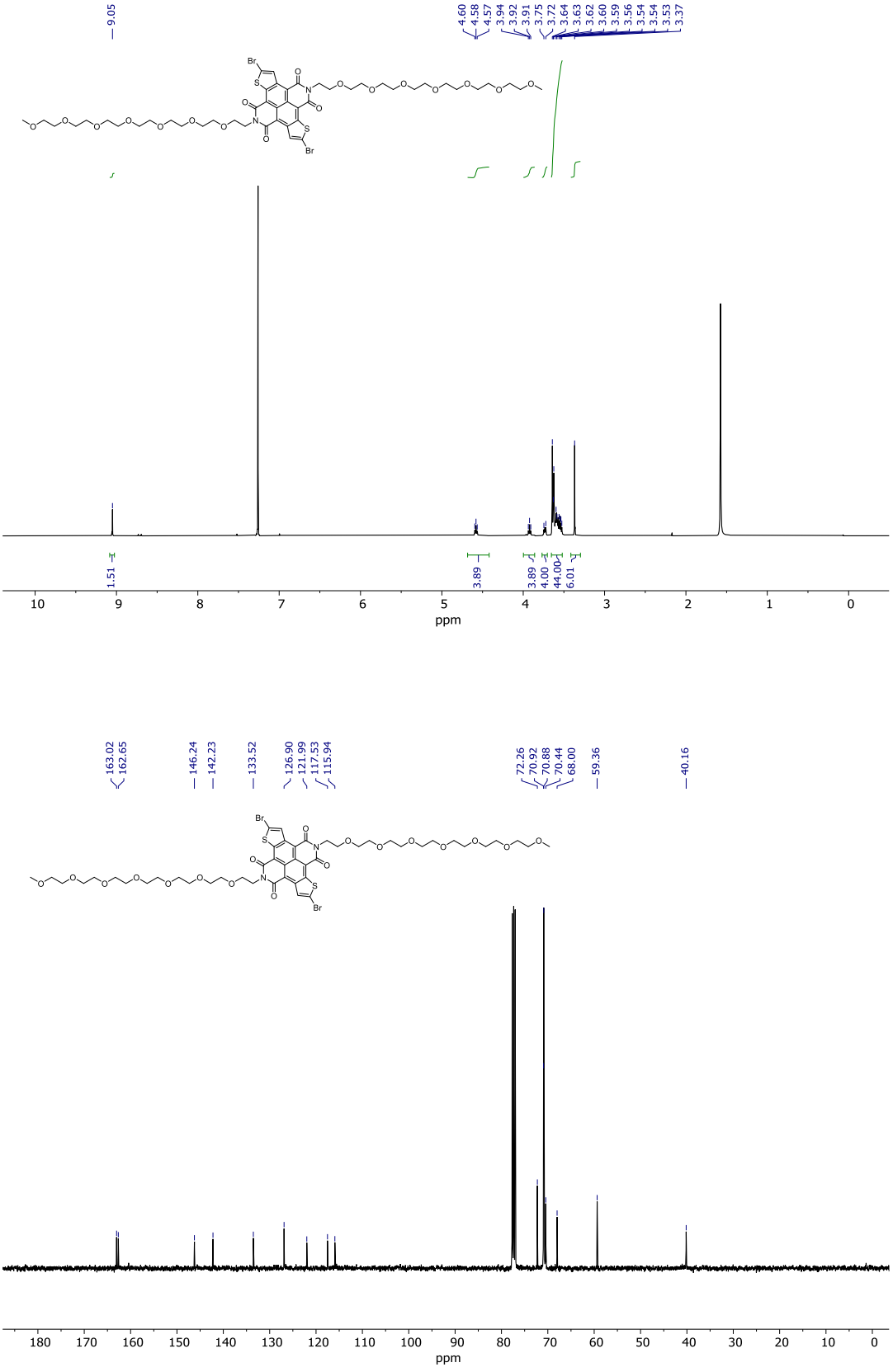


Figure E9. ^{1}H NMR (400 MHz) and ^{13}C NMR (100 MHz) spectra of **3.35** in $CDCl_3$.

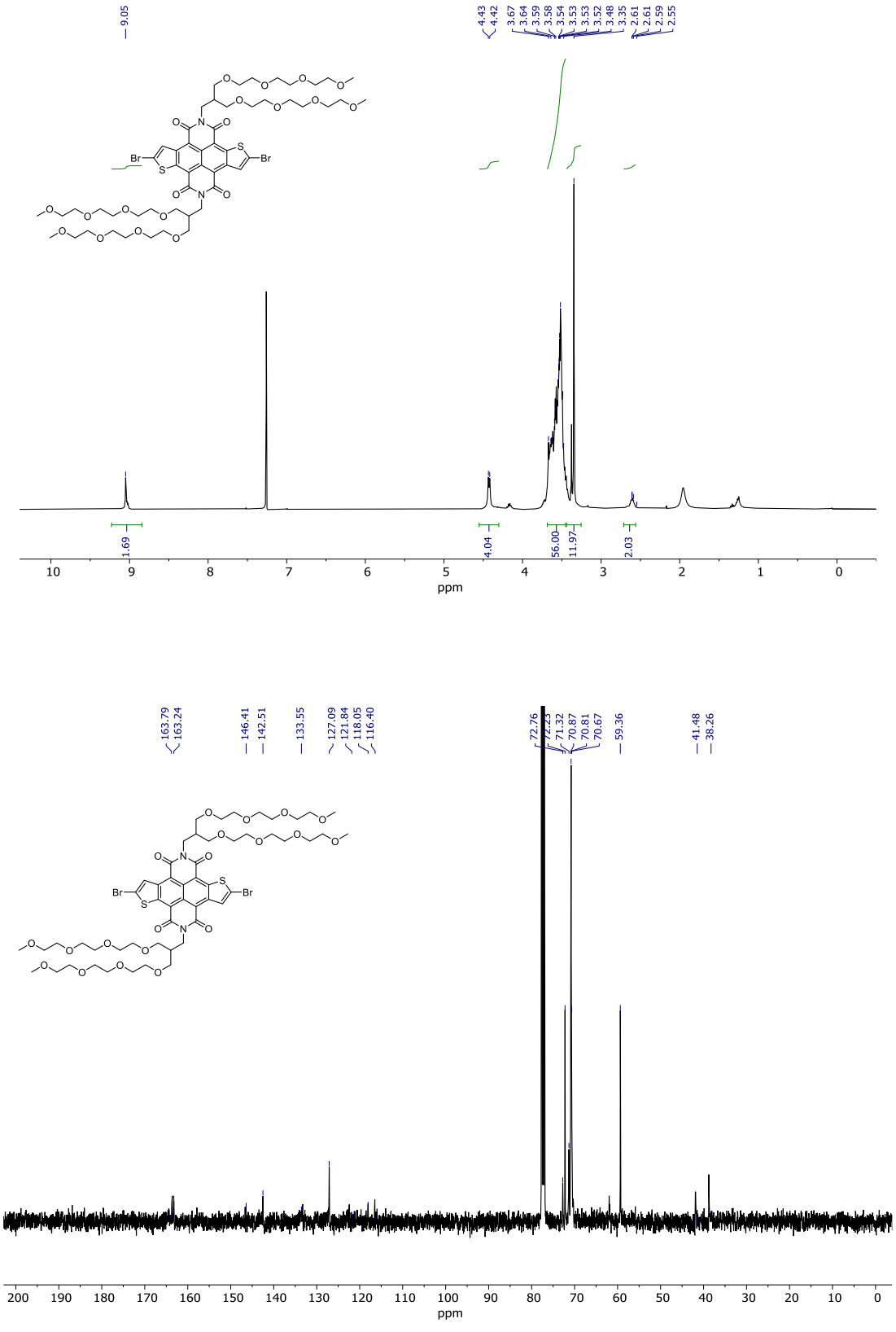


Figure E10. ^{1}H NMR (400 MHz) and ^{13}C NMR (100 MHz) spectra of **3.36** in $CDCl_3$.

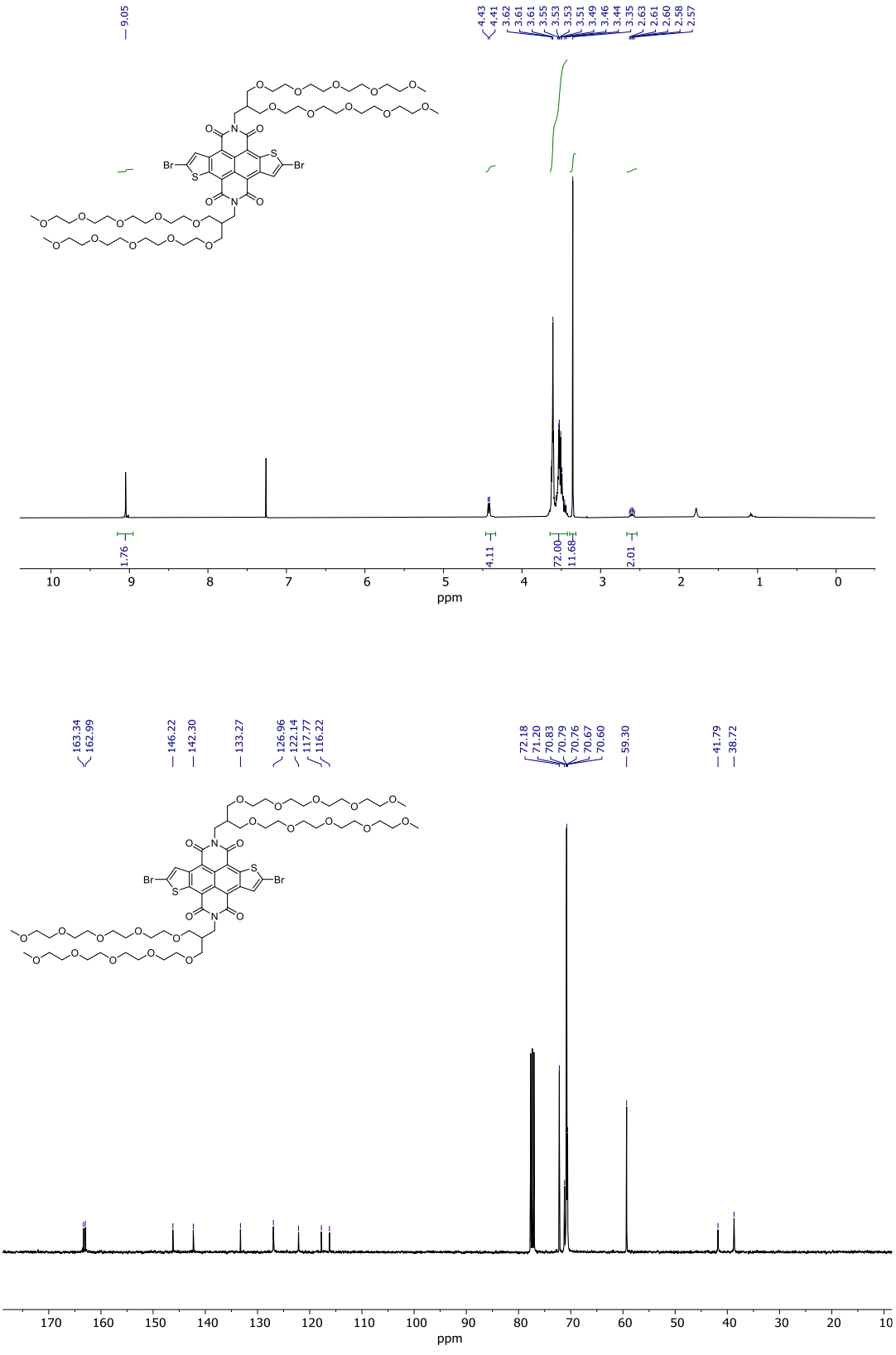


Figure E11. ^{1}H NMR (400 MHz) and ^{13}C NMR (100 MHz) spectra of **3.37** in $CDCl_3$.

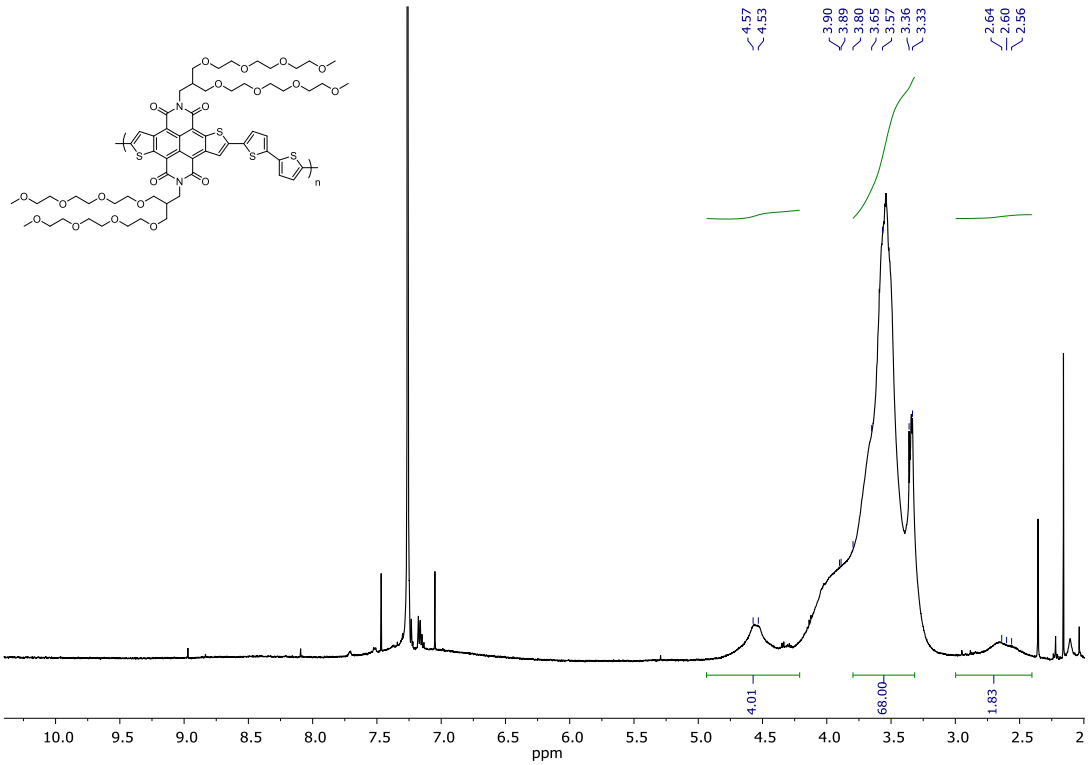


Figure E12. ^{1}H NMR (500 MHz) spectrum of **P3gNDTI** in $CDCl_3$ at 328 K.

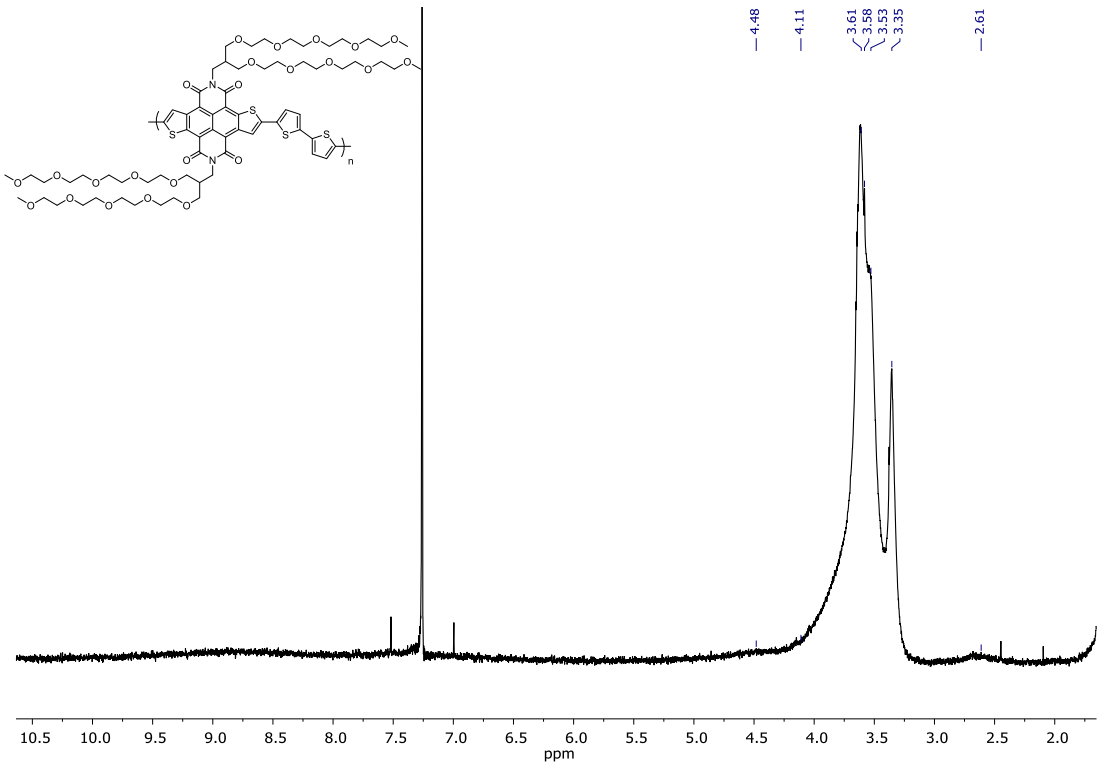


Figure E13. ^{1}H NMR (400 MHz) spectrum of **P4gNDTI** in $CDCl_3$.

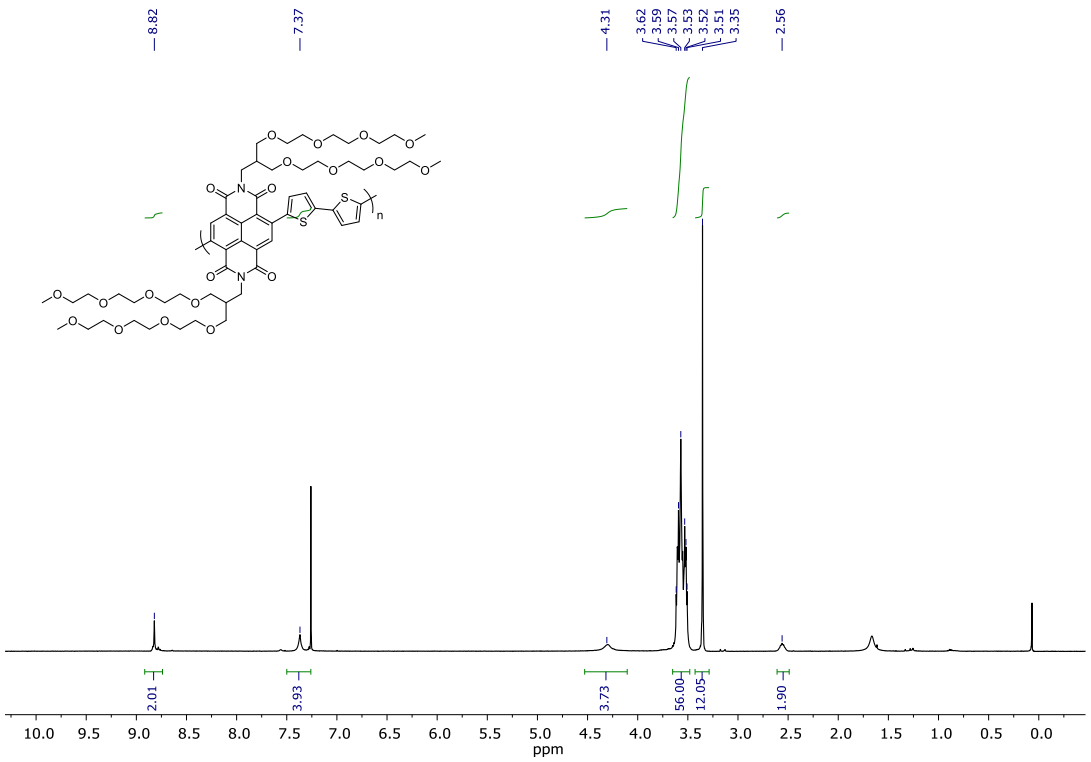


Figure E14. ^{1}H NMR (400 MHz) spectrum of **P3gNDI** in $CDCl_3$.

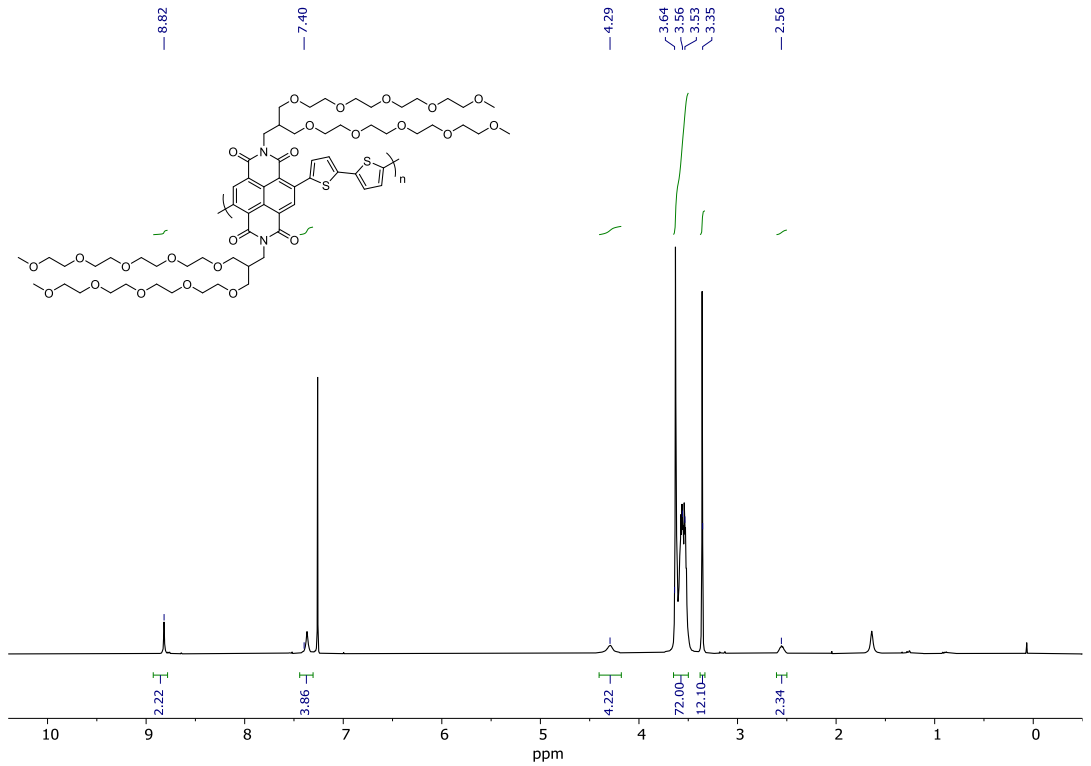


Figure E15. ^{1}H NMR (400 MHz) spectrum of **P4gNDI** in $CDCl_3$.

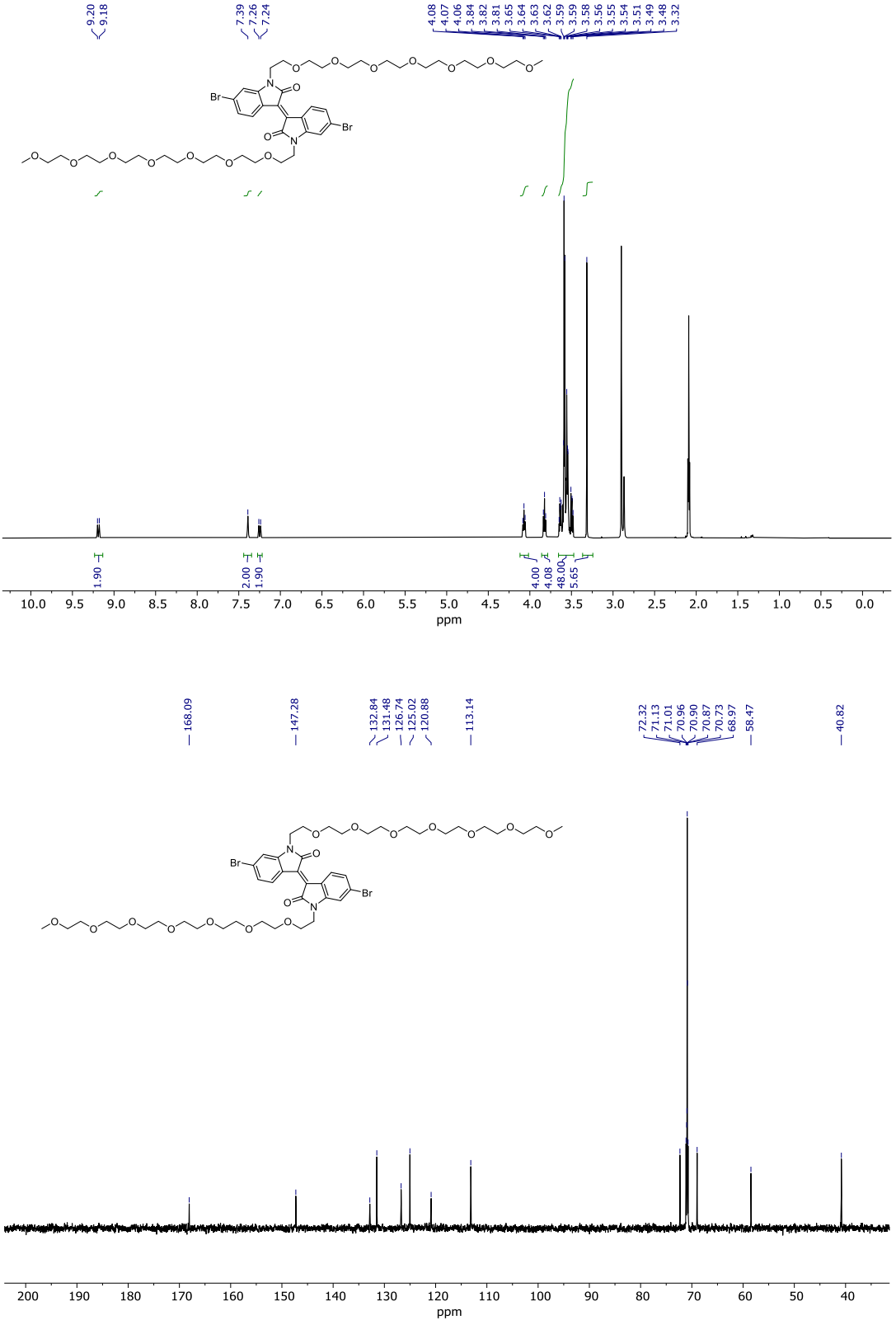


Figure E16. ^{1}H NMR (400 MHz) and ^{13}C NMR (100 MHz) spectra of **4.2** in acetone-d_6.

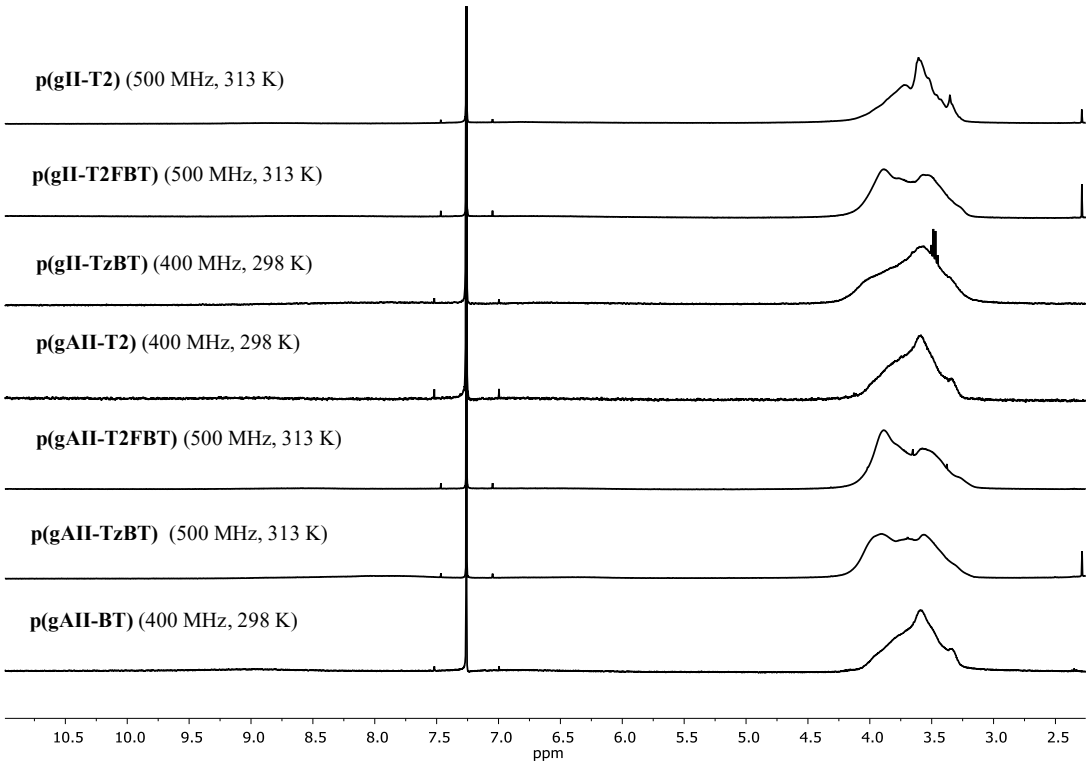


Figure E17. ^{1}H NMR spectrum of (aza)isoindigo copolymers in $CDCl_3$.

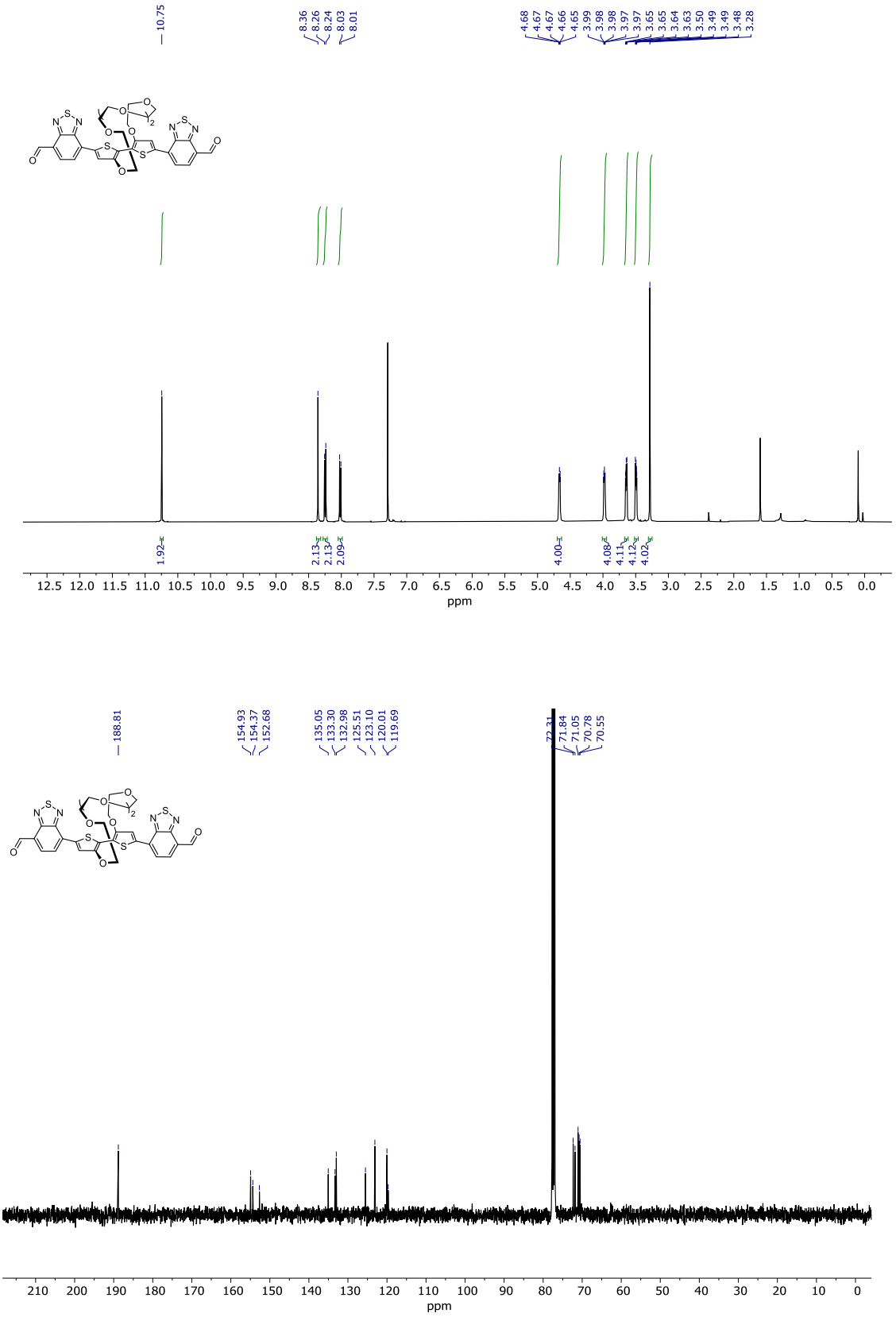


Figure E18. ^{1}H NMR (400 MHz) and ^{13}C NMR (100 MHz) spectra of **(20-crown-6)T2BT** in $CDCl_3$.

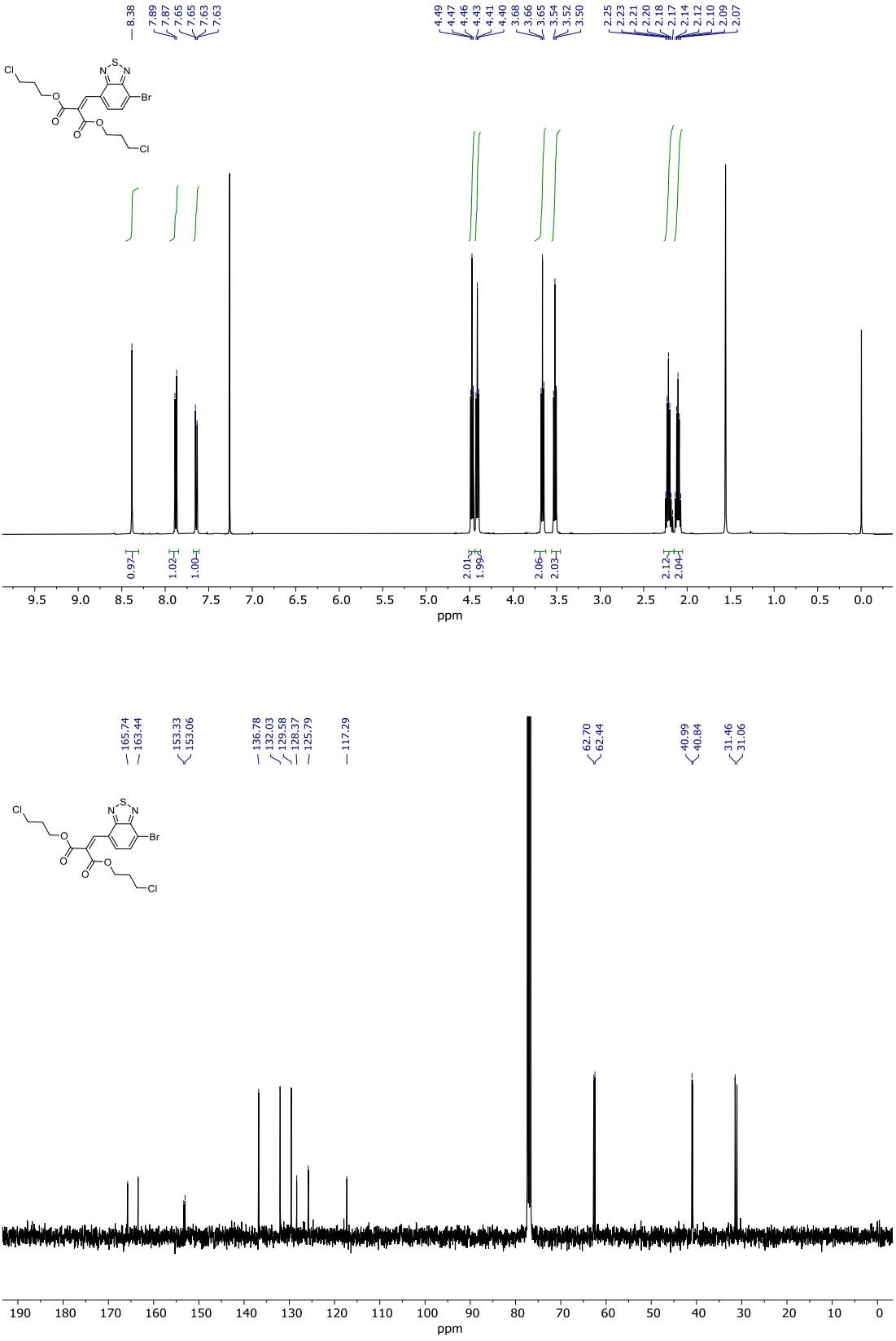


Figure E19. ^{1}H NMR (400 MHz) and ^{13}C NMR (100 MHz) spectra of **S10** in $CDCl_3$.

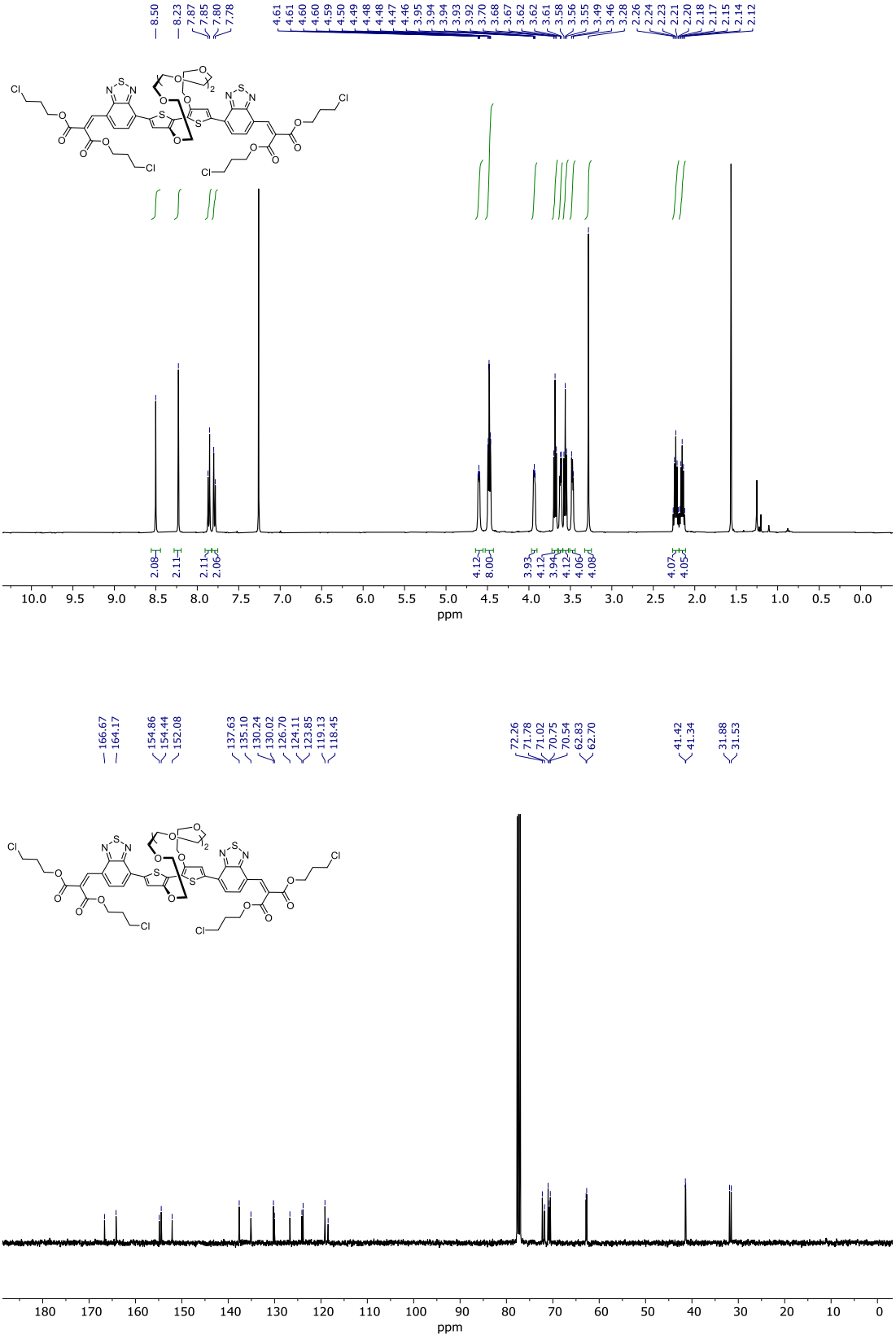


Figure E20. ^{1}H NMR (400 MHz) and ^{13}C NMR (100 MHz) spectra of **S8** in $CDCl_3$.

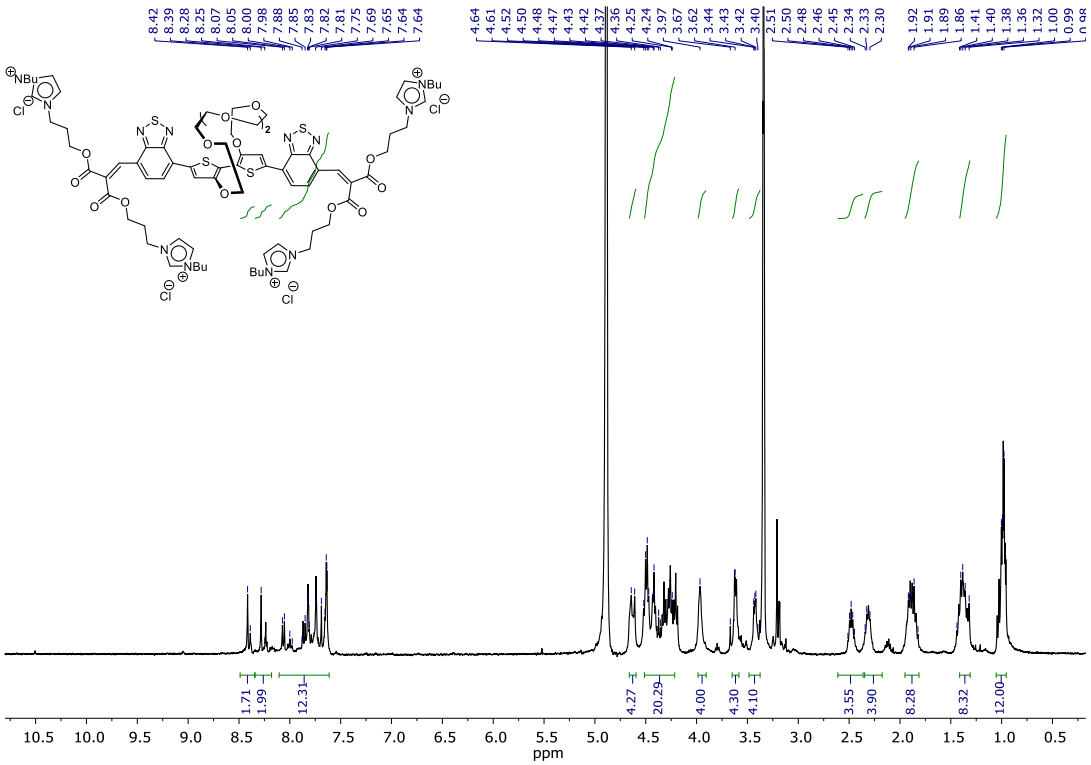


Figure E21. ^{1}H NMR (400 MHz) spectrum of **(20-crown-6)T2BTI** in methanol-*d*.